Dielectric and Magnetic Properties of Fe and Ti Based Perovskite Oxides

A Thesis Submitted

By

Bipul Deka

Roll No: 11612112

In Partial Fulfillment of the Requirements for the Award of the Degree of

Doctor of Philosophy in Physics

Department of Physics
Indian Institute of Technology Guwahati
Guwahati-781039, India

September, 2017

Statement

The work contained in the thesis entitled **"Dielectric and Magnetic Properties of Fe and Ti Based Perovskite Oxide"** has been carried out by me under the supervision of Prof. S. Ravi and Prof. A. Perumal, Department of Physics, Indian Institute of Technology Guwahati. This work has not been submitted elsewhere for the award of any degree.

September, 2017

(Bipul Deka)
Department of Physics
Indian Institute of Technology Guwahati
Guwahati – 781039, India

Certificate

It is certified that the work contained in the thesis entitled **"Dielectric and Magnetic Properties of Fe and Ti Based Perovskite Oxides"** by Mr. Bipul Deka, a PhD student of the Department of Physics, Indian Institute of Technology Guwahati for the award of the degree of *Doctor of Philosophy* has been carried out under our supervision. This work has not been submitted elsewhere for the award of any degree.

September, 2017

Dr. S. Ravi
Professor
Department of Physics
IIT Guwahati
Guwahati-781039
India

Dr. A. Perumal
Professor
Department of Physics
IIT Guwahati
Guwahati-781039
India

Dedicated

to

My Family

Acknowledgements

I express my sincere gratitude to my research supervisors Prof. S. Ravi and Prof. A. Perumal, Department of Physics, Indian Institute of Technology Guwahati for their inspiration, supports and belief on me during my PhD tenure. Their constant guidance and encouragement have been the main driving force to complete the thesis work. It's been a great journey of learning a vast field of Condensed Matter Physics especially magnetism and related experimental techniques from them.

I am thankful to my Doctoral Committee members, Dr. D. Pal (Chairman), Dr. D. Pamu and Prof. G. Pugazhenthi for assessing me during my PhD tenure. I appreciate their comments and suggestions for improving the quality of my research work.

I was surrounded by a group of lab mates and they inspire me in many occasions. I find no words to thank Ranganadha Gopalarao, Junmoni Barman, Bibhuti Bhushan Dash, Pratap Behera, Aakansha, Mahananda Brahma and Ritupon Bora, with whom I grew better and better. I offer my sincere gratitude to my seniors Dr. Biswanath Samantaray, Dr. Sunita Mohanty and Dr. Tribedi Bora for their advice during the early days of my research work.

I am thankful to all the faculty members of the Department of Physics for the atmosphere they created in the department. I recall the help provided by Prof. P. Poulose (present HoD), Prof. S. Basu and Prof. S. Ravi (former HoDs) and their advices.

I am thankful to Dr. Sidananda Sarma and other staff members of the department for their help.

I am thankful to HoC and his teams at Central Instruments Facility (CIF) IIT Guwahati for enabling me to avail several sophisticated instruments to perform experiments during my PhD tenure. I also acknowledge Dr. M. Kar, IIT Patna for extending FE-SEM and ferroelectric loop tracer facilities. I acknowledge Department of Science and Technology for facilitating Vibrating Sample Magnetometer and X-ray Diffractometer (Rigaku, TTRAX III).

I am grateful to Dr. D. Pamu for kind heartedly extending the LCR meter facility to carry out dielectric measurements.

I express my sincere gratitude to Dr. Hitesh Deka, (VC, K. K. Handique State Open University, Assam), Dhrubajyoti Deka and their family for their economic help during my days in post-graduation at Gauhati University. I am indebted to them throughout my life. I am also thankful to Tunu Ram Deka for introducing me to those good personalities.

I express my sincere gratitude to Dr. B. K. Devchoudhury, Principal, Pub-Kamrup College, Assam who had introduced me to the beautiful world of Physics. I am also thankful to my graduation batch-mates at Pub-Kamrup College for their inspiring words then and now.

It's my pleasure to thank my batch-mates at IIT Guwahati. I am also thankful to my seniors Dr. T. Santhosh Kumar, Dr, Bhargab Deka, Dr. Akhilesh Kumar Singh, Dr. Padam Rajender, Dr. Shyni PC and Bhagaban Kishan for being so supportive towards me in many occasions. I admire the help from all the lab mates from Magnetism Group Anabil Gayan, Aneeta M. Pradhan, Ravikumar Patta, Rajkumar Modak, Camelia Das, Dolly Taparia. I am thankful to Dr. P. Mahesh for valuable discussions during the data analysis.

I am grateful to my family members and relatives for their love, care and supports. I admire the help of my neighbors in my village they provided to us.

Last but not the least, I am grateful to Indian Institute of Technology Guwahati and Ministry of Human Resource and Development for providing the financial support to carry out part of the present research work. I am also thankful to Board of Research in Nuclear Science for giving me chance to work in a project supported by them at IIT Guwahati.

Bipul Deka
IIT Guwahati, India
September 2017

Abstract

Multiferroism is a phenomenon of occurrence of two or more ferroic orderings such as ferroelectricity, ferromagnetism and ferroelasticity in the same phase. The recent interest in multiferroics materials is due to their magneto-electric effect and associated applications in multifunctional devices such as multi-state memory elements, spintronic devices, *etc*. In addition to that these materials are studied to understand the fundamental mechanisms responsible for multiple ferroic ordering and the coupling between the ferroic properties. In ferromagnetic materials, the magnetization is controlled by the applied magnetic field and in ferroelectric materials the electric polarization is controlled by the applied electric field. In multiferroic materials due to possible magneto-electric effect, the electric control of magnetization and magnetic control of electric polarization are possible. This coupling offers the design of energy efficient memory devices for recording, reading and spintronics devices. Even though, the original definition for multiferroics includes only for compounds having two or more ferroic ordering, the present trend is to include materials having antiferroic ordering as well.

The potential applicability of a multiferroic compound stems on the magneto-electric coupling. The identified ferroelectric compounds for potential multiferroic applications compounds mostly lack the magnetism. Even if they co-exist, such as in $BiFeO_3$, their origins are quite different and hence the magneto-electric coupling is very weak. Moreover, most of the multiferroic compounds are found to be electrically conducting and making it difficult to switch and withstand the polarization. Dielectric constant of polycrystalline materials is severely affected by their microstructure and heterogeneity such as grains and grain boundaries. The Maxwell-Wagner effect occurring at the grain boundaries often produce apparent colossal dielectric constant misleading to magnetoelectric coupling. Therefore, it is very important to use the impedance spectroscopy together with dielectric and electric modulus formalism to figure out the different electroactive regions in a potential multiferroic compound and their contribution to dielectric constant.

In the present thesis work, we have carried out extensive investigation of magnetic and dielectric properties of some of multiferroic compounds by measuring and analyzing

impedance, dielectric constant and electric modulus and the magnetization. The samples chosen for the present studies are:

(1) $YFe_{1-x}Mn_xO_3$ (x = 0 to 0.3)

(2) $Bi_{1-x}Sm_xFeO_3$ (x = 0 to 0.3)

(3) $PbTi_{1-x}Fe_xO_3$ (x = 0 to 0.3)

(4) $BaTi_{1-x}Fe_xO_3$ (x = 0 to 0.3)

The phase formation and crystal structural properties of the above samples were studied by recording X-ray diffraction (XRD) patterns and analyzing them by Rietveld refinement technique using FULLPROF program. The Raman spectroscopy was used to understand the structural properties further. The microstructural studies were carried out by recording micrographs using a field emission scanning electron microscope (FESEM) and scanning electron microscope (SEM). Field and temperature variations of magnetization were measured using a vibrating sample magnetometer (VSM). The samples were further characterized by using electron spin resonance (ESR/EPR) spectrometer. Dielectric constant and electric modulus data were obtained by recording impedance data using an LCR meter.

Chapter 1 presents a brief introduction to the structure of perovskite oxides and their importance in various research areas. An introductory discussion on magnetism with special emphasis on different types of magnetic exchange interactions and the magnetic orderings is given. The effect of crystal environment, lattice distortion and magnetic anisotropy on the overall magnetic properties of a given material including the exchange bias behavior is discussed. The ac impedance spectroscopy, dielectric spectroscopy and electric modulus spectroscopy are briefly introduced as a tool to study the electrical properties, with special emphasize on different dielectric relaxation models. Finally, the crystal structures of chosen parent compounds and the review of literature on their magnetic and dielectric properties are presented.

Chapter 2 is devoted to detailed experimental techniques followed in the present thesis work for sample preparation and characterization. The method of material preparation and the experimental techniques employed for various physical measurements such as

impedance spectroscopy, dc magnetization etc. are presented. The working principles of relevant sophisticated instruments such as powder X-Ray diffractometer, scanning electron microscope, field emission scanning electron microscope, vibrating sample magnetometer are also discussed.

The structural, magnetic and impedance spectroscopy studies in $YFe_{1-x}Mn_xO_3$ ($x = 0 – 0.3$) compounds are discussed in Chapter 3. These samples crystallize into orthorhombic unit cell having *Pnma* space group. The substitution of Jahn-Teller active Mn^{3+} ions systematically contracts the *bc* plane of orthorhombic unit cell and expands the lattice constant *a*. Study of complex impedance spectrum, dielectric constant and ac electrical conductivity elucidates the role played by both grains and grain boundaries in shaping the dielectric relaxation. The depressed/asymmetric semicircular shape of Nyquist plots depicts the presence of non-Debye type dielectric relaxation and it is attributed to the short-range movement of oxygen vacancies. The magnitude of dielectric constant and its loss component is found to increase with increase in Mn concentration. The dielectric properties are further analyzed in terms of electric modulus formalism. The Nyquist plots are analyzed by fitting them to an equivalent electrical circuit comprising parallel R_GC_G (for grains) and $R_{GB}Q_{GB}$ (for grain boundaries) elements connected in series to electrode resistance. The contribution of conductivities of grains and grain boundaries were estimated.

The parent compound $YFeO_3$ exhibits antiferromagnetic transition with a Néel temperature (T_N) of 646 K. Substitution of Mn^{3+} for Fe^{3+} ions dilutes the superexchange interaction which leads to a decrease in T_N value to 428 K for $x = 0.3$. Mn substitution induces spin reorientation transition at low temperature from Γ_4 ($A_xF_yG_z$) to Γ_1 ($G_xC_yA_z$) spin configuration. The spin reorientation transition temperature is found to increase from 81 K for $x = 0.1$ to 295 K for $x = 0.3$. It is explained in terms of significant magnetic anisotropy introduced by the substituted Mn^{3+} ions. These samples exhibit interesting exchange bias behavior above room temperature. The maximum value of exchange bias field was found to be 1.2 kOe around 413 K. The observed exchange bias is explained in terms of anisotropic exchange interaction across the interface of two magnetic phases having dominant collinear antiferromagnetism and weak ferromagnetism respectively.

Chapter 4 presents the structural, magnetic and dielectric properties of $Bi_{1-x}Sm_xFeO_3$ (x = 0 – 0.3) compounds prepared by sol-gel method. Structural analysis based on XRD patterns and Raman spectroscopy confirms structural transition from rhombohedral to orthorhombic cell due to Sm substitution. Sm substitution reduces the average grain size from a sub-micron level to nanometric side.

Temperature variations of dielectric constant and its loss component show the presence of Polomska transition which shifts downward towards the room temperature with increase in Sm concentration. The frequency dispersion of complex dielectric permittivity was best explained in terms of Havriliak-Negami equation along with conductivity contribution towards permittivity. The Cole-Cole plots of complex dielectric permittivity show two distinct semicircular arcs corresponding to dielectric relaxation due to grains and grain boundaries, respectively. The relaxation dynamics is explained in terms of polaron hopping across Fe^{2+} and Fe^{3+} ions within the grains and short-range movement of oxygen vacancies at the grain boundaries. The dielectric properties were further analyzed in terms of electric modulus, ac impedance, ac conductivity. The Nyquist plots were analyzed by fitting them to an equivalent electrical circuit comprising parallel $R_GQ_GC_G$ (for grains) and $R_{GB}Q_{GB}C_{GB}$ (for grain boundaries) elements connected in series to electrode resistance.

Temperature variations of magnetization (M-T) under zero field-cooled (ZFC) and field-cooled (FC) conditions were measured for an applied field of H = 2 kOe and they indicate the presence of a weak ferromagnetic component of magnetization. Ferromagnetic like behavior with a clear opening in $M - H$ loop was observed for samples with $x \geq 0.15$ along with a linear increase in magnetization at higher applied fields. It reveals the dominance of the strong antiferromagnetic interaction even for the higher concentrations of Sm ions. We have also observed the presence of exchange bias like behavior for x = 0.15 and 0.2 samples. The maximum exchange bias field is found to be 1.36 kOe for x = 0.15 sample at 150 K. The anisotropic exchange interaction at the interface of collinear antiferromagnetic domains of *Pnma* phase and the weak ferromagnetic domains of ferroelectric *R3c* phase contributes towards the observed exchange bias like behavior. The disappearance of exchange bias in x = 0.25 and 0.3 samples is attributed to their monophasic nature of structure.

Chapter 5 presents the effect of Fe doping on the structural, dielectric and magnetic properties of $PbTiO_3$ prepared by solid-state reaction method. The $PbTi_{1-x}Fe_xO_3$ (x = 0 to 0.3) samples are found to crystallize into tetragonal cell with *P4mm* space group. Lattice constant a increases with increase in Fe concentration, while c is found to decrease. The overall variation of lattice parameters and tetragonality with x is discussed in terms of ionic size mismatch between Fe and Ti ions.

Combined Z'' and M'' spectra suggest the presence of three electroactive regions and they are identified as grains, grain boundaries and surface layers based on their capacitance value. Interestingly, the Z'' and M'' peaks for x = 0.25 and 0.3 are found to shift towards lower frequency with increase in temperature upto T = 373 K and 353 K respectively. It depicts the positive temperature coefficient of resistance (PTCR) for x = 0.25 and 0.3 samples. After that temperature, the resistance of these samples decreases with increase in temperature. The M'' and Z'' data were further analyzed both in PTCR and NTCR regions in terms of Bergman four-parameter formulae for generalized susceptibility. The value of relaxation activation energy suggests the ionized oxygen vacancy acts as dipole in tuning the observed dielectric relaxation. Moreover, the exponent used for fitting of Bergman equation shows an anomalous behavior across the PTCR region indicating a considerable interaction among the dielectric species. The Nyquist plots are analyzed by fitting them to an equivalent electrical circuit comprising parallel $R_{SL}C_{SL}$ (for surface layers) and $R_{GB}Q_{GB}C_{GB}$ (for grain boundaries) elements connected in series to grain resistance R_G. Interestingly, the resistance of all the three electroactive regions exhibits the positive temperature coefficient of resistance.

Fe substitution gradually induces ferromagnetic like behavior in $PbTiO_3$. The sample with x = 0.25 and 0.3 show ferromagnetic behavior at room temperature with transition temperature (T_C) 650 K and 660 K respectively. The observed ferromagnetism is explained in terms of double exchange interaction in $Fe^{3+} - O^{2-} - Fe^{4+}$ networks. The isothermal $M - H$ loops were analyzed in terms of law of approach to saturation. The temperature dependence of saturation magnetization and magnetocrystalline anisotropy is discussed. The coercivity is found to increase with the increase in temperature upto certain temperature and beyond that it

decreases. The anomalous increase in coercivity is discussed in the framework of coupling between magnetic and the electric ordering.

Chapter 6 discusses the structural, magnetic, dielectric and ferroelectric properties of $BaTi_{1-x}Fe_xO_3$ (x = 0 – 0.3). Substitution of Fe ions induces structural transition from tetragonal cell with space group *P4mm* to hexagonal (*P6₃/mmc*) phase. Temperature variations of dielectric constant at a fixed frequency show the presence of ferroelectric transition at 365 K for $BaTiO_3$. The ferroelectric transition temperature is found to shift downwards towards the room temperature with increase in Fe concentration. Room temperature ferromagnetism is observed for x = 0.15 – 0.3 samples. The temperature variation of saturation magnetization and coercivity for x = 0.15 – 0.3 are found to be similar to that observed for ferromagnetic compounds. The ferromagnetic transition temperature of the samples are found to be in the range of 397 K for x = 0.15 to 460 K for x = 0.3. The susceptibility data in the paramagnetic region were fitted to Curie-Weiss law. The estimated experimental values of effective magnetic moment (μ_{eff}) from the fitted parameters are found to be comparable to the theoretical μ_{eff} values of Fe^{3+} with high spin configuration (S = 5/2, μ_{eff}^{th} = 5.92 μ_B/Fe). The estimated θ_C values for x = 0.01 – 0.10 samples are found to be in the range -3 K to -50 K, which becomes positive for $x \geq 0.15$ sample. The value of $\theta_C < 0$ for x = 0.01 – 0.1 highlights the antiferromagnetic interaction, while its positive value suggest ferromagnetic interaction for $x \geq 0.15$. The magnetic interaction is discussed in terms of formation of bound magnetic polaron. The initial magnetization curves were fitted to bound magnetic polaron model and temperature variation of different parameters such as M_0, effective spontaneous magnetization m_{eff} are studied. For a given doping concentration, the M_0 values are found to decrease with increase in temperature and this could be understood in terms of reduction in FM interaction among the bound magnetic polarons due to increased thermal energy. However, m_{eff} follows a temperature dependence that is contradictory to M_0. Such temperature variation of m_{eff} could be related to the increase in the size of BMPs with increase ion temperature. The estimated values of bound magnetic polaron radius are found to be in the order of 10^2 Å and are comparable to the volume of the hexagonal phase.

Chapter 7 presents the summary of conclusions drawn from the analysis of experimental data of the above series of samples. We are successful in tailoring the materials

$BaTiO_3$ and $PbTiO_3$ series by Fe substitution to obtain room temperature ferromagnetism. Interesting exchange bias behavior at room temperature has been observed in $YFeO_3$ and $BiFeO_3$ based compounds. Impedance spectroscopic studies identify grains and grain boundaries contribution towards the dielectric relaxation of the samples. A brief write-up about the future scope of research in these types of materials is also presented.

------x------

List of Abbreviations

AFM	Antiferromagnetic(ism)
BMP	Bound Magnetic Polaron
BTO	$BaTiO_3$
BFO	$BiFeO_3$
CBH	Correlated Barrier Hopping
CC	Cole-Cole
CD	Cole-Davidson
CCR	Closed Cycle Refrigerator
CPE	Constant Phase Element
CW	Curie-Weiss
DE	Double Exchange
DM	Dzyaloshinskii-Moriya
EB	Exchange Bias
EDS	Energy Dispersive Spectra
ESR	Electron Spin Resonance
FE	Ferroelectric
FM	Ferromagnetic(ism)
FC	Field-Cooled
FE-SEM	Field Emission Scanning Electron Microscope
G	Grains
GB	Grain Boundaries
HN	Havriliak Negami
JPL	Jonscher's Power Law
JT	Jahn-Teller
KWW	Kohlrausch-Williams-Watts
LAS	Law of Approach to Saturation
NTCR	Negative Temperature Co-efficient of Resistance
OLPT	Overlapping Large Polaron Hopping
OV	Oxygen Vacancy
PTCR	Positive Temperature Co-efficient of Resistance
PTO	$PbTiO_3$
QMT	Quantum Mechanical Tunneling
RKKY	Ruderman-Kittel-Kasuya-Yosida
SE	Superexchange
SPT	Small Polaron Tunneling
TM	Transition Metal
UDR	Universal Dielectric Relaxations
VSM	Vibrating Sample Magnetometer
XRD	X-ray Diffraction
YFO	$YFeO_3$

Table of Contents

List of Figures

Page No.

Chapter 1

Chapter 2

Chapter 3

Chapter 4

Chapter 5

Chapter 6

List of Tables

Page No.

Chapter 3

Chapter 4

Chapter 5

Chapter 6

Chapter 1

Introduction

The ever shrinking size of electronic devices is expected to reach a dead end of a few nanometer sizes and in order to further improve the miniaturized energy efficient electronic devices, scientists are looking for alternate devices other than the conventional semiconductor devices where only the type and concentration of charge carriers are manipulated. Spintronic or spin-electronic devices can serve as energy efficient miniaturized electronic device, where in addition to type and concentration of charge carriers, the spin of the electrons is used as additional degree of freedom. These devices are expected to bring a revolutionary change in the field of energy storage, memory devices, reading and writing devices etc. The advent of multifunctional materials like multiferroics can realize such energy efficient devices, based on the charge-spin coupling through its own existing magnetic and ferroelectric ordering. Multiferroics can offer a possibility of writing the data in electric form (voltage) which can be read by using magnetic or magneto-resistive materials since they possess magnetoelectric coupling. This process is believed to be energy efficient too. Besides the large storage capacity and speed, another aspect of electronic devices is the miniaturizations. Therefore, the quest for multiferroics having significant magnetoelectric coupling and higher dielectric permittivity continues. In this context, perovskite oxides attract the attention of scientific community because of their strong electric polarization and dielectric permittivity.

The ideal perovskite oxide crystallizes in cubic structure with $Pm\bar{3}m$ space group. Its chemical formula is commonly expressed as ABO_3, where the cation B is 6-fold co-ordinated and the A-cation is 12-fold co-ordinated with the oxygen anions [1, 2]. The crystal structure of an ideal perovskite compound is shown in Fig. 1.1. Here the corner

sharing BO_6 octahedra form the skeleton of the structure and the A-site cations occupy the center of the cell. Alternatively, the structure can be viewed as B-site cations occupying the centre of the octahedron and A-site cations at the center of the cell [1, 3].

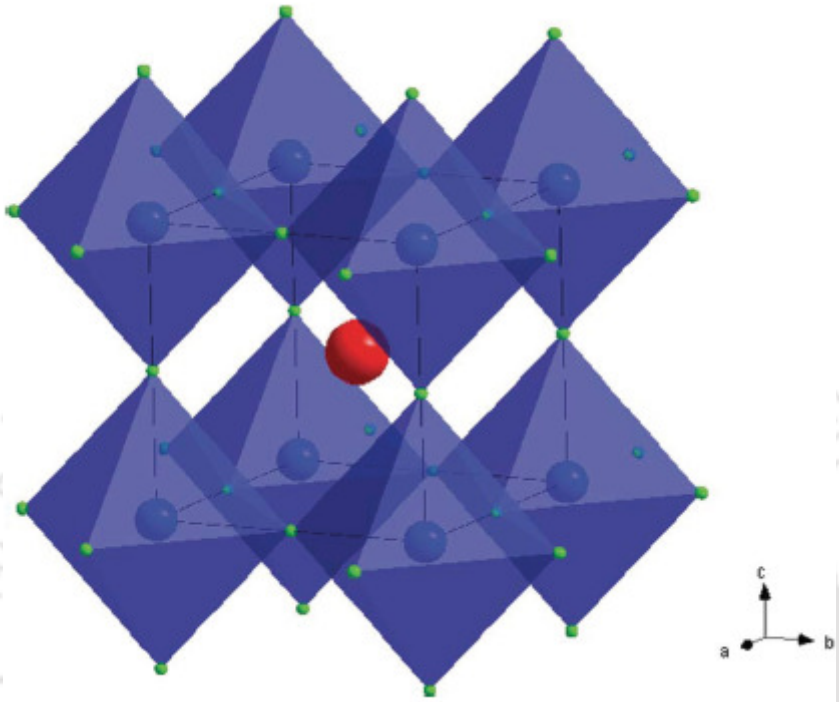

Figure 1.1 Ideal cubic perovskite structure. Red sphere indicates A^{2+} ion, blue sphere represents B^{4+} ions and green sphere represents oxygen ion [4].

The interest in perovskite family of compounds is ever growing due their structure which can accommodate almost all elements in the periodic table [5]. Moreover, the lattice distortion in ideal cubic perovskite structure provides further flexibility in incorporating ions having different sizes. The extent of such distortion from the ideal perovskite structure is determined by Goldschmidt tolerance factor (t) [6]

$$t = \left(\frac{r_A + r_O}{\sqrt{2}(r_B + r_O)} \right) \tag{1.1}$$

where r_A, and r_B are the ionic radii of *A*-site and *B*-site cations and r_O is the ionic radius of oxygen anion. For an ideal perovskite, the tolerance factor $t = 1$. Any deviation in the value of t from unity leads to the distorted structure such as tetragonal, orthorhombic, rhombohedral, etc. Such distortion is associated to (i) the stretching, tilting and rotation of BO_6 octahedra, (ii) the displacement of B-site cation from the center of the octahedron

and (iii) the displacement of A-site cation. These distortions produce low symmetry crystal structure and it plays a major role in various physical properties such as magnetism, dielectric, ferrolectricity, superconductivity, colossal magnetoresistance, charge ordering, *etc.* [5].

In last few decades, perovskite oxides have drawn renewed research interest due to their ferroelectric properties and for potential applications as multiferroics. Multiferroics refer to a class of materials where more than one ferroic ordering such as ferroelectricity, ferromagnetism, ferroelasticity are observed below the transition temperatures [7-9]. However, because of the scarcity of such materials the Ti- and Fe-based perovskite oxides are studied extensively since they carry excellent electrical and magnetic properties.

The following sections present some of the basic mechanisms which are responsible for the observation of rich magnetic and electric properties in perovskite oxides as well as in other compounds.

1.1 Environment Effects on Magnetism

Magnetism arises due to the interaction of magnetic moments or the magnetic dipoles of atoms or ions in a solid. In an isolated atom or ion, the magnetic moment originates from the orbital and spin angular momentum of electrons in the atom. . The collective effect of large number magnetic moments in solids gives rise to fascinating and complex magnetic behavior, which finds applications in every aspect of daily life. Moreover, the magnetic ions in some crystals strongly interact with its immediate environment and produce a large and significant effect. We briefly outline the effect of immediate environment in magnetism.

1.1.1 Crystal Field Effect

The crystal field is the electric field produced by the neighboring ions in a given atomic position [10]. For example, the crystal field in an octahedral environment in perovskite oxides arises mainly from the electrostatic repulsion between the electrons in the orbitals of oxygen anions and that of cation. The symmetry of the crystal determines the strength and nature of the crystal field. One of the most important outcomes of crystal field is the lifting of orbital degeneracy of *d*-orbitals in transition metal oxides. The *d*-

orbitals are subdivided into two sub-orbitals: (i) the t_{2g} orbitals denoted by d_{xy}, d_{yz} and d_{zx} which point in between x, y and z axes, and (ii) the e_g orbitals denoted by $d_{x^2-y^2}$ and $d_{3z^2-r^2}$ that point along x and y axes and z-axis respectively. In octahedral environment, the d_{xy}, d_{yz} and d_{zx} orbitals have lower overlap with p-orbitals of oxygen than that of $d_{x^2-y^2}$ and $d_{3z^2-r^2}$ orbitals. Due to this, the five-fold energy levels of d-orbitals split into threefold t_{2g} levels at lower energy and two fold e_g levels at higher energy as shown in Fig. 1.2.

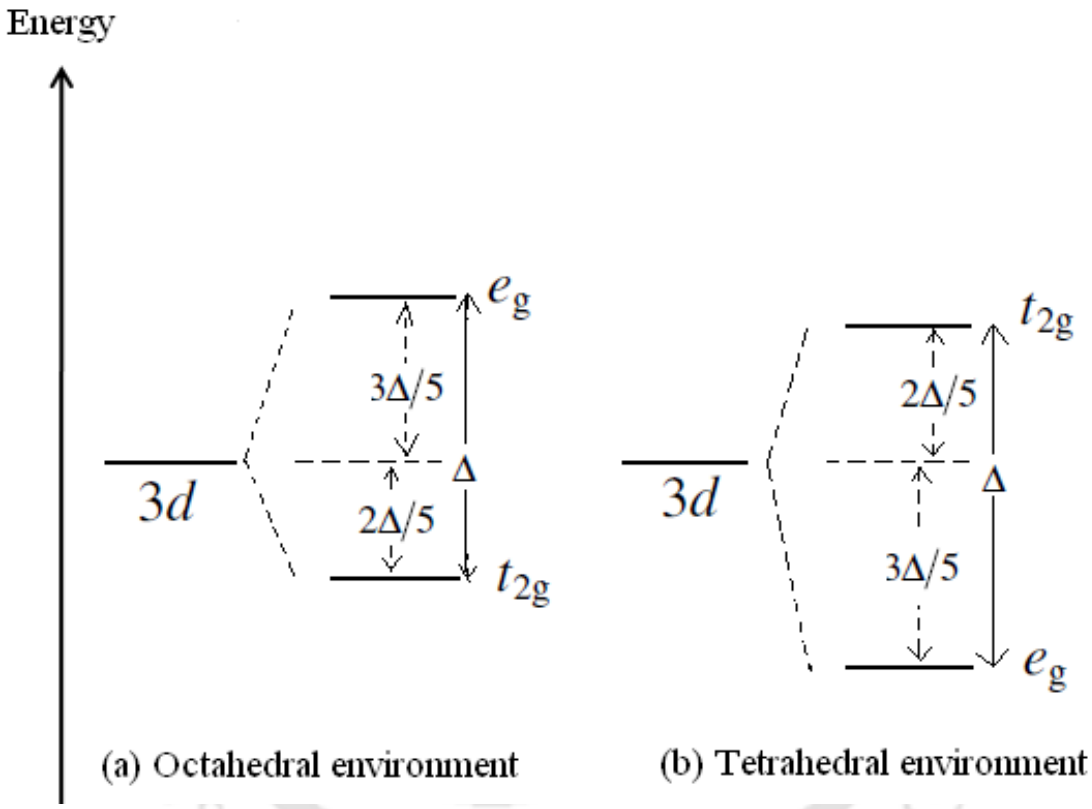

Figure 1.2 Crystal field effect in (*a*) octahedral and (*b*) tetrahedral environments of 3*d*-orbitals in transition elements.

On the other hand, in tetrahedral environment t_{2g} levels are lifted up and e_g levels are shifted down. The competition between the crystal field energy and the Hund's pairing energy determines the spin configuration (high spin or low spin) of transition metal (TM) ions having *d*-orbitals. If the crystal field energy is lower than the pairing energy, high spin state is favorable as the electrons enter the orbitals as per Hund's rule to keep the total spin quantum number (S) maximum. On the other hand, if the crystal field energy is stronger than the pairing energy, the electrons will doubly occupy the lower

energy orbitals before they enter the remaining higher energy levels and favor the low spin state.

Another important crystal field effect is the orbital quenching, which is commonly observed for 3*d* TM ions. The spin-orbit interaction determines the magnetic ground state of an ion and the magnetic moment of an atom or ion in its magnetic ground state is given by $\mu_{eff} = g\sqrt{J(J+1)}$ in the unit of μ_B. However, the experimental ground state magnetic moments of TM ions do not agree with the predicted value except for $3d^5$ and $3d^{10}$ ions for which $L = 0$. In this case, the crystal field interaction is much stronger than the spin-orbit interaction causing the orbital angular momentum to be quenched *i.e.*, $L = 0$. The magnetic moment of such system is only determined by the spin angular momentum. This effect is known as orbital quenching. The orbital quenching explains the experimentally observed ground state magnetic moment of 3*d* TM ions. However the 4*f*, 4*d*, 5*d* series do not possess such effect. In case of 4f ions, the orbital distribution of electrons do not extend far away to get influenced by the electron distributions of neighboring ions since they lie beneath the 5*s* and 5*p* orbitals. So, no crystal field effect comes into picture. For 4*d* and 5*d* series of TM ions, the effect of spin-orbit interaction and crystal field interaction is comparable and the effect is less clear-cut.

1.1.2 Jahn-Teller Distortion

As explained in the preceding section, crystal field lifts the degeneracy of *d*-orbitals by splitting into t_{2g} and e_g levels. The degeneracy of t_{2g} and e_g levels associated to certain electronic configurations can be further lifted by the spontaneous geometrical distortion of lattice. The lifting of orbital degeneracy due to orbital-lattice interaction is known as Jahn-Teller (JT) distortion. The JT distortion is significant for partially filled *d*-orbitals, where there is a net energy gain. The distortion leads to increase in elastic energy and decrease in electronic energy, thus reducing the net energy of the system. The JT distortion occurs in two ways, one by elongation and another by compression. In octahedral environment, the distortion leads to elongation along the *z*-axis and in such case, the overlapping of one of the e_g orbitals $d_{3z^2-r^2}$ with neighboring *p*-orbital of oxygen ions is reduced, while for other e_g orbital ($d_{x^2-y^2}$) it is enhanced. So, the energy level of $d_{x^2-y^2}$ orbital is lifted up compared to $d_{3z^2-r^2}$ level. Similarly in t_{2g} orbital, d_{xy} level is lifted up compared to d_{yz} and d_{zx} levels. On the other hand, the distortion is compressive

in a tetrahedral environment. In such case, $d_{3z^2-r^2}$ level is lifted up compared to $d_{x^2-y^2}$ level in e_g orbital and similarly d_{yz} and d_{zx} levels are lifted up with respect to d_{xy} level in t_{2g} orbital. The Jahn-Teller distortion in Mn^{3+} ion in octahedral environment is shown in Fig.1.3.

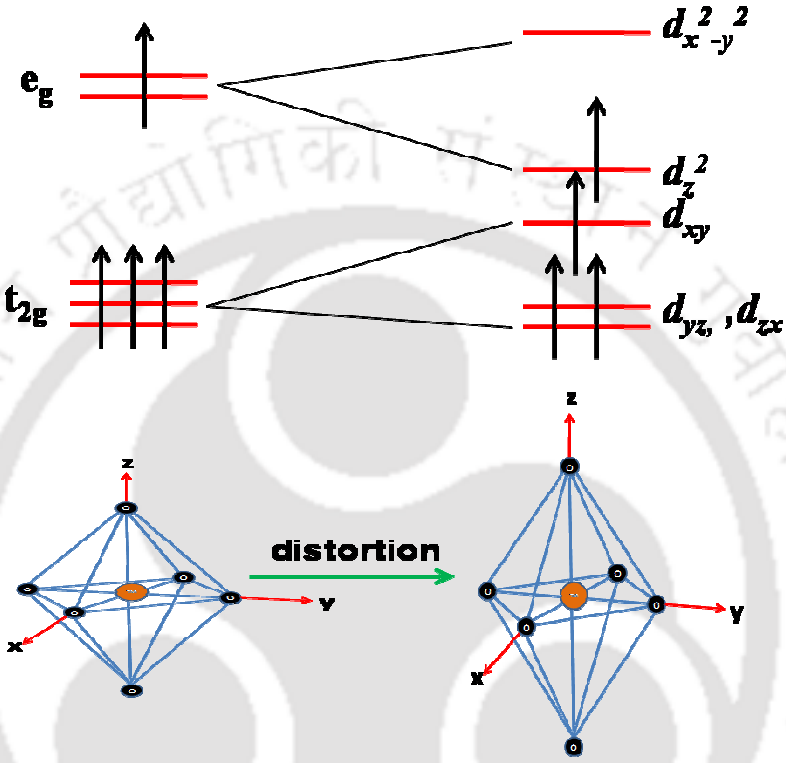

Figure 1.3 Splitting of energy levels due to Jahn-Teller distortion.

1.2 Magnetic Exchange Interactions

In the previous section we have discussed the environmental effects on the electronic configurations and hence the magnetic moment of an isolated atom or ions. In this section, we describe the exchange interactions between such magnetic moments in microscopic scale such that they give rise to long-range magnetic ordering.

Exchange interaction is a quantum mechanical phenomenon and is responsible for the long-range ordering of magnetic moments. The exchange interaction is due to the overlap of electrons wave functions in conjunction with Pauli's exclusion principle. When the spins of two interacting electrons are parallel, the spatial part of the total wave function is antisymmetric under the exchange and when they are opposite, the wave

function is symmetric. The probability distribution of the wave function in space is different for symmetric and antisymmetric wave function. Hence, the electrostatic energy will be different for the symmetric and antisymmetric case. This difference in electrostatic energy is known as exchange interaction, which depends on the orientation of the spins of electrons [10, 11].

There are different types of magnetic interactions and are described briefly as follows:

1.2.1 Direct Exchange Interaction

Two neighboring magnetic moments can interact with each other directly without the aid of any intermediate molecules or ions. This interaction is known as direct exchange (DE). In reality, there is hardly any interesting magnetic phenomenon that could be explained based on the direct exchange. As there is insufficient overlapping of participating magnetic orbitals, direct exchange is not an important mechanism in controlling the magnetic properties.

1.2.2 Superexchange Interaction

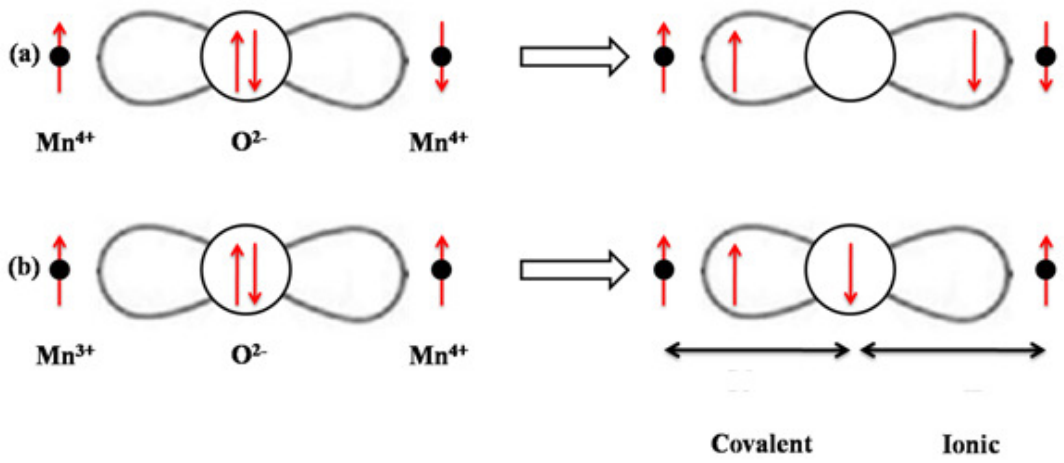

Figure 1.4 Arrangement of spins and orbitals in (*a*) an antiferromagnetic superexchange interaction, and (*b*) a ferromagnetic superexchange interaction.

Superexchange interaction is an indirect exchange interaction, where two non-neighboring magnetic ions interact with each other through an intermediate non-magnetic ion. According to Kramers' model [12], interaction between the cations having more than

half filled *d*-shells gives rise to the antiferromagnetic interaction, while such interaction among cations having less than half filled *d*-shells gives rise to ferromagnetic interaction.

Schematic representations of superexchange interactions producing antiferromagnetism (AFM) and ferromagnetism (FM) are shown in Fig. 1.4 (*a*) and (*b*) respectively. Fig. 1.4 (*a*) shows the situation, where the 3*d* orbitals are pointing towards the O-2*p* orbital. The overlapping of 3*d* and *p* orbitals facilitates the simultaneous covalent bond formation between the cations (Mn^{4+}) and the intermediate anion (O^{2-}). Here, out of two valence electrons of oxygen, the up spin electron spends some time with the cation in one side having up spin configuration and the down spin electron spends some time with other cation having down spin configuration to satisfy the Hund's rule. In this process, each cation-anion pair has ferromagnetic (parallel) alignment of electrons and the net cation-cation interaction is antiferromagnetic.

According to Goodenough [13], the above covalent bonding is not permissible if the core spins of magnetic cations are aligned parallel as shown in Fig. 1.4 (*b*). In such situation, out of two valence electrons of O^{2-}, the spin up electron forms covalent bonding with left side cation (Mn^{3+}) having spin up electron, while the spin down electron of oxygen forms ionic bond with right side cation (Mn^{4+}) [13]. The direct exchange between oxygen and the right side cation is antiferromagnetic. So, overall ferromagnetic interaction prevails between Mn^{3+} and Mn^{4+} ions.

1.2.3 Ruderman-Kittel-Kasuya-Yoshida Interaction

It is a special kind of indirect exchange interaction commonly seen in metals having localized magnetic moments and the interaction is mediated via the itinerant electrons. The localized magnetic moment of an ion spin-polarizes the conduction electrons and this spin-polarized electrons couple to the neighboring localized magnetic moment at a distance *r* away [14-16]. The coupling takes the form of an *r*-dependent exchange interaction $J_{RKKY}(r)$ given by

$$J_{RKKY}(r) \propto \frac{\cos(2k_F r)}{r^3} \tag{1.2}$$

where k_F is the Fermi wave vector of the electron gas. It is a long range coupling and anisotropic, and in addition to that it exhibits the oscillating behavior over the space.

Hence, the Ruderman-Kittel-Kasuya-Yoshida (RKKY) interaction could be FM or AFM depending on the distance between the magnetic ions.

1.2.4 Double Exchange Interaction

Zener [17, 18] introduced the concept of double exchange (DE) interaction in 1951, and showed that FM interactions are energetically favored in the presence of mixed valence cations. Similar to RKKY interaction, DE interaction is also a carrier mediated exchange interaction and is observed commonly in mixed-valence compounds. For such compounds the conduction electrons hop from the lower valent cations to higher valent cations through oxygen anions. In such case, Hund's rule is satisfied on both ions only if they are oriented parallel to each other and hence leads to FM. The FM alignment due to DE interaction can be understood as shown in Fig.1.5. The movement of electron can be shown as, $Mn^{3+}_{1\uparrow}O_{2\uparrow,3\downarrow}Mn^{4+} \rightarrow Mn^{4+}O_{1\uparrow,3\downarrow}Mn^{3+}_{2\uparrow}$, where the electron spins are labeled as 1, 2 and 3. Anderson and Hasegawa [19] presented the DE mechanism in detail by visualizing a second order process in which the electron transfer takes as follows $Mn^{3+}_{1\uparrow}O_{2\uparrow,3\downarrow}Mn^{4+} \rightarrow Mn^{3+}_{1\uparrow}O_{3\downarrow}Mn^{3+}_{2\uparrow} \rightarrow Mn^{4+}O_{1\uparrow,3\downarrow}Mn^{3+}_{2\uparrow}$.

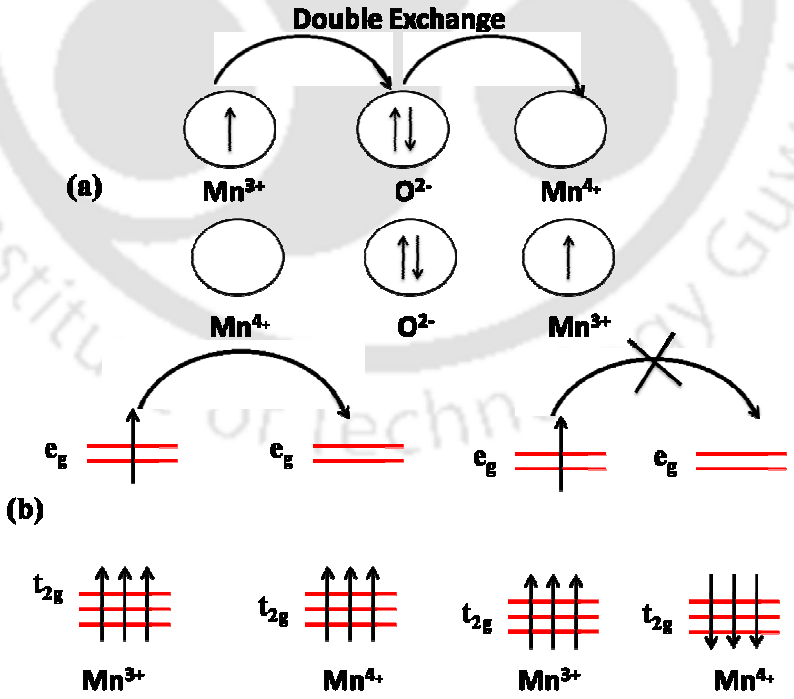

Figure 1.5 (*a*) Double exchange interaction between Mn ions and (*b*) Hopping of electron is possible only if the localized spins are polarized.

Double exchange interaction always gives rise to FM. The configurations Mn^{3+}-O^{2-}-Mn^{4+} and Mn^{4+}-O^{2-}-Mn^{3+} will be degenerated as shown in Fig. 1.5 (*a*). If the magnetic spins are not parallel, the electron transfer becomes more difficult due to strong onsite Hund's coupling as shown in Fig. 1.5 (*b*). The electron transfer is also more difficult if the Mn-O-Mn bond is considerably bent. When the Mn–O–Mn bond angle is 180°, the overlap of the manganese *d*-orbitals and the oxygen *p*-orbital is the largest and hence the strongest interactions and the interaction strength decrease with deviation from this bond angle.

1.2.5 Dzyaloshinskii-Moriya Exchange Interaction

The Dzyaloshinskii-Moriya (DM) exchange interaction is a type of anisotropic exchange interaction between the excited state of a magnetic ion produced by the spin-orbit interaction and the ground state of the other magnetic ions [20, 21]. The DM exchange interaction produces small canting of the spins and produces weak ferromagnetism in an otherwise antiferromagnetic system. The DM exchange energy is defined as:

$$H_{DM} = \boldsymbol{D} \cdot (\boldsymbol{S_1} \times \boldsymbol{S_2}) \qquad (1.3)$$

where $\boldsymbol{S}_1$ and $\boldsymbol{S}_2$ are two neighboring spins and $\boldsymbol{D}$ is Dzyaloshinskii-Moriya constant. The DM interaction tries to align the vectors $\boldsymbol{S_1}$ and $\boldsymbol{S_2}$ at right angles in a plane perpendicular to the vector $\boldsymbol{D}$. Its very effect is to cant the spins by a small angle. The DM interaction is responsible for the observation of weak ferromagnetic moment for antiferromagnetic samples. The antisymmetric exchange interaction is of importance for the study of magnetism induced electric polarization in multiferroic systems.

1.3 Magnetic Ordering

Isolated magnetic moments, which do not interact with others, give rise to two simple magnetic effects: diamagnetism and paramagnetism. However, in some of the solids, the isolated magnetic moments interact with each other such that they produce the collective magnetism. The collective magnetism is in different ground states depending on the nature of interaction. The different ground states include ferromagnetism, antiferromagnetism, spin glasses, spiral and helical structures etc. In this section, we briefly discuss about the basic magnetic orderings.

1.3.1 Diamagnetism

Diamagnetism is the tendency of a material to oppose the external magnetic field. Here, an externally applied magnetic field induces magnetic moments, which align antiparallel to the applied magnetic field according to the Lenz's law. Hence, the magnetic susceptibility of a diamagnetic substance is always negative. A few examples are nearly all organic materials, metals like Hg, superconductors below the critical temperature, etc.

1.3.2 Paramagnetism

Paramagnetism (PM) corresponds to positive susceptibility, where the applied field tends to align the magnetic moments along the field direction. However, due to thermal agitation, they cannot be completely aligned along the field direction. So, they give rise to small positive magnetization or susceptibility. Here, as the magnetic moments do not interact with each other, there is no directional orientation of magnetic moments in the absence of applied field and hence the net magnetization is zero. The magnetic moments can be localized or itinerant nature. The inner shell electrons in partially filled 4*f* orbitals in rare-earth metals and 5*f* orbitals in actinides are examples of localized moments. This class of paramagnetism is known as Langevin paramagnetism. On the other hand, electrons in the vicinity of Fermi level cause the itinerant moments and the susceptibility associated to itinerate moment is known as Pauli paramagnetism. The Langevin paramagnetism is very large compared to Pauli paramagnetism.

The paramagnetic susceptibility or Langevin paramagnetism varies inversely with temperature. By considering the quantum mechanical approach, the paramagnetic susceptibility at low magnetic field can be written as [10]:

$$\chi = \frac{N\mu_0 g^2 \mu_B^2 J(J+1)}{3k_B T} \tag{1.4}$$

where, g is Landé g-factor and it is written as [10],

$$g = \frac{3}{2} + \frac{S(S+1) - L(L+1)}{2J(J+1)} \tag{1.5}$$

Here L, S and J represent orbital, spin and total angular quantum number of the magnetic element, N is the number of dipoles per unit volume (for volume susceptibility) and μ_0 is the permeability of free space. On the other hand, Pauli paramagnetism does not depend on temperature.

1.3.3 Ferromagnetism

Ferromagnetism (FM) corresponds to the non-zero value of magnetic susceptibility even in the absence of applied magnetic field. It is because of the parallel alignment of the magnetic moments, due to presence of an internal magnetic field. According to Weiss molecular field theory, the magnetic moment or magnetic spin of each atom/ion is under the influence of molecular field produced by other magnetic spins. Here the molecular field aligns all neighboring moments parallel to each other such that there is a net magnetization even in the absence of magnetic field.

However, such ferromagnetic behavior is observed below a critical temperature known as the transition temperature T_C. For $T > T_C$, mostly they behave like a paramagnet with susceptibility,

$$\chi = \frac{C}{T - \theta_C} \tag{1.6}$$

where C and θ_C are Curie constant and Curie temperature respectively. The above equation is known as Curie-Weiss law. Here $C = \mu_0 N g^2 \mu_B^2 J(J+1)/3k_B$ or $C = \mu_0 N \mu^2/3k_B$, where μ is the magnetic moment of each dipole. Some of common ferromagnetic materials are Fe, Co and Ni. Typical θ_C values of Fe, Ni and Co are 1043 K, 1394 K and 631 K respectively.

1.3.4 Antiferromagnetism

For an antiferromagnetic (AFM) substance, the molecular field is such that it aligns the nearest neighbor magnetic moments antiparallel to each another so that the net magnetic moment is zero below certain temperature known as Néel temperature (T_N) and above that it mostly behaves like paramagnet. The magnetic susceptibility in the paramagnetic region of such substance is written as,

$$\chi = \frac{C}{T + T_N} \tag{1.7}$$

The examples of antiferromagnetic materials are MnF_2, MnO, CoO, FeO, Cr_2O_3, α-Fe_2O_3 with respective Néel temperature of 67 K, 116 K, 292 K, 116 K, 307 K and 950 K.

1.3.5 Ferrimagnetism

Ferrimagnetism (FiM) is a special type of antiferromagnetism where the magnitude of magnetization of the sublattices is not equal and therefore unlike antiferromagnetism a net magnetization is observed. Here in some of the materials, the different temperature dependences of sublattice magnetization can give rise to magnetic compensation (M = 0) and negative magnetization. This is known as magnetization reversal. Some of the FiM materials are $NiCr_2O_4$ and $CoFe_2O_4$ based materials.

1.4 Magnetic Anisotropy

Magnetic anisotropy is the directional dependence of material's magnetic properties. The magnetic moments tend to align easily along certain crystallographic axis since such easy axis is energetically favorable. Magnetic anisotropies determine the shape of magnetic hysteresis loop, initial magnetization, magnetization value, remnant magnetization, coercivity etc. Below we describe briefly some of the most important types of magnetic anisotropies:

Magneto-crystalline Anisotropy:

The spin-orbit interaction of electrons results in preferred alignment of magnetic moment along certain crystallographic axis [11]. Therefore, along a specific direction, it is easier to magnetize the material compared to other directions and is known as the magneto-crystalline anisotropy. The magneto-crystalline anisotropy energy is smaller compared to that of exchange interaction. The energy associated in the crystal having magnetization orientation away from the easy axis is given as [10, 11]:

$$E_{an} = K_0 + K_1\left(\alpha_1^2\alpha_2^2 + \alpha_2^2\alpha_3^2 + \alpha_3^2\alpha_1^2\right) + K_2\left(\alpha_1^2\alpha_2^2\alpha_3^2\right) + \cdots \qquad (1.8)$$

Here K_0, K_1 and K_2 are constants for a particular crystal at a particular temperature and α_1, α_2 and α_3 are the direction cosines of the magnetization with respect to crystallographic axes a, b and c. The anisotropic energy is generally larger for low symmetric crystals. For example, cubic Fe and Ni have $K_1 = 4.8\times10^4$ Jm^{-3} and -5.7×10^3 Jm^{-3} respectively but for hexagonal Co $K_1 = 5\times10^5$ Jm^{-3} [10]. The anisotropy energy sharply decreases with

increase in temperature and it vanishes at Curie temperature. Anisotropy gives rise to the enhanced coercive field.

The microscopic origin of magneto-crystalline anisotropy is the spin-orbit coupling. Because of the spin-orbit coupling, the orbitals are strongly coupled to the lattice, and hence the attempt by the external field to rotate the spin is resisted. In most materials, the spin-orbit coupling is very weak compared to the exchange interaction. The spin-orbit coupling is particularly strong in case of rare-earth systems [11].

Stress Anisotropy:

When magnetized, a magnetic system can undergo change in its dimensions, which is known as the magnetostriction. The microscopic origin of magneto-striction is the spin-orbit coupling. The inverse effect can also occurs i.e., a uniaxial stress can produce an easy axis for magnetization provided the magnitude of the stress is such that it overcomes all other anisotropies [11, 22].

Shape Anisotropy:

The shape of a polycrystalline magnetic sample can produce magnetic anisotropy. A magnetized body can itself create a magnetic field, which is known as demagnetizing field. If one of the dimension of a sample is quite large compared to other dimensions, it is easy to magnetize along the longer axis due to its small demagnetization factor compared to shorter axis. This phenomenon is known as shape anisotropy.

1.5 Exchange Bias

Exchange bias (EB) is one of the important properties of some of the magnetic materials which find applications in permanent magnet, recording media and spintronic devices. It is experimentally observed in terms of shifting of center of magnetic hysteresis loop along either positive or negative field axis. Exchange bias is generally observed in multilayer system or compounds having interfaces between ferromagnet and antiferromagnet. When such a system is cooled through the Néel temperature (T_N) of the antiferromagnet in the presence of static magnetic field then anisotropy is developed at the interface between FM and AFM and such anisotropy is called exchange anisotropy. Due to the exchange anisotropy, the center of hysteresis loops shift from the origin towards either negative or positive field axis and is called exchange bias phenomenon.

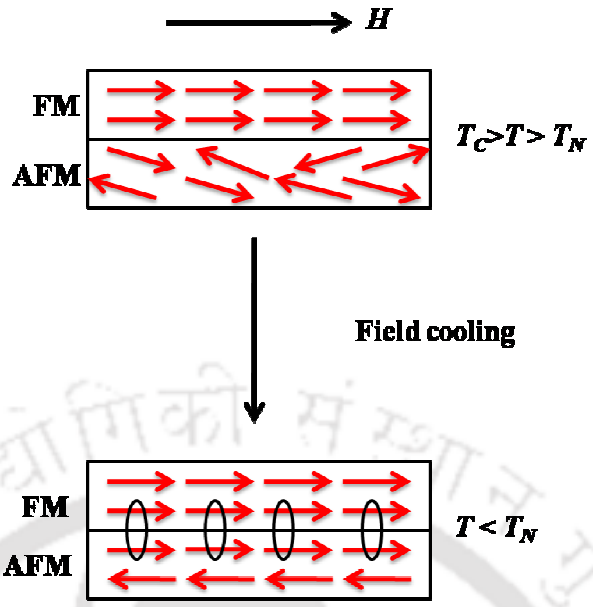

Figure 1.6 Schematic spin configurations at the interface of FM-AFM substance before and after the field cooling process [23].

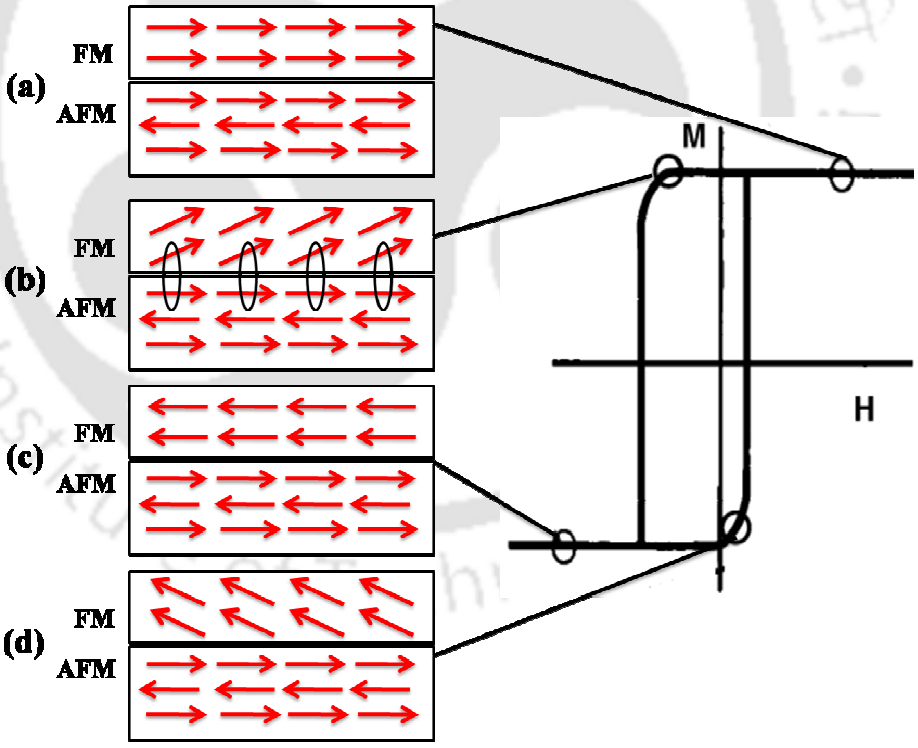

Figure 1.7 Schematic diagram of spin configuration at the interface of FM-AFM substance at different stages of a shifted $M - H$ loop, for a system with large AFM magnetic anisotropy [23].

The exchange bias was first discovered by Meiklejohn and Bean in 1956 in Co particle coated with CoO layer [24]. The shifting of the *M*– *H* loop can be quantitatively described by the EB field (H_{EB}) using the relation:

$$H_{EB} = \frac{H_{C1} + H_{C2}}{2} \tag{1.9}$$

where H_{C1} and H_{C2} are the field corresponding to $M = 0$ for ascending and descending branches of $M - H$ loop respectively.

The physical origin of EB is rather generally accepted in terms of exchange interaction at the interface of AFM and FM phases. It is discussed in terms of alignment of AFM spins at the AFM-FM interface parallel to the FM spins during field cooling process. The coupling between the two components generates anisotropy that applies additional torque to the FM spins such that a larger value of negative magnetic field is required to overcome it [23]. The spin configurations of AFM and FM components before and after field cooling process through T_N are shown in Fig.1.6.

The typical $M - H$ loop with negative exchange bias field is shown in Fig. 1.7. Here the FM moments align along the direction of cooling field, while the AFM spins are randomly oriented for the temperature $T_N < T < T_C$. When the system is cooled through T_N *i.e.*, $T < T_N$ the spins at the AFM-FM interface interact with each other such that the AFM spin layer (1st layer) in contact with the FM spins tend to align along the direction of spins of FM layers. However, the successive layers of AFM spins beneath the 1st layer orients antiparallel to each layer to produce the net zero magnetization in the AFM phase and fulfill the AFM ordering. Once the field cooling process is over, the AFM and FM spins at the interface couple ferromagnetically. When the magnetic field is reversed, the FM spins try to rotate, but their rotation is retarded due to the strong anisotropy associated to the AFM layer. In other words, the AFM will exert a microscopic torque in opposite direction to that of applied magnetic field. Thus a higher negative magnetic field is required to completely rotate the spin along the field direction compared to that for uncoupled state. Therefore, coercive field in negative field branch will increase. On the other hand, when the field is reversed back to positive values, the rotation of coupled FM spins will be easier compared to that of uncoupled spins *i.e.*, the AFM will exert a microscopic torque on the FM spins along the same (positive field) direction of the applied field. Therefore, the coercive field in the positive branch will reduce. The net

effect is the shift of $M - H$ loop along the negative field direction [23, 25]. The $M - H$ loops also known to shift along the positive field direction, whenever we have an AFM (antiparallel) interaction at the FM/AFM interface.

1.6 Dielectric Properties of Materials

Dielectric is a class of materials that lack free charges but contain bound charges. The bound charges form electric dipoles and their orientation under an electric field E causes a macroscopic dipole moment, which is measured in terms of polarization. For a linear isotropic and uniform dielectric, the polarization $\boldsymbol{P}$ depends on the strength of the electric field $\boldsymbol{E}$,

$$\boldsymbol{P} = \varepsilon_0 \chi \boldsymbol{E} \tag{1.10}$$

where ε_0 is dielectric permittivity of free space and χ is dielectric susceptibility.

In general, there are four basic polarization mechanisms: (i) electronic polarization, (ii) ionic polarization, (iii) orientation polarization and (iv) interfacial (Maxwell-Wagner) polarization. The electronic polarization arises due to the distortion of electron charge cloud in an atom when an electric field is applied. The ionic polarization arises due to the relative displacement of positive and negative ions in a molecule or compound. The orientation polarization is observed due to the orientation of permanent or induced dipoles under an applied field. It is also known as dipolar polarization. Finally, the interfacial polarization occurs at the interface of two phases having different conductivities and permittivity. Due to their different conductivity and permittivity values, space-charge builds up at their interface and it gives rise to the electric field and the polarization. Unlike other polarization mechanism, no dipole displacement is involved in interfacial polarization.

Dielectric properties of materials depend on these polarization mechanisms, which are quantified in terms of a few complex parameters as discussed below.

1.6.1 Complex Electric Impedance

The concept of complex electric impedance (Z^*) was first introduced by Heaviside in 1880 and further developed by Kennelly and Steinmertz [26]. Complex Electric impedance is the resistance offered to the AC current in a system and is defined in terms of Ohm's law:

$$Z^*(\omega) = Z' - jZ'' = \frac{V^*(\omega)}{I^*(\omega)} \tag{1.11}$$

where Z' is real part of complex impedance, Z'' is imaginary part of complex impedance, $V^*(\omega)$ is voltage across the dielectric and $I^*(\omega)$ is the current through the dielectric. For an ideal dielectric, $Z' = 0$. Hence, the net impedance is capacitive and is given by $Z^*(\omega) = -j/\omega C$, where ω is angular frequency and C is capacitance.

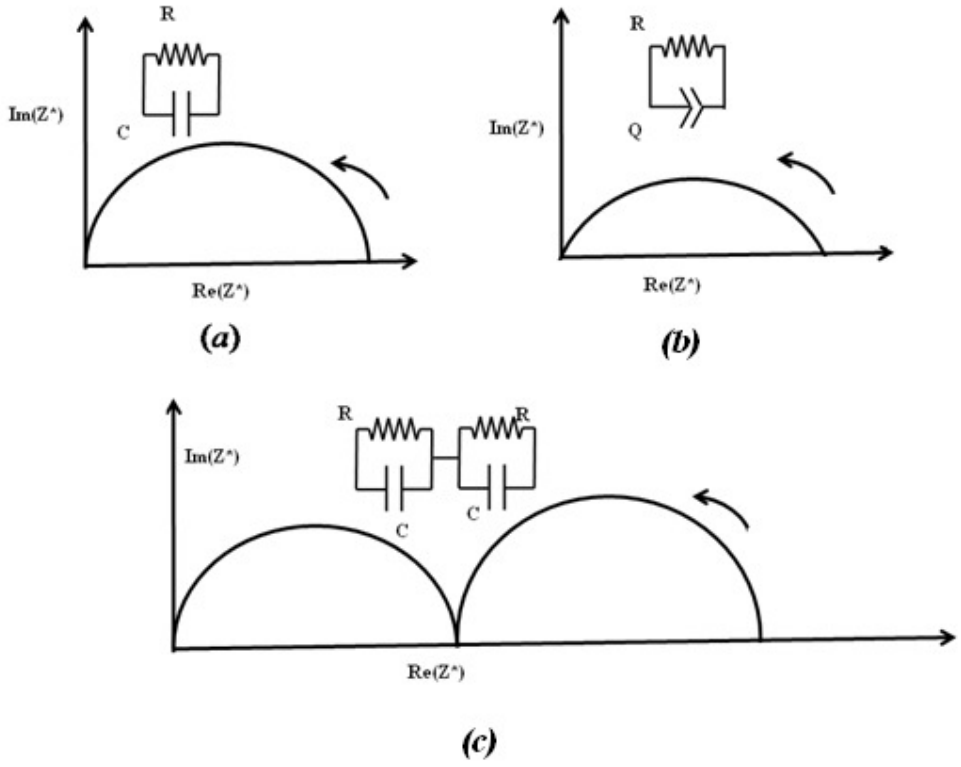

Figure 1.8 Nyquist plots for different electrical circuits.

A special representation of Z^* in complex plane, *i.e.*, plots of Im(Z^*) vs. Re(Z^*) provide various information about the electrochemical process inside a dielectric. This plot is known as Nyquist plots [26]. For example, the Nyquist plot for a parallel combination of R and C components of a sample is always a semicircle as shown in Fig. 1.8 (*a*) and its center lies on the Z' axis. One can estimate the value of resistance which is equal to the diameter of the semicircle. A perfect semicircle without any distortion/depression is observed only for ideal R and C elements. In reality, R and C are not ideal and in such cases, the semicircles are depressed such that their centers lie below the Z' axis and their shapes are distorted as shown in Fig. 1.8 (*b*). However, the situation

is different for polycrystalline samples. Polycrystalline samples are always composed by grains separated by a thin grain boundary. Grains are often more conductive, less capacitive as compared to grain boundaries. Therefore, one observes two distinct semicircles in the Nyquist plots of polycrystalline samples as shown in Fig. 1.8 (*c*) if the difference between the time constants ($\tau = 1/RC$) of grains and grain boundaries are quite large. The semicircle in the low frequency region (higher Z') corresponds to the grain boundaries, while the semicircle in the high frequency region (low Z') is due to grains. The grains and grain boundaries resistances are estimated from the diameters of corresponding semicircles. It is a signature of departure of the relaxation process from the ideal Debye like behavior. In such case, the departure of a certain elements from its ideality is represented by Constant Phase Element (CPE, denoted by Q), whose impedance is defined as,

$$Z_{CPE} = {}^{1}\!\!\diagup\!\!{}_{A(j\omega)^{n}} \tag{1.12}$$

where A is a constant, n is the relaxation time distribution factor such that $0 \leq n \leq 1$. The CPE represents an ideal capacitor when $n = 1$ and an ideal resistor for $n = 0$.

1.6.2 Complex Dielectric Constant

The complex dielectric constant (ε^*) is defined as,

$$\varepsilon^* = \varepsilon' - j\varepsilon'' = \frac{1}{j\omega C_0 Z^*} \tag{1.13}$$

$$\varepsilon' = \frac{Z''}{\omega C_0 (Z'^2 + Z''^2)} \tag{1.14}$$

$$\varepsilon'' = \frac{Z'}{\omega C_0 (Z'^2 + Z''^2)} \tag{1.15}$$

where ε' and ε'' are respectively the real and imaginary parts of ε^*, ω is angular frequency, C_0 is geometrical capacitance.

When an AC electric field is applied to a dielectric, the dipoles do not respond to the electric field instantaneously. Therefore, the polarization takes a characteristic time to

reach its equilibrium value. This is known as dielectric relaxation. The relaxation process can be formulated in terms of generalized Havriliak-Negami equation [27]:

$$\varepsilon^* = \varepsilon' - j\varepsilon'' = \varepsilon_\infty + \frac{\varepsilon_s - \varepsilon_\infty}{\left(1+(j\omega\tau)^{1-\alpha}\right)^\beta} \tag{1.16}$$

where ε_∞ is the permittivity at high frequency, ε_s is static, low frequency permittivity, τ is the most probable relaxation time. The difference between ε_s and ε_∞ i.e., ε_s-ε_∞ = $\Delta\varepsilon$ gives the dielectric strength. The exponents α ($0 < \alpha < 1$) and β ($0 < \beta < 1$) signify the broadness and asymmetry of corresponding spectra respectively. For an ideal Debye relaxation case one expects a single relaxation time with $\alpha = 0$, $\beta = 1$ and for any deviation from these values, the relaxation would be broader with distribution of relaxation time. For $\beta = 1$, $0 < \alpha < 1$, the relaxation behavior can be studied using Cole-Cole (CC) model, while $\alpha = 0$, $0 < \beta < 1$ represents Cole-Davidson (CD) relaxation model. The relaxation time τ is related to the time (τ_{max}) corresponding to maximum value of ε'' as [28]:

$$\tau_{max} = \tau\left[\frac{\sin\left(\frac{\pi(1-\alpha)\beta}{2(\beta+1)}\right)}{\sin\left(\frac{\pi(1-\alpha)}{2(\beta+1)}\right)}\right]^{\frac{1}{1-\alpha}} \tag{1.17}$$

1.6.3 Complex Electric Modulus

Another important dielectric parameter is complex electric modulus (M^*). The complex electric modulus approach began when the reciprocal of complex dielectric permittivity is thought to be the analogue of mechanical shear modulus [29]. It is particularly important for dielectrics containing mobile charges. Complex electric modulus is defined as,

$$M^* = M' + jM'' = \frac{1}{\varepsilon^*} = \frac{\varepsilon'}{\varepsilon'^2 + \varepsilon''^2} + j\frac{\varepsilon''}{\varepsilon'^2 + \varepsilon''^2} \tag{1.18}$$

From the physical point of view, electric modulus corresponds to the relaxation of the electric field in the material when the electric displacement remains constant [30]. Complex electric modulus is very useful in studying the dynamical process of electric transport phenomena as it surpasses the electrode polarization and apparent conductivity

[31]. Mathematically, M^* can be obtained from a relaxation of Kohlrausch-Williams-Watts (KWW) decay function $\Phi(t)$ [32, 33] as given by

$$M^*(\omega) = M_\infty \left[1 - \int_0^\infty e^{-j\omega t} \frac{d\phi(t)}{dt} dt \right] \tag{1.19}$$

The KWW function is defined as [34, 35]

$$\phi(t) = \exp\left(-\left(t/\tau \right)^{\beta_{KWW}} \right) \quad , 0 \le \beta_{KWW} \le 1 \tag{1.20}$$

where β_{KWW} is the stretching parameter and τ is the relaxation time. The eqns. (1.19) and (1.20) are in time domain. In the frequency domain, the frequency variation of M'' data can be formulated in terms of the four-parameter formula for generalized susceptibility χ'' (where χ'' can be M'', Z'', ε'') given by Bergman [36]:

$$\chi''(\omega) = \frac{\chi''_{\max}(\omega)}{\frac{(1-|n-m|)}{n+m}\left(m\left(\frac{\omega}{\omega_{\max}} \right)^{-n} + n\left(\frac{\omega}{\omega_{\max}} \right)^{m} \right) + |n-m|} \tag{1.21}$$

where $\chi''_{\max}$ is the peak value of imaginary part of complex susceptibility (χ'') and $\omega_{\max}$ is the corresponding peak frequency. The parameters n and m are the stretching parameters ($0 < n < 1$, $0 < m < 1$) at low (below peak frequency) and high frequency (above peak frequency) regions respectively.

1.6.4 Complex AC Conductivity

The complex ac conductivity (σ^*) is defined as [26]

$$\sigma^*(\omega) = \sigma' + j\sigma'' = j\omega\varepsilon_0\varepsilon^* \tag{1.22}$$

with its real and imaginary parts

$$\sigma'(\omega) = \omega\varepsilon_0\varepsilon'' \tag{1.23}$$

$$\sigma''(\omega) = \omega\varepsilon_0\varepsilon' \tag{1.24}$$

The frequency dependence of $\sigma'(\omega)$ can be represented in terms of Jonscher's power law [37], which is expressed as,

$$\sigma'(\omega) = \sigma(0) + A\omega^s \tag{1.25}$$

Here, $\sigma(0)$ is limiting zero frequency conductivity, A is pre-exponential constant and s ($0 \leq s \leq 1$) is frequency exponent. The combination of eqns. (1.23) and (1.25) gives

$$\varepsilon'' \propto \omega^{s-1} \tag{1.26}$$

This behavior is well known as universal dielectric response (UDR) [37].

1.7 Literature on Potential Multiferroics

The research interest in perovskite multiferroics is ever growing especially after the discovery of magnetically controlled ferroelectricity in $TbMnO_3$. However, such fascinating phenomenon in $TbMnO_3$ occurs at cryogenic temperature since the ferroelectricity is induced by the magnetic ordering at low temperature. In this context, the Fe-based perovskite oxides having magnetic transitions above room temperature are potential candidates for multiferroics and they are $SmFeO_3$, $YFeO_3$, $GaFeO_3$, $LaFeO_3$ *etc.* Here, the ferroelectricity is induced due to the magnetic origin of DM anisotropic exchange interaction of the FeO_6 octahedra. However, the magneto-electric coupling in these compounds is quite week due to their small magnetization values. Hence, the attempt to tailor such multiferroic materials continues towards stronger magneto-electric coupling at room temperature. The other approach towards multiferroicity is by inducing ferromagnetism in ferroelectric compounds with the help of appropriate doping of magnetic elements. The Ti-based perovskites such as $BaTiO_3$, $PbTiO_3$ *etc.* having ferroelectric transition above room temperature are potential candidates to induce multiferroicity as per the above method.

In the present thesis, we have taken up $BiFeO_3$ and $YFeO_3$ (Fe-based perovskites) because of their high T_N values and, PbTiO3 and BaTiO3 (Ti-based perovskites) because of their excellent ferroelectric properties. In the following subsections, we briefly review the structural, electrical and magnetic properties of Fe-based perovskite oxides such as $YFeO_3$ and $BiFeO_3$, and the Ti-based perovskite oxides such as $PbTiO_3$ and $BaTiO_3$.

1.7.1 $YFeO_3$ series

$YFeO_3$ is known to crystallize in orthorhombically distorted perovskite structure with space group *Pnma* [38, 39]. The distortion in $YFeO_3$ is mainly due to the position of

Y^{3+} ions, whereas the Fe^{3+} ions are located in the octahedral environment of oxygen anions. The crystal structure of $YFeO_3$ is shown in Fig. 1.9 which can be viewed in terms of three dimensional networks of FeO_6 octahedra. One of the oxygen anions forms the common apex of two octahedra and mediates the superexchange interaction between two nearest Fe^{3+} ions. Each Fe^{3+} ion in $YFeO_3$ is coupled to nearest Fe^{3+} ions via superexchange interaction, and hence it exhibits AFM with T_N = 640 K [40]. However, the Fe^{3+} spins are not collinear but cant considerably due to the presence of Dzyaloshinskii-Moriya interaction and as a result a small non-zero magnetization is observed. There are three possible spin configurations for Fe^{3+} sublattice in orthoferrites: Γ_1 ($A_xG_yC_z$), Γ_2($F_xC_yG_z$) and Γ_4($G_xA_yF_z$) [40] which are shown in Fig. 1.10. The Γ_4 ($G_xA_yF_z$) configuration describes the canting induced weak ferromagnetism in most of the orthoferrites. However, in the presence of magnetic rare-earth ions and the associated magnetic anisotropy in R^{3+} – O^{2-} –Fe^{3+} networks, the spin configuration undergoes a transition from Γ_4 to Γ_2 upon cooling which is known as spin re-orientation transition.

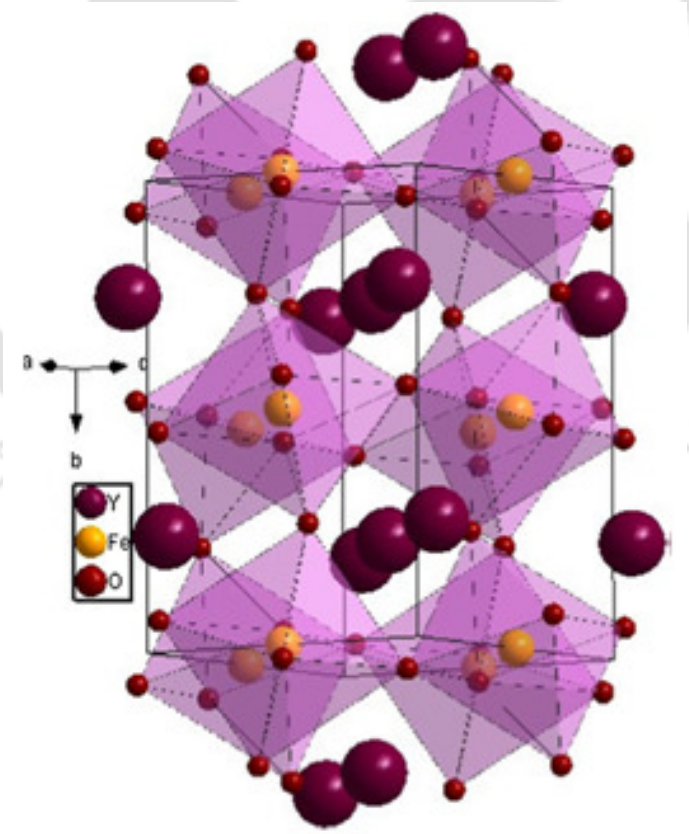

Figure 1.9 Crystal structure of $YFeO_3$ [38]. (Maroon spheres: Y, Yellow sphere: Fe and Red sphere: O).

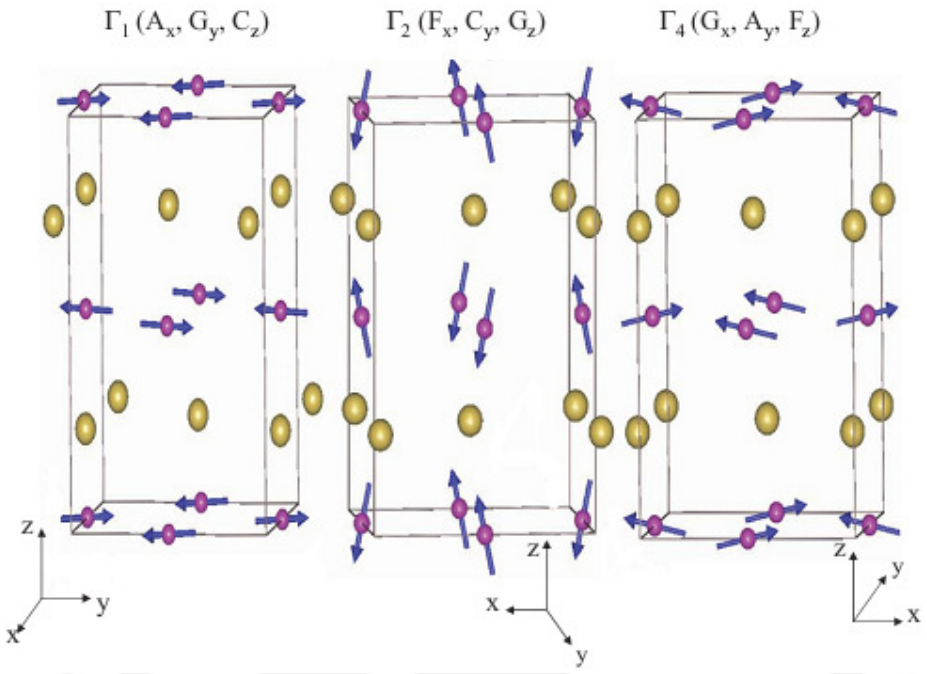

Figure 1.10 Spin configurations of orthoferrites [41]. (Purple sphere: Fe, Yellow sphere: O, the arrow on the purple sphere represents magnetic moment).

Most of the earlier works on orthoferrites are devoted to the study of magnetic properties and in particular to understand the field induced spin re-orientation [42-44]. A few authors have studied the dielectric and ferroelectric properties of $YFeO_3$. Two dielectric relaxation peaks are reported for $YFeO_3$ within the temperature range 123 K – 623 K [45]. The relaxation peak observed at low temperature is attributed to the polar ordering of Fe^{2+} and Fe^{3+} ions due to electron hopping between them. On the other hand, the dielectric relaxation at high temperature is attributed to the doubly ionized oxygen vacancy related point defects [45]. Ma *et al.* [46] reported a single dielectric relaxation peak in $YFe_{1-x}Mn_xO_3$ (x = 0.1, 0.2, 0.3) compounds below room temperature and it shifts towards higher temperatures with increase in Mn concentration. They have also reported the appearance of $P - E$ hysteresis loops below 153 K which is the characteristic behavior of a true ferroelectric system. These materials are also reported to exhibit a weak ferromagnetism [46]. Lee *et al.* [47] reported improper ferroelectricity in centrosymmetric $SmFeO_3$ compound at room temperature and is reported to be induced by the canting of the Fe spins. Inspired by the reports of Lee *et al.* [47], Shang *et al.* [48] reported a similar spin-canting induced ferrolectricity in $YFeO_3$ with clear $P - E$ loops.

1.7.2 $BiFeO_3$ series

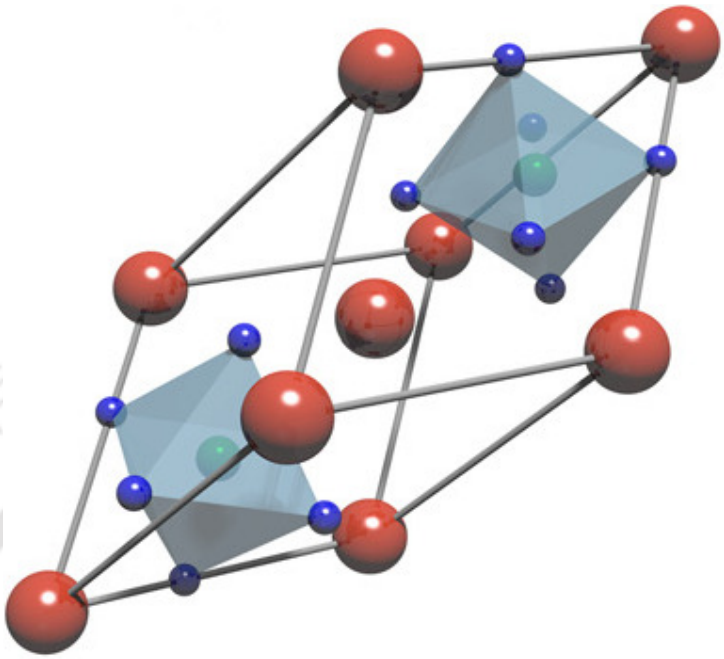

Figure 1.11 Crystal structure of $BiFeO_3$ (Red spheres: Bi, Green spheres: Fe and Blue sphere: O) [49].

$BiFeO_3$ (BFO) crystallizes into rhombohedrally distorted simple cubic perovskite structure with space group *R3c* [50-53]. The rhombohedral unit cell has a lattice parameter a = 3.965 Å with the rhombohedral angle α = 89.3° – 89.4° at room temperature [53]. Alternatively, the unit cell can be described in the co-ordinate system of hexagonal structure with lattice parameter a_h = 5.587 Å and c_h= 13.867 Å [50]. The crystal structure of BFO in hexagonal settings is shown in Fig. 1.11. The Bi^{3+} ions are in eightfold co-ordination with oxygen ions and Fe^{3+} ions are in sixfold co-ordination. The oxygen octahedron is distorted by a minimum and maximum O – O distances of 2.701 Å and 3.015 Å respectively and is rotated by $\pm\alpha$ = 13.8° with respect to three-fold rotation axis. The Fe atoms are shifted away from the center of the deformed oxygen octahedron by about 0.134 Å along the threefold axis, while the Bi atom is shifted with respect to the center of two neighboring octahedra by 0.540 Å along the threefold axis [53]. Such distortion in the crystal structure results in polarization along $[111]_c$ or $[001]_h$ direction [53]. The ferroelectric Curie temperature for $BiFeO_3$ is about 1100 K [54].

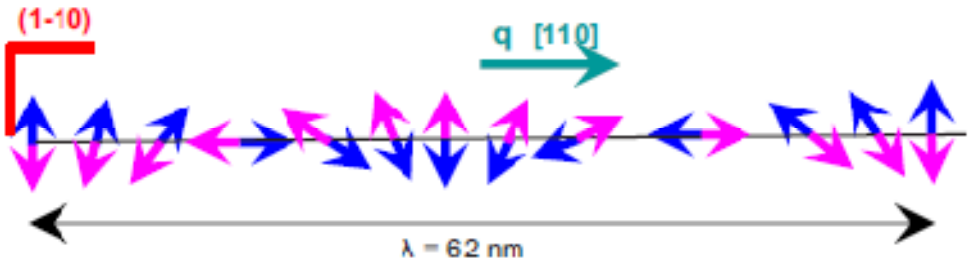

Figure 1.12 Schematic antiferromagnetic structure of $BiFeO_3$.The propagation vector **q** is along [110] direction and spin-rotation is in (1-10) plane. The dark blue and pink arrows represent two AFM sublattices oriented along a cycloidal spiral [55].

The rotation of octahedral assembly of oxygen ions directly manipulates the Fe – O – Fe angle in the range of 154 – 156° [53, 56, 57]. The Fe –O –Fe angle is critical for the orbital overlap and hence the superexchange interaction leading to the magnetic ordering. Basically, the local magnetic ordering in $BiFeO_3$ leads to *G*-type antiferromagnetic structure, where each Fe^{3+} spin is surrounded by six nearest neighbor antiparallel spins of Fe^{3+} ions. In other words, the Fe^{3+} spins are coupled ferromagnetically in (111) plane and antiferromagnetically between the adjacent planes and hence results in the *G*-type antiferromagnetic structure [52]. Moreover, the *G*-type antiferromagnetic ordering of the Fe^{3+} ions are further superimposed by a spatially modulated cycloid spin having a periodicity of 62 nm with its propagation vector along the [110] direction as shown in Fig. 1.12 [58, 59].

Several anomalies in the temperature variation of dielectric constant measurements have been reported for $BiFeO_3$ such as at 50, 140, 200, 230, and 458 K other than the common magnetic (T_N ~ 650 K) and ferroelectric transitions (T_{FE} ~ 1100 K). Most of the anomalies observed at low temperature are found to be of magnetic origin [60, 61]. The most intriguing of these transitions is that observed at 458 K and is known as Polomska transition. It was first reported by Polomska in polycrystalline $Bi_{1-x}La_xFeO_3$ samples [62]. However, such transition is not observed in single crystalline samples of $BiFeO_3$ and it is yet to be understood [63]. Hunpratub *et al.* [64] reported three dielectric relaxations in the temperature range of T = 225 K – 473 K for the polycrystalline sample of $BiFeO_3$ sintered at 700 °C. They reported that dielectric relaxation induced by the carrier hopping between Fe^{2+} and Fe^{3+} ions is dominant at low temperature (225 K – 293 K); while grain boundaries effect and defect

ordering/conduction induced relaxation are dominant in the high temperature range of T = 300 K – 400 K and 400 K – 473 K respectively [64]. However, relaxation dynamics was found to be greatly influenced by doping [65]. The carrier hopping induced dielectric relaxation was found to shift towards the high temperature range of 313 K – 473 K for thin film of $Bi_{0.9}La_{0.1}Fe_{0.98}Mg_{0.02}O_3$ sample [65]. Beyond T = 473 K, another relaxation was reported due to the short range movement of singly ionized oxygen vacancies [65]. On the other hand, both singly ionized and doubly ionized oxygen vacancy related dielectric relaxations were observed in thin films of $Bi_{0.9}La_{0.1}FeO_3$, $BiFe_{0.95}Ti_{0.05}O_3$ and $Bi_{0.9}La_{0.1}Fe_{0.95}Ti_{0.05}O_3$ samples prepared by RF-sputtering [66].

The peculiar magnetic structure of $BiFeO_3$ locks the magnetization in $BiFeO_3$ and hence, the magneto-electric coupling in $BiFeO_3$ is negligible. In order to generate substantial magneto-electric coupling in $BiFeO_3$, it is suggested to break the peculiar magnetic structure of $BiFeO_3$ [67, 68]. Such suppression of spiral structure could be achieved by applying a high magnetic field [67, 69] or by *A*-site substitution by rare-earth as well as alkaline metal ions [70-77]. In most of the cases, the substitution driven suppression of spiral structure is realized via the structural phase transition from the parent rhombohedral phase (*R3c*) to other low symmetric crystal structure. Zhang *et al.* [70] reported such structural phase transition from rhombohedral to orthorhombic cell in La doped $BiFeO_3$ samples prepared by conventional solid state method. Such structural phase transition was found to suppress the spiral magnetic structure and significantly enhance the M_r value from 0.002 emu/g for rhombohedral $Bi_{0.95}La_{0.05}FeO_3$ to 0.08 emu/g for orthorhombic $Bi_{0.6}La_{0.4}FeO_3$ [70]. Similar structural phase transition induced enhancement of magnetization was observed for La doped $BiFeO_3$ prepared by quenching process [78], Nd doped $BiFeO_3$ [79], *etc*.

1.7.3 $PbTiO_3$ series

$PbTiO_3$ (PTO) crystallizes into tetragonal structure at room temperature with *P4mm* space group and it has one formula unit per unit cell [80]. The typical values of lattice parameters are $a = b$ = 3.904 Å and c = 4.152 Å [80]. The crystal structure of PTO at room temperature is shown in Fig. 1.13. The large Pb cation is in 12-fold co-ordination with the oxygen anions, while the Fe cation is in octahedral co-ordination with six nearest oxygen anions. The oxygen octahedron is elongated along the [001] direction and also shifted by 0.54 Å with respect to Pb^{2+} ion. The Ti^{4+} ion shifts along [001] direction from

the center of the cell by 0.17 Å. As a result, the Ti ion occupies an off-centre position within the shifted octahedron [80, 81]. The off-centering of Ti ion produces large value of spontaneous polarization and significantly high ferroelectric Curie temperature ($T_{C\text{-}FE}$ ~763 K) [82, 83].

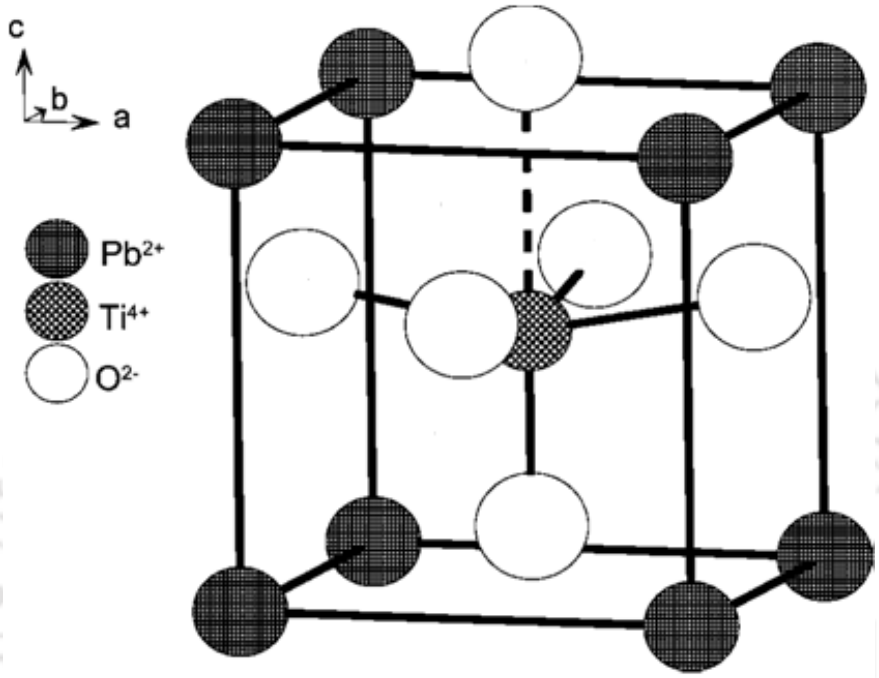

Figure 1.13 Tetragonal structure of $PbTiO_3$ [81].

The recent interest of PTO is due to its potential to exhibit ferromagnetism along with its well known ferroelectricity. The parent compound is diamagnetic due to the absence of active *d*-electrons in Ti^{4+} ion. However, magnetic ordering can be induced in diamagnetic PTO by the creation of defects related to Ti or oxygen and by doping magnetic ions for Ti ion [84-86]. Zhang *et al*. [84] reported oxygen vacancy induced ferromagnetism in ferroelectric $PbTiO_3$ nanocrystals. They have also reported a considerable degree of magneto-dielectric coupling at room temperature. Ren *et al*. [85] reported vacancy induced FM in Fe doped nanocrystals of PTO mediated by the *F*-center exchange mechanism. Similar *F*-centre exchange induced ferromagnetism was reported for Fe doped PTO nanocrystals along with improved dielectric properties at room temperature by other group [87]. Palkar *et al*. [86] reported FM in $PbTi_{0.5}Fe_{0.5}O_3$ at room temperature along with considerable magneto-electric coupling in the vicinity of ferroelectric transition temperature.

1.7.4 $BaTiO_3$ series

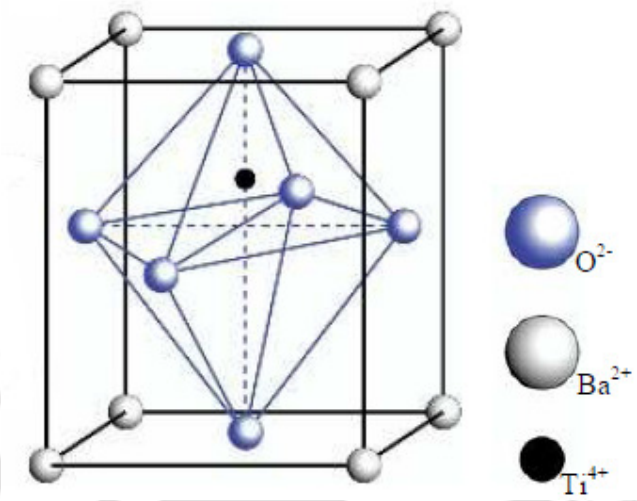

Figure 1.14 Crystal structure of $BaTiO_3$ [88].

$BaTiO_3$ (BTO) exhibits tetragonal crystal structure at room temperature with *P4mm* space group having one formula unit per cell. The tetragonal crystal structure of BTO is shown in Fig. 1.14. The typical values of lattice parameters at room temperature (in tetragonal phase) are $a = b = 3.990$ Å and $c = 4.035$ Å [89]. It has classic ABO_3 type cubic structure at high temperature. The cubic structure is centrosymmetric with Ba^{2+} ions at the corner, Ti ions at the center and oxygen ions at the face center of the cube. As the temperature is lowered, $BaTiO_3$ undergoes successive transitions to three different structures which are slightly distorted from the ideal cubic structure and are characterized by the observation of ferroelectricity along three different axes. The first such transition occurs at 393 K where it undergoes from cubic cell to tetragonal cell. On further lowering of temperature, it goes second structural transition to orthorhombic cell at 278 K, followed by final transition to rhombohedral at 183 K. Each of these structures can be thought as elongation of cubic unit cell along the edge [001] *i.e.*, tetragonal, along the face diagonal [011] *i.e.*, orthorhombic or along the body diagonal [111] *i.e.*, rhombohedral. These distortions result in net displacement of cations with respect to oxygen octahedra along these directions and generates spontaneous polarization along these directions [89].

Similar to PTO, the recent studies of $BaTiO_3$ is mainly to induce magnetic ordering in its ferroelectric phase. A few theoretical and experimental studies were conducted to induce ferromagnetism in $BaTiO_3$ [90-92]. Nakayama *et al*. [90] have

carried out first principle calculations on $BaTi_{1-x}M_xO_3$ where M = Sc, V, Cr, Mn, Fe, Co, Ni, Cu and predicted room temperature ferromagnetism for Fe, Mn, Cr doping in $BaTiO_3$. Xu *et al.* [91] reported the simultaneous occurrence of ferromagnetism and ferroelectricity in $BaTi_{0.95}Fe_{0.05}O_{3-\delta}$ with ferromagnetic and ferroelectric transition temperatures at 670 K and 365 K, respectively along with reasonable values of saturation magnetization and remanent polarization. Rajamani *et al.* [93] reported ferromagnetism in $BaTi_{1-x}Fe_xO_3$ thin films ($0.15 < x < 0.5$) prepared by pulse laser deposition. They observed that the saturation magnetization increased with increase in Fe concentration.

1.8 Motivation

Fe based perovskite oxides are very rich in magnetic properties but they lack the ferroelectric ordering. On the other hand, the Ti based perovskite oxides are ferroelectric, but they lack any magnetic ordering. In 2011, Lee *et al.* [47] reported spin-canting induced improper ferroelectricity in one of the Fe based perovskite oxide $SmFeO_3$. Similar ferroelectric ordering was reported in the centrosymmetric compound $YFeO_3$ in 2013 [48]. However, the reported *P*– *E* loop at room temperature exhibits a very small value of polarization. Besides, there is a lack of detailed investigation of dielectric properties of $YFeO_3$. On the other hand, as per literature, the synthesis of single- phase $BiFeO_3$ compound is the main hurdle in its application as multiferroics and the obstacle is the large leakage current. Moreover, the peculiar antiferromagnetic structure of $BiFeO_3$ gives rise to very small magnetization. Such small value of magnetization produces very feeble magneto-electric coupling. This problem needs to be addressed for its potential applicability as multiferroics. On the otherhand, introducing ferromagnetism in otherwise ferroelectric Ti-based perovskite oxides without degrading its ferroelectric properties is quite challenging. Moreover, the systematic investigation of dielectric relaxation in terms of different microstructural effect in Ti-based perovskite oxides and with appropriate doping is lacking. In order to understand the different dielectric relaxation dynamics in Fe- and Ti-based perovskite oxides and doping driven evolution of magnetic properties, we have chosen the following series of samples for the present thesis work:

(1) $YFe_{1-x}Mn_xO_3$ (x = 0 to 0.3)

(2) $Bi_{1-x}Sm_xFeO_3$ (x = 0 to 0.3)

(3) $PbTi_{1-x}Fe_xO_3$ (x = 0 to 0.3)

(4) $BaTi_{1-x}Fe_xO_3$ (x = 0 to 0.3)

The phase formation and crystal structural properties of the above samples are studied by recording X-ray diffraction (XRD) patterns and analyzing them by Rietveld refinement technique using FULLPROF program. The Raman spectroscopy is used to understand the structural parameters further. The morphological studies are carried out by recording micrographs using a field emission scanning electron microscope (FESEM) and scanning electron microscope (SEM). Field and temperature variations of magnetization were measured using a vibrating sample magnetometer (VSM). EPR spectra at room temperature were recorded by an EPR spectrometer. Dielectric and electric modulus data were obtained by measuring impedance data recorded by using an LCR meter.

Chapter 2

Experimental Techniques

The experimental techniques followed for material preparation and various physical measurements are briefly discussed in this chapter. The samples were prepared either by solid state route or sol-gel method. Home made and commercial high temperature furnaces were used for heat treating and sintering the starting compounds towards achieving the required single phase samples with good densification. The details of design and fabrication of homemade furnaces and the technical details of commercial furnaces are presented in this chapter. The prepared materials were characterized by using X-ray diffractometer (XRD) to check their phase purity and crystal structure. XRD patterns were refined by Rietveld refinement technique using FULLPROF software to further understand the doping driven effect on crystal structure and other related parameters such as lattice parameter, volume percentage of each phase, etc. The observed structural change in some of the samples was further analyzed using Raman spectra obtained from a micro-Raman spectrometer. The microstructural properties were studied by recording microstructural images using scanning electron microscope (SEM) and field emission scanning electron microscope (FE-SEM). The frequency and temperature variations of complex impedance spectra were recorded using an LCR meter. The dielectric properties were studied in terms of impedance spectroscopy, dielectric spectroscopy and electric modulus spectroscopy. Magnetic properties were studied in terms of field and temperature variations of magnetization measured using a vibrating sample magnetometer (VSM). The basic working principle of VSM is also presented in

this chapter. The samples were further characterized using an electron paramagnetic resonance (EPR) spectrometer.

2.1 Sample Preparation

The most widely used methods for preparing polycrystalline oxides are the solid state reaction route and sol-gel technique. Even though, the desired phase is thermodynamically favored, solids do not usually react together at ambient temperature over laboratory time scales and it is necessary to heat the reactants at high temperatures to overcome the kinetic barriers. The powders of stoichiometric ratio of starting compounds are often pressed into pellets before heating to high temperature to increase the contact between particles. Reaction times are usually several days and it is best to repeat the process to ensure homogeneous samples. The starting materials are usually single cation oxides, carbonates, nitrates or hydroxides which decompose to form oxides when heated. Carbonates are popular for the alkali and alkaline earth elements because they are not hygroscopic and therefore can be weighed accurately in air. During the initial heating or calcinations of carbonate mixtures, carbon dioxide is produced and it escapes from the solid. This prevents good sintering of the material into a dense ceramic and requiring an additional heating.

Sol-gel method is a chemical process, where the nitrates or acetates of cationic materials are dispersed in a solvent and are then converted into a gel form through the hydrolysis reaction of polymerization. The heating of the gel leads to combustion reaction, with an end product of fine dry powders in nano-metric scale. The advantage of sol-gel technique compared to the solid state route is as follows. (1) In sol-gel technique, the mixing of the starting materials at the molecular level is possible due to the dispersion of the materials in a solvent. (2) The incorporation of dopant elements is even to achieve uniform doping on a molecular level. (3) The required temperature for annealing is relatively small compared to the case of solid state route and the diffusion of components is in the nanometer range.

The samples were prepared using the following starting compounds such as, Bismuth oxide (Bi_2O_3), Ferric nitrate ($Fe(NO_3)_3.9H_2O$), Samarium oxide (Sm_2O_3), Yttrium oxide (Y_2O_3), Manganese acetate ($Mn(CH_3COO)_2.4H_2O$), Barium carbonate ($BaCO_3$), Lead nitrate ($Pb(NO_3)_2$), Titanium dioxide (TiO_2), Ferric oxide (Fe_2O_3) and Ethylene glycol with their purity better than 99 %.

2.1.1 Solid State Reaction Method

The stoichiometric ratios of starting compounds were weighed using an electronic balance supplied by Mettler Toledo (model no. AG135) with an accuracy of ± 0.01 mg. The weighed compounds were grinded under the medium of acetone (99%) using an agate mortar and pestle. The homogeneous mixture of starting compounds was transferred to an alumina crucible and was presintered in the temperature range of 1073 to 1173 K for over 24 – 36 h followed by furnace cooling to room temperature. The presintered powder was grinded again to get a homogeneous mixture. The presintered homogenous powder was pressed into cylindrical shape pellets by using a 13 mm die and a hydraulic press supplied by Techno Search instruments, Thane, India with a maximum load of 2.94×10^8 N/m^2. The sintering in pellet form was carried out in a step by step process in air at different temperatures with several intermediate grindings and re-pelletizing. The final sintering temperatures were different for different series of the samples and these details are discussed in Chapters 3, 4, 5 and 6 for the respective series of materials.

2.1.2 Sol Gel Method

Here, the stoichiometric amounts of starting compounds and/or elements were converted into metal nitrates by adding nitric acid. They were converted into citrate by adding excess amount of citric acid and ethylene glycol. The uniform mixture of the above solution was slowly evaporated in a hot plate at 348 K to 373 K until a gel was formed. The polymeric gel was completely dried up by keeping at 348 K for 12 hr. The product was heated to 473 K to induce self combustion. The combustion derived fine power was heat treated at 673 K to decompose the remaining organic reagents. The obtained precursor powder was pre-sintered in the temperature range 873 K to 1173 K depending on the nature of material. The presintering was repeated couple of time with intermediate grinding. The final sintering in pellet form was carried out in the temperature range 1273 K to 1473 K depending on the nature of materials.

2.2 High Temperature Furnaces

High temperature furnaces were used for material preparation. Homemade muffle furnaces with a maximum operating temperature of 1473 K and commercial high temperature furnaces with the maximum operating temperature of 1673 K were used for

sintering the samples. The commercial furnaces were supplied by N. R. Enterprises and Bysakh & Company, Kolkata, India. The furnace supplied by N. R. Enterprises was powered by a thyristor unit of 30 A rating. The temperature was controlled using; West, UK make, PID programmable temperature controller (model no. 6400) with 16 segment programming facility. The platinum versus platinum-rhodium (Platinum + 10 % Rh) thermocouple was used for sensing the temperature. The heating elements were based on Si-Carbide rods. The temperature was controlled to an accuracy of ± 1 K. The furnace could be operated upto a maximum temperature of 1673 K. The other furnace supplied by Bysakh & Co. contains (1) a thyristor unit with a rating of 35 A, (2) a PID programmable temperature controller (model no. PRC-300) with 16 segment programming feature, (3) a platinum versus platinum-rhodium (Platinum + 13 % Rh) thermocouple wire, (4) Si-Carbide rods based heating elements. The maximum operating temperature was 1723 K.

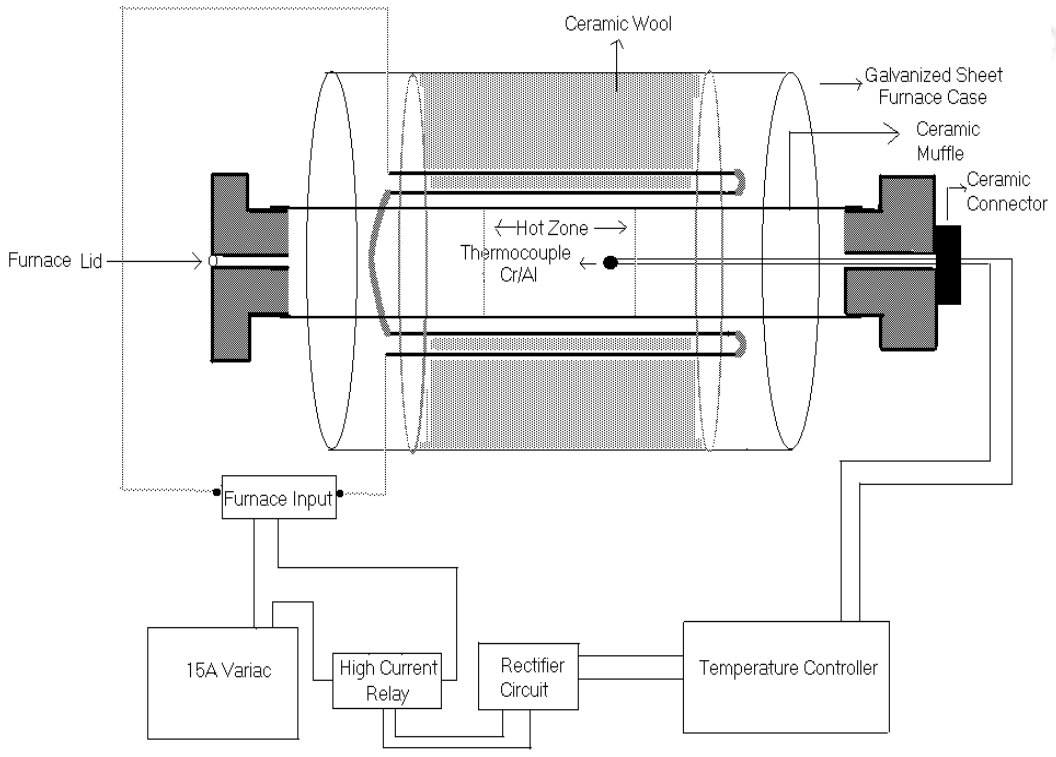

Figure 2.1 Block diagram of the furnace with maximum operating temperature of 1473 K.

The home made furnace was fabricated using a cylindrical alumina muffle with an inner diameter of 5.8 cm and 50 cm length. Six Si-Carbide rods of 45 cm length each

were used as heating element. The muffle loaded with heating elements was housed in a cylindrical container of 50 cm diameter and 50 cm length and it was made up of galvanized aluminum sheet. High temperature ceramic bricks and ceramic wools were used as thermal insulation. Chromel-Alumel (Cr-Al) thermocouple and a commercial on/off type temperature controller were used for temperature measurement and controlling. The input power to the furnace was regulated using a variac (dimmerstat) of 15 A capacity. An external on/off relay (15 A capacity) was used for controlling the power supply to the heater wire. The relay was triggered using the temperature controller. The block diagram of the furnace is shown in Fig. 2.1. The furnace could be operated upto a maximum temperature of 1473 K. The temperature could be controlled with an accuracy of ± 5 K.

2.3 X-ray Diffraction

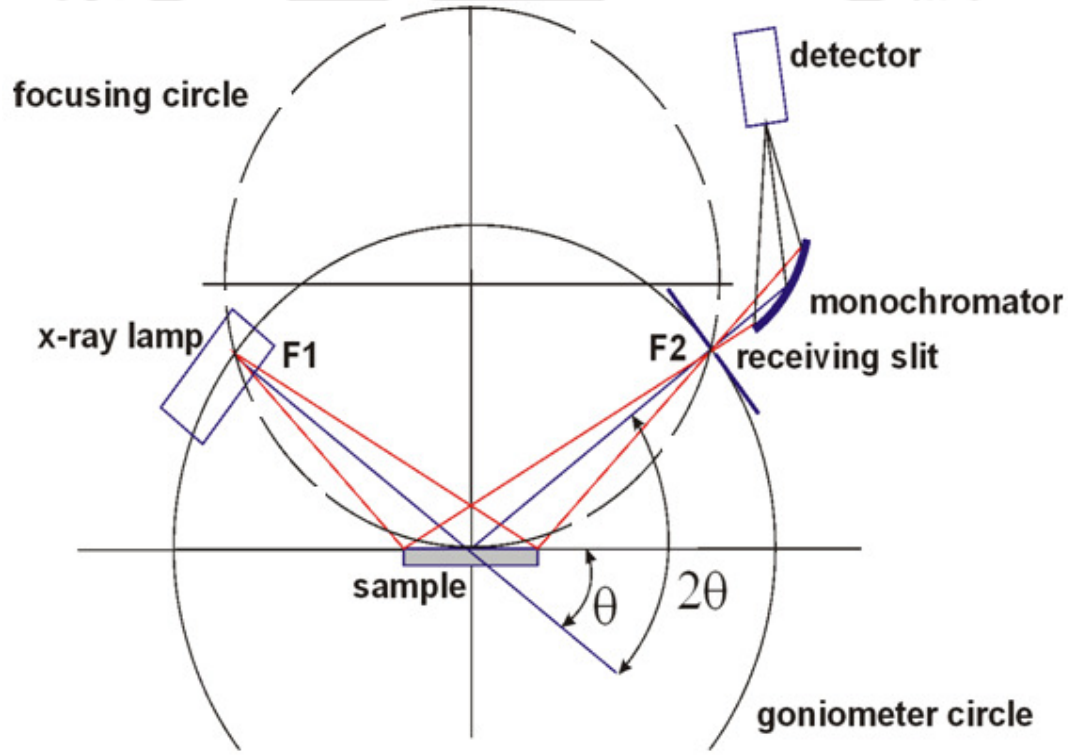

Figure 2.2 Ray diagram of X- ray diffractometer [94].

The X- ray diffraction (XRD) technique has been used to study the phase purity and crystal structure of the prepared compounds. Powder XRD patterns were recorded at room temperature using commercial Rigaku make TTRAX III high power X-ray

diffractometer by employing CuK_α radiation (λ = 1.54056 Å). In the present investigation, all the XRD patterns were recorded with the setting of 200 mA current and 50 kV voltage for X-ray generator. The instrument is based on the Bragg-Brentano geometry as shown in Fig. 2.2. In this geometry, the X-ray source (F1), sample and the slit in the detector (F2) lie always in a circle so that X-rays produced from source and diffracted from any point on the dotted circle by an angle 2θ will arrive exactly at the same point F2. In other word, the focusing is perfect in such geometry where the X-ray source, sample and detector lies in the dotted circle. This circle is known as focusing circle. The data were collected in an usual $\theta - \theta$ scan with an angular speed of 3°/minute and a step size of 0.03°.

The XRD patterns were analyzed with the help of Fullprof program by employing Rietveld refinement technique [95]. The background was refined using a polynomial function. Pseudo-Voigt function was chosen for peak shape. The global parameters, such as coefficients of background polynomial, scaling factor, half width parameters (*u*, *v*, *w*) and lattice parameters (*a, b, c*) were mainly varied during the refinement. In addition to that nuclear structure variables such as fractional atomic co-ordinates (*x*, *y*, *z*), isotropic displacement (temperature) parameters and occupancy values were varied. Here, occupancy is the chemical occupancy normalized to the multiplicity of the general position of the group. The occupancy of oxygen was taken as 1 (full occupancy) for all the refinements and it was not varied during the refinement. The quality of the refinements are known based on the values of reliability factors such as R_p, R_{wp}, R_{exp}, R_{Bragg}, R_F and χ^2 and they are defined as follows.

$$\text{Profile factor, } R_p = 100\frac{\sum_{i=1,n}\left|y_i - y_{c,i}\right|}{\sum_{i=1,n} y_i} \tag{2.1}$$

Here y_i is the observed point (experimental) and $y_{c,i}$ is the calculated point and n represents the number of data points.

$$\text{Weighted profile factor, } R_{wp} = 100\left[\frac{\sum_{i=1,n}\omega_i\left|y_i - y_{c,i}\right|^2}{\sum_{i=1,n}\omega_i y_i^2}\right]^{1/2} \tag{2.2}$$

Here $\omega_i = \frac{1}{\sigma_i^2}$, σ_i^2 is the variance of observation y_i.

$$\text{Expected weight factor, } R_{\exp} = 100\left[\frac{n-p}{\sum_{i=1,n}\omega_i y_i^2}\right]^{1/2} \tag{2.3}$$

Here $(n - p)$ is the number of degrees of freedom where p is the number of refined parameters.

$$\text{Reduced chi-square, } \chi^2 = \left[\frac{R_{wp}}{R_{\exp}}\right]^2 \tag{2.4}$$

$$\text{Bragg factor, } R_B = 100\frac{\sum_h \left|I_{obs,h} - I_{calc,h}\right|}{\sum_h I_{obs,h}} \tag{2.5}$$

Here h is the vector which levels the Bragg reflections. The $I_{obs,h}$ is the observed integrated intensities and $I_{calc,h}$ is the calculated intensities.

$$\text{Crystallographic } R_F \text{ factor, } R_F = 100\frac{\sum_h \left|F_{obs,h} - F_{calc,h}\right|}{\sum_h F_{obs,h}} \tag{2.6}$$

Here $F_{obs,h}$ and $F_{calc,h}$ are the observed and calculated structural factors, respectively.

2.4 Raman Spectroscopy

Raman spectroscopy is a vibrational spectroscopic technique generally used to study properties such as crystalline phases, defects, strain, *etc*. in a system. It is basically a light scattering phenomenon based on the famous Raman effect which corresponds to the photon-phonon interaction. In Raman spectroscopy, the sample is illuminated with a monochromatic laser beam which interacts with the molecular vibration and are scattered. A fraction of the scattered beam has wavelength different from the incident wavelength and constitute the main features of Raman spectrum. If the scattered wavelength is shorter than the incident wavelength, the scattered lines are known as Stokes line, while if the scattered wavelength is longer, then they are known as anti-Stokes lines. The Raman spectra studied in the present thesis work were recorded at room temperature by using

micro-Raman spectrometer (LabRam HR800, Horiba Jobin Yvon) in the wave number range of 150 – 1000 cm^{-1} with an excitation wavelength of 514 nm.

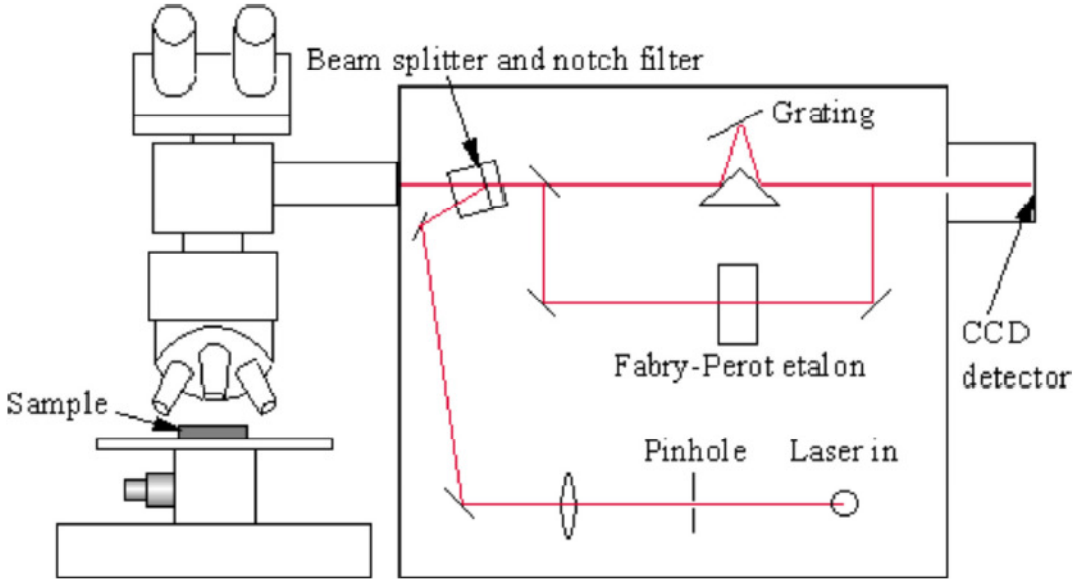

Figure 2.3 Schematic diagram of Raman spectrometer.

Raman spectrometer can be dispersive and non-dispersive. Dispersive spectrometer use grating or prism while non-dispersive spectrometer uses interferometer such as Michelson interferometer. Fig. 2.3 shows the basic building block of dispersive micro-Raman spectrometer which we have used for sample characterization. Here the intense laser beam is incident on a sample through a microscope with a spot size of a few microns. The microscope is coupled confocally to a spectrometer of 800 mm focal length and equipped with two switchable gratings. The excitation photon can be supplied by using two sources namely He-Ne laser (wavelength 632.8 nm) or Argon laser (488 and 514 nm). The beam splitter splits the beam into two parts having same wavelengths. The beam was allowed to fall on the sample where both Rayleigh and Raman scattering occur. The notch filter, allows only the Raman scattered wavelength while it blocks the incident wavelength. The inelastically scattered light was allowed to pass through the grating and etalon which in turn resolves the weak inelastically scattered wavelength coming from the sample more efficiently. Further the beam was allowed to enter into a charge coupled device where it detects the change in polarizability of the sample from the change in wavelength and converts into the intensity. We could see intensity vs. wave number graph in the computer screen.

2.5 Scanning Electron Microscope (SEM)

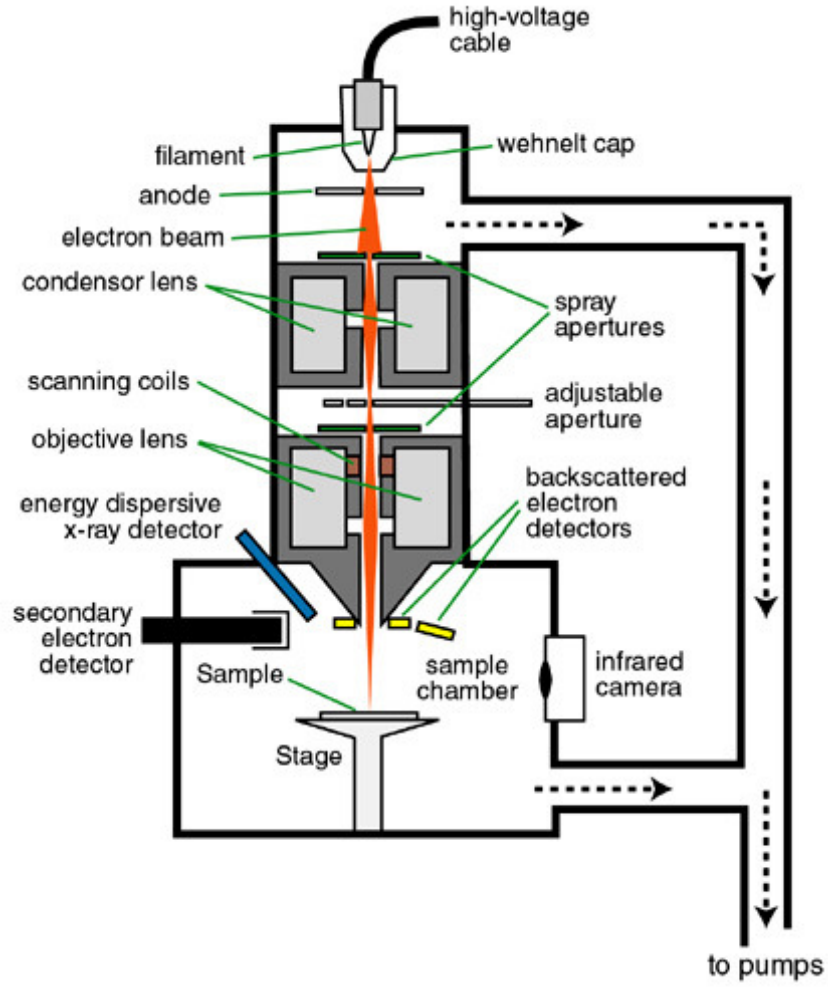

Figure 2.4 Schematic view of scanning electron microscope [96]

Recording of microstructural images and compositional analysis have been carried out by using LEO Scanning Electron Microscope (SEM, Leo 1430VP) equipped with Oxford energy dispersive spectrometer (EDS). Basic principles of SEM and EDS analysis are given briefly as following.

The scanning electron microscope (SEM) is a type of electron microscope that uses electrons to form an image of objects and to study surface morphology, fractured components, foreign particles and residues *etc*. The schematic view of SEM is shown in Fig. 2.4. The thermionically emitted electrons from a tungsten filament are drawn towards anode and were focused by two successive condenser lenses into a beam with a narrow spot size (~50 Å). The shorter wavelength of electrons permits image magnifications of up to 100,000 times in SEM. Pair of scanning coils located at the objective lens deflect

the beam either linearly or in raster fashion over a rectangular area of specimen surface. These primary bombarding electrons on the surface of the specimen dislodge electrons from the specimen. Upon electron impingement on the surface, the interaction volume assumes a tear drop shape. These dislodged electrons are known as secondary electrons, which are attracted and collected by a positively biased grid or detector, and then translated into signals. These signals are then amplified, analyzed and translated into images of the topography being inspected.

Apart from secondary electrons, the back scattered electrons (BSE), characteristic x-rays, light (cathode-luminescence), specimen current and transmitted electrons are produced by SEM. These types of signal require specialized detectors and all such detectors are not present in a single machine. The primary electron beam results in the emission of BSE from the specimen. BSE possess more energy than secondary electrons and have a definite direction. As such, they cannot be collected by a secondary electron detector, unless the detector is directly in their path of travel. All emissions above 50 eV are considered to be BSE. BSE imaging is useful in distinguishing one material from another, since the yield of the collected BSE increases monotonically with the specimen's atomic number Z (~ 0.05 $Z^{1/2}$). Backscattered imaging can distinguish elements with atomic number difference of at least 3.

Energy dispersive X-ray spectroscopy (EDS or EDX) is an analytical technique used for the elemental analysis or chemical characterization of a sample. Its characterization capabilities originate from the fact that each element has a unique atomic structure, which emits its unique characteristic X-ray. To stimulate the emission of characteristic X-rays from a specimen, a high energy beam of charged particles such as electrons or protons, or a beam of X-rays, is focused into the sample being studied. At rest, an atom within the sample contains ground state (or unexcited) electrons in discrete energy levels or electron shells bound to the nucleus. The incident beam may excite and eject an electron from an inner shell and it results in a hole or electron vacancy in the shell. An electron from the outer higher-energy shell then fills the hole, and the difference in energy between the higher-energy shell and the lower energy shell is released in the form of an X-ray. The atoms of every element releases X-rays with unique amounts of energy during the above process. Thus, by measuring the value of energy of X-rays being released by a specimen during electron beam bombardment, the identity of the atoms present in the specimen can be established. Thus, we get the EDS spectrum as an output

and it is just a plot of how frequently an X-ray is received for each energy level. An EDS spectrum normally displays peaks corresponding to the energy levels for which the X-rays had been received. Each of these peaks is unique to an atom, and therefore corresponds to a single element. The intensity of the peaks depends on the concentration of the elements present.

In the present work, a thin solid pellet was mounted on carbon coated tape. In case of conducting sample, the direct SEM and EDS measurements could be carried out without any metal coating. But our samples are semiconductor and the electrons are trapped on the surface and create charge segregation which will not allow the further bombardment of electrons, and hence the electrons cannot reach the detector. So, a coating of metal layer serves our purpose.

2.6 Field Emission SEM (FE-SEM)

A FE-SEM is used to visualize very small topographic details on the surface of pellets or fractioned objects. Researchers in biology, chemistry and physics apply this technique to observe structures that may be as small as 1 nm. In the present work ZEISS make FE-SEM (ΣIGMA) and Hitachi make FE-SEM (S-4800) were used to study the surface morphology of the samples. The resolution of this FE-SEM is 1.3 nm at 50 kV and 2.8 nm at 1 kV.

Field emission (FE) is an emission of electrons induced by external electromagnetic fields. FE can happen due to the promotion of electrons, from the valence to the conduction band of semiconductors. The related effect is cold electronic emission, i.e., the emission of electrons in strong static (or quasi-static) electric fields. The electron gun is basically a zirconium oxide coated tungsten (ZrO_2/W) emitter, which operates in a thermally assisted Schotky emission mode. This type of gun provides narrower probing beams as well as high electron energy, resulting in both improved spatial resolution and minimized sample charging and damage.

Electrons are liberated from a field emission source and accelerated in a high electrical field gradient. Within the high vacuum column, these so-called primary electrons are focused and deflected by electronic lenses to produce a narrow scan beam that bombards the object. As a result, secondary electrons are emitted from each spot on the object. The angle and velocity of these secondary electrons depend on the surface structure of the object. A high efficient annular in-lens ac-detector catches the secondary

electrons and produces an electronic signal. One more detector, i.e., solid state back scattered detector is used to detect the BSE.

The advantages of FE-SEM over SEM are as follows: (1) FE-SEM produces clearer, less electrostatically distorted images with spatial resolution down to 1 nm., *i.e.*, 3 to 6 times better than conventional SEM; (2) smaller-area contamination spots can be examined at electron accelerating voltages compatible with Energy Dispersive X-ray Spectroscopy; (3) Closer to the immediate material surface can be probed due to the reduced penetration of low kinetic energy electrons; (4) high quality, low voltage images are obtained with negligible electrical charging of samples. (Accelerating voltages range from 0.5 to 30 kV).

In order to observe FE-SEM for objects, the sample should have electrically conducting. This can be done by coating them with an extremely thin layer (1.5 - 3.0 nm) of gold or carbon by using respective coater.

2.7 Vibrating Sample Magnetometer

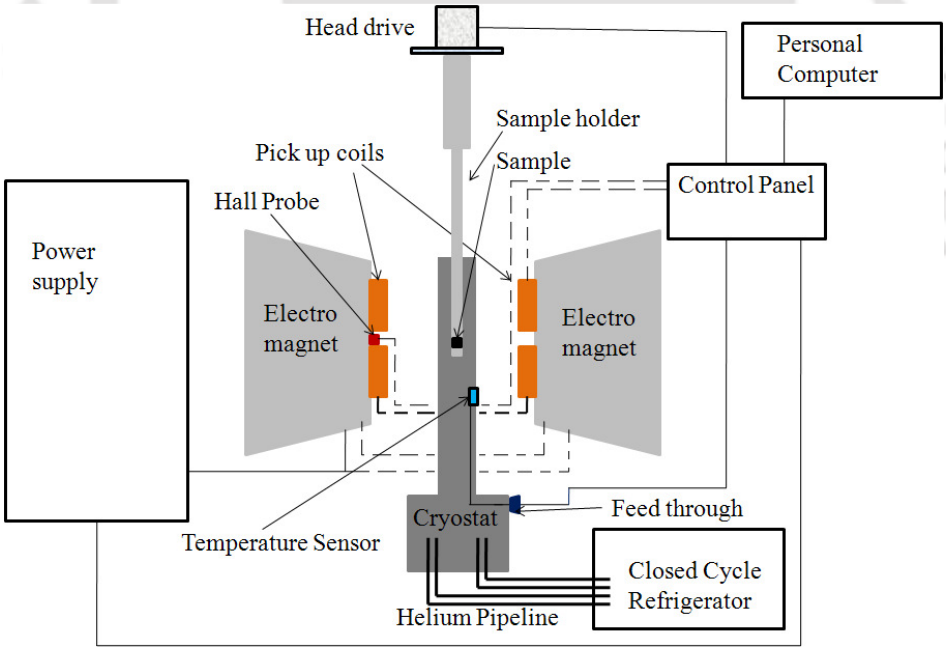

Figure 2.5 Block diagram of the vibrating sample magnetometer.

The vibrating sample magnetometer (VSM) has become a widely used instrument for measuring the magnetic properties of a large variety of magnetic materials. The vibrating sample magnetometer (VSM) developed originally by Foner [97] has, however,

been the most successful for low temperature and high magnetic field studies of correlated electron systems. It has a flexible design and combines high sensitivity with ease of sample mounting and exchange. Samples can be changed rapidly even at any operating temperature. Using a vibrating sample magnetometer, one can measure the DC magnetic moment as a function of temperature, magnetic field and time. So, it allows performing susceptibility and magnetization studies. Magnetic moments as small as 5×10^{-5} emu are measurable with a VSM [97].

The temperature variations of zero field cooled (ZFC) and field cooled (FC) magnetization (M) were measured by using the Lakeshore, model no. 7410 vibrating sample magnetometer. The basic block diagram of a VSM equipped with the low temperature measurement attachment is shown in Fig. 2.5. The temperature variation down to 20 K was achieved using an OXFORD make CCR cryostat (model N125) along with the temperature controller. For measuring magnetic properties in the high temperature range 300 – 1273 K, another similar VSM provided by Lakeshore is used with a high temperature oven supplied by Lakeshore (Model 74034). During the experiment in the high temperature, Ar gas was kept flowing into the oven throughout the experiment. The magnetic field was produced by using a 10 inch electromagnet. The magnetization loop was measured by varying field upto 2 T. Calibration of the vibrating sample magnetometer was done by measuring the magnetic moment of a standard pure Ni sample.

The VSM is based upon Faraday's law, according to which an emf is induced in a conductor by a time-varying magnetic flux. If a sample of any magnetic material is placed in a uniform magnetic field, a dipole moment will be induced. If the sample vibrates with sinusoidal motion, there is some magnetic flux change. This induces a voltage in the pick-up coils, which is proportional to the magnetic moment of the sample. Voltage, $V(t)$ can be detected to a high resolution and accuracy by means of suitable VSM signal detector (e.g. Lock in Amplifier).

2.8 Electron Paramagnetic Resonance

Electron Paramagnetic Resonance (EPR) or Electron Spin Resonance (ESR) spectrometer is based on a non-destructive spectroscopic technique where the interaction between electromagnetic radiation and the intrinsic spin magnetic moment of electrons leads to resonance condition. It is based on Zeeman effect that explains the splitting of

energy level of a particle having spin ½ in a magnetic field. The energy difference between the two levels is given by

$$\Delta E = g\mu_B B \tag{2.7}$$

where, g is the Landé g-factor, μ_B is Bohr magneton and B is the amplitude of applied magnetic field. Since the energy difference between the two states depends on the magnetic field, electrons at the lower energy state can jump to the excited state at a particular value of the magnetic field. Alternatively, one can fix the magnitude of the applied field and vary its frequency. At certain value of frequency, the electrons can jump to the higher state giving rise to absorption peak in the spectra. At resonance,

$$h\nu = g\mu_B B \tag{2.8}$$

where υ is the frequency of the electromagnetic signal h is Planck's constant. Neither the field nor the frequency for resonance is a unique fingerprint for a system because spectra can be obtained at different value of B or frequency satisfying the eqn. (2.8). It is therefore the g-factor is the most useful parameter for the characterization of EPR spectra.

The basic building blocks of an EPR are shown in Fig. 2.6 [98]. The microwave generator generates and supplies microwave at controlled frequency and power which are transmitted to the sample cavity through a waveguide. The sample cavity is mounted in the midst of the electromagnet pole pieces perpendicular to the magnetic field, B which can be varied in a controlled way. In addition to the main magnetic field, another magnetic field which is weaker compared to the main field is generated and superimposed on the cavity by Zeeman modulation coils. Thus the signal response from the cavity is modulated at the Zeeman modulation frequency. The ideal way for EPR spectra is to fix the magnitude of the magnetic field and continuously vary its frequency. However, microwave generators are tunable only to a limited range of frequency. Hence, the microwave frequency is fixed and magnitude of the magnetic field is varied. The magnetic field is swept until it reaches a stage where the sample can absorb the microwave signal of a particular frequency and jump to the higher energy level and at this stage the, EPR absorption occurs [98].

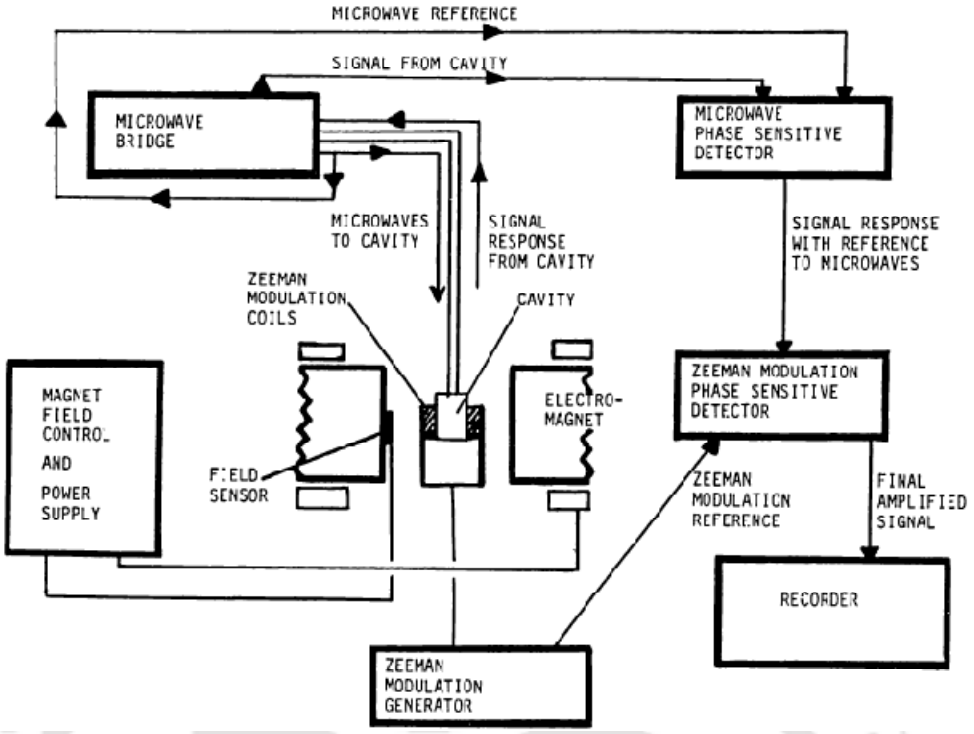

Figure 2.6 A block diagram for a typical continuous wave EPR spectrometer [98]

Commercial EPR spectrometer works in different frequency range *i.e.*, 1-2 GHz (L-band) and 2-4 GHz (S-band), 8-10 GHZ (X-Band), 35 GHz (Q-band) and 95 GHz (W-band). In the present investigation, we have carried out the EPR measurement in powder form using JEOL Spectrometer (JES-FA200) operating at X-band frequency (ν = 9.4 GHz) with 100 kHz magnetic field modulation.

2.9 Dielectric Measurement

Impedance data were measured by using a Wayne Kerr make LCR meter (Model 1J4300R/43100R) in the frequency range of 10^2 – 10^6 Hz with an AC voltage of 1.0 V_{rms}. The data were collected by WAYNE KERR LCR METER software provided by WayneKerr which connects the LCR meter to personal computer through RS232 interface. The temperature variation is carried out using a high temperature oven. The Chromal-Alumel (Cr-Al) thermocouple and a Eurotherm make temperature controller (Model no. 3216) are used for temperature measurements and controlling. For electric measurements, samples were taken in pellet form with typical thickness of 1 – 1.5 mm and radius 5 – 6 mm. The thickness and radius are calculated using a screw gauge and a digital verniar caliper respectively. Electrodes are fabricated by painting silver pastes

(McMillan) on both sides of the pellets. The samples were fired at 150 °C in air for 2 h and furnace cooled to room temperature before carrying out the electrical measurement.

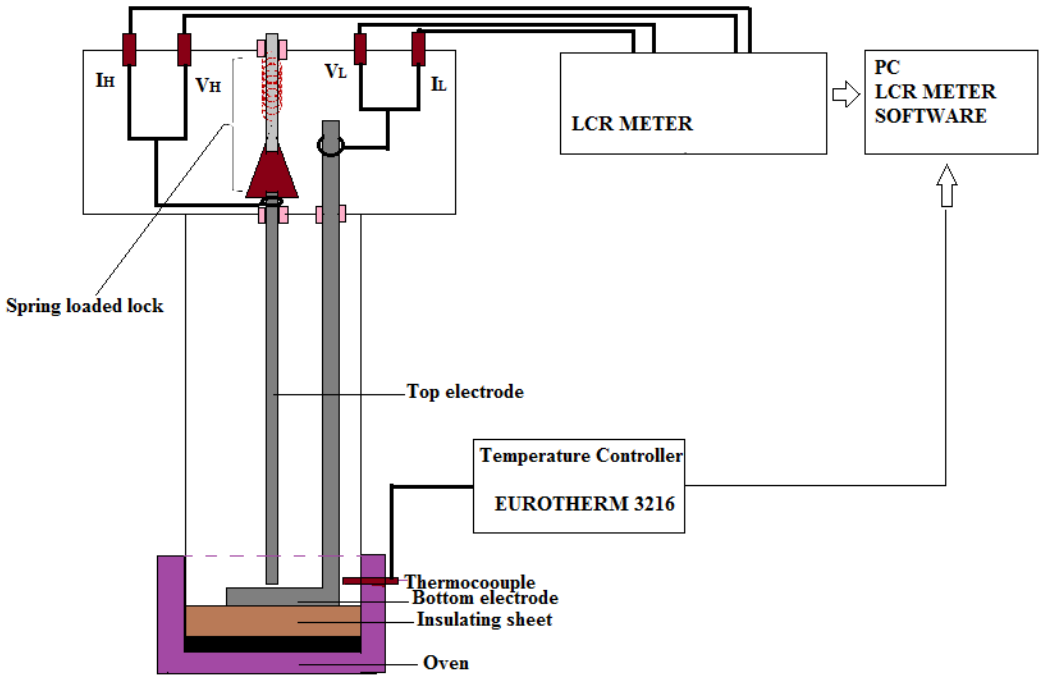

Figure 2.7 Block diagram for dielectric measurements.

The basic block diagram for impedance measurement set up is shown in Fig. 2.7. The set up consist of an LCR meter which is connected to a sample holder through four BNC connectors. The sample holder is made up of stainless steel. The measurements are carried put in a parallel plate capacitor arrangement by employing the four terminals method. The top electrode is spring loaded, thus making it possible to adjust depending on the sample dimension. The top electrode is connected to the terminals VH and IH, while the bottom electrode is connected to VL and IL terminals. The IH/IL pair is connected to signal generator to pass the current through the sample, while VH/VL pair is used for voltage measurement. The LCR meter measures the voltage across the device under test (DUT) by sending current of certain frequency (ω) and calculates the impedance of DUT using the relation:

$$Z^*(\omega) = V^*(\omega)/I^*(\omega) \tag{2.9}$$

where $Z^*(\omega)$, $V^*(\omega)$, $I^*(\omega)$ are complex. The LCR meter used in the present work internally calculates and displays the real (Z') and imaginary (Z'') parts of Z^* and capacitance. In the present study, we measure Z' and Z'' in the frequency range of 10^2 –

10^6 Hz and calculate the related parameter such as real and imaginary part of dielectric constant (ε' and ε''), loss tangent (tanδ), electric modulus (M' and M''), conductivity (σ') using the following relations:

$$\varepsilon' = \frac{-Z''}{\omega C_0 \left(Z'^2 + Z''^2\right)} \tag{2.10}$$

$$\varepsilon'' = \frac{Z'}{\omega C_0 \left(Z'^2 + Z''^2\right)} \tag{2.11}$$

$$M' = \frac{\varepsilon'}{\left(\varepsilon'^2 + \varepsilon''^2\right)} \tag{2.12}$$

$$M'' = \frac{\varepsilon''}{\left(\varepsilon'^2 + \varepsilon''^2\right)} \tag{2.13}$$

$$\tan\delta = \frac{\varepsilon''}{\varepsilon'} \tag{2.14}$$

$$\sigma' = \omega \varepsilon_0 \varepsilon'' \tag{2.15}$$

where C_0 is the geometrical capacitance of the DUT having thickness t and area A which is given by

$$C_0 = \frac{\varepsilon_0 t}{A} \tag{2.16}$$

Thus we have given a brief overview of experimental techniques used in material preparations, characterization and the relevant physical measurements to study their electric and magnetic properties.

Chapter 3

Mn doped $YFeO_3$ series

Rare-earth orthoferrites mostly crystallize in orthorhombically distorted perovskite structure with space group *Pnma* [40, 99, 100]. The recent interest in $RFeO_3$ (*R* = rare-earth element) type compounds is mainly due to the presence of magneto-electric coupling that allows electric field control of magnetism, which in turn has potential application in memory devices [101, 102]. The unusual magnetic properties such as field and temperature dependent spin reorientation phenomena, exchange bias, magnetization reversal, *etc*. are due to the exchange interactions in R^{3+} –O^{2-}–R^{3+}, R^{3+}–O^{2-}–Fe^{3+} and Fe^{3+}–O^{2-}–Fe^{3+} networks. The superexchange interaction in the Fe^{3+}–O^{2-}–Fe^{3+} networks gives rise to the antiferromagnetic transition in the temperature range 650 –700 K with typical *G*-type AFM structure [40]. However, Dzyaloshinskii-Moriya (DM) antisymmetric exchange interaction in this system tends to cant the Fe^{3+} spins resulting in a small net magnetic moment and is commonly referred as weak FM [48, 103]. There are three basic spin configurations for Fe^{3+} sublattice in orthoferrites [40, 104] which are: Γ_1 ($G_xC_yA_z$), Γ_2 ($C_xG_yF_z$) and Γ_4 ($A_xF_yG_z$). In the presence of magnetic rare-earth element and the associated magnetic anisotropy in R^{3+}–O^{2-}–Fe^{3+}networks, the spin configuration undergoes transition from Γ_4 to Γ_2 (or Γ_1) phase upon cooling. In orthoferrites having non-magnetic rare-earth ions, the Γ_4 configuration is stable without undergoing any spin re-orientation [40].

$YFeO_3$ is a well known orthoferrite having distorted perovskite structure with *Pnma* space group, where each Fe^{3+} ion is octahedrally co-ordinated to six nearest oxygen ions [39, 105]. It is basically a *G*-type antiferromagnet with its Néel temperature (T_N) around 650 K [48, 103]. $YFeO_3$ draws considerable research attention because of the possibility of inducing ferroelectric order by the spin canting [47]. The spin induction model predicts improper ferrolectricity in weak ferromagnet due to the presence of $\boldsymbol{S_i} \times \boldsymbol{S_j}$ type coupling [47]. Shang *et al*. [48] reported such improper ferroelectricity in $YFeO_3$, where they observed a clear $P - E$ loop at room temperature. Acharya *et al.* reported similar improper ferroelectric ordering in $LaFeO_3$, with a maximum value of saturation polarization of 0.3229 $\mu C/cm^2$ [106]. As the magnetism induced ferroelectricity vanishes at the magnetic transition temperature, it may lead to large dielectric anomaly across the transition temperature. It is very interesting to tune such anomaly around the room temperature by shifting the magnetic transition temperature to room temperature. In this chapter, we look for such possibilities and the dielectric anomalies across the Néel temperature of $YFe_{1-x}Mn_xO_3$ (x = 0 – 0.3) compounds by using the impedance, dielectric and electric modulus spectroscopy.

3.1 Sample Preparation and Characterization

$YFe_{1-x}Mn_xO_3$ compounds for x = 0.0 – 0.3 were prepared by the standard solid state reaction method. Stoichiometric amounts of Y_2O_3, $Mn(CH_3COO)_2.4H_2O$ and Fe_2O_3 of purity better than 99 % were weighed and grinded using agate mortar and pestle under acetone medium for about 1 h. The above uniform mixture was presintered at 1173 K for 12 h. The presintered powder was pressed into cylindrical pellets of approximately 10 mm diameter and 2 mm of thickness at a pressure of 2.94×10^8 N/m^2 by using a hydraulic press. The final sintering was carried out at 1723 K for 24 h in air atmosphere with a heating rate of 5 K/ min, followed by furnace cooling to room temperature. Crystal structure of the samples was determined using x-ray diffraction (XRD) patterns recorded by using a Rigaku make TTRAX III X-ray diffractomerter by employing Cu-K_α radiation. Microstructural analysis was carried out using ZEISS make field emission scanning electron microscope (FE-SEM, ΣIGMA) equipped with EDS facility. Temperature and field variations of magnetization measurements were carried out using a vibrating sample magnetometer (Lakeshore, model 7410) in the temperature range of 25– 700 K. For the electrical characterization, electrodes were fabricated by painting silver pastes on both

sides of the sample of typical thickness of 1–1.5 mm. The samples were fired at 423 K in air for 2 h and furnace cooled to room temperature before carrying out the electrical measurement. The frequency dependent dielectric measurements over a frequency range of 10^2–10^6 Hz at several temperatures (303 K – 673 K) were measured using an LCR meter (Wayne Kerr Electronics Pvt. Ltd., 1J43100). Here the ac voltage of 1.0 V_{rms} was set during the measurements. The impedance spectra were analyzed using commercially available ZSimpWin software (version: 3.21).

3.2 Structural Properties

Fig. 3.1 shows the XRD patterns of $YFe_{1-x}Mn_xO_3$ samples with x = 0.0 – 0.3. No additional reflections other than the $YFeO_3$ phase are observed in the figure, which clearly reveals that the prepared samples are in single phase form. The detailed analysis of XRD patterns were carried out by refining them as per Rietveld refinement technique using *FULLPROF* software [107]. Here we have taken the *Pnma* space group *i.e.*, with orthorhombic structure. Typical Rietveld refinement of XRD patterns of $YFe_{1-x}Mn_xO_3$ samples with x = 0, 0.10, 0.2 and 0.3 are shown in Figs. 3.2 and 3.3. Typical values of lattice parameters of x = 0 sample are found to be a = 5.5948(2) Å, b = 7.6066(3) Å and c = 5.2834(2) Å and they are comparable to those reported in literature [48]. The different structural parameters obtained from the Rietveld refinement of XRD patterns for all samples are presented in Table 3.1. As can be seen in the table, substitution of Mn in Fe site leads to the contraction of *bc*-plane and the expansion of unit cell along *a*-axis. The substitution of smaller Mn^{3+} (0.580 Å) ions at Fe^{3+} (0.645 Å) site is expected to reduce the lattice parameters and the same is observed for lattice constants *b* and *c*. However, the observed increase in a value with Mn concentration can be attributed to Jahn-Teller distortion associated with Mn^{3+} ions [104, 108, 109] or due to the counter effect of shrinkage along *bc*-plane.

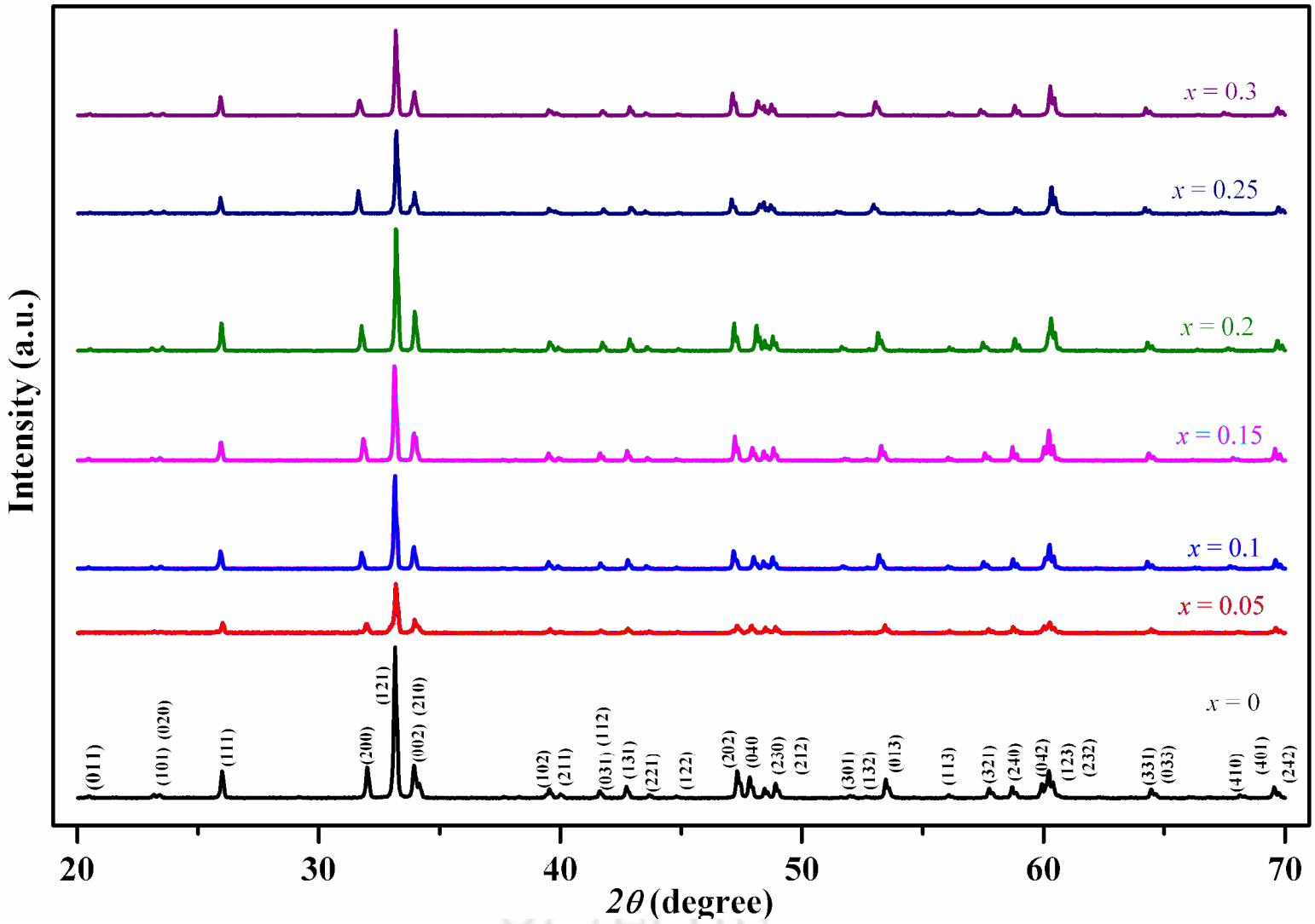

Figure 3.1 XRD patterns for $YFe_{1-x}Mn_xO_3$ ($x = 0 – 0.3$) samples

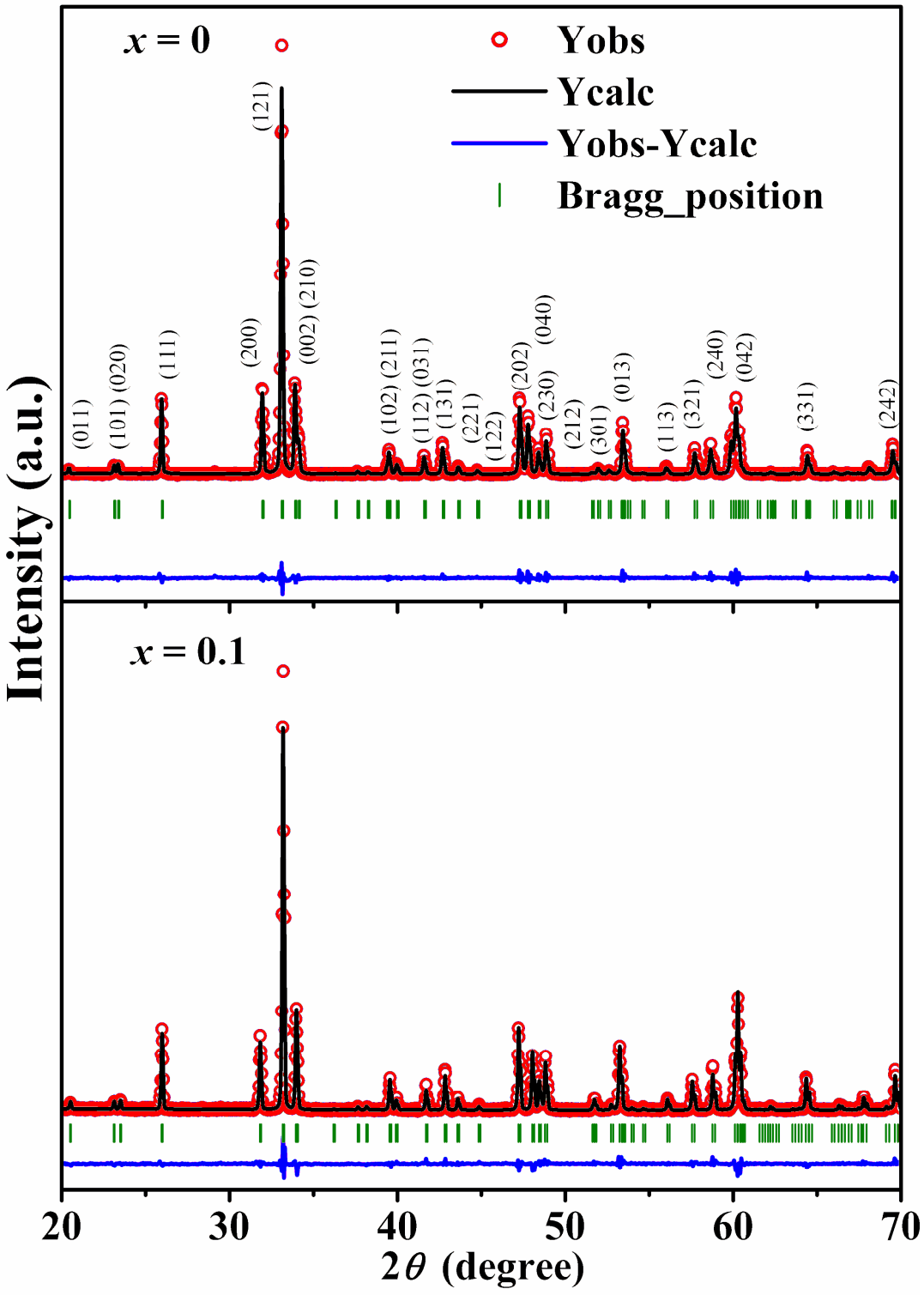

Figure 3.2 XRD patterns along with Rietveld refinement of $YFe_{1-x}Mn_xO_3$ samples with x = 0 and 0.10.

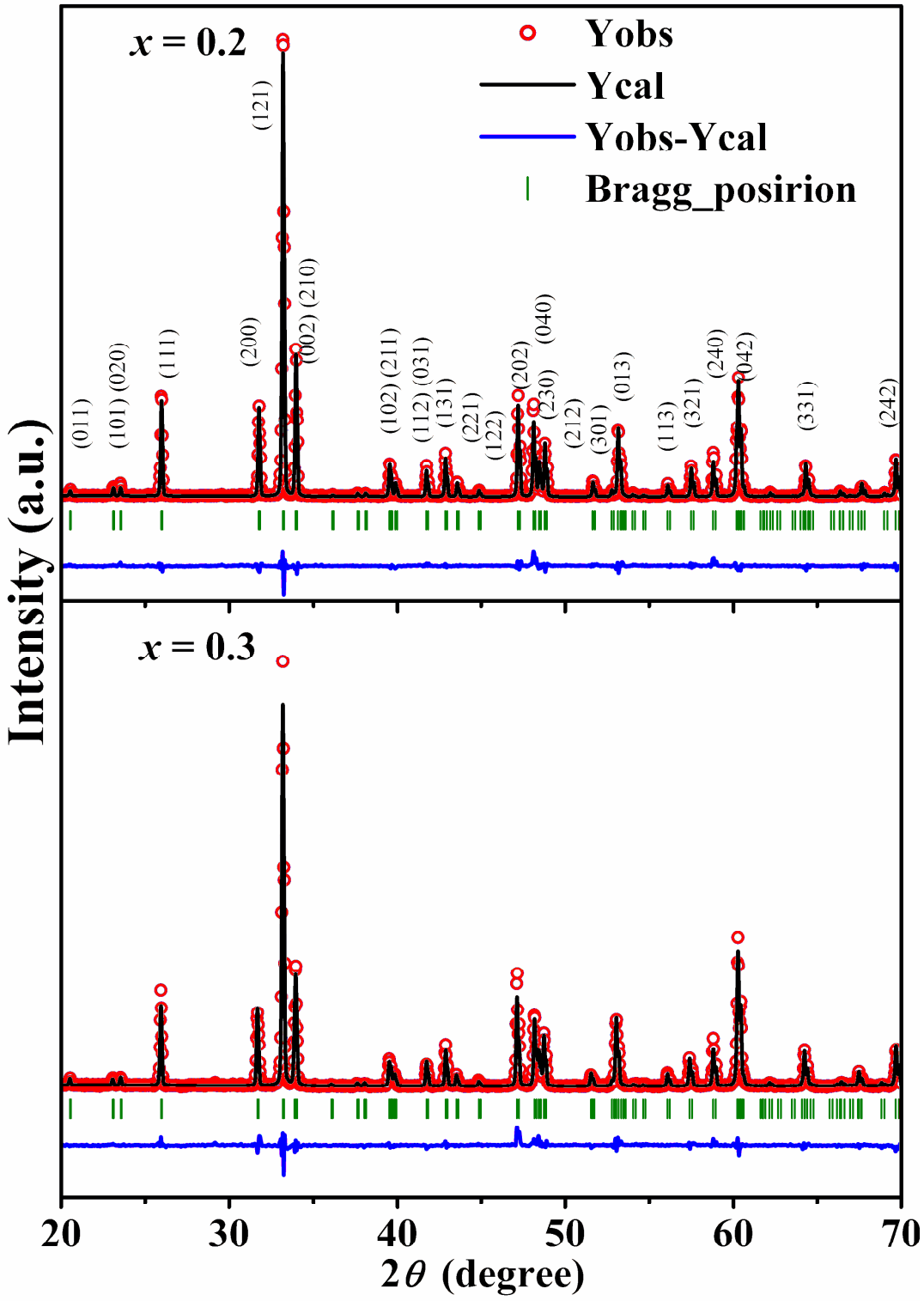

Figure 3.3 XRD patterns along with Rietveld refinement of $YFe_{1-x}Mn_xO_3$ samples with x = 0.20 and 0.30.

Table 3.1 Parameters obtained from the Rietveld refinement of XRD patterns of $YFe_{1-x}Mn_xO_3$ (x = 0 – 0.3) samples. R_f, R_{Bragg}, R_P and χ^2 are the reliability factors (* SG: Space group).

Parameters	Samples (x)						
	0	0.05	0.10	0.15	0.20	0.25	0.30
SG*	*Pnma*	*Pnma*	*Pnma*	*Pnma*	*Pnma*	*Pnma*	*Pnma*
a (Å)	5.5948	5.6038	5.6149	5.6221	5.6336	5.6434	5.6551
b (Å)	7.6066	7.5973	7.5859	7.5715	7.5629	7.5517	7.5400
c (Å)	5.2834	5.2828	5.2803	5.2769	5.2761	5.2753	5.2743
V (Å^3)	224.84	224.91	224.91	224.62	224.79	224.89	224.82
R_f (%)	2.16	4.73	5.19	6.11	4.36	6.64	7.10
R_{Bragg}(%)	2.38	5.13	5.74	5.39	5.12	5.54	6.92
R_P (%)	6.98	9.61	10.5	9.50	9.18	10.6	10.8
χ^2	3.37	3.35	3.35	3.77	3.80	3.93	4.07

The surface morphology of samples is characterized by recording FE-SEM images. Typical FE-SEM images of x = 0, 0.1, 0.2 and 0.3 samples of $YFe_{1-x}Mn_xO_3$ are shown in Fig. 3.4. The average grain size is estimated by using ImageJ software and employing the linear intercept method. The average grain size for x = 0 sample is found to be 8 μm, which slightly reduces to 7 μm for x = 0.1, 0.2 and 0.3 samples. There is no appreciable change in grain size due to Mn doping. The typical cationic ratio Y: Fe: Mn estimated from the EDS spectra of x = 0.1 and 0.3 samples are found to be 1.01:0.89:0.11 and 1.01:0.69:0.31 respectively and they are comparable to their nominal starting compositions.

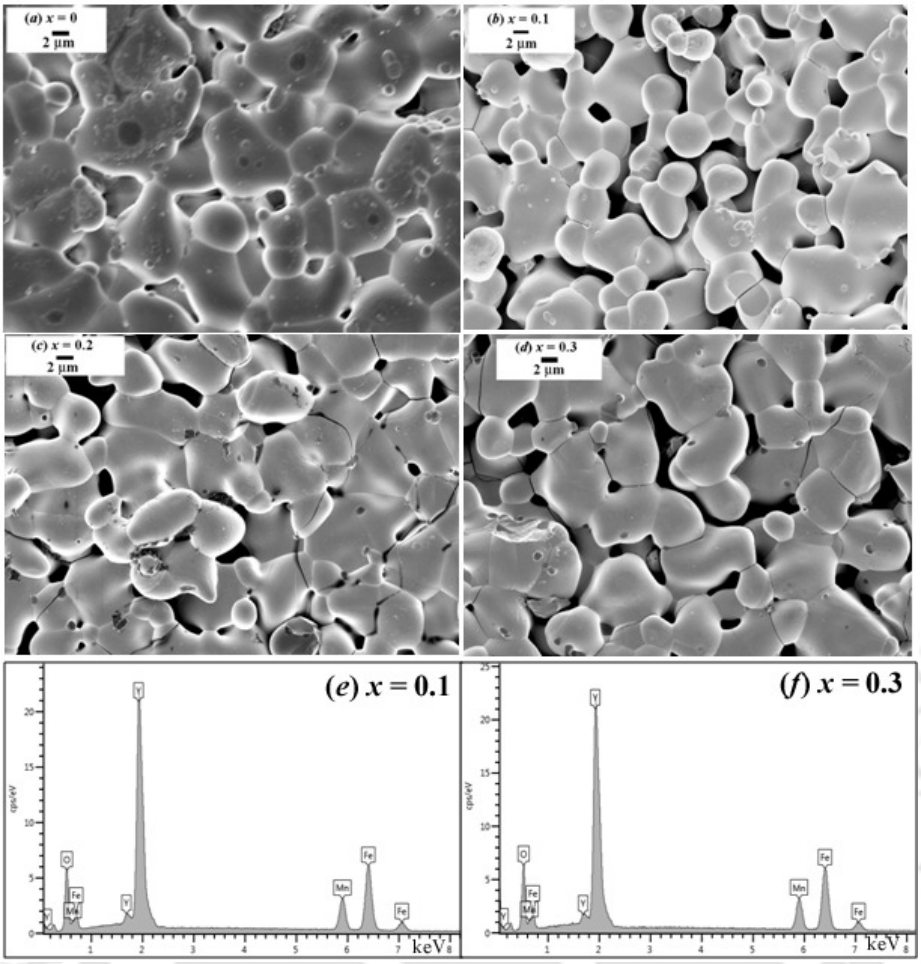

Figure 3.4 FE-SEM images of (*a*) $x = 0$, (*b*) $x = 0.10$, (*c*) $x = 0.20$ and (*d*) $x = 0.30$ samples of $YFe_{1-x}Mn_xO_3$ samples along with EDS spectra for (*e*) $x = 0.10$ and (*f*) $x = 0.20$ samples.

3.3 Complex Impedance Spectroscopy

The typical plots of frequency variations of real part (Z') of complex impedance (Z^*) are shown in Fig. 3.5 for $YFe_{1-x}Mn_xO_3$ samples with $x = 0$, 0.10, 0.20 and 0.25 at different temperatures. The Z' as a function of frequency at a given temperature exhibits a plateau-like behavior at low frequency followed by rather sharp fall in Z' at higher frequency. The impedance response of a sample arises due to motion of charge carriers in the intra-grain, inter-grain regions and material-electrode interface. There are various ways of charge carriers' movement such as long-range/short-range displacement, dipole reorientation and via the formation of space charges, *etc*. The frequency dependence of Z' is governed by all these type of charge carriers movement. The observation of plateau-

like region in Z' spectra followed by its sharp fall with increase in frequency reveals the relaxation process in the samples. The Z' value for a particular composition decreases with increase in temperature and it suggests that the material possesses the negative temperature coefficient of resistance (NTCR). The effect of increasing Mn concentration is observed in terms of the decrease in the value of Z'.

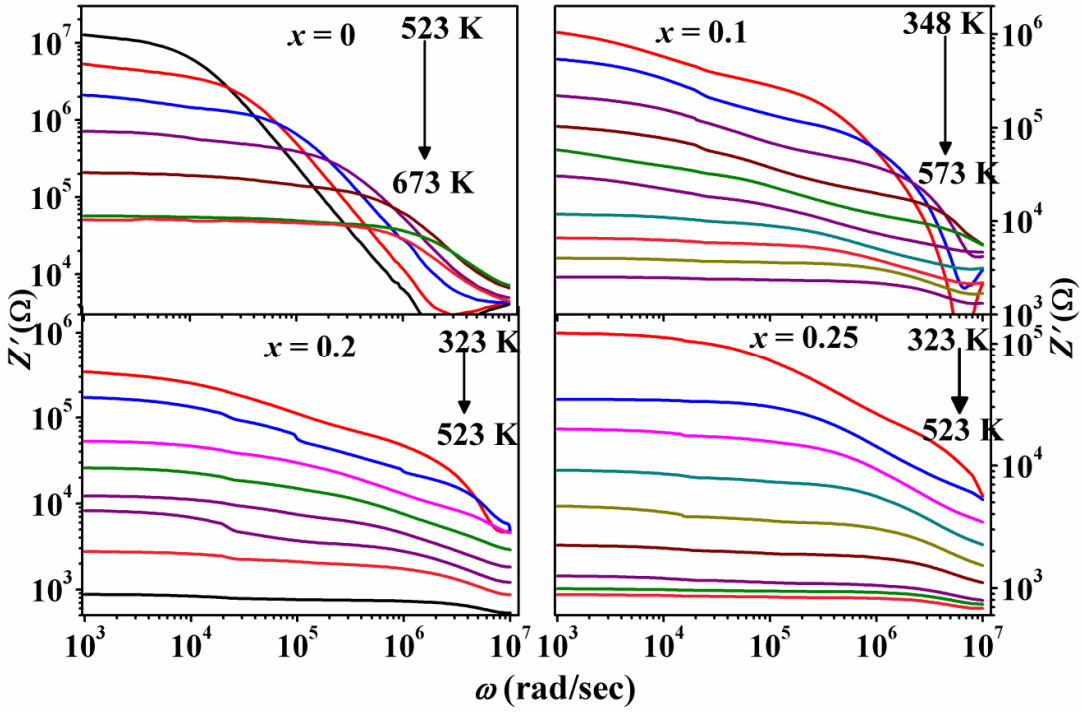

Figure 3.5 Frequency variations of Z' of x = 0, 0.10, 0.20 and 0.25 samples of $YFe_{1-x}Mn_xO_3$ at different temperatures in logarithmic scale.

Fig. 3.6 shows the frequency dependence of imaginary part ($-Z''$) of complex impedance at different temperatures for x = 0, 0.10, 0.20 and 0.25 samples. The interesting feature of the spectra is the observation of atleast one relaxation peak, which shifts towards higher frequency with increase in temperature along with decrease in the magnitude of Z''. The relaxation peak for x =0 sample at T = 523 K occurs at a relaxation frequency, f_{max} = 600 Hz (*i.e.*, at ω_{max} = 3768 rad/sec). These relaxation peaks are attributed to the grain relaxations. Closer inspection of the spectra indicates the presence of another peak especially for the measurements carried out in the temperature range of 573 – 643 K and they are found to get suppressed with increase in temperature. This peak is attributed to grain boundaries relaxation. Similar relaxation peaks due to grains and grain boundaries are observed for other samples, but unlike the case of x = 0, grain

boundaries relaxations are found to be quite dominant for other samples. The peak shift towards the higher frequency with further increase in temperatures signifies the presence of thermally activated relaxation dynamics. The shift of relaxation frequency or the frequency maximum with temperature can be explained in terms of Arrhenius law.

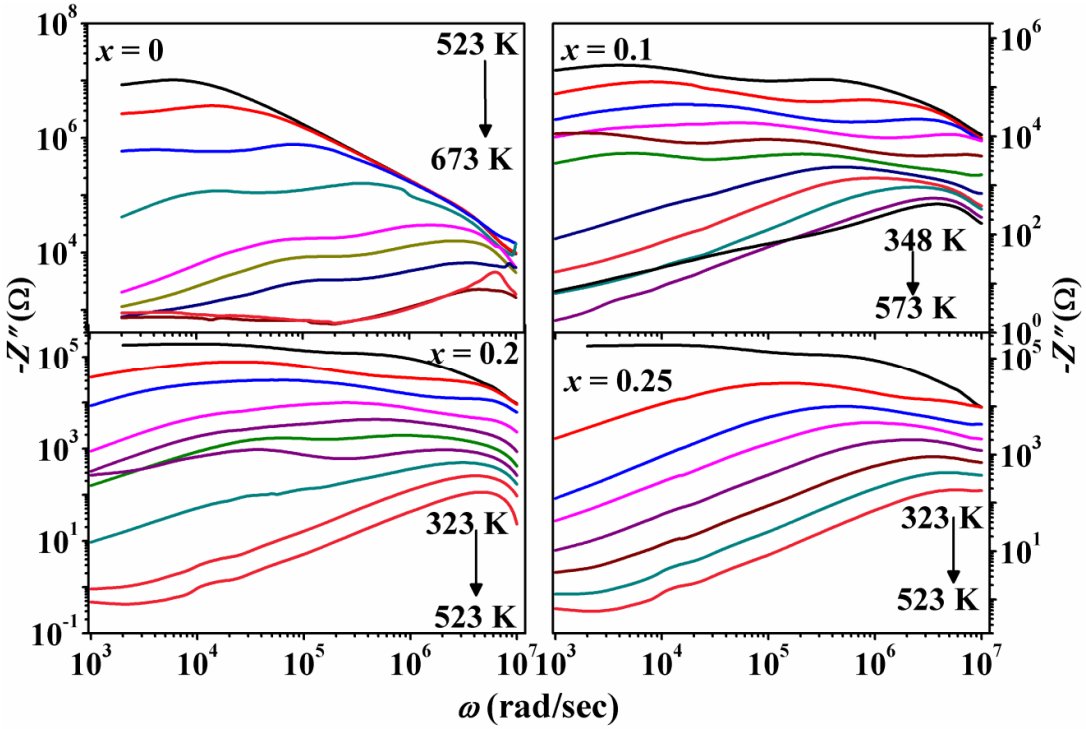

Figure 3.6 Frequency variation of $-Z''$ of x = 0, 0.10, 0.20 and 0.25 samples of $YFe_{1-x}Mn_xO_3$ at different temperature in logarithmic scale.

3.3.1 Nyquist Plots

Fig. 3.7 shows the Nyquist plots *i.e.*, $-Z''$ vs. Z' plots of $YFe_{1-x}Mn_xO_3$ samples with x = 0, 0.10, 0.20 and 0.30 at different temperatures. The Nyquist plot for x = 0 takes the shape of an arc at T = 473 K. The arc bends towards the Z' axis to form a semicircular shape with increase in temperature and it is attributed to the decrease in the resistance [110]. Finally, a clear semicircle develops at around 548 K. The Nyquist plots for other samples consist of two semicircular arcs at low temperature. The semicircle at higher frequency region moves beyond the measured frequency range with further increase in temperature, and thus only a single semicircle is seen.

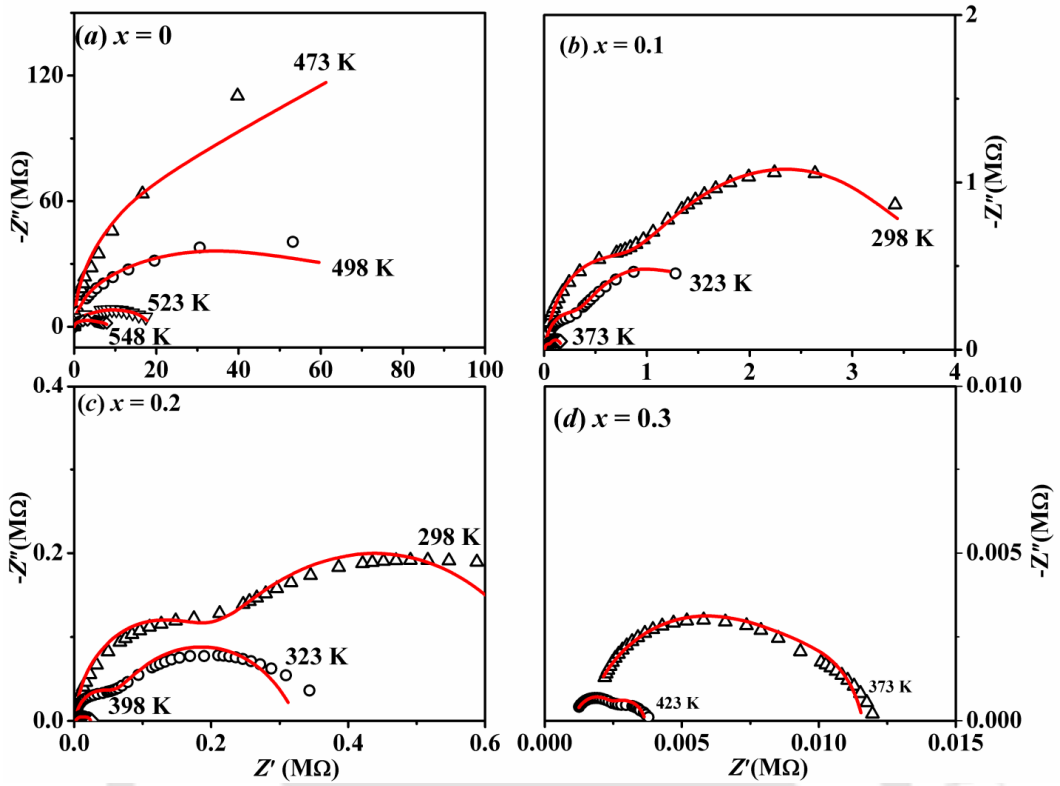

Figure 3.7 Nyquist plots of $YFe_{1-x}Mn_xO_3$ samples for x = 0, 0.10, 0.20 and 0.30 at different temperatures. The solid lines are fitted data to the circuit shown in Fig.3.8.

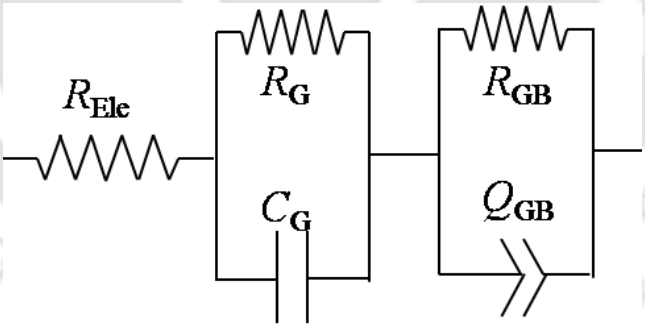

Figure 3.8 Equivalent electrical circuit

The interesting feature of the Nyquist plots is that the semicircles are distorted and depressed such that their centers lie off the Z' axis. Depression of semicircles is attributed to the statistical distributions of relaxation times. For a single relaxation time a perfect semicircle is obtained with its center on the Z' axis. This is known as the ideal Debye behavior. On the otherhand, distortion occurs if there are more than one relaxation processes and the mean relaxation times for the relaxation processes differ by two orders

of magnitude [26]. They are due to the non-uniformity of the microstructures and the electromagnetic diffusions in intragrain/intergrain regions. An equivalent circuit as shown in Fig. 3.8 is used to analyze the Nyquist plots to estimate the contributions to impedance from the different electroactive regions *viz.* grains, grain boundaries *etc.* Here, R_{Ele} is the resistance of electrodes. Q represents the constant phase element (CPE) and its impedance is given by $Z_{CPE} = 1/A(j\omega)^n$. From the fitting the grain resistance (R_G), grain boundary resistance (R_{GB}), grain capacitance (C_G), grain boundaries CPE (CPE_{GB}) and the frequency exponent (n) are estimated and are listed in Table 3.2 for different temperatures**.** The values of R_G and R_{GB} decrease with increase in temperature suggesting the negative temperature coefficient of resistance and in addition to that they are found to decrease with increase in Mn concentration. It is attributed to the enhancement of leakage current due to the possible increase in oxygen vacancies (OVs). The increase in density of OVs lead to increase in Fe^{2+}/Fe^{3+} ratio, thereby increasing the possibility of charge hopping between Fe^{2+} and Fe^{3+} ions. Moreover, the possible cluster formation of OVs due to higher density of OVs makes their movement easier and enhances the conductivity. The hopping of charges between Fe^{2+} and Fe^{3+} ions is similar to the oscillation of dipole in the presence of electric field. The charge hopping increases with increase in temperature and Mn concentrations which leads to the observed increase in C_G with increase in temperature and Mn concentration.

Table 3.2 Grains resistance (R_G), grains capacitance (C_G), grain boundaries resistance (R_{GB}), grain boundaries CPE (CPE_{GB}) and frequency exponent (n) at different temperatures obtained from the analysis of Nyquist plots.

x	T (K)	Grains		Grain boundaries		
		R_G (Ω)	C_G (pF)	R_{GB} (Ω)	CPE_{GB}($nF.s^{n-1}$)	n
0	543	1.50×10^{7}	9.54	--	--	--
	573	1.37×10^{6}	9.05	8.65×10^{5}	0.350	0.91
	598	2.60×10^{5}	10.83	1.08×10^{5}	0.730	0.90
	623	8.2×10^{4}	14.80	1.82×10^{4}	89.505	0.78
0.05	323	2.50×10^{7}	6.03	--	--	--
	373	1.48×10^{6}	8.13	2.06×10^{6}	4.418	0.56
	423	2.20×10^{5}	8.40	3.22×10^{5}	12.17	0.56
	473	3.23×10^{4}	16.90	9.97×10^{4}	23.30	0.56
0.10	323	1.66×10^{6}	9.20	-	-	-
	373	1.33×10^{5}	13.86	5.52×10^{5}	14.30	0.56
	423	1.91×10^{4}	8.32	9.88×10^{4}	49.50	0.56
	473	3.60×10^{3}	446.69	1.46×10^{4}	89.70	0.57
0.15	323	4.33×10^{5}	7.97	1.82×10^{6}	169.61	0.21
	373	6.21×10^{4}	13.77	2.32×10^{5}	28.00	0.49
	423	3.42×10^{3}	169.37	3.26×10^{4}	45.68	0.49
	473	--	--	6.95×10^{3}	54.98	0.49
0.20	323	5.37×10^{4}	11.55	3.34×10^{5}	13.80	0.57
	373	1.67×10^{4}	17.55	3.35×10^{4}	117.72	0.56
	423	--	--	7.13×10^{3}	63.87	0.56
	473	--	--	1.27×10^{3}	0.484	0.56
0.25	323	1.93×10^{4}	120.16	5.12×10^{4}	18.82	0.36
	373	4.6×10^{3}	271.27	5.60×10^{3}	908.96	0.36
	423	--	--	2.37×10^{3}	1844.03	0.34
	473	--	--	0.26×10^{3}	6342.45	0.33
0.30	323	--	--	2.53×10^{5}	9.42	0.57
	373	--	--	1.50×10^{4}	24.02	0.56
	423	--	--	2.46×10^{3}	42.32	0.56
	473	--	--	0.46×10^{3}	111.03	0.56

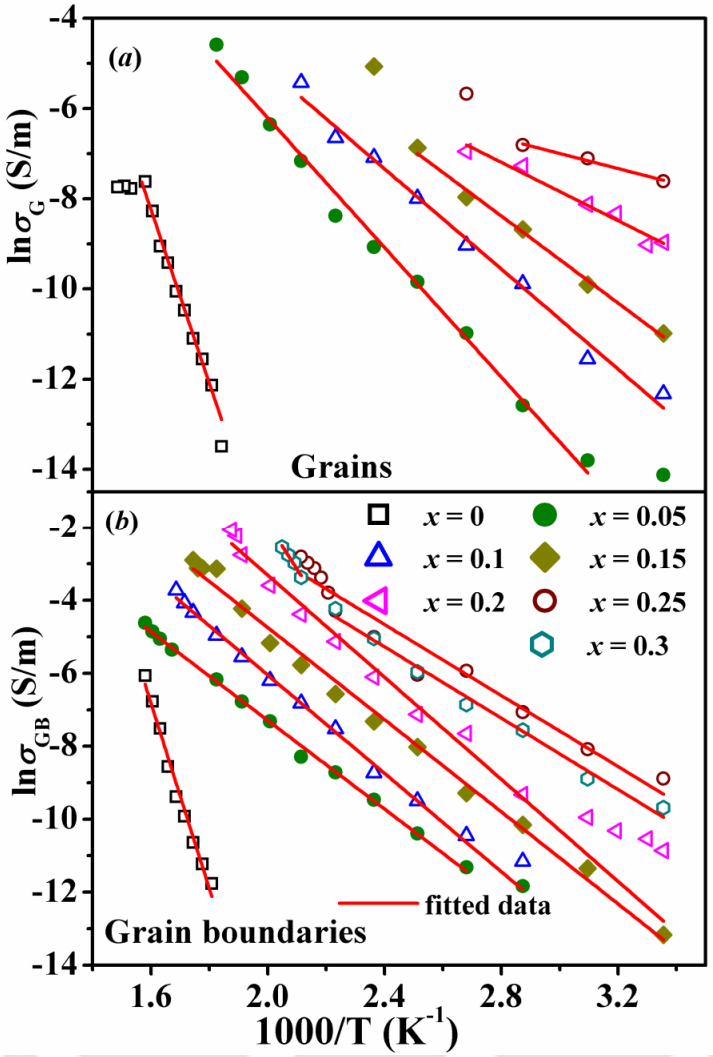

Figure 3.9 Arrhenius plots for grains and grain boundaries conductivities of $YFe_{1-x}Mn_xO_3$ samples ($x = 0 – 0.3$).

The dc conductivity contributions of the grains (σ_G) and grain boundaries (σ_{GB}) were estimated from their respective resistance values using the relations $\sigma_G = t/AR_G$ and $\sigma_{GB} = t/AR_{GB}$ where t and A are respectively the thickness and circular area of the samples. Both σ_G and σ_{GB} follow the Arrhenius law [111]:

$$\sigma = \sigma_0 \exp\left(-E_C / k_B T\right) \tag{3.1}$$

where σ_0 is the pre-exponential factor, E_C is the activation energy for conduction, k_B is Boltzmann constant and T is the temperature. Fig. 3.9 shows the plots of $\ln\sigma_G$ and $\ln\sigma_{GB}$ vs. $1000/T$ plots for all samples. The E_C values are estimated by carrying out the linear

fitting of $\ln\sigma_G$ and $\ln\sigma_{GB}$ vs. $1000/T$ plots. The conduction activation energy associated to grains and grain boundaries are tabulated in Table 3.3. The E_C values decrease with increase in Mn concentrations, which could be attributed to the increase in the concentration of Fe^{2+} ions due to oxygen vacancies and it results in enhanced charge carrier movement across Fe^{2+}-Fe^{3+} centers.

Table 3.3 Conduction activation energy of grains and grain boundaries of $YFe_{1-x}Mn_xO_3$ (x = 0 – 0.3) samples

	Conduction activation energy (E_C in eV)	
x	E_C (R_G)	E_C (R_{GB})
0	1.66	1.92
0.05	0.62	0.52
0.10	0.48	0.58
0.15	0.44	0.54
0.20	0.42	0.53
0.25	0.41	--
0.30	0.41	--

3.4 Complex Dielectric Permittivity

The real (ε') and imaginary (ε'') parts of complex relative dielectric permittivity (ε^*) are calculated from complex impedance using the relations:

$$\varepsilon' = \frac{-Z''}{\omega C_0 \varepsilon_0 (Z'^2 + Z''^2)} \tag{3.2}$$

$$\varepsilon'' = \frac{Z'}{\omega C_0 \varepsilon_0 (Z'^2 + Z''^2)} \tag{3.3}$$

where Z' and Z'' are respectively the real and imaginary parts of complex impedance (Z^*), ω is the angular frequency, C_0 is the geometric capacitance and ε_0 is the permittivity of free space. Typical plots of (angular) frequency variations of ε' and are ε'' are shown in Fig. 3.10 and Fig. 3.11 respectively for $YFe_{1-x}Mn_xO_3$ samples with x = 0, 0.10, 0.20 and 0.30. The slope of ε'' versus ω plots in log-log scale in the lower frequency region is nearly equal to -1, and such power law dependence of ε'' on ω reveals the contribution of

conductivity to the dielectric response [112]. On the otherhand, the ε' vs. ω plots feature a plateau like behavior followed by sharp fall in ε' value as the frequency is increased, which indicates the relaxation process.

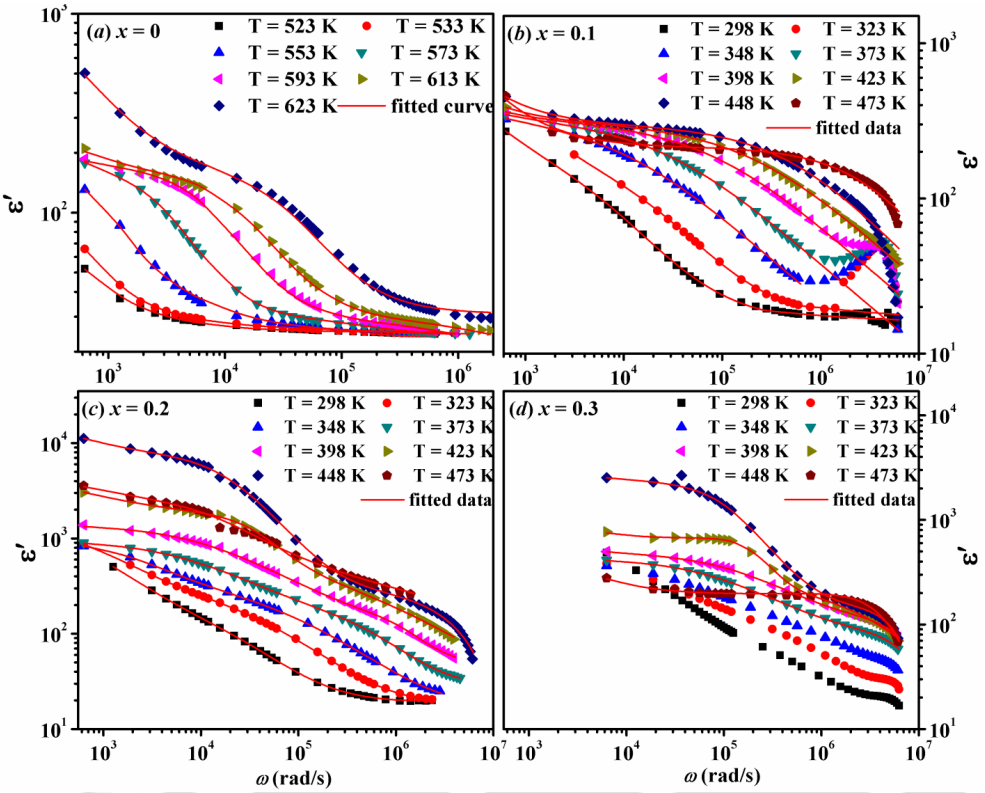

Figure 3.10 ε' vs. ω plots of x = 0, 0.1, 0.2 and 0.3 samples of $YFe_{1-x}Mn_xO_3$ at different temperatures. The solid lines represent the fitted data to eq. (3.4).

The frequency dispersion of ε^* is fitted to the equation (1.16) considering $\beta = 1$ *i.e.*, to Cole-Cole equation along with the contribution of conductivity with the expressions for ε' and ε'' as given below:

$$\varepsilon' = \varepsilon_\infty + \frac{(\varepsilon_s - \varepsilon_\infty)(1+\omega\tau)^{1-\alpha}\sin\left(\frac{\alpha\pi}{2}\right)}{1+2(\omega\tau)^{1-\alpha}\sin\left(\frac{\alpha\pi}{2}\right)+(\omega\tau)^{2(1-\alpha)}} + \frac{\sigma''}{\varepsilon_0\omega^s} \tag{3.4}$$

$$\varepsilon'' = \frac{(\varepsilon_s - \varepsilon_\infty)(1+\omega\tau)^{1-\alpha}\cos\left(\frac{\alpha\pi}{2}\right)}{1+2(\omega\tau)^{1-\alpha}\sin\left(\frac{\alpha\pi}{2}\right)+(\omega\tau)^{2(1-\alpha)}} + \frac{\sigma'}{\varepsilon_0\omega^s} \tag{3.5}$$

where ε_s and ε_∞ are the permittivity at low and high frequency respectively. The fitted data of ε' and are ε'' as per eqs. (3.4) and (3.5) are shown as solid lines in Fig. 3.10 and Fig. 3.11 respectively. The fitted data closely follow the experimental data. The parameter α signifies the deviation of relaxation process from the ideal Debye behavior, for which α = 1. For x = 0, α is found to be in the range 0.86 to 0.88, which is smaller than that for the ideal Debye process. Mn doping further reduces the value of α to 0.48 – 0.52 signifying further deviation of the relaxation from the ideal Debye process due to the increased interaction between electric dipoles.

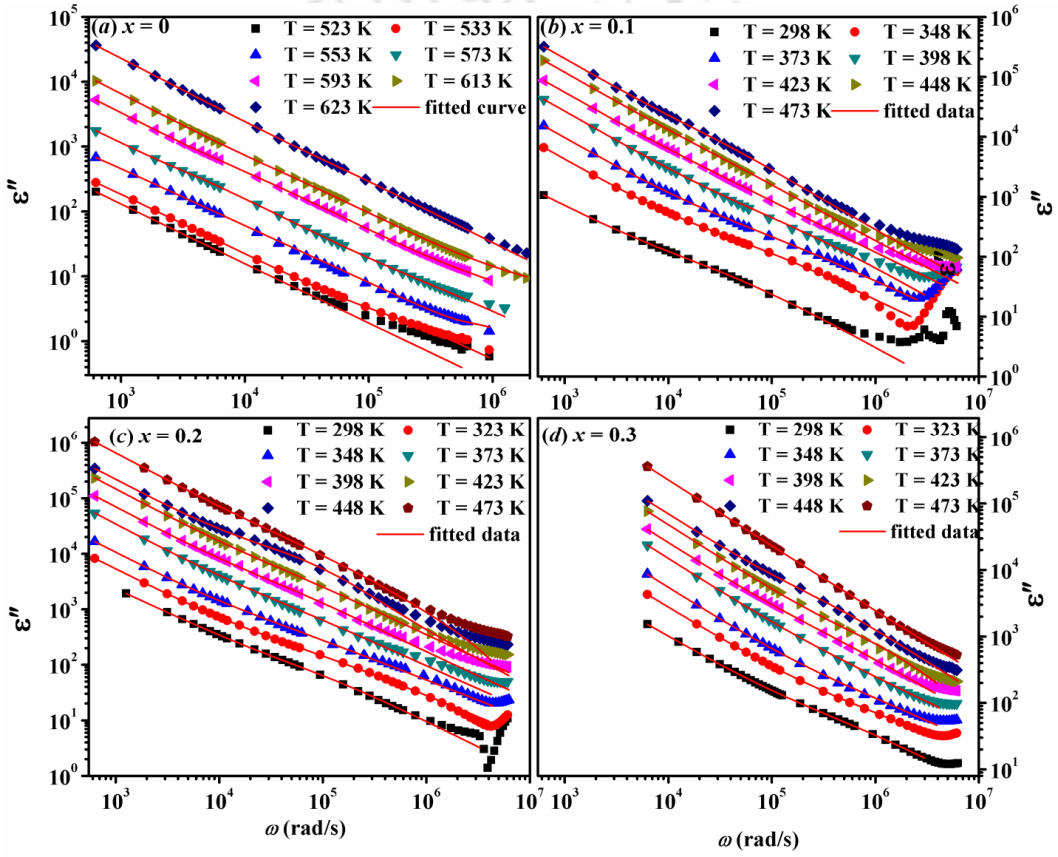

Figure 3.11 ε'' vs. ω plots of x = 0, 0.1, 0.2 and 0.3 samples of $YFe_{1-x}Mn_xO_3$ at different temperatures. The solid lines represent the fitted data to eq. (3.5).

The value of ε' at 323 K for x = 0 sample measured at a frequency of 100 kHz is found to be 22, which is comparable to that reported for other orthoferrites such as $LuFe_{0.95}Mn_{0.05}O_3$ etc [113]. The corresponding values of ε' for the Mn doped samples are found to be in the range of 23 to 54 for x = 0.05 to 0.30. On the other hand, the values of ε' at T = 473 K measured at the frequency of 100 kHz are found to be in the range of 24 to

428 for $x = 0 – 0.3$ samples. The increase of ε' value with increase in Mn concentration can be explained in terms of formation of electric dipoles due to the presence of Fe and Mn ions in multivalent states such as Fe^{3+}/Fe^{2+} and Mn^{3+}/Mn^{4+} respectively. The hopping of electrons among the cations having different valence state is similar to the reversal of electric dipoles under an electric field. Increase in Mn concentration increases such cations pairs and thereby increases the value of dielectric constant. On the other hand, the electron hopping produces the leakage current, which essentially increases the value of ε''.

The temperature dependence of ε' and $\tan\delta$ ($= \varepsilon''/\varepsilon'$) of $x = 0$, 0.05, 0.10 and 0.15 samples measured at different frequencies from 200 Hz to 100 kHz are shown in Fig. 3.12. The values of ε' and $\tan\delta$ of $x = 0$ sample almost remain temperature and frequency independent for $T < 500$ K. As the temperature is increased beyond $T = 500$ K, the values of ε' and $\tan\delta$ increase with increase in temperature showing pronounced frequency dispersion. However, we can see fluctuation in the value of ε' accompanied by a peak like shape in the $\tan\delta - T$ plots for $x = 0$ at around 650 K. Detailed investigation of the magnetic properties of $YFe_{1-x}Mn_xO_3$ samples is discussed in section 3.8 and it reveals that the sample with $x = 0$ undergoes an antiferromagnetic transition with T_N around 650 K. The anomalies observed in the ε' and $\tan\delta$ plots around 650 K suggest the coupling between the electric and magnetic ordering as reported in literature [114-117]. We have also observed such magnetism induced anomalies for $x = 0.05$ and 0.10 samples in terms of a peak in $\tan\delta - T$ plots around their respective T_N values of 630 K and 575 K. In addition to the magnetism related above peaks, we observe peaks in $\varepsilon' - T$ plots of $x \geq 0.05$ at around 450 K. These peaks are similar to those reported in literatures for $RFeO_3$ compounds and is attributed to the short- range movement of OVs.

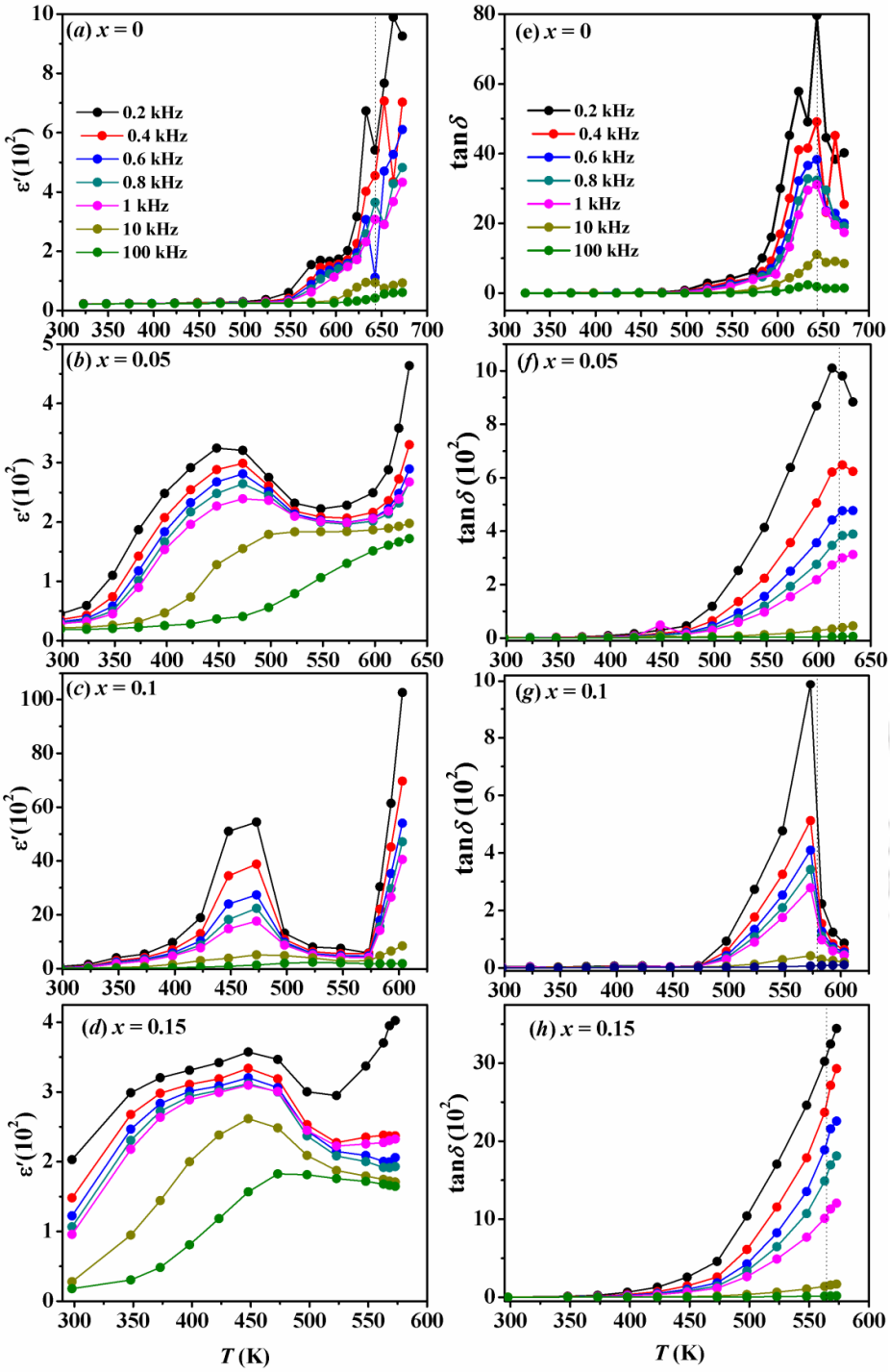

Figure 3.12 Temperature dependence of ε' and tanδ of x = 0, 0.05, 0.10 and 0.15 samples of $YFe_{1-x}Mn_xO_3$ at different frequencies from 200 Hz to 100 kHz.

Dielectric anomalies in the vicinity of magnetic phase transition are reported in many compounds [114-117]. In Nd and Mn doped $BiFeO_3$, Kumari *et al.* [114] observed

dielectric anomaly due to disappearance of grain boundaries contribution around its T_N. On the other hand, magnetoresistive response induced dielectric anomaly is reported in Ba^{2+} and Gd^{3+} co-doped $BiFeO_3$ [115]. Lee *et al.* [47] reported antisymmetric DM exchange interaction led spin canting (weak ferromagnetism) induced improper ferroelectricity in antiferromagnetic $SmFeO_3$. Subsequently, such electronic mechanism was reported to induce improper electric polarization in $YFeO_3$ [48] and $LaFeO_3$ [106]. From the study of magnetic properties of $YFe_{1-x}Mn_xO_3$, it is found that the samples exhibit weak ferromagnetism due to the canting of Fe^{3+} (Mn^{3+}) spins as a result of antisymmetric DM exchange interaction. Such canting of Fe^{3+} (Mn^{3+}) spins may give rise to a feeble electronic polarization in $YFe_{1-x}Mn_xO_3$ [47, 48], which vanishes beyond T_N because of the disappearance of the magnetic ordering. Hence, the observed anomalies across T_N may be associated to the fluctuation of polar order due to the rearrangement of Fe^{3+} (Mn^{3+}) spins *i.e.*, the change in $\boldsymbol{S_i} \times \boldsymbol{S_j}$ near T_N reduces the value of ε' sharply. With increase in Mn concentration the magnetic exchange interaction is weakened and the T_N values are reduced, so for $x \geq 0.15$ magnetism induced anomaly (peak) coincides with that of short-range movement of OVs and as a result broad peak is observed.

3.5 Complex Electric Modulus

Complex electric modulus is defined as $M^* = M' + j\,M'' = 1/\varepsilon^*$ and its real and imaginary parts are given by:

$$M' = \frac{\varepsilon'}{\varepsilon'^2 + \varepsilon''^2} \tag{3.6}$$

$$M'' = \frac{\varepsilon''}{\varepsilon'^2 + \varepsilon''^2} \tag{3.7}$$

The complex electric modulus is useful to estimate the electric response of the low capacitive region such as grains which cannot be estimated from the impedance formalism. Moreover, electric modulus formalism suppresses the contributions of electrode polarization. The typical frequency variation of M'' for $YFe_{1-x}Mn_xO_3$ with $x = 0$, 0.10, 0.20 and 0.30 at different temperatures are shown in Fig. 3.13.

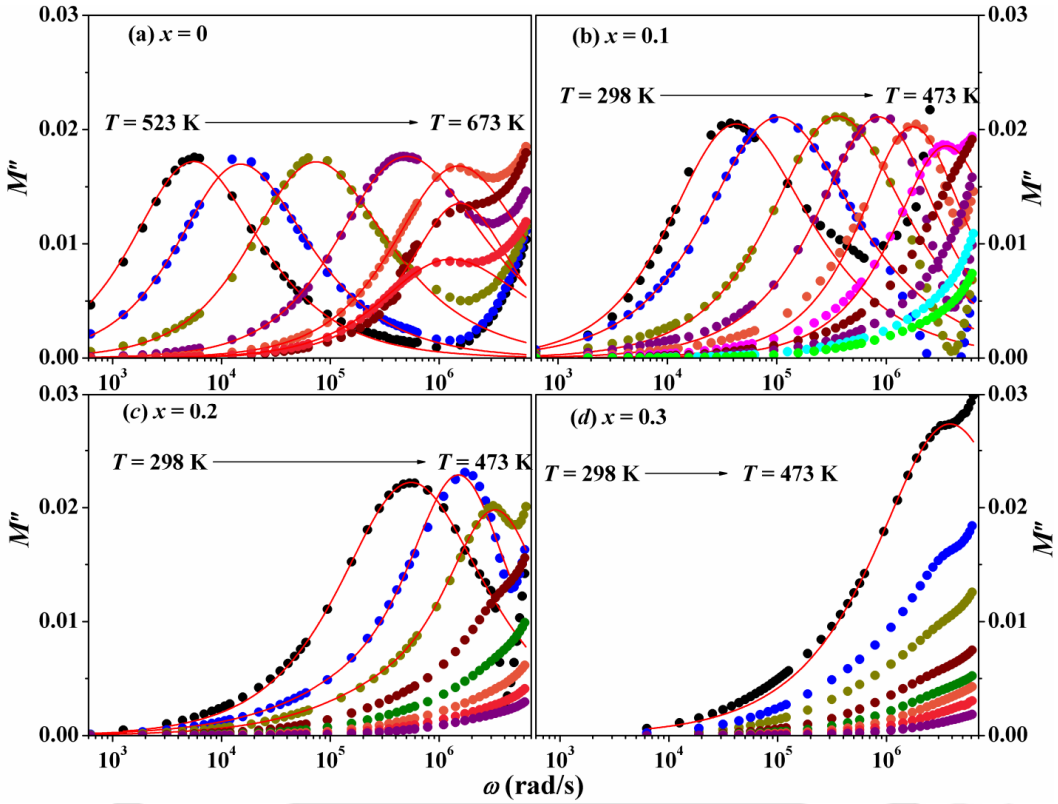

Figure 3.13 M'' vs. ω plots of x = 0, 0.10, 0.20 and 0.30 samples of $YFe_{1-x}Mn_xO_3$ at different temperatures. The solid lines are the fitted data to eq. (3.8).

The frequency range below the peak frequency in M'' vs. ω plots determines the range in which the charge carriers are mobile in long-distances. For frequency values above the peak frequency, the charge carriers are within a potential well and undergo only the short range movements. The M'' spectra are fitted to eq. (1.21), which is reproduced in eq. (3.8):

$$M''(\omega) = \frac{M''_{max}(\omega)}{\frac{(1-|n-m|)}{n+m}\left(m\left(\frac{\omega}{\omega_{max}}\right)^{-n} + n\left(\frac{\omega}{\omega_{max}}\right)^{m}\right) + |n-m|} \tag{3.8}$$

The fitted data are shown as solid lines in Fig. 3.13. The observed peak shifts towards higher frequency with increase in temperature and it obeys the Arrhenius law of temperature dependence.

3.6 Arrhenius Plots and Activation Energy

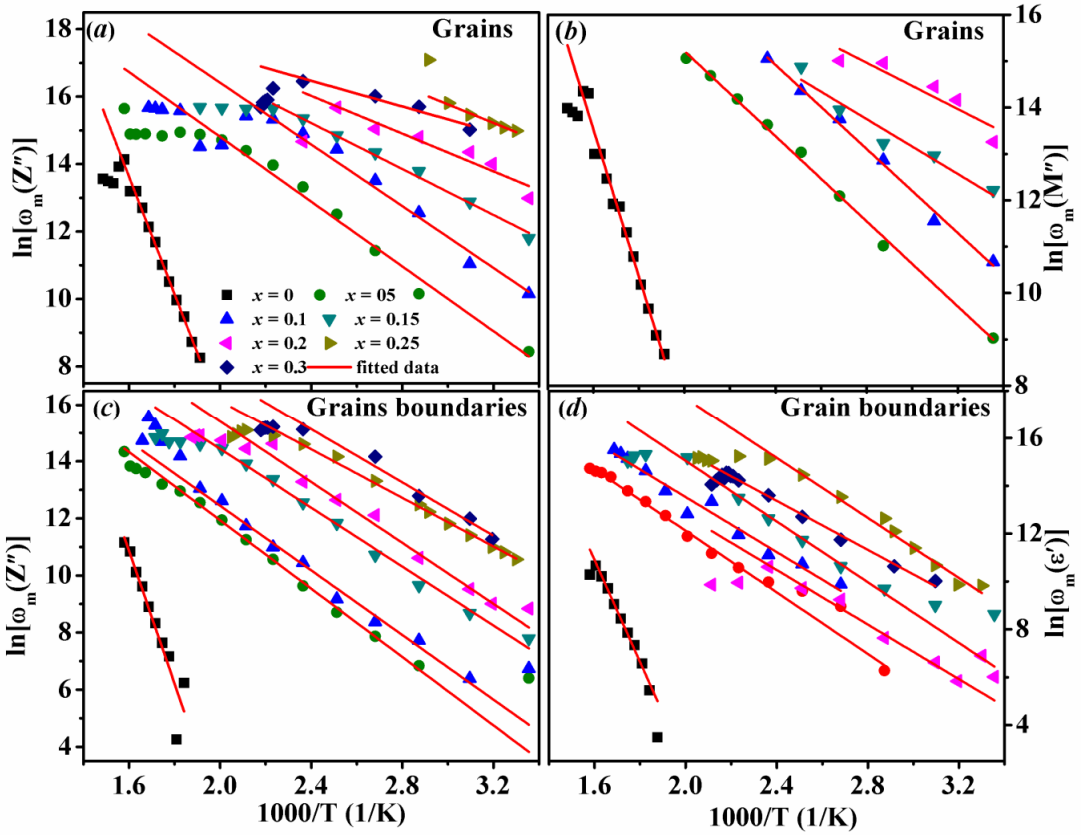

Figure 3.14 Arrhenius plots of $YFe_{1-x}Mn_xO_3$ samples.

The peak frequency (ω_m) corresponding to Z'', M'' as well as that corresponding to ε' obtained from the fit to eq. (3.4) are found to shift towards high frequency sides and obey the Arrhenius law [111]:

$$\omega_m = \omega_0 \exp\left(-Ea/k_B T\right) \tag{3.9}$$

where ω_0 is pre-factor, E_a the activation energy for the relaxation process, and k_B the Boltzmann constant. The activation energy E_a was determined by plotting $\ln(\omega_m)$ versus 1000/T and carrying out the linear fit as shown in Fig. 3.14 and are presented in Table 3.4. As seen in Fig. 3.14, the experimental data beyond a certain temperature deviate from the Arrhenius plot. The magnetic measurements of the samples reveal that this temperature corresponds to the Néel temperature. The anomaly of ω_m across the Neel temperature signifies the coupling between the electric and magnetic ordering. The values of activation energy estimated from the fitting to Arrhenius law are tabulated in Table 3.4.

Table 3.4 Relaxation activation energy of grains and grain boundaries of $YFe_{1-x}Mn_xO_3$ (x = 0 – 0.3) samples

	Relaxation activation energy (E_a in eV)			
	Grains		Grain boundaries	
x	E_a (Z'')	E_a (M'')	E_a (Z'')	E_a (ε')
0	1.53	1.48	1.83	1.83
0.05	0.43	0.40	0.51	0.55
0.10	0.42	0.40	0.51	0.54
0.15	0.30	0.25	0.44	0.51
0.20	0.24	0.21	0.42	0.49
0.25	0.23	--	0.40	0.46
0.30	0.21	--	0.38	0.44

The values of activation energy calculated from the grains and grain boundaries relaxation are different and they mostly decrease with increase in Mn concentration. In general materials synthesized in air at high temperature losses oxygen and contain OVs. Such OVs create conduction electrons which can be described as [66]:

$$V_O \leftrightarrow V_O' + e^- \tag{3.10}$$

$$V_O' \leftrightarrow V_O'' + e^- \tag{3.11}$$

where V_O, V_O' and V_O'' represent the neutral, single and doubly ionized oxygen vacancies respectively. The oxygen vacancies (V_O', V_O'') are the most mobile ionic defects in perovskites at higher temperature. They are activated in different temperature range which depends on the nature of the materials. For Fe based perovskites such as $BiFeO_3$, the activation energy below 0.7eV ($E_a < 0.7$ eV) is attributed to the singly ionized oxygen vacancies and for $E_a > 0.70$ eV, it is due to the doubly ionized oxygen vacancies [66]. As tabulated in Table 3.4, E_a corresponding to grains and grain boundaries calculated from Z'', M'' and ε' data of x = 0.05 – 0.30 samples are close to the activation of V_O'. Therefore, it is reasonable to consider that the short-range motion of singly ionized OVs give rise to the observed dielectric relaxation. However, the E_a values for x = 0 sample is larger compared to that of Mn doped samples and this can be attributed to the lower concentration of OVs. The decrease of E_a with increase in Mn concentration is directly

related to increase in OVs. As the Mn concentration increases, the concentration of OVs also increases forming a cluster with good correlations among themselves and in such case the movement of OVs become easier [118]. The experimental values of activation energy for conduction (E_C) are found to be closer to that of E_a. The quite similar value of E_C and E_a suggests that the conduction and relaxation process are dominated by the oxygen vacancies.

3.7 AC Conductivity

The real part (σ') of ac conductivity (σ^*) is calculated using the empirical relation [114]:

$$\sigma'(\omega) = \omega\varepsilon_0\varepsilon' \tan\delta \tag{3.12}$$

where ω is angular frequency and ε_0 is the vacuum permittivity. The study of frequency dispersion behavior of σ' offers an opportunity to gain insight into the details of migration process of charge carriers, particularly their interaction with other defects [119]. Fig. 3.15 shows the typical frequency dependence of σ' for $YFe_{1-x}Mn_xO_3$ compounds for x = 0, 0.10, 0.20 and 0.30 at several temperatures. As can be seen from the Fig.3.15, the conductivity plot at a particular temperature is characterized by the appearance of a frequency independent plateau region (dc conductivity) at lower frequency and a frequency dispersive region at higher frequency. The frequency independent plateau at low frequency is attributed to long range translational motion of charge carriers. The dispersion of conductivity in the higher frequency region can be explained in terms of Funke's jump relaxation model (JRM) [120]. According to JRM, at higher frequency there could be two different processes: (i) the jumping ion may jump back to its initial position i.e. unsuccessful hopping, and (ii) the neighborhood ions become relaxed with respect to the jumping ions position and the jumping ions stay in the new sites, i.e. successful hopping. With increase in the ratio of successful to unsuccessful hopping, a dispersive conductivity at higher frequency could be observed. Such a frequency dispersion of σ' can be studied using the Jonscher Power Law (JPL) [37]:

$$\sigma'(\omega) = \sigma(0) + A\omega^S \tag{3.13}$$

where $\sigma(0)$ is the frequency independent (dc) conductivity. The term $A\omega^s$ represents the frequency dependence and characterizes all dispersion phenomena. The pre-exponential

factor *A* and the frequency exponent *s* depend on temperature and the materials' intrinsic properties. The value of *s* signifies the degree of interaction of mobile charges with the lattice around them and its temperature dependence could reveal the underlying conduction mechanism. Moreover, the value of *s* defines if the motion of the charge carriers is either translational or localized. If the value of *s* is less than unity, the motion is translational, while *s* value greater than unity represents a localized or orientation hopping. The observed values of *s* i.e. $0 < s < 2$ in present case for higher frequency are similar to those reported for $Pr_{0.6}Sr_{0.4}Mn_{0.6}Ti_{0.4}O_{3\pm\delta}$ [121], $BaZr_{0.05}Ti_{0.95}O_3$ [122] compounds and they correspond to a localized or re-orientation hopping motion.

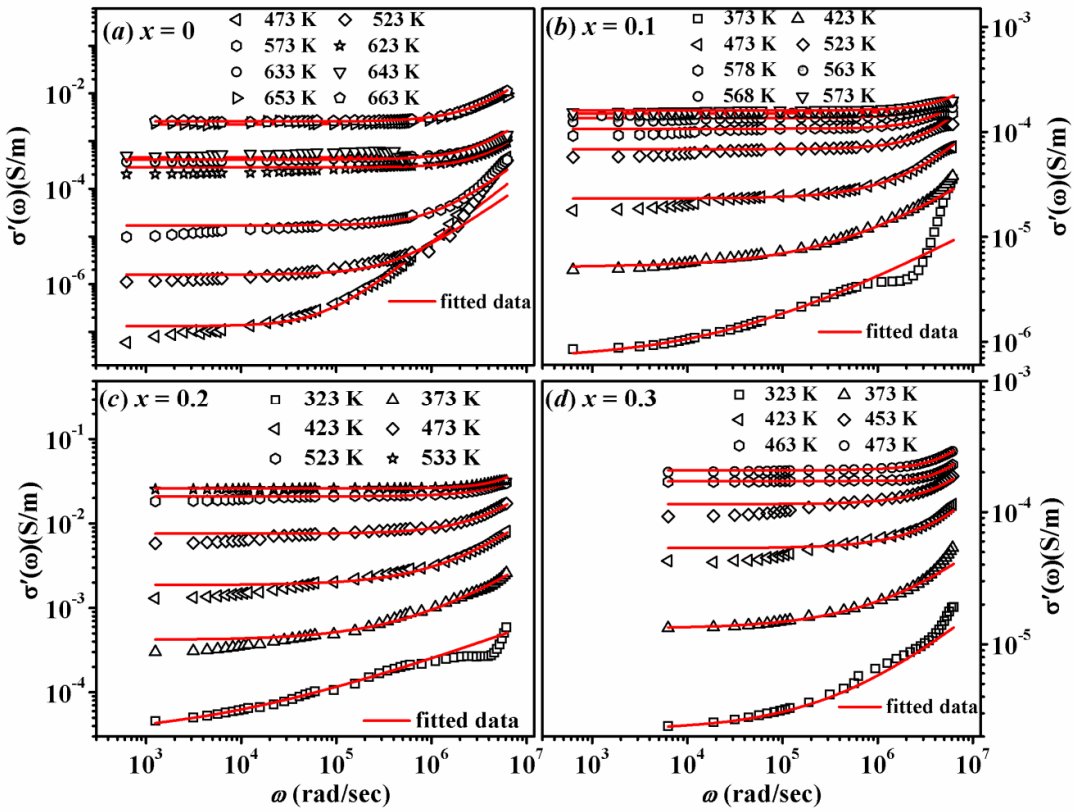

Figure 3.15 Real part (σ') of ac conductivity as a function of angular frequency for $YFe_{1-x}Mn_xO_3$ samples with (*a*) $x = 0$, (*b*) $x = 0.10$, (*c*) $x = 0.20$ and (*d*) $x = 0.30$. The solid lines represent the fitted data to eq. (3.13)

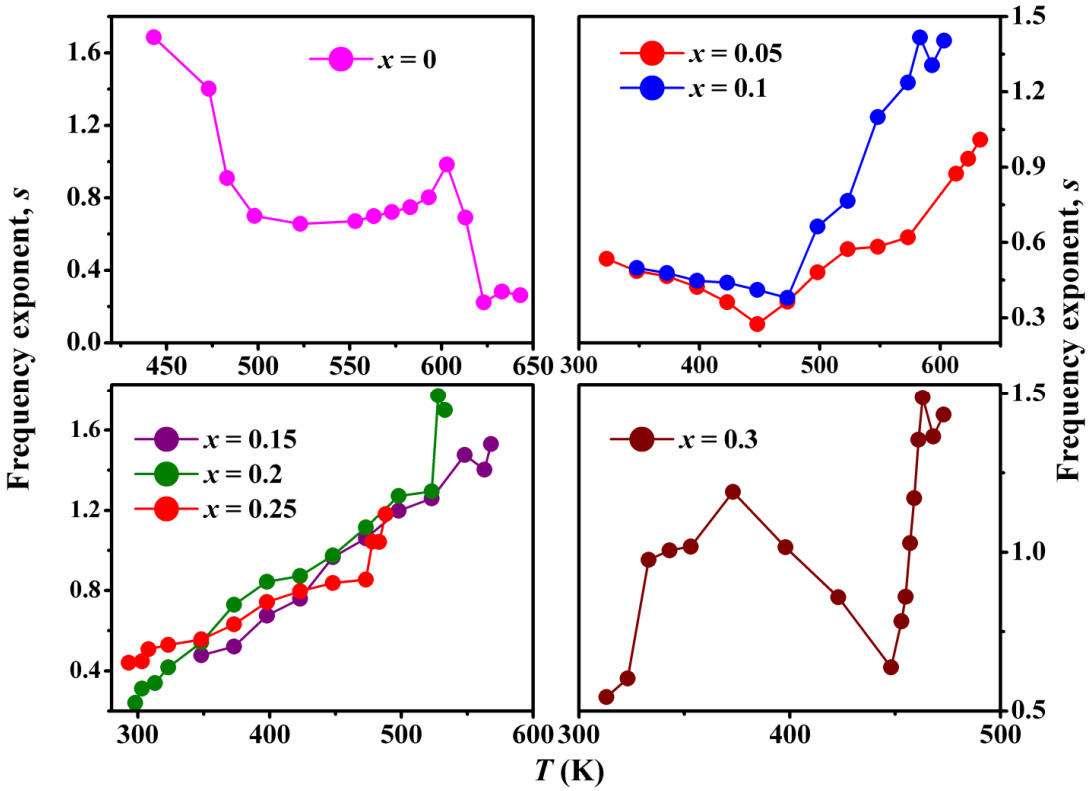

Figure 3.16 Frequency exponent (s) of $YFe_{1-x}Mn_xO_3$ (x = 0 – 0.3) sample as a function of temperature.

The temperature dependence of frequency exponent s of $YFe_{1-x}Mn_xO_3$ samples is shown in Fig.3.16. It is observed that s of x = 0 sample slowly decreases with increase in temperature, reach a minimum and again increases with increase in temperatures upto 600 K. It decreases with further increase in temperature beyond T = 600 K. The frequency exponent s of x = 0.05 and 0.10 samples first decreases with increase in temperature, reach a minimum and increases with further increase in temperature. On the otherhand for further increase in doping concentration, *i.e.*, for x = 0.15 to 0.25, s continuously increases with increase in temperature. The x = 0.30 sample shows a distinct behavior of broad peak in the temperature range of 300 K to 450K and beyond that the s value increases monotonously. The value of $s > 1$ was attributed to local movement of OVs among the nonequivalent oxygen positions in ceramics [123]. Khadhraoui *et al.* [121] observed an increase of s with increase in temperature for $Pr_{0.6}Sr_{0.4}Mn_{0.6}Ti_{0.4}O_{3\pm\delta}$ compound, such that $s < 1$ below 233 K and $s > 1$ above 233 K. The less than unity value of s can be attributed to the hopping conduction of mobile charge carriers (ions) over barriers between two sites [124], while the s value greater than 1 can be ascribed to the

motion of charge carriers (oxygen vacancy) from site to site with quantum mechanical tunneling between asymmetric double-well potential [121]. It is well known that if *s* shows an increasing trend as a function of temperature then the conduction mechanism is attributed to the small polaron tunneling (SPT) [125, 126]. In contrast, if *s* decreases with increase in temperature, reach a minimum and again increases with increase in temperature, it is likely that that conduction mechanism is due to the overlapping large polaron tunneling (OLPT) [127]. The temperature independence of *s* reveals that the quantum mechanical tunneling (QMT) is the conduction mechanism [127]. On the otherhand, a continuous decreasing value of *s* with temperature corresponds to correlated barrier hopping (CBH) phenomenon [127]. The observed temperature dependence of *s* suggests that OLPT is the conduction mechanism for $x = 0 - 0.25$ samples, while both SPT and OLPT are observed for $x = 0.30$ samples.

3.8 Magnetic Properties

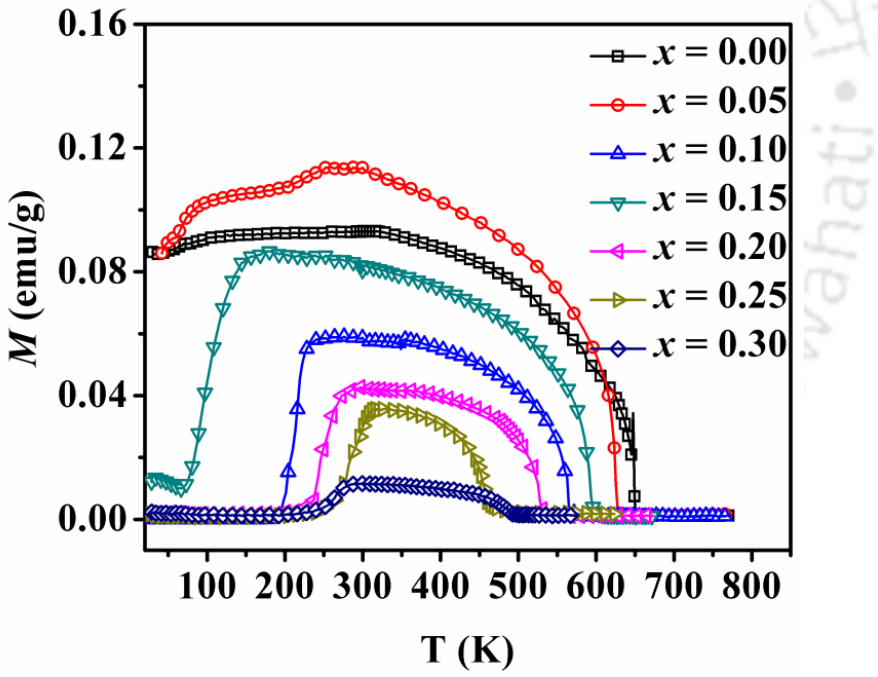

Figure 3.17 Temperature variation of magnetization ($M - T$) of $YFe_{1-x}Mn_xO_3$ ($x = 0$ to 0.3) samples for an applied field $H = 100$ Oe.

Temperature variations of magnetizations ($M - T$) for $YFe_{1-x}Mn_xO_3$ samples measured at an applied field of 100 Oe are shown in Fig. 3.17. They exhibit antiferromagnetic transition along with the signature of weak ferromagnetic component

for $T < T_N$. The values of T_N are determined from the peaks of dM/dT versus T plots and its value is found decrease from 646 K for x = 0 to 428 K for x = 0.3. The antiferromagnetic ordering in $YFeO_3$ is due to the super-exchange interactions in the Fe^{3+}–O^{2-}–Fe^{3+} networks. Substitution of Mn ions leads to increase in concentration of Fe^{3+}–O^{2-}–Mn^{3+} and Mn^{3+}–O^{2-}–Mn^{3+} networks at the expense of Fe^{3+}–O^{2-}–Fe^{3+} networks. This results in the weakening of super-exchange interactions and causes the decrease in T_N value.

A sharp fall in magnetization is observed at low temperature especially for $x \geq 0.10$, which is attributed to spin re-orientation transition from Γ_4 to Γ_1 configuration. The spin re-orientation temperature (T_{SR}) determined from the plot of dM/dT vs. T is found to shift towards the room temperature with increase in Mn concentration, *i.e.*, from 81 K for x = 0.10 to 295 K for x = 0.30. Such an increase in T_{SR} value can be attributed to the substitution of Mn^{3+} ions having larger anisotropic energy at Fe^{3+} site. The Mn^{3+} ions at octahedral site contribute significant magnetic anisotropy at low temperature and as a result the antiferromagnetic spin alignment rotates from c - axis for $T > T_{SR}$ to a - axis for $T < T_{SR}$ [109]. Thus the strength of magnetic anisotropy of Fe^{3+} and Mn^{3+} ions and their temperature dependence decide the T_{SR} value [109, 128]. This confirms that with increase in Mn concentration, the associated magnetic anisotropy increases and hence T_{SR} shift towards higher temperature.

The paramagnetic susceptibility data were fitted to the Curie-Weiss law:

$$\chi = \frac{C}{T - \theta_C} \tag{3.14}$$

where C is the Curie constant, θ_c is the Curie temperature. From the fitted value of C, we have calculated the effective magnetic moment (μ_{eff}) by using the relation $\mu_{eff} = \sqrt{3k_B C / N}$, where k_B is the Boltzmann constant, and N is Avogadro's number. The value of μ_{eff} is found to decrease from 4.92 μ_B/f.u. for x = 0 to 4.2 μ_B/f.u. for x = 0.15. The expected effective moment values were calculated by assuming both Mn and Fe ions are in trivalent state and using the relation $\mu_{eff}^{th} = \sqrt{(1-x)\mu_{eff}^2(Fe^{3+}) + x\mu_{eff}^2(Mn^{3+})}$. The experimental μ_{eff} values are found to be smaller than that of expected theoretical values

and this could be mostly due to the presence of some of these magnetic cations at higher valence state.

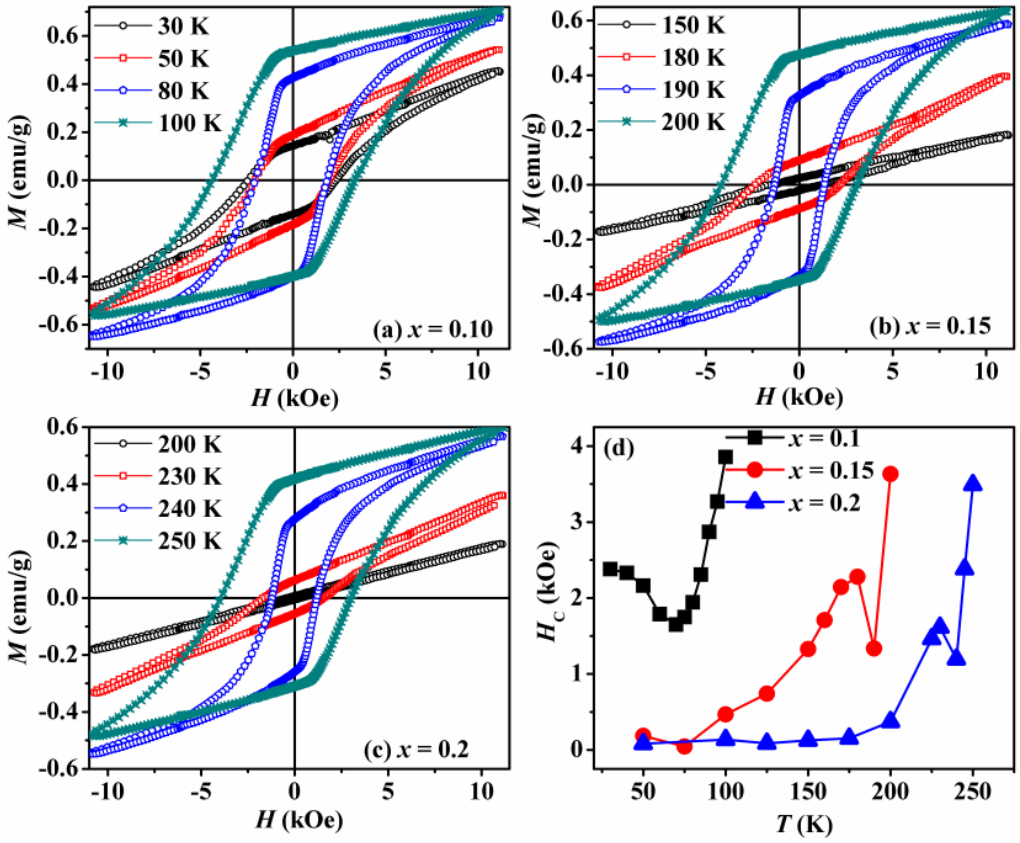

Figure 3.18 $M - H$ loops of $YFe_{1-x}Mn_xO_3$ samples with (*a*) $x = 0.10$, (*b*) $x = 0.15$, (*c*) $x = 0.20$ recorded in the vicinity of T_{SR} and (*d*) temperature variation of coercive field.

Typical $M - H$ loops recorded in the vicinity of T_{SR} are shown in Fig. 3.18 for $x = 0.10$, 0.15 and 0.20 samples. At higher temperature ($T > T_{SR}$) the $M - H$ loops exhibit large hysteresis *i.e.*, with large coercivity and spontaneous magnetization. For $T < T_{SR}$ they are found to decrease considerably. It highlights the transition of magnetic structure from Γ_4 configuration having large magnetic anisotropy and associated weak ferromagnetism and large coercive field (H_C) to Γ_1 configuration. The temperature variation of H_C is shown in Fig 3.18 (*d*), where in addition to the decrease of H_C with decrease in temperature an anomaly in the vicinity of T_{SR} is seen and the observed trend is comparable to those of $ErFeO_3$ and $TmFeO_3$ [129].

In order to estimate the exchange anisotropic field (H_E), DM anisotropy field (H_D) and canting angle (α), we have analyzed M - H loop using the following relation [108, 130, 131]:

$$E = \lambda \vec{M}_1 \cdot \vec{M}_2 - \vec{H} \cdot (\vec{M}_1 + \vec{M}_2) - \vec{D} \cdot (\vec{M}_1 \times \vec{M}_2) - \frac{K_B}{M_0^2}(M_{1x}^2 + M_{2x}^2) \quad (3.15)$$

where $M_0 = \left|\vec{M}_1\right| = \left|\vec{M}_2\right|$ with sublattice magnetization $\vec{M}_1$ and $\vec{M}_2$. The first three terms represent exchange energy, magneto-static energy and DM energy respectively. The energy associated with magneto-crystalline anisotropy is given as last term. The characteristic constant λ, D and K_B can be related to M_0 as per equations, $H_E = \lambda M_0$, $H_D = DM_0$ and $H_B = 2K_B/M_0$. The canting angle (α_0) can be determined using the relation [130, 131]:

$$\alpha_0 \approx \frac{H_D}{2H_E} \approx \frac{M_{wf}}{2M_0} \quad (3.16)$$

where M_{wf} represents the weak ferromagnetic component of magnetization. The weak ferromagnetic component was estimated by fitting the linear region of $M - H$ loop to the equation $M(H) = M(0) + \chi H$, where $M(0)$ is the value of magnetization at $H = 0$ and it gives the weak-ferromagnetic component (M_{wf}) and χ represents the susceptibility of the AFM matrix. The exchange field H_E and DM field H_D were estimated using the relations: $H_E = M_0/\chi$ and $H_D = M_{wf}/\chi$ [100, 131]. Typical plots of H_E, H_D and α_0 as a function of temperature for $x = 0.20$ are shown in Fig. 3.19. The observed results are comparable to those reported for $YFeO_3$ in literature [130, 131]. The trend of variation of α_0 with the temperature is similar to that obtained by Mössbauer studies for $YFe_{0.8}Mn_{0.2}O_3$ [108]. It is observed that the canting angle and DM field decrease with the decrease in temperature as expected due to spin re-orientation transition.

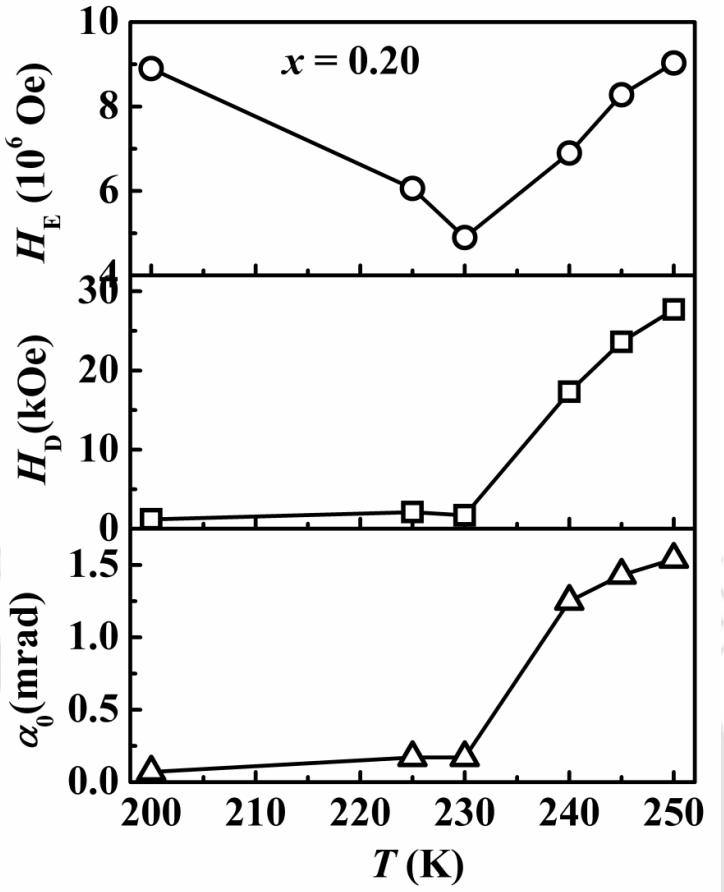

Figure 3.19 Temperature variation of estimated angle (α_0), DM field (H_D) and exchange field (H_E) for x = 0.20 sample.

3.8.1 Exchange Bias

In order to explore the exchange bias (EB) phenomenon, we have cooled the samples through their T_N under the application of a magnetic field H_{FC} = 2 kOe and measured the $M - H$ loops at different temperatures. Fig. 3.20 shows the FC M –H loops for x = 0.05 – 0.3 samples at different temperatures. These loops are found to shift along the negative field axis and it highlights the presence of negative exchange bias field, H_{EB}. In order to further confirm the EB and rule out the possibility of any experimental artifact, $M - H$ loops at respective temperatures were recorded after reversing the cooling field, i.e. H_{FC} = - 2kOe. In this case we have observed the shifting of loops towards positive field axis. Typical plots of temperature variation of H_{EB} for H_{FC} = + 2kOe and – 2 kOe are shown in Fig. 3.21 for x = 0.3 sample. We can see an exponential rise of negative H_{EB} value with decrease in temperature for H_{FC} = + 2kOe (positive cooling field). Similar

behavior with comparable magnitude is observed for H_{FC} = – 2kOe but with an opposite sign (positive) of H_{EB}. This clearly demonstrates the intrinsic exchange bias behavior in the present system.

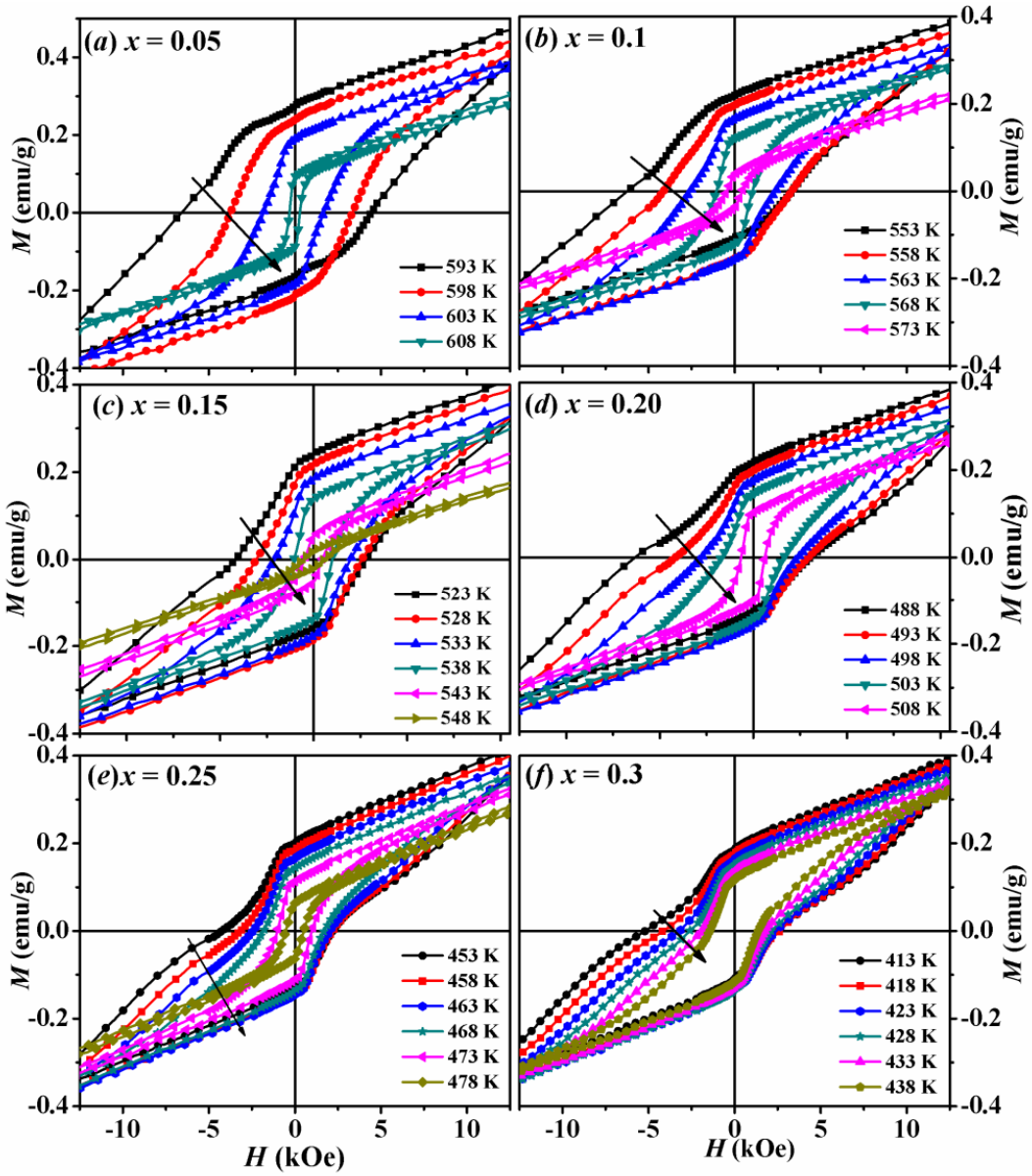

Figure 3.20 *M* – *H* loops measured at different temperatures for $YFe_{1-x}Mn_xO_3$ (x = 0.05 – 0.3) samples after field cooling through T_N.

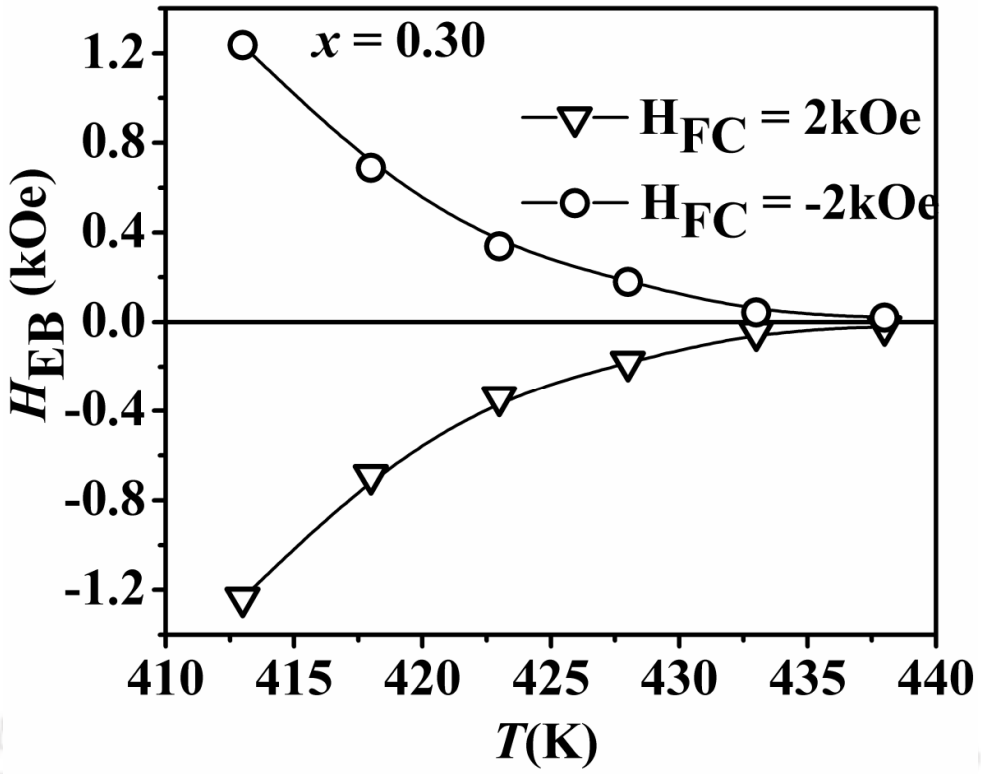

Figure 3.21 Temperature variation of H_{EB} for x = 0.30 sample under positive field cooling and negative field cooling conditions.

The maximum value of H_{EB} is found to be in the order of a few kOe and is comparable to that obtained in nanoparticles of $LaFeO_3$ at 5 K [132] and Zn doped $LaFeO_3$ nanoparticles [133]. Typical plots of temperature variation of H_{EB} for x = 0.05 – 0.30 samples are shown in Fig. 3.22. It is found that H_{EB} exhibits an exponential rise in magnitude with decrease in temperature below T_N and the data were fitted to the relation $H_{EB}(T) = H_{EB}(0)\exp(-T/T_1)$, where T_1 and H_{EB} (0) are constant. The fitted data are shown as solid line and they closely follow the experimental data. Same data in semi-logarithmic scale are shown in the insets of Fig. 3.22, where they exhibit linear behavior. So the present set of samples has a potential to yield large room temperature EB for various applications. The maximum H_C value determined from the above measurements is 3.5 kOe at 413 K and they mostly increase linearly with decrease in temperature.

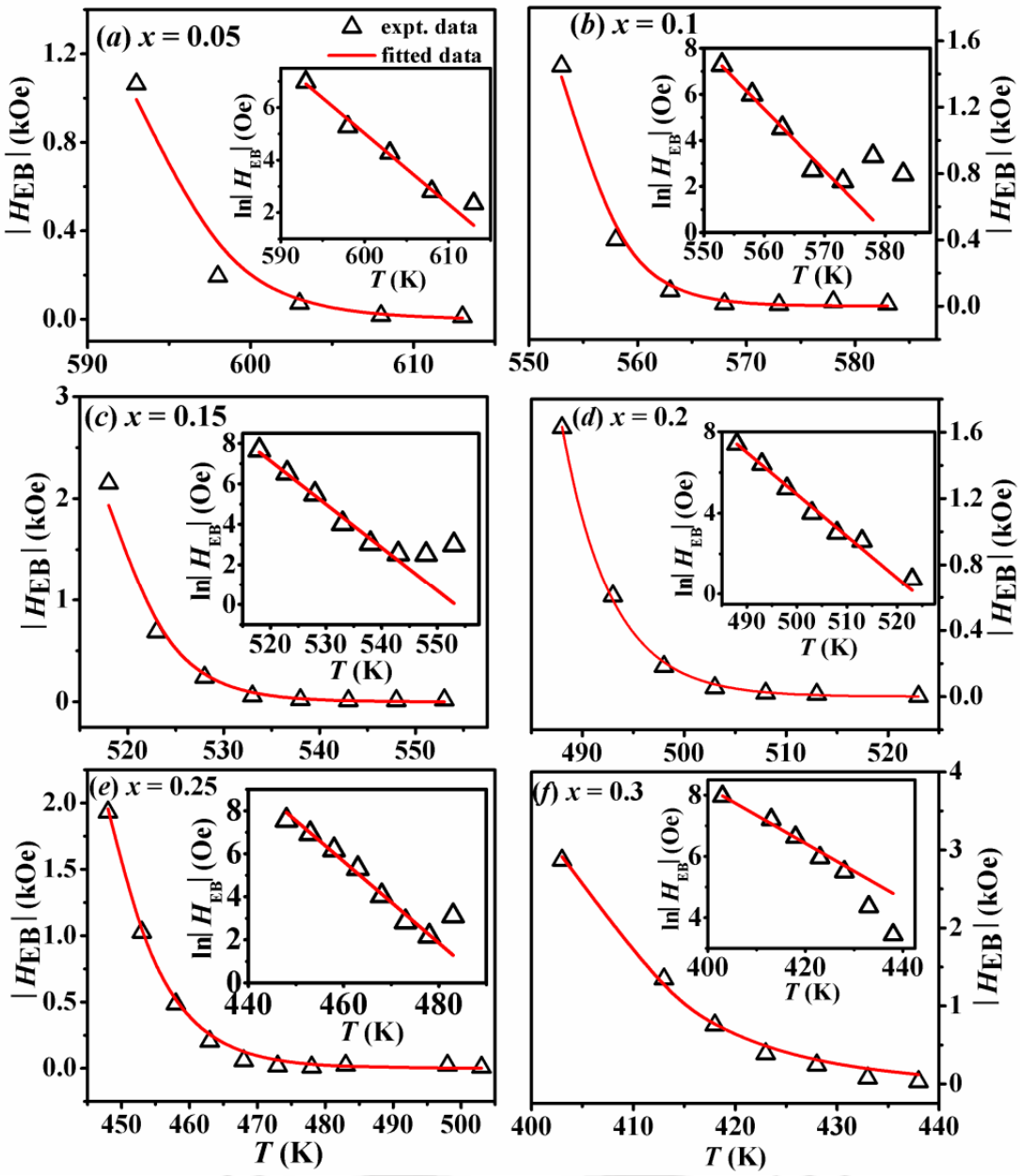

Figure 3.22 Temperature variation of $|H_{EB}|$ of $YFe_{1-x}Mn_xO_3$ samples with x = 0.05 – 0.30. Insets show the same data in semi-log scale. The fitted data are shown as solid line.

Generally EB is explained in terms of exchange interaction at the interface of two magnetic phases such as FM/AFM, FiM/AFM, *etc*. EB in rare-earth orthoferrites such as nanoparticles of $LaFeO_3$ [132], Zn doped $LaFeO_3$ [133] and $DyFeO_3$ [134] is attributed to conventional core-shell model. As we are dealing with bulk materials, the core-shell model approach is not likely to play a role in the present set of samples. The contribution of magnetic impurity phases such as $Y_3Fe_5O_{12}$, $YMnO_3$ and Fe_2O_3 can be ruled out

because the samples are found to be in single phase form as per XRD analysis. Moreover, we have not observed any trace of magnetic transition corresponding to above impurity phases. EB in spinel compounds (AB_2O_4) is explained by considering the anisotropic exchange interaction between the longitudinal ferrimagnetic and the transverse antiferromagnetic components due to spin canted ferrimagnetic interaction across the magnetic sublattices in tetrahedral and octahedral environments [135, 136]. Here no such long range ferrimagnetic interaction is known to exhibit. It is known that structurally and chemically single phase $YFeO_3$ undergoes spin reorientation from $\Gamma_4(A_xF_yG_z)$ to $\Gamma_1(G_xC_yA_z)$ phase at around 70 K as the temperature is decreased. We have also shown that the spin reorientation transition temperature increases upon Mn substitution, i.e. close to room temperature. Here the Γ_4 phase contains considerable weak ferromagnetic component while the Γ_1 phase promotes the collinear AFM. For $T < T_N$, *i.e.*, much above room temperature, the presence of Γ_1 phase under the matrix of Γ_4 phase cannot be ruled out [137]. There is also a possibility that the concentration of Γ_1 phase increases under the FC condition. The above argument can be supported from the observed reduction in the magnitude of saturation and remanent magnetization upon field cooling as can be seen in Fig. 3.23, where typical ZFC and FC $M - H$ loops are shown for x = 0.05 and 0.15 samples. The anisotropic exchange interaction at the interface of Γ_1 and Γ_4 phase is expected to contribute towards the observed EB field. Such combination of $\Gamma_4(A_xF_yG_z)$ and $\Gamma_1(G_xC_yA_z)$ magnetic phases upon field cooling is reported in $Y_{0.9}Pr_{0.1}CrO_3$ system [138]. So, the observed large EB field above room temperature in $YFe_{1-x}Mn_xO_3$ compounds suggests that these materials can serve as one of the group of potential candidates for application towards magnetic recording, *etc*.

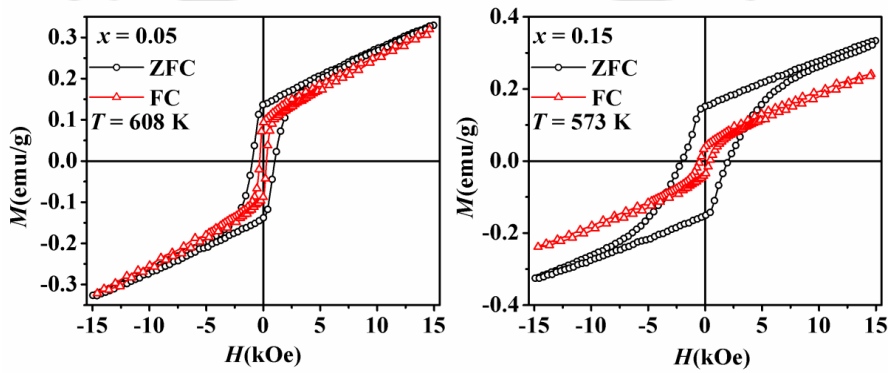

Figure 3.23 $M - H$ loops recorded under ZFC and FC (H_{FC} = 2 kOe) conditions for (*a*) x = 0.05 and (*b*) x = 0.15 samples of $YFe_{1-x}Mn_xO_3$.

3.9 Conclusion

Single phase polycrystalline samples of $YFe_{1-x}Mn_xO_3$ for $x = 0$ to 0.3 are prepared by solid state route. The XRD patterns of all samples are refined using orthorhombic unit cell with *Pnma* space group. The lattice constant *a* increases, while *b* and *c* decrease with increase in Mn concentrations, which is explained in terms of Fe and Mn ionic size mismatch and the Jahn-Teller distortion. Well defined relaxation peaks associated to grains and grain boundaries are seen in the Z'' spectra, which shift towards higher frequency region with increase in temperature depicting thermally activated relaxation process. The broad and distorted relaxation peaks suggest the non-Debye type relaxation in grains and grain boundaries. The Nyquist plots for all samples are characterized by depressed and distorted semicircles whose centers lie below the Z' axis, which is due to the non-Debye like dielectric relaxation. The Nyquist plots are fitted to an electric equivalent circuit comprised of *RC* and *QR* element, where the constant phase element *Q* describes the observed deviation from the ideal behavior. The activation energy estimated from the Z'' and M'' peaks suggest the vital role of oxygen vacancies towards the relaxation process of the materials. Frequency dispersion of ε' and ε'' are analyzed in terms of Cole-Cole equation along with the contribution of dc conductivity depicting universal dielectric response (UDR) behavior. Temperature dependences of ε' and $\tan\delta$ suggest fluctuation of polar order across T_N. On the other hand, all samples exhibit antiferromagnetic transition with decrease in Néel temperature with increase in Mn concentration. The Néel temperature decreases from 646 K for $x = 0$ to 456 K for $x = 0.3$ due to the dilution of Fe^{3+}– O^{2-}– Fe^{3+} networks by the random substitution of Mn^{3+} ions. We have observed the interesting spin re-orientation transition at low temperature and it is found to increase with Mn concentration due to the dominant magnetic anisotropy associated with Mn^{3+} ions. The detailed analysis of magnetization shows the presence of considerable magnetic anisotropy and Dzyaloshinskii-Moriya interaction in addition to the antiferromagnetic exchange interaction. The spin canting angle and Dzyaloshinskii-Moriya anisotropy constant are found to decrease as the sample is cooled through spin re-orientation transition. These samples exhibit exchange bias behavior with a maximum exchange bias field of 1.2 kOe around 413 K. The observed exchange bias is explained by considering the anisotropic exchange interaction at the interface of two magnetic phases

with one of them having dominant collinear antiferromagnetic behavior while the other one having considerable weak ferromagnetic component.

Chapter 4

Sm doped $BiFeO_3$ series

$BiFeO_3$ (BFO) crystallizes in rhombohedral structure with *R*3*c* space group [50-52]. It undergoes AFM transition around T_N = 640 K. The magnetic properties of BFO are solely governed by the FeO_6 octahedra and it is basically a *G*-type canted antiferromagnetic system, where the canting of Fe spins is due to Dzyaloshinskii-Moriya (DM) interaction [21, 139]. Besides this, the magnetic structure is modulated by a spiral arrangement of spins with an incommensurate long-wavelength of 62 nm [58]. Such a peculiar magnetic structure offers (i) practically zero magneto-electric coupling (although its space group allows linear magneto-electric coupling) and (ii) a very small value of magnetization at room temperature [58]. On the other hand, the net ferroelectric polarization (> 98 %) in BFO is due to $6s^2$ lone pair electrons of Bi^{3+} ions [139]. Spontaneous electric polarization of magnitude 88-100 $\mu C/cm^2$ along the pseudo-cubic (111) direction has been predicted for BFO [139, 140]. Lebeugle *et al.* [59] reported a polarization value similar to the theoretically predicted value of 100 $\mu C/cm^2$ in BFO single crystal grown by flux method. However, the polarization state is not stable and its value reduces upon continuous cycling of the electric field. Similar higher value of polarization has been reported in thin films of BFO [141], but its origin is still not clear. Polycrystalline samples exhibit much lower value of polarization (4-8 $\mu C/cm^2$) with unsaturated polarization loop [142, 143]. Such a small value of spontaneous polarization and magnetization at room temperature does not meet the required standard

for commercial application. The difficulty in achieving the spontaneous polarization in BFO to the value predicted by first principle calculations has been linked to the predominant leakage current due to the presence of Fe in Fe^{2+} states [143]. As reported by many research groups, a change in synthesis strategy results in phase pure sample of BFO, which includes (i) two stage liquid phase sintering, (ii) air quenching the metastable BFO phase, (iii) partial impurity substitution, etc. Substitution at Bi site (*A*-site) has been more effective as it reduces the formation of secondary phases and thus enhances ferroelectric properties. Moreover, the Bi-site substitution either distorts the crystal structure or promotes structural transformation from rhombohedral (space group: *R3c*) to orthorhombic (space group: *Pnma*) symmetry. The structural transformation/distortion suppresses the spiral spin structure and increases the net magnetization. Hence, a large enhancement of magnetization in terms of increase in the value of remanent magnetization and coercive field has been achieved in rare-earth substituted BFO [79, 144-147]. Rao *et al.* [144] reported an enhancement of remnant magnetization (M_r ~ 0.075 emu/gm) and coercive field (H_C ~ 6.4 kOe) for 10 mol. % of Eu substitution in BFO and it has led to a mixed structure of rhombohedral and orthorhombic phases (*R3c*+*Pnma*). Similar enhancement of M_r (~ 0.27 emu/g) and H_C (~ 19 kOe) values has been reported by Suresh *et al.* [145] for sol-gel derived orthorhombic (*Pbnm*) $Bi_{0.6}La_{0.4}FeO_3$. Such enhancement was attributed to the substitution driven structural transformation. Suresh *et al.* [146] reported an increase in the maximum value of magnetization from 2×10^{-4} emu/g at room temperature for $BiFeO_3$ to 5.67 emu/g for $Bi_{0.8}Ho_{0.2}FeO_3$ for a maximum applied magnetic field 9T [146]. They found the combined effect of structural distortion due to substitution of larger Ho^{3+} in Bi^{3+} ions and new magnetic interactions in Ho^{3+}–Ho^{3+} and Ho^{3+}–Fe^{3+} networks contribute to the enhancement of magnetization.

Sm substitution at Bi-site of BFO has drawn considerable research interest due to its ability to transform the crystal structure and enhance the magnetization, *etc.* [148-151]. It will be very interesting to explore the complex magnetic phenomena such as exchange bias in Sm doped $BiFeO_3$ due to the possible phase co-existence of collinear antiferromagnetism associated to $SmFeO_3$-like structure and the weak ferromagnetism of the parent $BiFeO_3$. In this chapter, we present the detailed investigation of effect of Sm doping in Bi site by studying their structural, dielectric and magnetic properties.

4.1 Sample Preparation and Characterization

$Bi_{1-x}Sm_xFeO_3$ (x = 0 – 0.3) ceramics were prepared using sol-gel method. High purity Bi_2O_3, Sm_2O_3 and $Fe(NO_3)_3.9H_2O$ (purity > 99%) taken in a stoichiometric molar ratio were dissolved either in HNO_3 or in distilled water. Citric acid (purity > 99%) was added to the mixture in an appropriate proportion and the mixture was stirred for 1 h at room temperature. Finally, ethylene glycol was added to the mixture followed by heating at 343 K in a hot plate with continuous stirring. The above process lead to a highly viscous gel and on further heating at 523 K yielded a fine uniform powder. The powder was pressed into cylindrical pellets of approximately 10 mm diameter and 2 mm of thickness at a pressure of 2.94×10^8 N/m^2 by using a hydraulic press. The final sintering was carried out at 1073 K for 20 min in air atmosphere followed by quenching in air to room temperature. X-ray diffraction (XRD) patterns were recorded by using a Rigaku make TTRAX III high power X-ray diffractometer by employing Cu-K_α radiation (λ = 1.54056 Å). These patterns were refined with the help of Rietveld method using FULLPROF software. The surface morphology of the samples was studied by recording microstructural images using a ZEISS make field emission scanning electron microscope (FE-SEM, ΣIGMA) equipped with EDS facility. Raman spectra at room temperature were obtained by using micro-Raman spectrometer (LabRam HR800, Jobin Yvon) in the wave number range of 100 to 700 cm^{-1} with excitation wavelength of 514 nm. The frequency dependent dielectric measurements at different temperatures (300 – 573 K) over a frequency range of 10^2 –10^6 Hz and for an ac voltage of 1.0 V_{rms} were carried out using an LCR meter (Wayne Kerr, model 1J43100). For the electrical contacts, electrodes were fabricated by painting silver pastes on both sides of the sample of typical thickness of 1–1.5 mm. The samples were fired at 423 K in air for 2 h and furnace cooled to room temperature before carrying out the electrical measurement. Temperature and field variations of magnetization measurements were carried out using a vibrating sample magnetometer (Lakeshore, model 7410) in the temperature range of 25 – 300 K.

4.2 Structural Properties

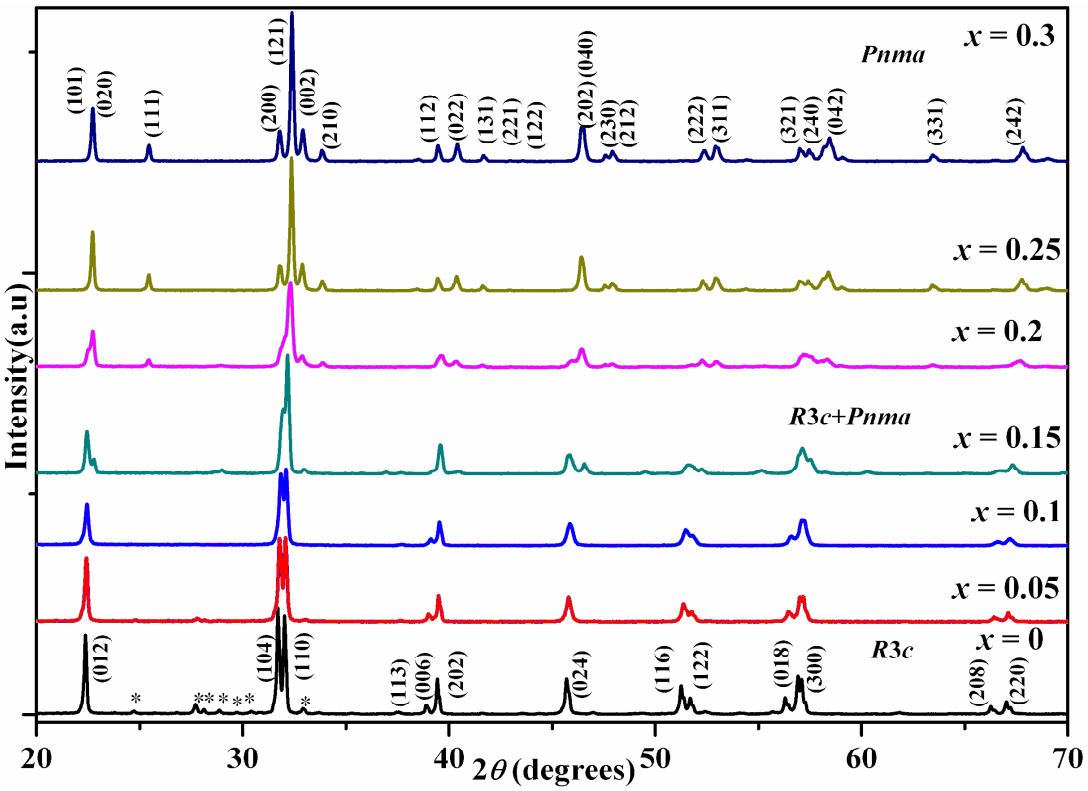

Figure 4.1 XRD patterns of $Bi_{1-x}Sm_xFeO_3$ samples (x = 0 – 0.3) recorded at room temperature.

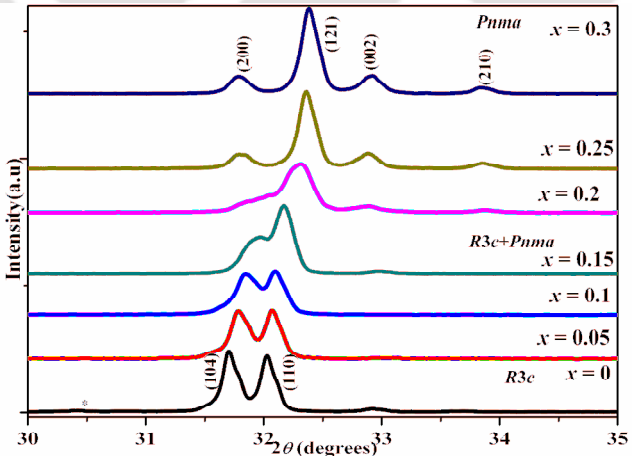

Figure 4.2 Expanded view of XRD patterns of $Bi_{1-x}Sm_xFeO_3$ samples in the range 2θ = 30° to 35°.

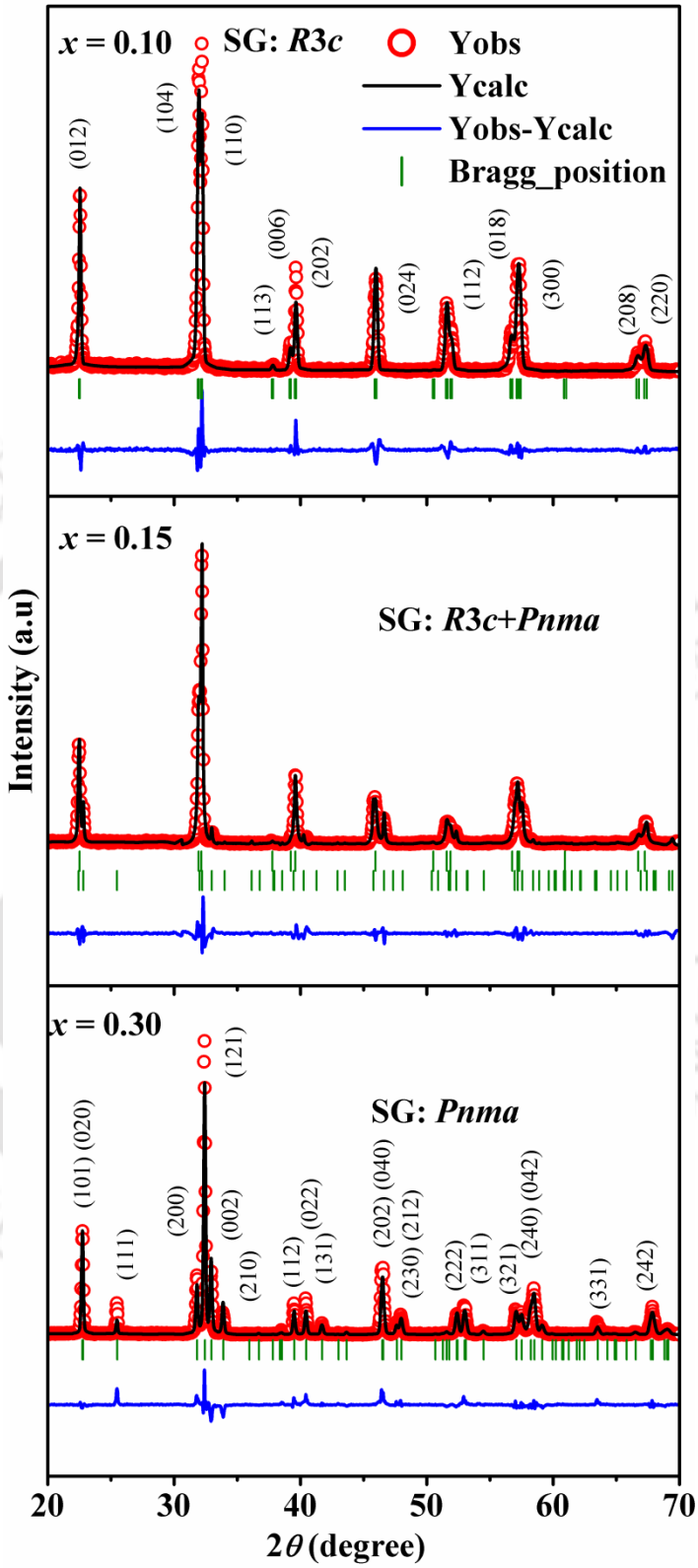

Figure 4.3 XRD patterns of $Bi_{1-x}Sm_xFeO_3$ samples with x = 0.10, 0.15 and 0.30 along with Rietveld refinement.

XRD patterns of $Bi_{1-x}Sm_xFeO_3$ (x = 0.0 – 0.3) ceramics are shown in Fig. 4.1. Traces of secondary phases like $Bi_2Fe_4O_9$/$Bi_{25}FeO_{39}$ (* marked in the figure) or other perovskites phases in the Bi_2O_3-Fe_2O_3 systems are observed for x = 0 and 0.05 samples. The unavoidable formation of secondary phases due to volatile nature of Bi_2O_3 is reported by several authors [145, 146]. Interestingly, Sm substitution suppresses the formation of these impurity phases resulting in a completely phase pure compound for $x \geq 0.1$. As an indicative of Sm incorporation into the Bi site, initially we observe the shifting of XRD peaks towards higher 2θ values as shown in Fig. 4.2 in the expanded scale for 2θ = 30° to 35°. Further increase in Sm concentration brings in some new peaks in the XRD pattern of x = 0.15 (Fig. 4.1); for instance the peaks at 2θ = 22.78° and 32.92° which could not be indexed to *R3c* space group. The intensity of those peaks increases for further increase in Sm concentrations, such that the XRD patterns for x = 0.25 and 0.3 are completely different from that of *R3c* phase, signifying a total structural transformation.

The XRD patterns of x = 0, 0.05 and 0.1 samples are refined using rhombohedral unit cell with *R3c* space group. On the other hand, we carried out double phase refinement for x = 0.15 and 0.20 samples where the best refinement is obtained for the mixture of rhombohedral (*R3c*) and orthorhombic (*Pnma*) phases. Finally, XRD patterns for x = 0.25 and 0.30 are refined by choosing *Pnma* space group in the orthorhombic structure. The typical Rietveld refinement of XRD patterns of $Bi_{1-x}Sm_xFeO_3$ samples with x = 0.10, 0.15 and 0.30 are shown in Fig. 4.3. In other words, we have observed a complete structural transformation of BFO due to Sm doping through the sequence: *R3c* → *R3c*+*Pnma* →*Pnma* and similar structural transition is reported in literatures [145, 147]. The typical lattice parameters for x = 0 sample are found to be a = 5.578 Å and c = 13.867 Å and it is comparable to the literature [145, 147, 152]. The weight fractions of individual phases are determined by using the relation [95]:

$$Wp = S_p\left(ZMV\right)_p \Big/ \sum_{i=1}^{n} S_i\left(ZMV\right)_i \qquad (4.1)$$

where W_p is the weight fraction of a phase p in a mixture of n phases. S, Z, M and V are respectively the scale factor, the number of formula units per cell, molecular mass of the phase and the unit cell volume (in $Å^3$). The weight percentage of each phase was obtained by multiplying Wp by 100. The various structural parameters obtained from the Rietveld

refinement of XRD patterns of $Bi_{1-x}Sm_xFeO_3$ samples are tabulated in Table. 4.1. The lattice parameters *c* and *a* of rhombohedral phase decrease with increase in Sm concentrations. The decrease of lattice parameters *c* and *a* is consistent to the substitution of larger Bi^{3+} ions (r_i = 1.03Å) by smaller Sm^{3+} ions (r_i = 0.96Å).

Table 4.1 Parameters obtained from the Rietveld refinement of XRD patterns of $Bi_{1-x}Sm_xFeO_3$ (x = 0 – 0.3) samples. R_f, R_{Bragg}, R_P and χ^2 are the reliability factors (* SG: Space group).

SG	Parameters	Samples (x)						
		0	0.05	0.1	0.15	0.2	0.25	0.3
R3c	$a = b$ (Å)	5.5782	5.5744	5.5666	5.5593	5.5473	--	--
	c (Å)	13.8674	13.8350	13.7983	13.7751	13.6821	--	--
	V (Å^3)	373.70	372.30	370.30	368.69	364.63	--	--
	R_f (%)	6.82	6.10	5.42	5.32	4.99	--	--
	R_{Bragg}(%)	6.23	4.68	5.62	4.75	3.21	--	--
	Wt.%	100	100	100	80	20	0	0
Pnma	a (Å)	--	--	--	5.5978	5.6002	5.6164	5.6184
	b (Å)	--	--	--	7.9328	7.8374	7.8037	7.7947
	c (Å)	--	--	--	5.4361	5.4423	5.4376	5.4324
	V (Å^3)	--	--	--	241.40	238.87	238.33	237.91
	R_f (%)	--	--	--	5.08	3.57	5.18	3.71
	R_{Bragg}(%)	--	--	--	4.47	4.22	4.50	3.51
	Wt.%	--	--	--	20	80	100	100
	R_P (%)	9.52	8.45	8.1	7.19	7.20	7.87	7.98
	χ^2	3.45	3.23	2.60	3.66	3.32	3.70	3.53

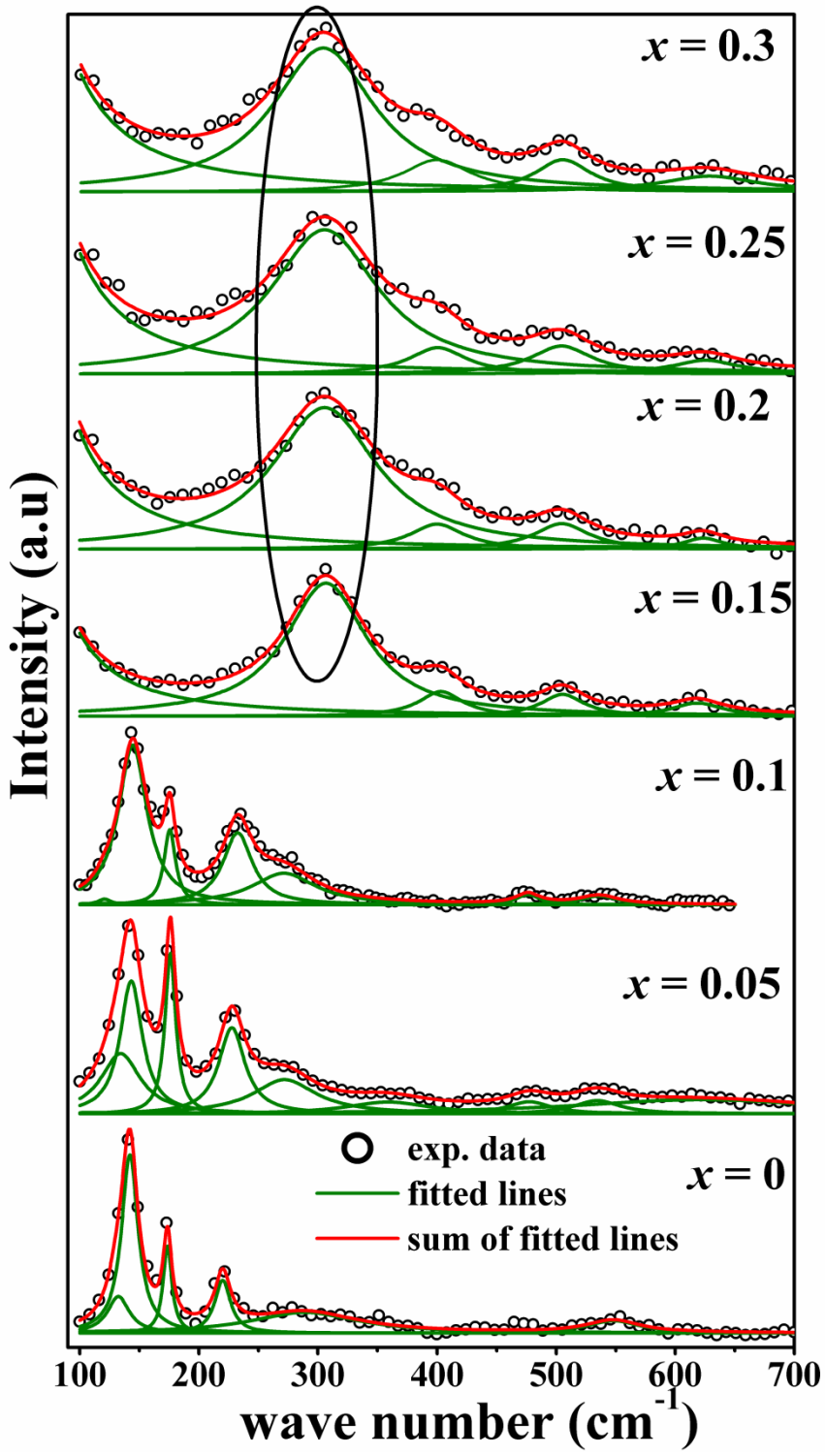

Figure 4.4 Raman scattering spectra of $Bi_{1-x}Sm_xFeO_3$ samples (x = 0 – 0.3) recorded at room temperature, together with their fitted spectra (red line) and the decomposed active modes (green lines).

In order to further confirm the substitution driven structural phase transformation, we have recorded the Raman spectra of $Bi_{1-x}Sm_xFeO_3$ samples at room temperature and they are shown in Fig. 4.4. The observed shifting of Raman modes and the appearance of new modes with gradual increase in Sm concentration reveal the structural distortion as well as transformations. Thirteen ($4A_1 + 9E$) Raman active modes are reported for the rhombohedral BFO having *R3c* space group [153]. We have observed a total of six Raman modes for $x = 0$: three *E* modes at 132 (*E*1), 288 (*E*2), 547 (*E*3) cm^{-1} and three A_1 modes at 142 (A_1-1), 172 (A_1-2), 219 (A_1-3) cm^{-1} which are comparable to literature [154]. We consider here the most intense A_1-1 mode at 142 cm^{-1} for our discussions. With Sm substitution, the most intense A_1-1 mode is found to be blue shifted to 143 cm^{-1} and 148 cm^{-1} for $x = 0.05$ and 0.10 samples respectively. This mode completely disappears as the Sm concentration is increased beyond $x \geq 0.15$. Similarly, the full width at half maximum (FWHM) for A_1-1 mode increases from 16.80 cm^{-1} for $x = 0$ to 29.21 cm^{-1} for $x = 0.15$ samples. The widening of the Raman modes with increase in Sm concentration is consistent with the reduction in the average grain size value as demonstrated in Fig. 4.5. For $x \geq 0.15$, a broad peak is observed at 306 cm^{-1} as shown in Fig. 4.4 within the encircled region. This mode can not be assigned to any vibration in *R3c* space group but is attributed to A_g mode corresponding to the vibration of Sm – O bonds in the orthorhombic cell with *Pnma* space group [155]. Interestingly, the position of A_g mode remains almost unchanged, but its FWHM increases from 83.09 cm^{-1} for $x = 0.15$ to a maximum value of 109 cm^{-1} for $x = 0.25$ sample. The large broadening is attributed to the further reduction in the average grain size.

Figure 4.5 shows the typical FE-SEM images of $Bi_{1-x}Sm_xFeO_3$ samples with $x = 0$, 0.10, 0.20 and 0.30 along with the typical EDS spectra of $x = 0.10$ and 0.25 samples. Densely packed grains separated by well-defined grain boundaries are formed, especially for $x = 0$, 0.10, and 0.20 samples, while the agglomerated grains with considerable pores are seen for $x = 0.30$ sample. A significant number of tiny grains are seen scattered over the bigger grains of BFO, which gradually disappears in the doped samples. These tiny grains can be attributed to the secondary phases such as $Bi_2Fe_4O_9$ and whose presence was observed from the XRD patterns of parent compound and for $x = 0.05$. The reduction of grain size with increase in Sm concentration is consistent with previous results [156, 157]. The average grain size for *x*

= 0 is found to be 1.6 µm and it reduces to 1.2 µm, 0.8 µm and 0.6 µm for x = 0.10, 0.20 and 0.30 samples respectively.

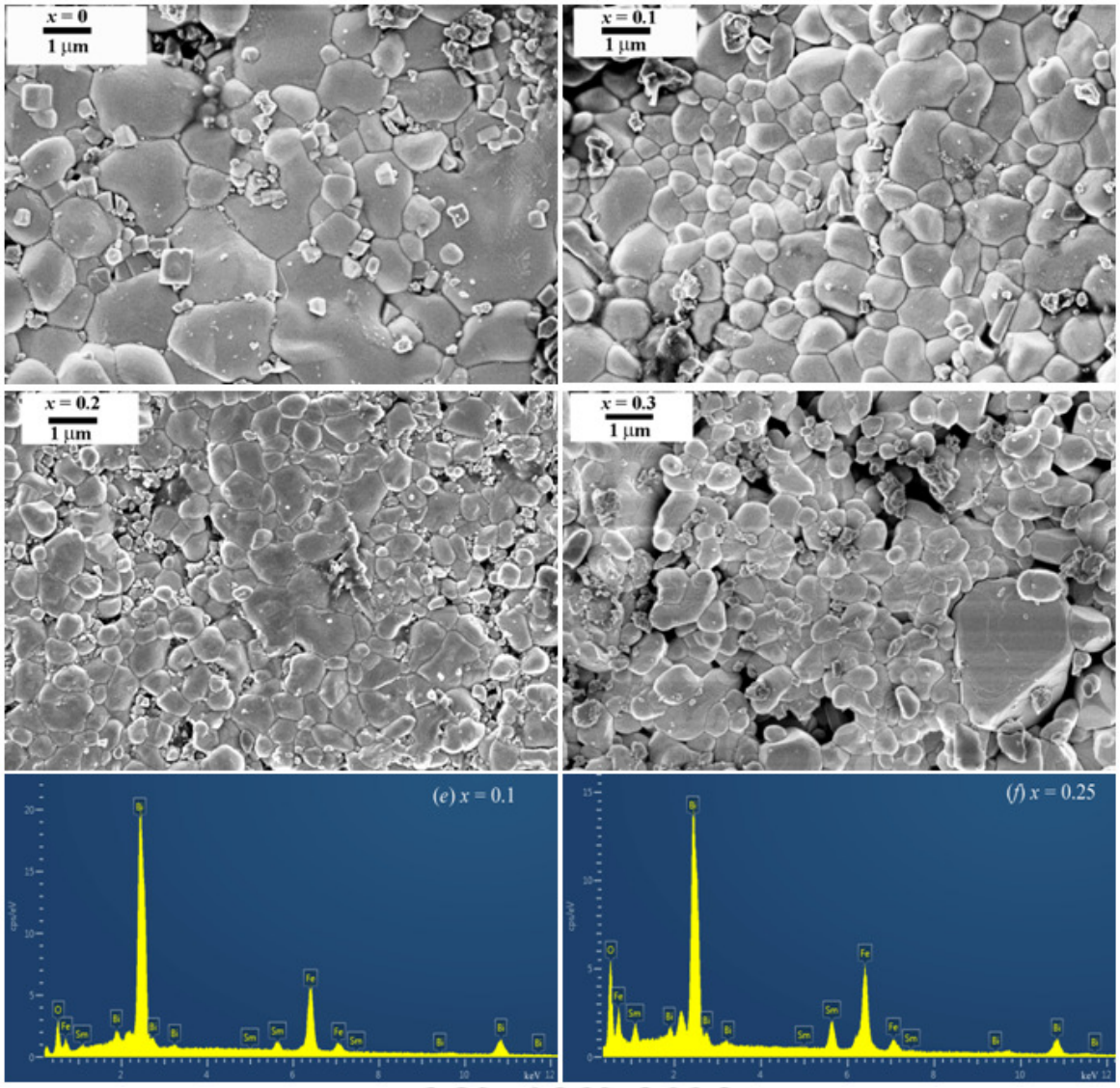

Figure 4.5 FE-SEM images of $Bi_{1-x}Sm_xFeO_3$ samples with x = 0, 0.10, 0.20 and 0.30 along with the EDS spectra of x = 0.10 and 0.25 samples.

The mobility of grain boundaries during the sintering of ceramics determines the grain growth. They can be affected by two ways either by the defect chemistry and the dopant-defect associations or due to the presence of oxygen vacancies (OVs) [158, 159]. The defect chemistry and dopant-defect affect the grain boundary diffusion of host ions. The OVs

facilitate the cation diffusions in solids and, hence, the mobility of grain boundaries through interstitial or the OVs. However, substitution of Sm in $BiFeO_3$ reduces the Bi loss, which in turn reduces the concentrations of OVs. With decrease in number of OVs the cation diffusion is impeded and hence, grain growth is slowed down. Such grain growth inhibition due to the suppression of OVs is reported in BiFeO3 compounds with the substitution of Fe by Nb^{5+}, Zr^{4+} *etc*. [160-162]. Furthermore, there is a possibility that a small concentration of Sm ions segregates at the grain boundary and inhibit the grain boundary movement. The cationic ratios Bi: Sm: Fe of x = 0.1 and 0.25 samples obtained from EDS analysis are found to be 0.912: 0.087: 1 and 0.734: 0.266: 1 respectively which are comparable to their nominal starting compositions.

4.3 Complex Impedance Spectroscopy

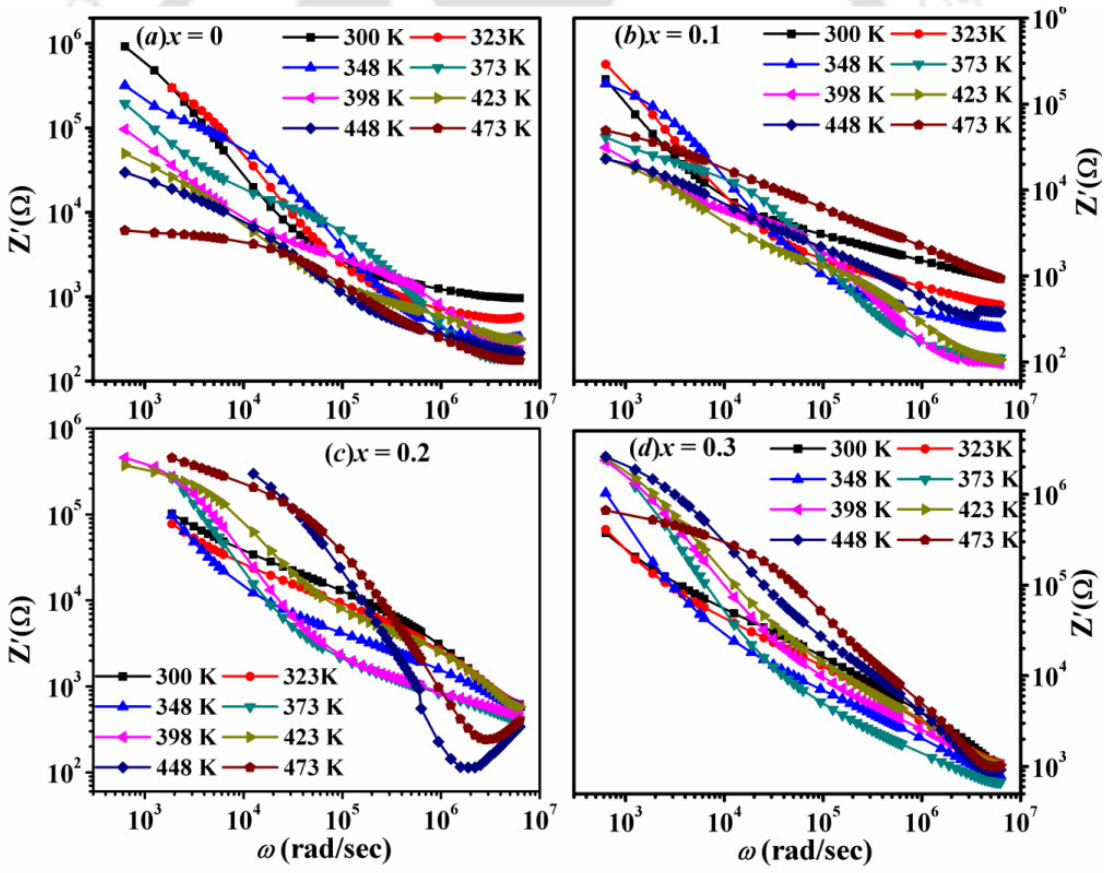

Figure 4.6 Frequency variation of Z' of $Bi_{1-x}Sm_xFeO_3$ samples with x = 0, 0.10, 0.20 and 0.30.

The typical plots of frequency variations of real part (Z') of complex impedance (Z^*) are shown in Fig. 4.6 for $Bi_{1-x}Sm_xFeO_3$ samples with x = 0, 0.10, 0.20 and 0.30 at different temperatures. The value of Z' at a particular temperature decreases with the increase in frequency. The impedance response of a sample arises due to motion of charge carriers at the intragrain, intergrain regions and material-electrode interface. There are various ways of charge carrier movement such as long-range/short-range displacement, dipole reorientation and via the formation of space charge, *etc*. The frequency dependence of Z' is governed by all these motions of charge carriers. The observation of plateau-like regions in Z' spectra followed by its sharp fall with increase in frequency reveal the relaxation process in these samples. The Z' value for x = 0 decreases with the increase in temperature in the entire range of temperature. This is known as negative temperature coefficient of resistance (NTCR). As can be seen in Fig. 4.6 (*b*), the Z' value for x = 0.1 first decreases with increase in temperature upto 398 K and after that it increases. Similar behavior is observed for the other samples. The increase of Z' is observed across the Polomska transition, which will be discussed in section 4.4.

Figure 4.7 shows the variation of $-Z''$ of Z^* as the function of frequency at different temperatures for $Bi_{1-x}Sm_xFeO_3$ samples with x = 0, 0.10, 0.20 and 0.30. Two broad peaks are observed at a particular temperature for x = 0 sample and they can be clearly seen especially for T $\geq$ 373 K. The high frequency peak is attributed to grains while the low frequency is attributed to grain boundaries. The peaks shift towards the higher frequency region with increase in temperature depicting the thermal activation of the relaxation process. Similarly other samples also exhibit two peaks corresponding to relaxations in grains and grain boundaries. The peaks of x = 0.10 sample are found to initially shift towards the higher frequency region with increase in temperature upto 398 K and beyond that they shift in opposite direction. We have observed similar downward shift of relaxation peaks towards lower frequency region with increase in temperature for other samples. Such shifting of peaks towards the lower frequency region has been explained on the basis of Polomska transition as discussed in section 4.4.

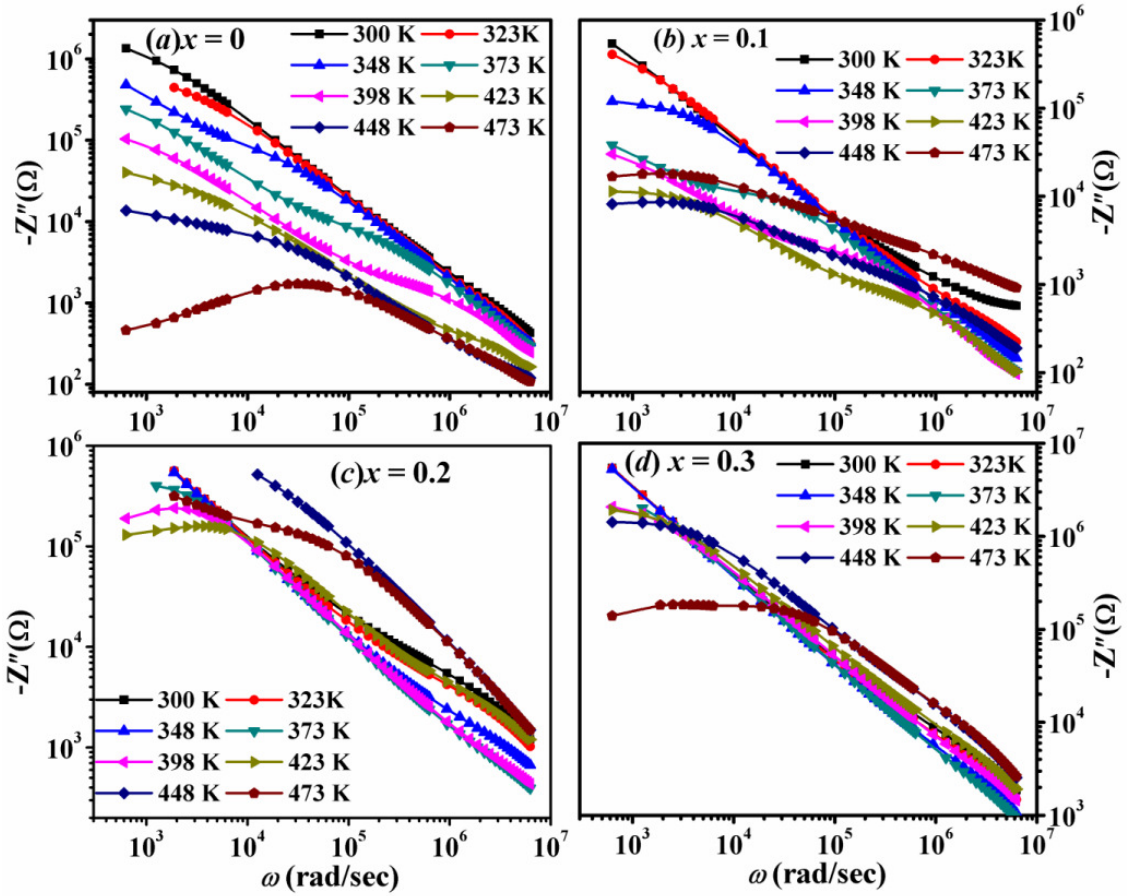

Figure 4.7 Frequency variation of -Z'' of $Bi_{1-x}Sm_xFeO_3$ samples with x = 0, 0.10, 0.20 and 0.30.

4.3.1 Nyquist Plots

The Nyquist plots of $Bi_{1-x}Sm_xFeO_3$ samples typically for x = 0, 0.10, 0.20 and 0.30 at different temperatures are shown in Fig. 4.8 in log-log scale. Two distorted semicircular arcs are seen and they are attributed to grains and grain boundaries respectively at higher (lower Z') and lower (higher Z') frequency regions. In order to estimate the magnitude of resistance and capacitance of the grains and grain boundaries we have modeled the Nyquist plots to the equivalent circuit as shown in Fig. 4.9. The values of capacitance and resistance corresponding to grains and grain boundaries obtained from the modeling of Nyquist plots (Fig. 4.8) to the equivalent circuit at some selected temperatures are listed in Table 4.2.

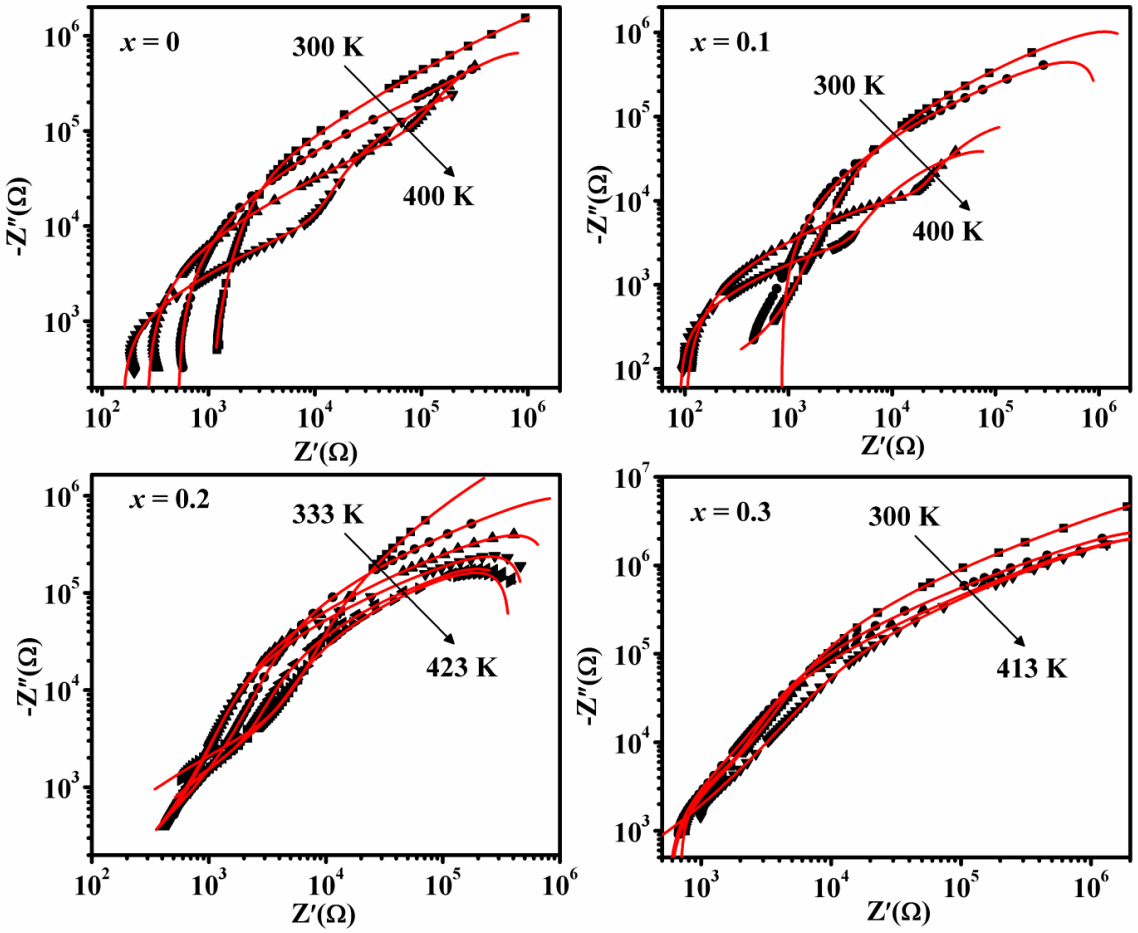

Figure 4.8 Nyquist plots of $Bi_{1-x}Sm_xFeO_3$ samples with x = 0, 0.10, 0.20 and 0.30.

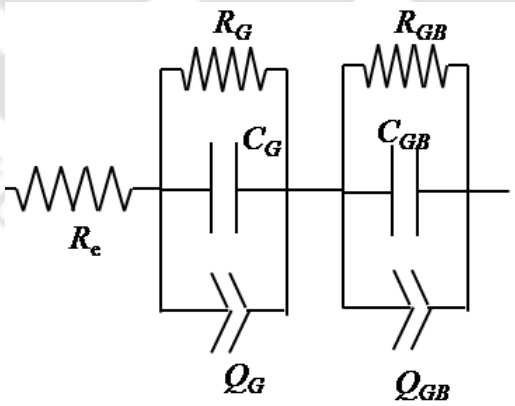

Figure 4.9 Electrical equivalent circuit.

Table 4.2 Capacitance (C_G, C_{GB}) and resistance (R_G, R_{GB}) values corresponding to grains (G) and grain boundaries (GB) obtained from the fitting of Nyquist plots.

		Temperature						
x	Parameters	323K	348K	373K	398K	423K	448K	473K
0	C_G (nF)	0.151	0.10	0.10	0.125	0.167	0.031	0.01
	C_{GB} (nF)	0.124	0.26	0.44	0.445	0.545	0.564	0.40
	R_G (kΩ)	141.7	54.5	41.7	3.0	0.61	0.35	0.23
	R_{GB}(kΩ)	4620.1	1531.2	480.2	252.5	173.2	45.1	5.2
0.05	C_G (nF)	0.004	0.40	0.67	0.85	0.90	0.42	0.006
	C_{GB} (nF)	1.244	1.131	1.23	1.40	1.72	1.36	1.28
	R_G (kΩ)	1.07	0.55	0.40	0.26	1.10	0.11	0.04
	R_{GB} (kΩ)	704.1	355.2	247.3	115.0	927.3	424.5	17.3
0.1	C_G (nF)	0.002	0.20	0.40	0.36	0.21	--	--
	C_{GB} (nF)	0.24	0.31	0.05	1.35	0.95	0.06	--
	R_G (kΩ)	0.92	1.441	24.41	4.145	1.159	--	--
	R_{GB} (kΩ)	1152.1	815.3	201.3	124.4	274.3	100.1	--
0.15	C_G (nF)	0.02	0.03	0.04	0.03	0.06	--	--
	C_{GB} (nF)	0.22	0.16	0.15	0.17	0.23	--	--
	R_G (kΩ)	19.53	8.57	6.05	5.54	4.23	--	--
	R_{GB} (kΩ)	32700	6620	881.2	665.4	243.5	--	--
0.2	C_G (nF)	0.09	0.15	0.41	0.11	0.38	--	--
	C_{GB} (nF)	0.20	0.17	0.15	0.16	0.17	--	--
	R_G (kΩ)	7.96	5.47	2.50	1.57	3.93	--	--
	R_{GB} (kΩ)	34310	5351.2	824.3	506.2	371.3	--	--
0.25	C_G (nF)	--	0.02	0.04	0.006	0.009	--	--
	C_{GB} (nF)	--	0.05	0.07	0.06	0.01	--	--
	R_G (kΩ)	--	0.36	0.20	0.03	0.02	--	--
	R_{GB} (kΩ)	--	5832.5	4913.4	337.6	220.5	--	--
0.3	C_G (nF)	--	0.05	0.05	0.02	0.08	--	--
	C_{GB} (nF)	--	0.02	0.03	0.13	0.19	--	--
	R_G (kΩ)	--	5.8	4.6	1.14	0.85	--	--
	R_{GB} (kΩ)	--	15210.1	5413.4	4133.6	2531.6	--	--

4.4 Complex Dielectric Permittivity

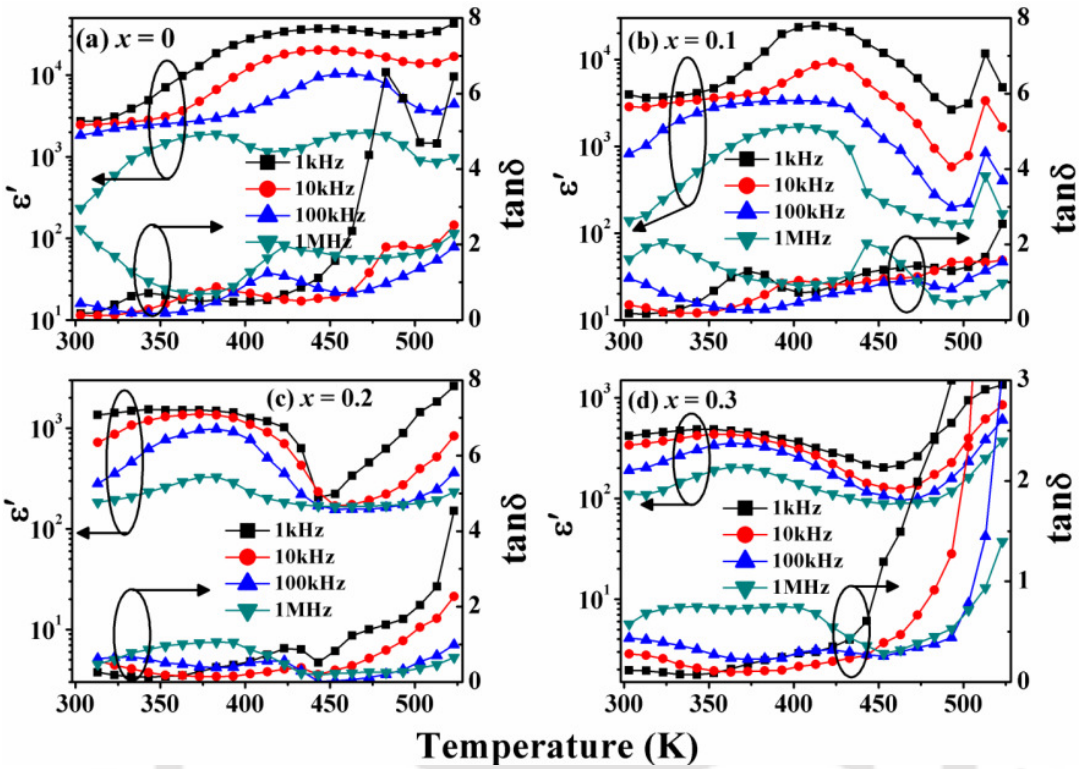

Figure 4.10 Temperature dependence of ε′ and tanδ measured at different frequencies for $Bi_{1-x}Sm_xFeO_3$ with (*a*) $x = 0$ (*b*) $x = 0.10$ (*c*) $x = 0.20$ and (*d*) $x = 0.30$.

The temperature dependence of real part (ε') of complex dielectric permittivity (ε^*) and dissipation factor ($\tan\delta = \varepsilon''/\varepsilon'$) for different frequencies such as 1, 10, 100 and 1000 kHz are shown in Fig. 4.10 for $Bi_{1-x}Sm_xFeO_3$ samples with $x = 0$, 0.10, 0.20 and 0.30. The main characteristic feature of $\varepsilon'(T)$ is its anomaly in terms of a broad peak followed by an increase in its value as the temperature is further raised. The rapid increase in the value of ε' at higher temperature is attributed to the thermal enhancement of conductivity of the grains. The value of ε' at the peak temperature, T_M *i.e.*, ε'_m decreases for all samples with increase in frequency. Polomska *et al.* [62] first reported a dielectric anomaly for $BiFeO_3$ at 458 K (185 °C), known as Polomska transition, which is quite different from the familiar magnetic and ferroelectric transition temperature. As no change in the crystal structure of $BiFeO_3$ around T_M is reported [163], the Polomska transition can not be attributed to any structural transition associated to the bulk. Marti *et al.* [164] have reported the existence of a skin layer confined within a few

nanometer of $BiFeO_3$ surface which is structurally different from the $BiFeO_3$ bulk. Such skin layer is reported to undergo structural transition around 548 K leading to $\varepsilon'(T)$ anomaly. Jarrier *et al.* [165] reported another such structural phase transition of the skin layer at 140 K. Kumar *et al.* [166] observed an anomalous overdamping of spin waves around 450 K in BFO thin film and it coincided with the dielectric loss anomaly. However, whether Polomska transition is truly a surface phase transition is still unclear as no change in lattice parameter of BFO surface was observed by Marti *et al*. at 458 K [164]. The Sm substitution in BFO is found to shift the Polomska transition temperature (T_M) towards room temperature and enhances the dielectric anomaly. It can be attributed to increase in surface to volume (S/V) ratio [165] as the concentration of Sm is increased and it is consistent with observed reduction in average particle size. Moreover, considerable concentration of Sm may substitute the Bi at the skin layer which is similar to inducing chemical pressure in the unit cell of the skin layer due to the ionic size mismatch of Sm^{3+} and Bi^{3+} ions. It is likely to change the symmetry of the skin layer, which may occur at relatively lower T_M values for higher Sm doped samples.

Figures 4.11, 4.12 and 4.13 show the variations of ε' and ε'' as a function of angular frequency for $Bi_{1-x}Sm_xFeO_3$ (x = 0 – 0.3) samples at different temperatures. The observed plateau like behavior followed by rather sharp fall in ε' value as the frequency is increased and the corresponding peak in ε'' vs. ω indicate the existence of relaxation like behavior. Moreover, as the frequency is reduced below 1 kHz, ε' is found to increase and is attributed to the space charge polarization. Such behavior is found to be dominant especially at higher temperature. Space charge (interfacial) polarization occurs due to the blockage of charge carriers at physical barriers such as grain boundaries, electrode-material interface *etc.*, where charges pile up and behave like dipoles when an electric field is applied. These dipoles produce large polarization locally which is known as space charge polarization.

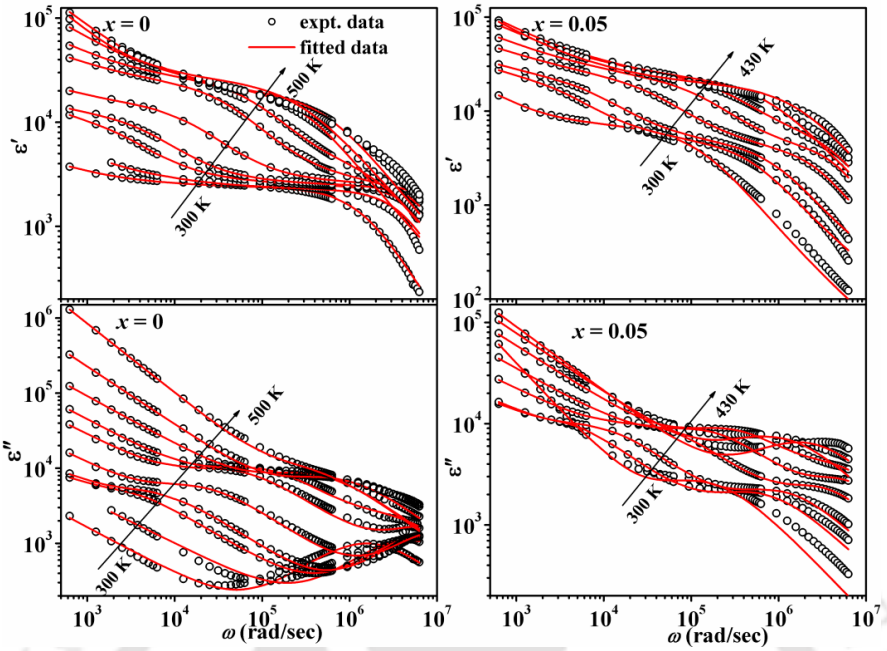

Figure 4.11 Frequency dispersion of ε' (upper panel) and ε'' (lower panel) of $x = 0$ and 0.05 samples of $Bi_{1-x}Sm_xFeO_3$ at different temperatures along with fitted data to the eqs. (4.2) and (4.3).

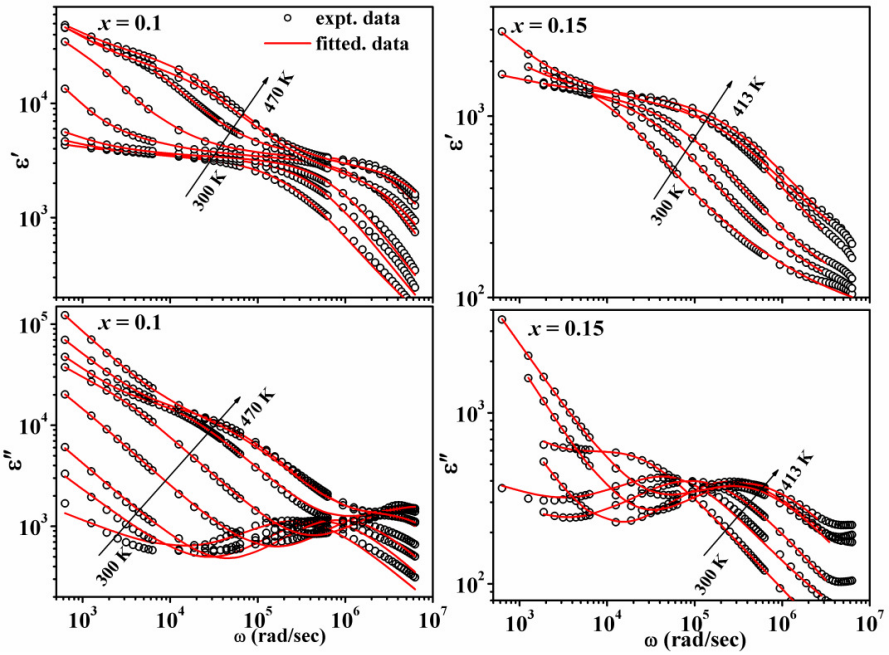

Figure 4.12 Frequency dispersion of ε' (upper panel) and ε'' (lower panel) of $x = 0.1$ and 0.15 samples of $Bi_{1-x}Sm_xFeO_3$ at different temperatures along with fitted data to the eqs. (4.2) and (4.3).

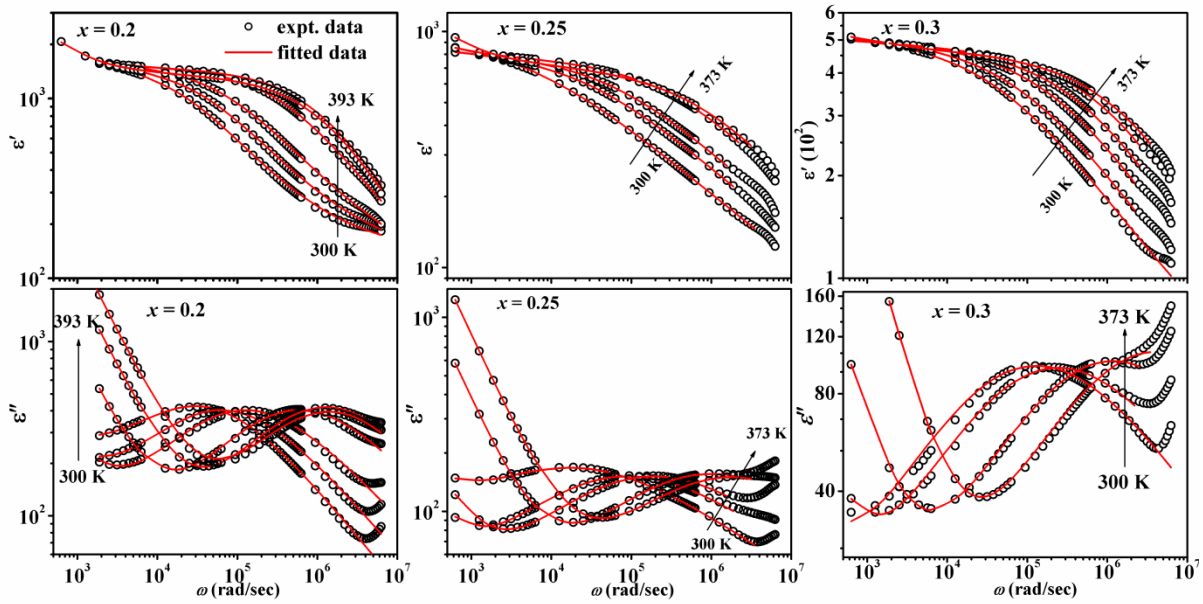

Figure 4.13 Frequency dispersion of ε' (upper panel) and ε'' (lower panel) of x = 0.2 – 0.3 samples of $Bi_{1-x}Sm_xFeO_3$ at different temperatures along with fitted data to the eqs. (4.2) and (4.3).

The density of charges contributing to space charge polarization rises as the temperature is increased. The frequency range of sensitivity for such polarization may extend from 10^{-3} Hz to kHz range, producing a large value of ε' especially in lower frequency region [167]. The observed decrease in ε' beyond the plateau region i.e., in the frequency range of 10^4 – 10^6 Hz is ascribed to the defect-dipole polarization effect. At a fixed temperature, such dipoles may get fully polarized at the low frequency of applied electric field resulting in the plateau region. Once this frequency is increased, the dipoles lag behind the applied electric field and hence contribute no net polarization resulting in sharp decrease in ε' value.

The frequency dispersion of ε^* is fitted to the equation (1.16) along with the contribution of conductivity with the expressions for ε' and ε'' as given below:

$$\varepsilon' = \varepsilon_\infty + \frac{\Delta\varepsilon\cos(\beta\phi)}{\left(1+2(\omega\tau)^{1-\alpha}\sin(\alpha\pi/2)+(\omega\tau)^{2-2\alpha}\right)^{\beta/2}} + \frac{\sigma''}{\varepsilon_0\omega^s} \qquad (4.2)$$

$$\varepsilon'' = \frac{\Delta\varepsilon \sin(\beta\phi)}{\left(1+2(\omega\tau)^{1-\alpha}\sin(\alpha\pi/2)+(\omega\tau)^{2-2\alpha}\right)^{\beta/2}} + \frac{\sigma'}{\varepsilon_0\omega^s} \tag{4.3}$$

where ε_∞ is the permittivity at high frequency, τ is the most probable relaxation time. The term $\Delta\varepsilon$ (= $\varepsilon_s - \varepsilon_\infty$, where ε_s is the permittivity at low frequency) gives the dielectric strength. The exponents α ($0 < \alpha < 1$) and β ($0 < \beta < 1$) signify the broadness and asymmetry of corresponding spectra respectively. On the other hand, σ' and σ'' represent the conductivity due to free charge carriers (dc conductivity) and space charges (localized charges) respectively [167]. The dimensionless exponent s is such that $s = 1$ for ideal complex conductivity and $s < 1$ for distribution in polarization mechanism. However, such contribution of conductivity degrades the dielectric character of a sample and it is undesirable due to large dielectric loss.

A careful look at the experimental data of $x = 0$ sample reveals a single plateau region in ε' accompanied by a characteristic loss peak in ε'' for the measuring temperature $T < 343$ K depicting grains relaxation. In the temperature range of 343K – 423 K another loss peak appears at the low frequency region due to the relaxation in grain boundaries. Hence, both grains and grain boundaries are active in this temperature range. For $T > 423$ K, the loss peak due to grains moves out of the measured frequency range. Similarly, $x = 0.05 – 0.10$ samples exhibit dual relaxations at grains and grain boundaries. Accordingly, the experimental data for $x = 0 – 0.1$ were analyzed in dual Havriliak-Negami (HN) equation (eq. (1.16)) in the temperature range where the relaxation peaks corresponding to grains and grain boundaries are observed. The fitted data are shown as solid lines in Figs. 4.11, 4.12 and 4.13 which are in clear agreement with experimental ε' and ε'' data (symbols) over the entire range of frequency and temperature. Here the permittivity data for $x = 0 – 0.10$ samples are fitted by keeping β as a fixed parameter at $\beta = 1$ throughout the entire temperature range, while varying α with the constraint $\alpha < 1$ [64]. The exponent α is found to increase from 0.08 for $x = 0$ to 0.15 for $x = 0.10$ sample. The value of $\beta = 1$ suggests that there is no asymmetry in the loss peaks. Hence, the observed deviation of relaxation for $x \leq 0.1$ from its idealness is solely due to broadening of relaxation peaks. Further increase in Sm concentration ($x \geq 0.15$) induces even stronger deviation of relaxation as loss peaks become wider and asymmetric. Consequently, permittivity data for $x \geq 0.15$ could be fitted to HN equation with $\alpha, \beta \neq 1$.

Here also the parameter α follows the same increasing trend with increase in Sm concentration from $\alpha = 0.36$ for $x = 0.20$ to $\alpha = 0.5$ for $x = 0.30$ sample. While the parameter α remains unchanged throughout the entire temperature range, β increases towards the value 1 with increase in temperature. Hence, we observed further deviation of relaxation dynamics suggesting higher disorder induced by Sm. It is interesting to note that α does not vary with temperature but varies with Sm concentration. As α signifies the interaction between dipoles [168], its temperature independent behavior suggests a stronger dipolar interaction in ferroelectric materials. On the other hand, the increment of α with increase in Sm concentration from a magnitude $\alpha = 0.08$ to 0.5 is attributed to substitution driven structural distortion. Analysis of structural properties reveals the reduction of unit cell size due to Sm substitution, which makes it easier for dipoles to interact themselves in a ferroelectric compound because of the reduction in separations between dipoles. Hence, the exponent α increases with increase in Sm concentrations. The values of different fitting parameters viz. $\Delta\varepsilon$, α, β, σ', σ'' at 303K and 373 K are given in Table 4.3.

Table 4.3 Dielectric strength ($\Delta\varepsilon$), α, β, σ', σ'' at 300 K and 373 K of $Bi_{1-x}Sm_xFeO_3$ ($x = 0 – 0.3$) samples obtained from the fitting to eqs. (4.2) and (4.3).

x	$\Delta\varepsilon(10^3)$		α		β		$\sigma'(10^{-6}$S/m)		$\sigma''(10^{-6}$S/m)	
	303K	373K	303K	373K	303K	373K	303K	373K	303K	373K
0.00	2.35	11.06	0.08	0.08	1.00	1.00	1.02	7.10	0.65	3.10
0.05	4.40	14.47	0.08	0.08	1.00	1.00	1.14	8.50	7.46	8.42
0.10	3.03	3.27	0.15	0.15	1.00	1.00	0.12	2.97	0.11	1.62
0.15	1.30	1.50	0.15	0.29	0.79	0.84	0.09	4.40	0.13	1.50
0.20	0.97	1.23	0.36	0.36	0.91	0.95	0.03	1.04	0.05	1.24
0.25	0.94	0.74	0.51	0.51	0.59	0.86	0.07	3.50	0.01	0.61
0.30	0.50	0.47	0.51	0.51	0.75	0.97	0.07	1.70	--	0.10

We found that $\Delta\varepsilon$ at 303 K increases from 2.35×10^3 for $x = 0$ to 4.40×10^3 for $x = 0.05$, beyond which it decreases with increase in Sm concentration. A $\Delta\varepsilon$ value as low as $\Delta\varepsilon = 0.5\times 10^3$ at 303 K was observed for $x = 0.3$ sample. Such variation could be mainly attributed to three reasons: (i) decrease in the number of highly polarizable Bi^{3+} ions, (ii) decrease in

the apparent conductivity contribution, and (iii) probable non-ferroelectric interaction among the dipoles due to increase in disorder. As can be observed from Table 4.3, the values of σ' and σ'' at a particular temperature significantly reduce for Sm-doped samples. Hence, the undesired contribution of conductivity towards ε' and ε'' decreases. Again, the $6s^2$ lone pair electrons of Bi^{3+} ions are attributed to the higher polarizability of $BiFeO_3$. Sm substitution reduces the number of Bi^{3+} ions containing the easily polarizable electron lone pairs and hence the value of polarizability and $\Delta\varepsilon$ are decreased with increase in Sm concentration. Further, there is a possibility of interaction among the dipoles which hinders the existing ferroelectric coupling to produce small net polarization, thereby reducing the value of $\Delta\varepsilon$.

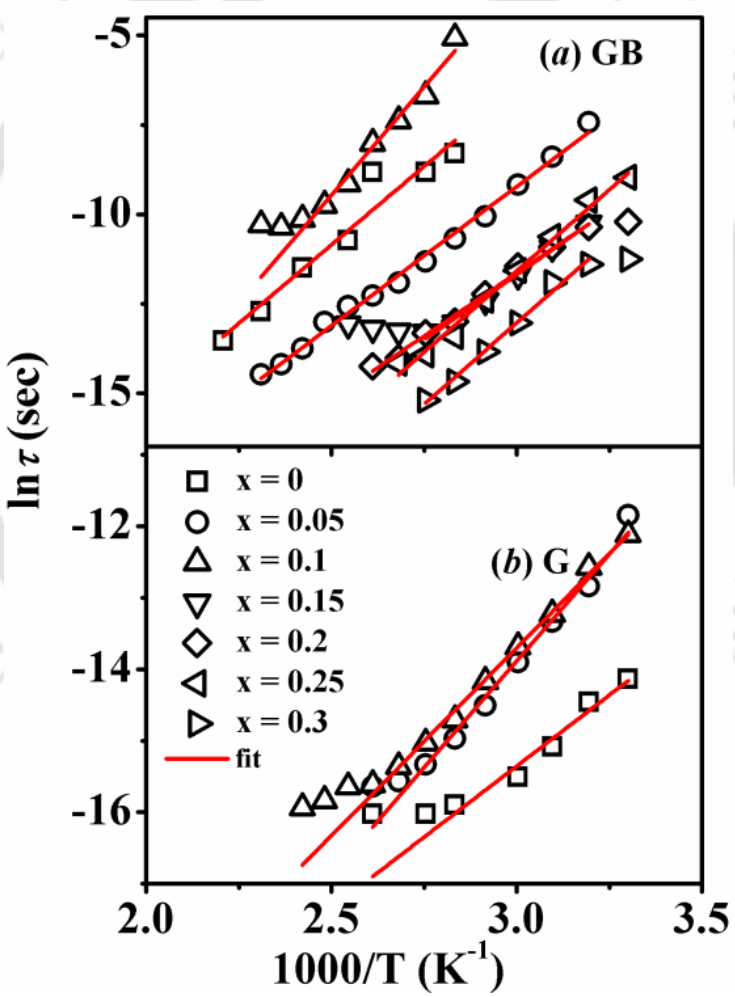

Figure 4.14 Arrhenius plots of relaxation times obtained for (*a*) grain boundaries (*b*) grains relaxation for $Bi_{1-x}Sm_xFeO_3$ samples ($x = 0 – 0.30$).

In order to elucidate the dielectric relaxation and identify the species taking part in the dielectric relaxation, we estimated the activation energy of relaxation. For a thermally activated relaxation process, the relaxation time ($\tau = 1/2\pi f_{max}$) follows the Arrhenius law:

$$\tau = \tau_0 \exp\left(\frac{E_a}{k_B T}\right) \tag{4.4}$$

where τ_0 is the prefactor, E_a is the activation energy for the relaxation process, and k_B is the Boltzmann constant. The activation energy E_a was determined by plotting ln(τ) versus $1/T$ and carrying out the linear fit as shown in Fig. 4.14. The calculated activation energies for grains and grain boundaries are tabulated in Table 4.4.

Table 4.4 Activation energy obtained from the Arrhenius fit to relaxation time corresponding to grains, grain boundaries and the tanδ peaks.

	E_a (eV)		
x	G(τ)	GB(τ)	tanδ
0	0.30	0.68	0.86
0.05	0.50	0.67	0.80
0.1	0.45	0.70	1.04
0.15	--	0.69	0.45
0.2	--	0.60	0.47
0.25	--	0.78	--
0.3	--	0.80	--

The calculated values of E_a for grains are found to be 0.3, 0.5 and 0.45 eV for x = 0, 0.05 and 0.10 samples respectively. The activation energy value of E_a = 0.3 eV for x = 0 is comparable to that reported by Hunpratub *et al.* [64] and is attributed to electrons hopping inside the grains. The presence of Fe ions in $BiFeO_3$ as Fe^{2+} and Fe^{3+} facilitate the electron hopping between them, which is similar to the reversal of dipoles and it contributes to dielectric relaxation inside the grains [169]. A slight increase in E_a of grains (~ 0.5 eV) for x = 0.05 and 0.1 samples could be attributed to reduction in electron hopping as a result of smaller concentration of Fe^{2+} ions. Sm substitution in $BiFeO_3$ is reported to decrease the oxygen vacancies, thereby reducing the formation of Fe^{2+} ions. On the otherhand, the obtained value of E_a = 0.68 – 0.8 eV is consistent with that reported by Hunpratub *et al.* [64]

and is close to the relaxation activation energy of grain boundaries [170, 171]. The value of E_a demonstrates that the short range movement of singly ionized OVs brings out the relaxation in grain boundaries.

Figure 4.15 shows the Cole-Cole (CC) plots for $Bi_{1-x}Sm_xFeO_3$ with x = 0, 0.10, 0.20 and 0.30 at some selected temperatures. The semicircular arcs in the high frequency region are attributed to grains, while that in some mid frequency region is due to grain boundaries. As the temperature rises, charge carriers are activated and such activation of charge carriers enhances the conductivity induced permittivity and loss value. As a result, the size of semicircular arcs becomes larger with increase in temperature. At higher temperature one more semicircle due to electrode contribution appears in the low frequency side.

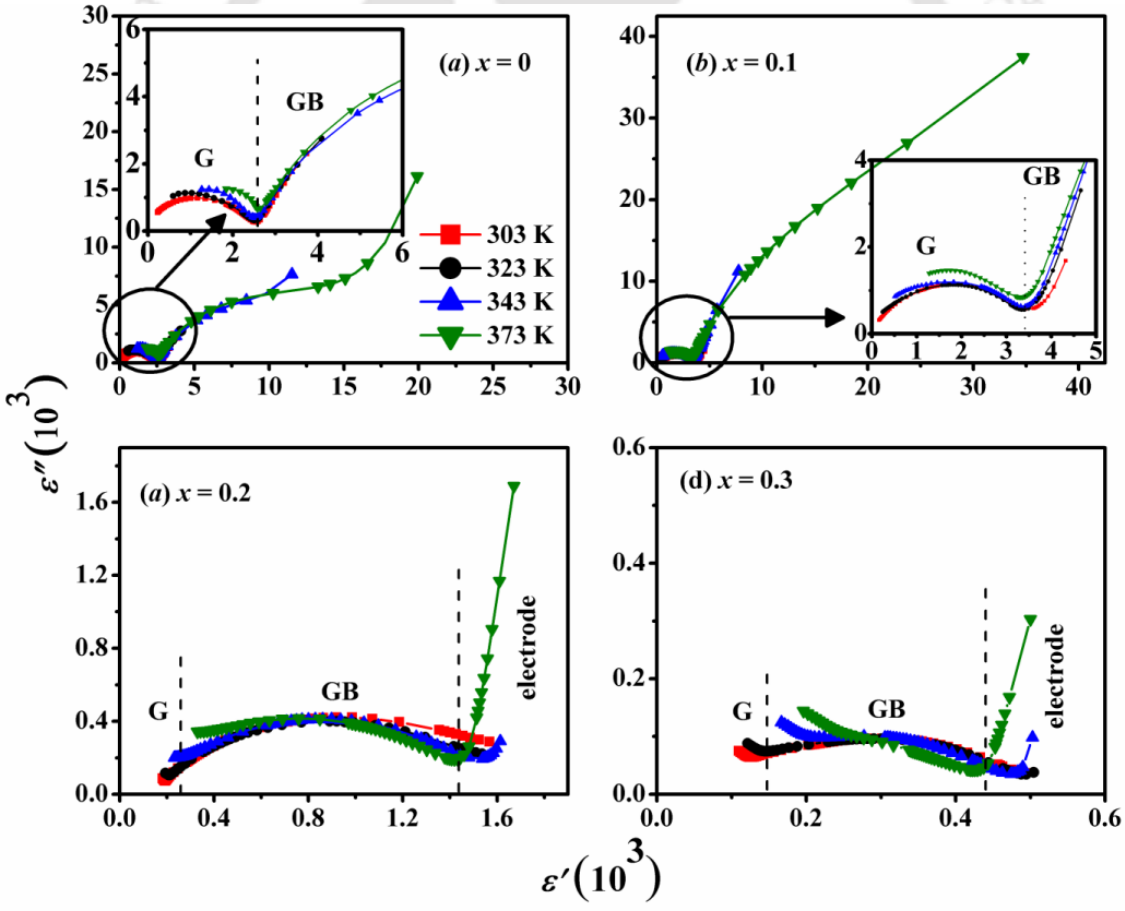

Figure 4.15 Cole – Cole plots for $Bi_{1-x}Sm_xFeO_3$ samples with x = 0, 0.10, 0.20 and 0.30 sample at some selected temperatures.

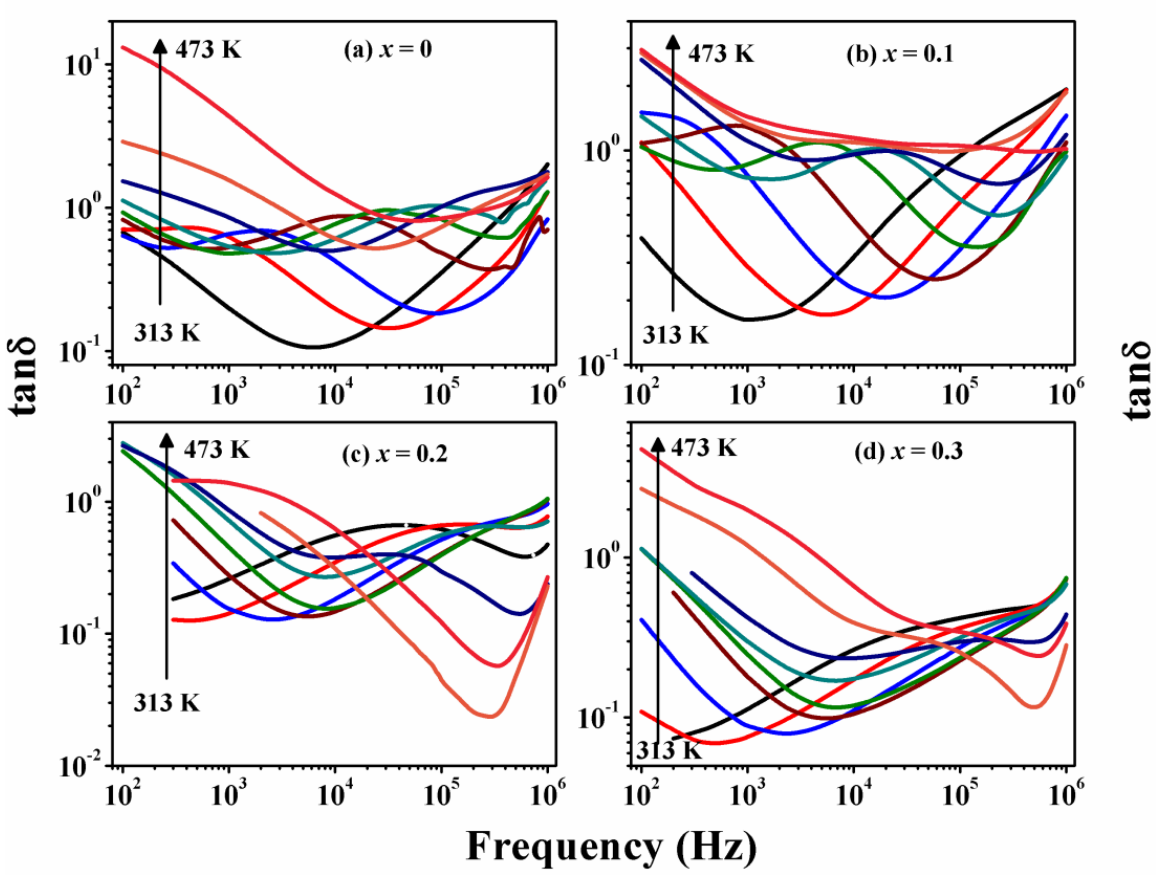

Figure 4.16 Variation of tanδ with frequency for $Bi_{1-x}Sm_xFeO_3$ samples with x = 0, 0.10, 0.20 and 0.30 at some selected temperatures in the range of 313 K – 473 K at an interval of 20 K.

Figure 4.16 shows the typical frequency variation of tanδ for $Bi_{1-x}Sm_xFeO_3$ samples with x = 0, 0.1, 0.2 and 0.3 at some selected temperatures. These plots show valley like behavior with large tanδ values at lower and higher frequencies with a minimum appearing at some intermediate frequency value. A high tanδ value both at the lowest and highest measured frequency with comparatively lower value in between is the main feature of its frequency variation. At some specific temperature range, we observe a peak that shifts towards the high-frequency region with increase in temperature. As demonstrated, the tanδ value for x = 0 decreases from a higher value at low frequency to a lower value at middle frequency and again increases with further increase in frequency for $T \leq 325$ K. At T = 333 K, a peak appears in tanδ spectrum for x = 0 from the low frequency window, which gradually shifts towards the higher frequency with increase in temperature. The tanδ value

again increases beyond the peak with further increase in frequency. The high tanδ value at low frequency is caused by the dc conduction. The peak in tanδ is resulted from the relaxation of active dipoles and the secondary increase in tanδ at the high-frequency region demonstrates the presence of another relaxation process where loss peak could not be seen due to the limitation of measured frequency range. The lower value of tanδ forming the valleys is resulted from the oscillation of the active dipoles. In a low-frequency range, the tanδ values of the Sm-doped samples were found to be lower than the undoped sample. For instance, Sm-substitution drastically reduces tanδ value from tanδ = 0.68 for x = 0 to 0.07 for x = 0.3 sample for a measuring frequency f = 100 Hz at 303 K. The higher tanδ value for x = 0 is attributed to the dominant contribution of dc conduction due to its larger grain size (low GB density) and higher oxygen vacancies. The reduction in tanδ value due to Sm substitution indicates its ability to suppress the dc conduction. The shift in tanδ peak frequency follows the Arrhenius law and activation energies are calculated from Arrhenius plots. The values of activation energies estimated from the Arrhenius fitting of tanδ peak frequency shift are presented in Table 4.4.

4.5 AC Conductivity

The real part (σ') of ac conductivity (σ^*) is calculated using the relation [114]:

$$\sigma'(\omega) = \omega\varepsilon_0\varepsilon'' \tag{4.5}$$

where ω is angular frequency and ε_0 is the permittivity of vacuum. The frequency variations of σ' of $Bi_{1-x}Sm_xFeO_3$ samples are shown in Fig. 4.17 typically for x = 0, 0.10, 0.20 and 0.30 at different temperatures. As can be seen from the Fig., the conductivity plot at a particular temperature is characterized by the appearance of a frequency independent plateau region (dc conductivity) at lower frequency and a frequency dispersive region at higher frequency. In fact, we have observed two frequency independent regions due to the conduction in grains and grain boundaries. The frequency independent plateau at low frequency is attributed to long range translational motion of charge carriers. The frequency dispersion of ac conductivity at higher frequency region can be explained in terms of Funke's jump relaxation model (JRM) [120]. According to JRM, at higher frequency there are two different processes: (i) the jumping ion may jump back to its initial position *i.e.* unsuccessful hopping,

and (ii) the neighborhood ions become relaxed with respect to the jumping ions position and the jumping ions stay in the new sites, *i.e.*, successful hopping. With increase in the ratio of successful to unsuccessful hopping, a dispersive region in the conductivity spectrum at higher frequency is observed.

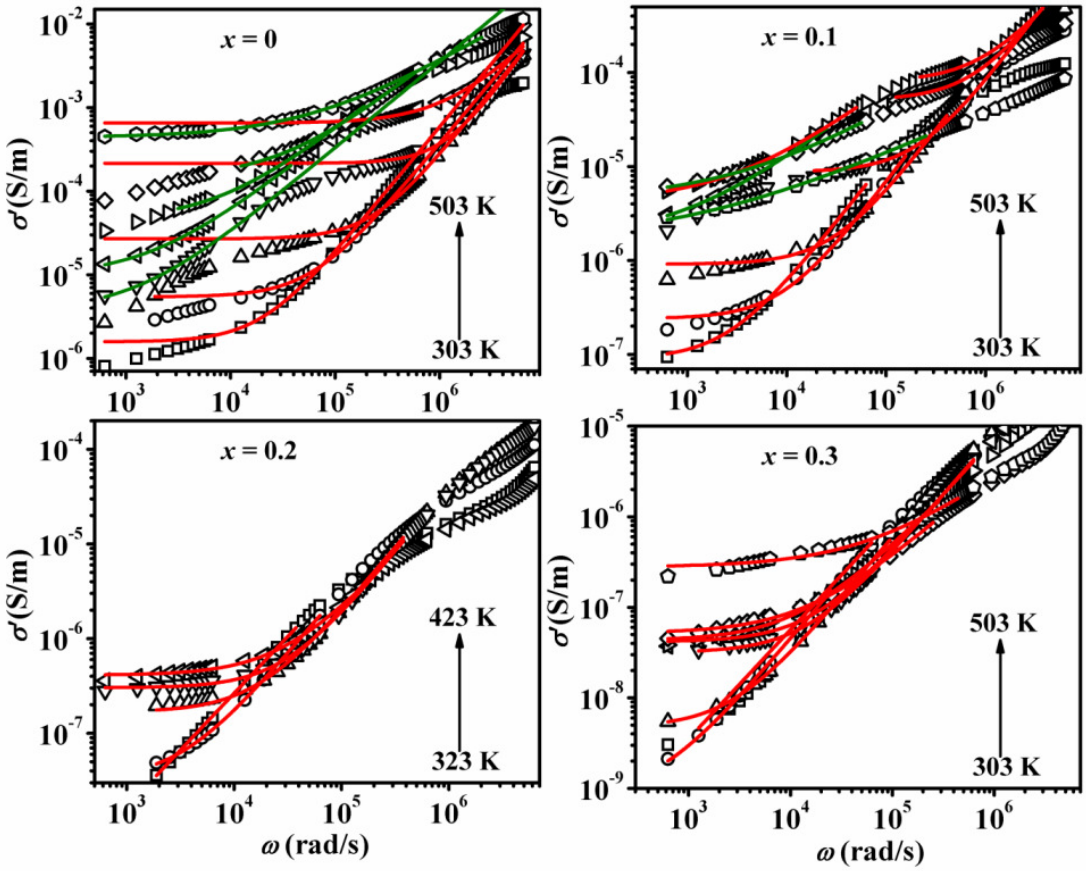

Figure 4.17 Frequency dispersion of conductivity (σ') at several temperatures for $Bi_{1-x}Sm_xFeO_3$ samples with x = 0, 0.10, 0.20 and 0.30. The solid lines are the fitted data to eq. (4.6).

The frequency dispersion of σ' can be described in terms of Jonscher Power Law (JPL) [37]:

$$\sigma'(\omega) = \sigma(0) + A\omega^{s} \tag{4.6}$$

where $\sigma'(\omega)$ is the real part of conductivity, $\sigma(0)$ is the frequency independent (dc) conductivity. The term $A\omega^s$ represents the frequency dispersion and characterizes all dispersion phenomena. The pre-exponential factor, A and the frequency exponent s depend

on temperature and the material's intrinsic properties. The parameter *s* signifies the degree of interaction of mobile charges with the lattice around them and its temperature dependence can reveal the underlying conduction mechanism. Moreover, the value of *s* defines if the motion of the charge carriers is either translational or localized. If the value of *s* is lesser than 1, the motion is translational, and if the value of $s > 1$, the motion is localized. The conductivity spectra of all samples were fitted to Jonscher power law and the fitted data are shown as solid lines in Fig. 4.17 for $x = 0$, 0.1, 0.2 and 0.3 samples. The fitted data closely follow the experimental data.

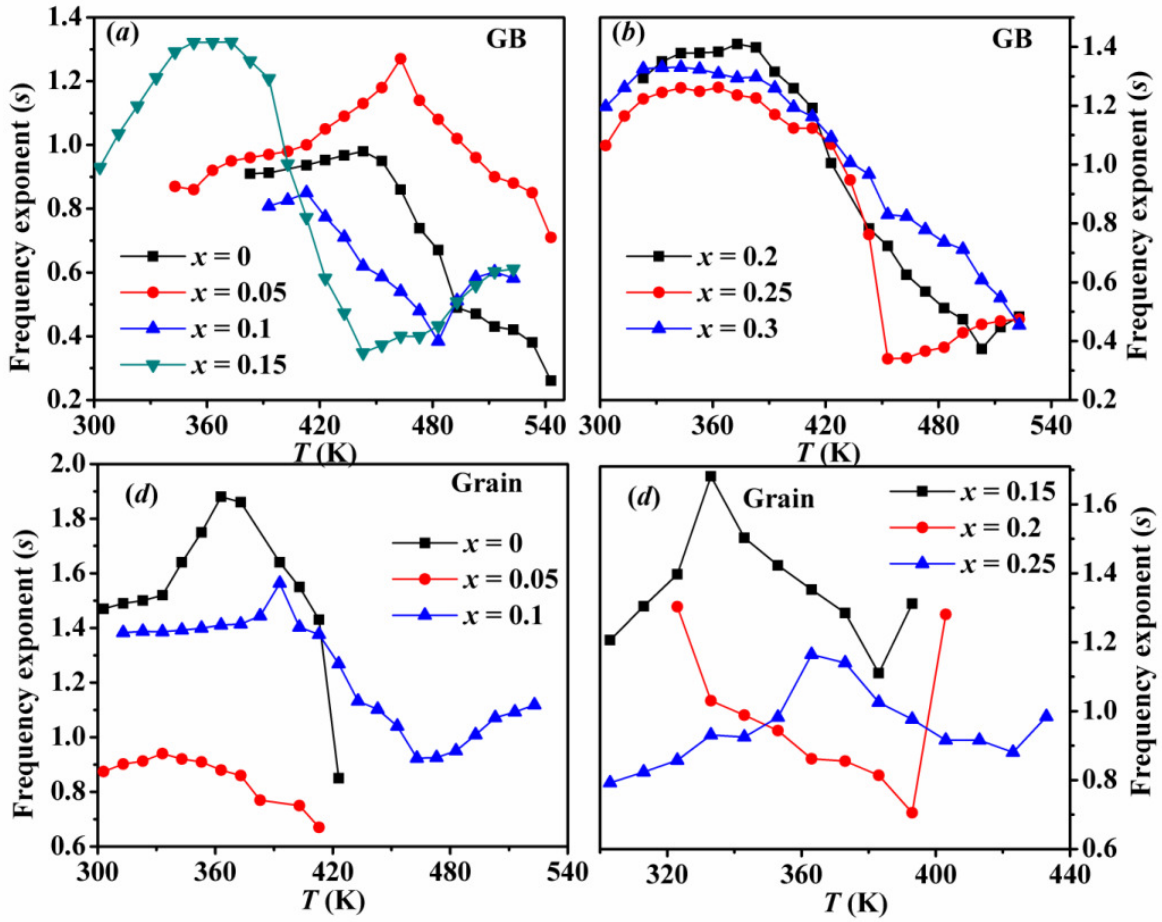

Figure 4.18 Temperature dependence of frequency exponent for grain boundaries and grains obtained from JPL fitting of ac conductivity of $Bi_{1-x}Sm_xFeO_3$ ($x = 0 – 0.3$) samples.

In order to understand the underlying conduction mechanism, the frequency exponents (*s*) obtained from the Jonscher power law fit of ac conductivity of $Bi_{1-x}Sm_xFeO_3$ ($x = 0 – 0.3$) samples are plotted in Fig. 4.18. It is observed that *s* initially increases with

increase in temperature and this increasing trend reveals the SPT mechanism for conduction. With further increase in temperature, *s* continuously decreases, reaches a minimum value and again increases with increase in temperature for most of the samples. This type of temperature dependence reveals the OLPT as another mechanism for conduction. As per theoretical prediction, the value of *s* must be within 1, however, no physical basis exists to restrict the value of *s* below one only [172]. The values of $s > 1$ are reported in literature for ion-conducting glasses [173, 174], single crystals of K_2SO_4 [175], $K_3H(SeO_4)_2$ [176], perovskite compounds such as $Pr_{0.6}Sr_{0.4}Mn_{0.6}Ti_{0.4}O_{3\pm\delta}$ [121], $Ca_{1-x}Sr_xTiO_3$ [177], $BaZr_{0.05}Ti_{0.95}O_3$ [122] and in multiferroic layered thin films of $PbZr_xTi_{1-x}O_3/CoFe_2O_4$ [178] *etc*. The observed temperature dependence of *s* for $Bi_{1-x}Sm_xFeO_3$ reveals that the conduction mechanism in grains and grain boundaries are temperature dependent.

4.6 Magnetic Properties

Temperature variations of magnetization ($M - T$) under zero field-cooled (ZFC) and field-cooled (FC) conditions are shown in Fig. 4.19. Deviation between ZFC and FC curves are observed for all the samples. A wide hump observed at 200 K for ZFC and FC curves for $x = 0$ is attributed to the Néel temperature of $Bi_2Fe_4O_9$ impurity phase [179]. The bifurcation of ZFC and FC curves along with considerable increase in magnetization below 100 K clearly indicates the weak ferromagnetic nature of the samples.

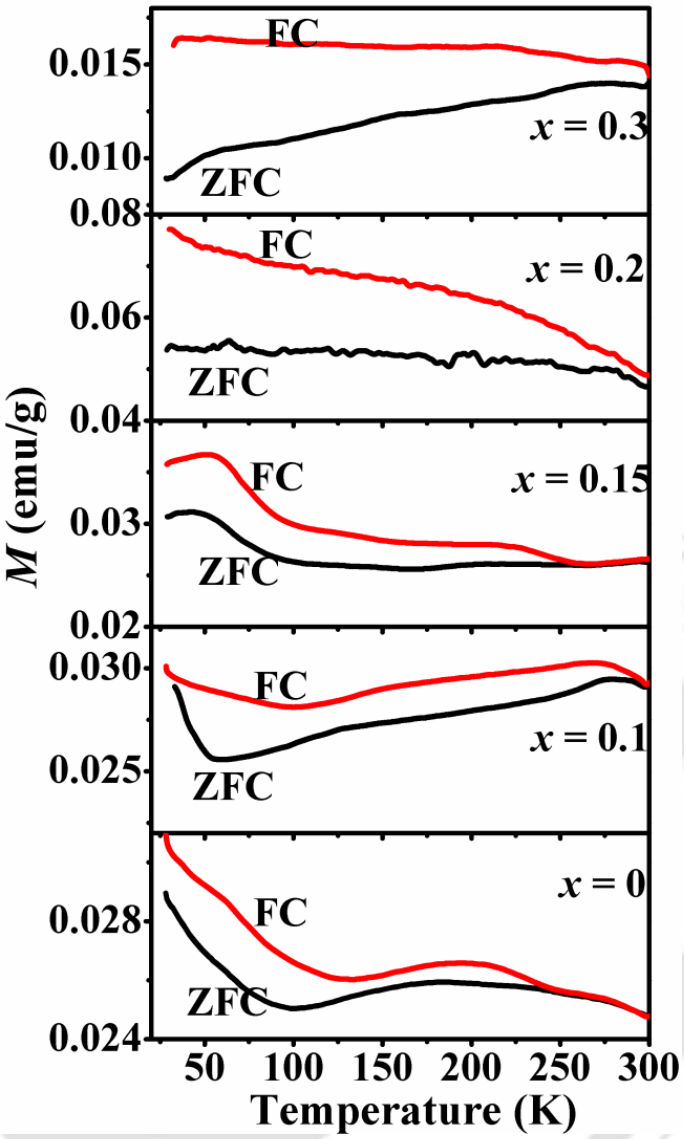

Figure 4.19 Temperature variation of magnetization (M – T) of $Bi_{1-x}Sm_xFeO_3$ (x = 0 to 0.3) samples for H = 2 kOe under ZFC and FC conditions.

Magnetic hysteresis (M – H) loops measured at room temperature (300 K) for $Bi_{1-x}Sm_xFeO_3$ are presented in Fig. 4.20 (a – c). We have found a non-zero value of remnant magnetization M_r (~ 0.004 emu/g) and coercive field, H_C (~150 Oe) for x = 0 which reduces to almost to zero for x = 0.05 sample. The smaller but non-zero value of M_r and H_C for x = 0 is resulted from the ferromagnetic interaction among a small concentrations of Fe ions which are in its mixed valence state. As explained before, a small concentration of Fe^{3+} ions are reduced to Fe^{2+} ions due to the presence of oxygen vacancies in x =0 sample. The double exchange interaction in Fe^{3+}– Fe^{2+} networks is likely to play a role for a non-zero value of M_r

and H_C for $x = 0$. The decrease in the values of M_r and H_C to almost zero for just 5 at.% of Sm substitution demonstrates the effect of Sm in controlling the Fe^{2+} concentration. The almost linear $M - H$ loops observed for $x = 0.05$ and 0.1 samples is due to the strong antiferromagnetic interaction among the Fe ions superimposed by the characteristic spiral spin structure. Ferromagnetic like behavior with a clear opening of $M - H$ loop is observed for samples with $x \geq 0.15$ along with a linear increase in M value at the higher applied field. The linear increase reveals the dominance of the strong antiferromagnetic interaction even for the higher doped samples. We estimated the remnant magnetization (M_r), magnetization at the highest magnitude of applied field ($M_{1.5T}$) and coercive field (H_C) for all samples and studied their variation with Sm concentration. Fig. 4.20 (*d*) shows the variation of these parameters at room temperature with Sm concentrations.

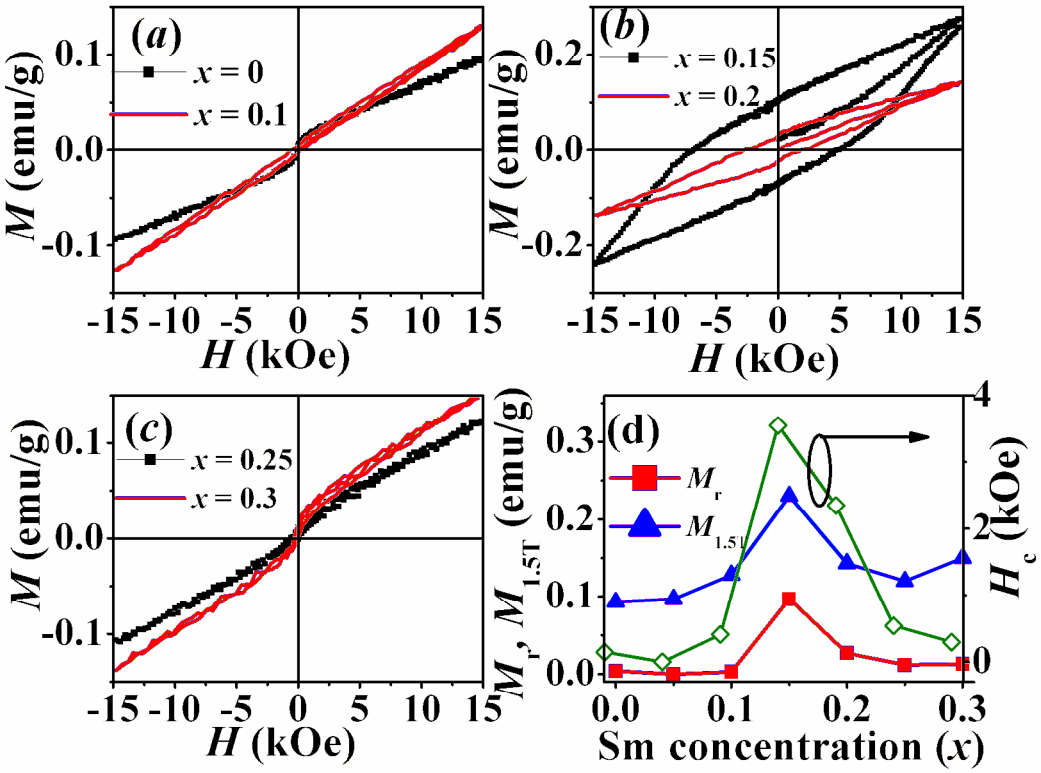

Figure 4.20 $M - H$ loops of $Bi_{1-x}Sm_xFeO_3$ samples with (*a*) $x = 0 - 0.1$, (*b*) $x = 0.15 - 0.2$ (*c*) $x = 0.25 - 0.3$ at room temperature. (*d*) Variation of M_r, $M_{1.5T}$ and H_C at 300 K with Sm concentration.

As can be seen from the Fig., M_r, $M_{1.5T}$, H_C values initially increases upto $x = 0.15$, and then decreases with further increase in Sm concentration. The maximum values of M_r, $M_{1.5T}$ and H_C are found to be $M_r \sim 0.097$ emu/g, $M_{1.5T} \sim 0.23$ emu/g and $H_C \sim 3.5$ kOe for $x = 0.15$ which decrease to $M_r \sim 0.027$ emu/g, $M_{1.5T} \sim 0.143$ emu/g and $H_C \sim 2.4$ kOe for $x = 0.2$ sample. However, the observed M_r and H_C values of present series of samples are much smaller than that reported in literature [145, 146]. It is reported that substitution of rare-earth ions in Bi sites suppresses the peculiar spiral spin structure, which is explained to be the main reason behind the enhancement of magnetization in many rare-earth doped $BiFeO_3$. This suppression will be more effective for higher concentrations of substituent and hence increase in M_r value is expected. Suresh *et al.* [145] attributed such a suppression of spiral spin structure enhances the M_r value to 0.274 emu/g for $Bi_{0.6}La_{0.4}FeO_3$ from almost zero value in $BiFeO_3$. Similar higher M_r value, which increases with increase in doping concentration, has been reported in Ho [146], Gd [79], Sm [150] doped $BiFeO_3$. But we have observed that the increasing trend of M_r with Sm concentration persists only upto $x = 0.15$, and it decreases for further increase in Sm concentrations. Moreover, the M_r values are very small compared to those reported in literatures [79, 145, 146, 150]. Although the spiral spin structure is effectively suppressed by Sm substitution so as to release the magnetization, the rather small M_r value of our samples can be attributed to the peculiar magnetic structure of *Pnma* phase. The Fe spins in orthoferrites like $SmFeO_3$ with *Pnma* space group take a collinear magnetic structure $\Gamma_2(G_zF_x)$ below 480 K [155]. As *Pnma* phase grows with increase in Sm concentrations in the present series of samples, collinear antiferromagnetic interaction in *Pnma* phase suppresses the weak ferromagnetism of the *R3c* phase. The deterioration of magnetization with further increase in Sm substitution concentrations beyond $x > 0.15$ is resulted from the evolution of collinear antiferromagnetism due to the structural transformation to *Pnma* phase.

Figure 4.21 shows the $M - H$ loops of $x = 0.15$ and 0.2 samples measured under field cooled condition with $H_{FC} = 5$ kOe. We have observed the shift of the FC $M - H$ loops along the negative field axis and it demonstrates the presence of exchange bias (EB) like behavior in these samples. We have estimated the value of EB field (H_{EB}) at different temperatures by using the relations $H_{EB} = (H_{C1} + H_{C2})/2$, where H_{C1} and H_{C2} represent magnetic field corresponding to $M = 0$ for the ascending and descending branches of $M - H$ loop

respectively. The temperature dependence of $|H_{EB}|$ for $x = 0.15$ and 0.2 samples are presented in Fig. 4.21 (*c*). For $x = 0.15$ sample, $|H_{EB}|$ increases with increase in temperature and reaches a maximum value of $|H_{EB}| \sim 1.36$ kOe at 150 K and it decreases with further increase in temperature. Similarly, we observe an increasing trend of $|H_{EB}|$ for $x = 0.2$ with temperature throughout the whole measured temperature range (50 – 300 K).

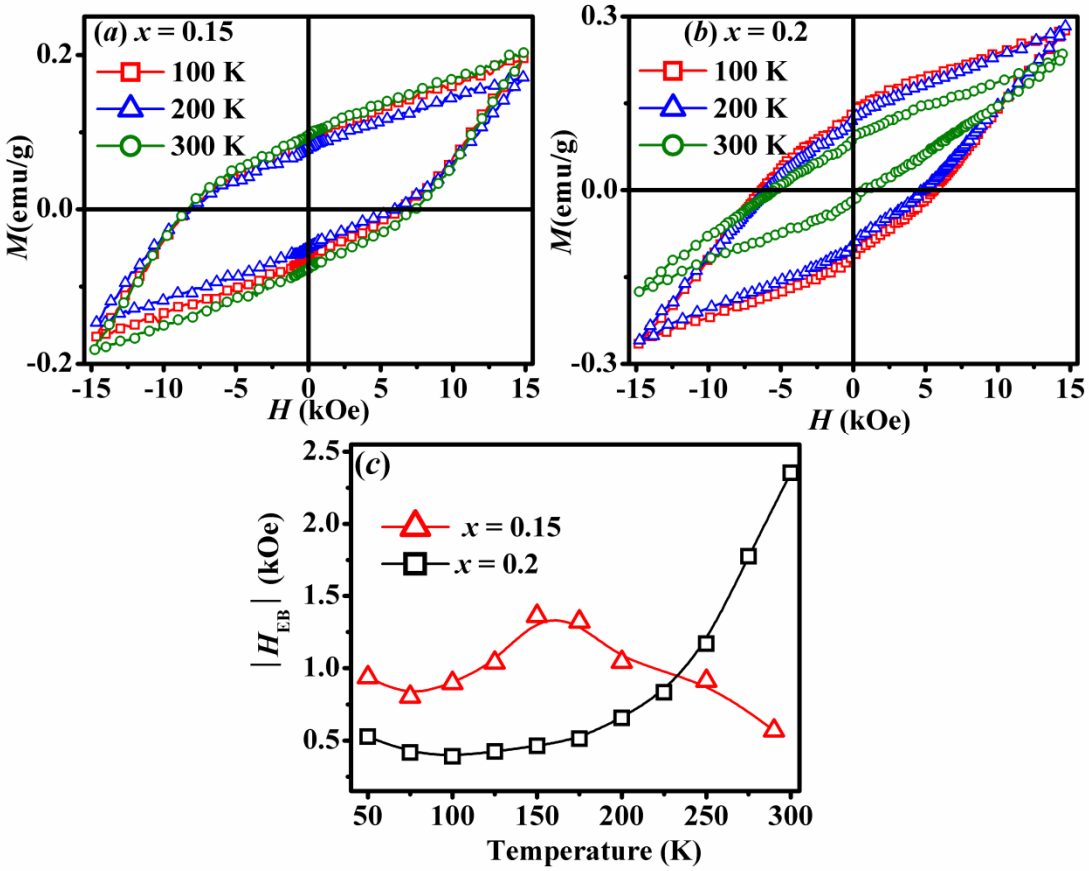

Figure 4.21 FC $M - H$ loops of $x = 0.15$ and 0.2 samples of $Bi_{1-x}Sm_xFeO_3$ at different temperatures. (*c*) Variation of $|H_{EB}|$ with temperatures.

It is very rare to explore the EB like behavior in bulk $BiFeO_3$, in particular the rare earth doped $BiFeO_3$. Very recently, Maity *et al.* [180] reported EB behavior in $BiFeO_3/Bi_2Fe_4O_9$ nanocomposite below 29 K. They attributed it to a local spin texture at the interface of ferromagnetic $Bi_2Fe_4O_9$ and antiferromagnetic $BiFeO_3$. Ahmmad *et al.* [181] reported exchange bias behavior in $Bi_{0.7}Ba_{0.3}Fe_{1-x}Ti_xO_3$ at room temperature which was explained in terms of the exchange interaction at the interface of ferri/ferromagnetic and antiferromagnetic domains. It is observed from the study of structural properties based on

analysis of XRD patterns that the samples $x = 0.15$ and 0.2 are biphasic in structure, *i.e.*, they contain rhombohedral ferroelectric *R3c* phase and orthorhombic non-ferroelectric *Pnma* phase. The detailed investigation on the Sm substitution effect in magnetization and the observed smaller value of M_r suggests that the non-ferroelectric *Pnma* phase which promotes the collinear antiferromagnetic interaction coexists with the weak ferromagnetic *R3c* phase in $x = 0.15$ and 0.2. The exchange interaction at the interface of collinear antiferromagnetic domains of *Pnma* phase and weak ferromagnetic domains of ferroelectric *R3c* phase contributes towards the observed exchange bias like behavior. The disappearance of exchange bias in $x = 0.25$ and 0.3 samples is attributed to its monophasic nature of structure.

4.7 Conclusion

In summary, we have studied the structural, dielectric and magnetic properties of $Bi_{1-x}Sm_xFeO_3$ ($x = 0 – 0.3$) ceramics prepared by sol-gel method. Substitution of Sm induces the structural phase transition from rhombohedral to orthorhombic cell. The structural phase transformation gives rise to reduction in dielectric strength ($\Delta\varepsilon$) as the Sm concentration is increased. The frequency dispersion of complex dielectric permittivity was explained in terms of polaron hopping within the grains and short range movement of oxygen vacancies across the grain boundaries based on the detailed analysis using Havriliak-Negami equation as well as by invoking the contribution of conductivity. The reduction in dielectric constant and its loss component with increase in Sm concentration is explained in terms of suppression of Fe^{2+} concentration induced by Sm^{3+} substitution and hence the decrease in undesired conductivity contributions. The relatively higher value of M_r and H_C for $x = 0.15$ was attributed to evolution of weak ferromagnetism due to partial breaking of spiral spin structure of rhombohedral $BiFeO_3$. However, due to growing collinear antiferromagnetism in *Pnma* phase for $x \geq 0.2$, magnetization decreases for $x \geq 0.2$. Interestingly, the coexistence of weak ferromagnetic *R3c* phase and collinear antiferromagnetic *Pnma* phase gives rise to exchange bias like behavior for $x = 0.15$ and 0.2.

Chapter 5

Fe doped $PbTiO_3$ series

$PbTiO_3$ (PTO) is a well known perovskite compound having a tetragonal structure with *P4mm* space group and it undergoes ferroelectric transition at T_C = 768 K [82, 83]. The ferroelectricity (FE) and hence the spontaneous polarization in this compound is mainly due to the stereo-chemical activity of lone electron pairs in Pb^{2+} ions [63]. The renewed interest in PTO is due to its potential application as a multiferroic material. The industrial demand for device functionality is a functional single phase multiferroic material at room temperature with a strong coupling between their ferroelectric and ferromagnetic (FM) order parameters such that they can be easily manipulated either by electric or magnetic field [182]. Hence once the above functional property is realized, multiferroics can serve in the field of spintronics, data storage, read heads, multi-state memory devices, *etc*. However, there are very few known single phase materials exhibiting multiferroism. Among these, $BiFeO_3$ is the most widely and extensively studied multiferroic material having antiferromagnetism (T_N ~ 640 K) as well as ferroelectricity (T_C ~ 1100 K) at room temperature. The major problem with $BiFeO_3$ is the large leakage current, which makes the electric polarization unstable and reduces its value. Moreover, the peculiar space modulated spiral spin structure of its magnetic moments locks its magnetization and allows practically no magneto-electric coupling. Hence, the researchers continue to look for other single phase multiferroics at room temperature.

The ferroelectric compounds like PTO and $BaTiO_3$ (BTO) do not exhibit any ferromagnetic behavior due to the lack of partially filled *d*-orbital in Ti^{4+} ions and they are found to be mostly in diamagnetic. However, the first-principle calculations based on spin-density-functional theory reveals that Ti and O vacancy induce FM in PTO [183]. Zhang *et al*. [84] have experimentally demonstrated the O-vacancy mediated FM in PTO nanocrystals. Hence over the years, a few studies are focused on the development of room temperature FM in BTO and PTO by substituting magnetic transition elements (TM) in place of Ti. Palker *et al.* [86] reported FM in $Pb(Fe_{0.5}Ti_{0.5})O_3$ at room temperature with a saturation magnetization (M_S) value of 0.5 μ_B/f.u along with a magneto-electric coupling. Ren *et al*. [85] observed room temperature FM in Fe doped PTO nanocrystals with a typical M_S value of 0.8×10^{-3} emu/g. Such a low M_S value is believed to be originated from the O vacancy and is explained in terms of the exchange interaction among Fe^{3+} ions through the trapped electrons in the bridging oxygen ions (*F*-center). Similar *F*-center induced FM in Fe^{3+}–$V^{\bullet\bullet}_O$ – Fe^{3+} networks with a maximum M_S value of 41.6×10^{-3} emu/g was reported in Fe doped PTO nanocrystals, where $V^{\bullet\bullet}_O$ refers oxygen vacancy [87].

It is very challenging to induce FM in perovskites like BTO, PTO by substituting magnetic TM ions like Fe, Mn, Co *etc.* at Ti site and at the same time keeping their FE intact. From the fundamental point of view, the coexistence of FE and FM presents an interesting challenge since the conventional mechanism of FE in perovskites requires *B* sites (Ti^{4+} in BTO, PTO) with empty *d* orbitals and it is incompatible to magnetism [184]. Moreover, achieving a strong magneto-electric coupling is quite difficult as many potential multiferroic candidates are not insulator and hence they cannot sustain the electric field necessary to switch the polarization. So, the alternate technique is the measurement of dielectric constant as a function of magnetic field [185]. Here in addition to magneto-electric coupling other extrinsic factors such as grain boundaries and electrode effect contribute to the dielectric constant [185]. In polycrystalline samples, the transport properties strongly depend on their microstructural heterogeneity such as grains (G), grain boundaries (GB), surface layers (SL) etc. In order to distinguish between the G and GB contributions, to understand the microscopic process of dielectric relaxation and the long range conductivity processes, the impedance spectroscopy has been widely used. In the present work, we have taken up a

systematic study of structural, magnetic and impedance spectroscopy properties of Fe substituted $PbTiO_3$ compounds.

5.1 Sample Preparation and Characterization

$PbTi_{1-x}Fe_xO_3$ (PTFO) (x = 0 – 0.3) ceramics were prepared using solid state reaction method. Stoichiometric amounts of $Pb(NO_3)_2$, TiO_2 and Fe_2O_3 (purity > 99%) were weighed and grinded using agate mortar and pestle under acetone medium for about 1 h. The above uniform mixture was presintered at 873 K for 36 h with intermediate grinding after every 12 h after furnace cooling to room temperature. The presintered powders were pressed into cylindrical pellets of approximately 12 mm diameter and 2 mm of thickness at a pressure of 2.94×10^8 N/m^2 by using a hydraulic press. The final sintering was carried out at 1373 K for 18 h in air atmosphere with a heating rate of 4 K/min followed by furnace cooling to room temperature. X-ray diffraction (XRD) patterns were recorded by using a Rigaku make TTRAXIII high power X-ray diffractomerter by employing Cu-K_α radiation (λ = 1.54056 Å). These patterns were refined with the help of Rietveld method using FULLPROF software. Raman spectra at room temperature were obtained by using micro-Raman spectrometer (LabRam HR800, Jobin Yvon) in the wave number range of 100 to 800 cm^{-1} with an excitation wavelength of 514 nm. The microstructure of the samples was studied by recording FE-SEM images by using ZEISS make field effect scanning electron microscope (ΣIGMA) equipped with EDS facility. Room temperature electron paramagnetic resonance (EPR) measurement was carried out in powder form using JEOL Spectrometer (JES-FA200) operating at X-band frequency (ν = 9.4 GHz). Temperature and field variations of magnetization measurements were carried out using a vibrating sample magnetometer (Lakeshore, model 7410) in the temperature range of 300 K – 900 K. The frequency dependent dielectric measurements at several temperatures (300 K – 573 K) over a frequency range of 10^2 – 10^6 Hz with an ac voltage of 1.0 V_{rms} were carried out using an LCR meter (Wayne Kerr, model 1J43100). For the electrical characterizations, electrodes were fabricated by painting silver pastes on both sides of the sample of typical thickness 1 to 1.5 mm. These samples were fired at 423 K in air for 2 h and furnace cooled to room temperature before carrying out the electrical measurements.

5.2 Structural Properties

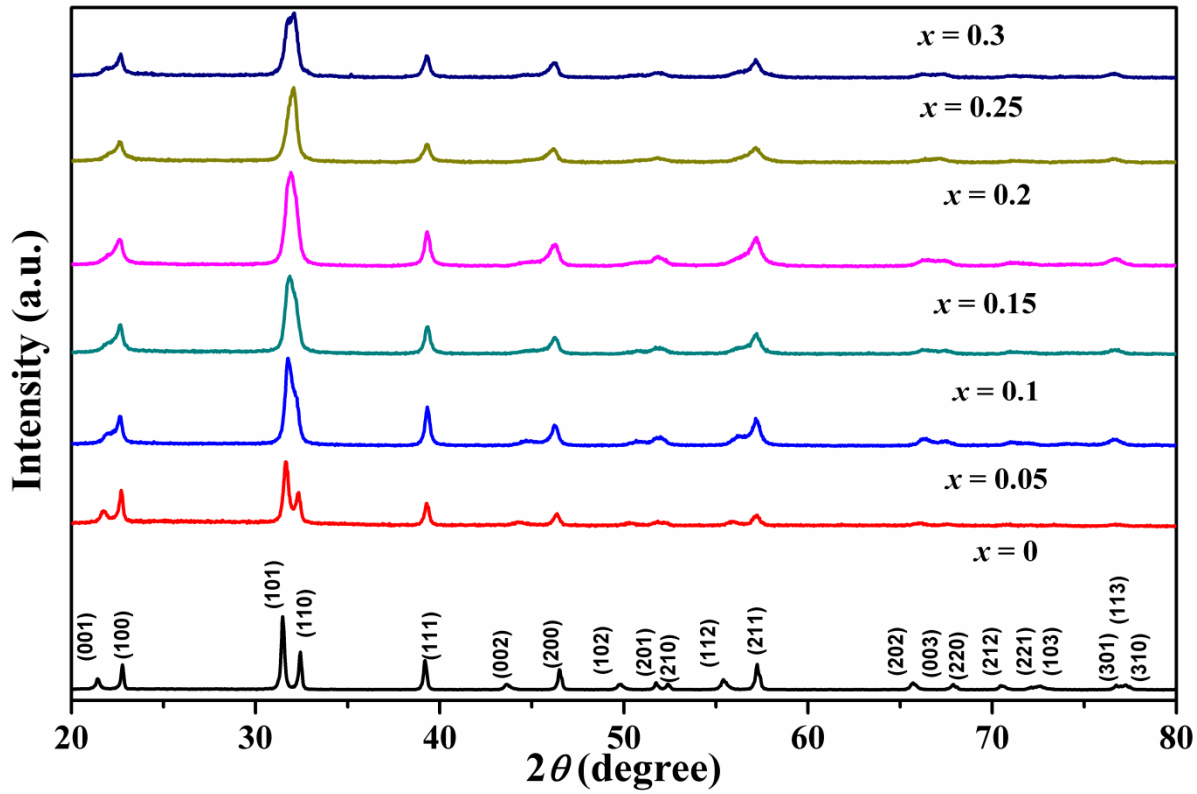

Figure 5.1 XRD patterns of $PbTi_{1-x}Fe_xO_3$ (x = 0 – 0.3) samples.

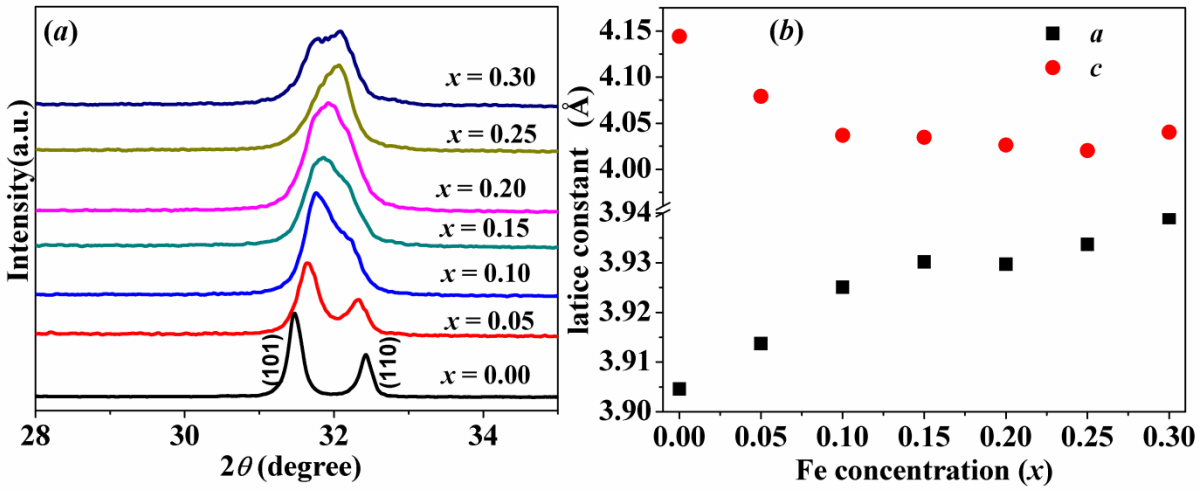

Figure 5.2 (*a*) Expanded view of (101) and (111) peaks of XRD patterns of $PbTi_{1-x}Fe_xO_3$ (x = 0 – 0.3) samples, (*b*) variation of lattice constant *a* and *c* with Fe concentration.

Fig. 5.1 shows the XRD patterns of $PbTi_{1-x}Fe_xO_3$ for x = 0 – 0.3. The samples are found to be in single phase form. The enlarged view of XRD patterns in the vicinity of (101) and (110) peaks are shown in Fig. 5.2 (*a*) where we can see the gradual merging of these peaks into a single peak as the Fe concentration is increased. It highlights the decrease of tetragonality and the tendency towards the cubic phase formation with increase in x values; however, no complete transition into cubic phase is seen. The XRD patterns of all samples are refined by choosing *P4mm* space group in tetragonal unit cell. The typical XRD patterns along with Rietveld refinement for x = 0, 0.10, 0.20 and 0.30 samples are shown in Fig. 5.3 and 5.4.

The parameters obtained from the Rietveld refinement of XRD patterns of $PbTi_{1-x}Fe_xO_3$ (x = 0 – 0.3) are tabulated in Table 5.1. Lattice constant a increases and c decreases with increase in Fe concentration as shown in Fig. 5.2 (*b*). The decrease in c value can be understood in terms of coordinated counter effect of expansion of the cell along *ab* plane. The observed variation of lattice constant with Fe concentration is similar to that reported in literature for Fe doped $BaTiO_3$ and is attributed to the larger ionic radius of Fe^{3+} ions (0.645Å) substituting Ti^{4+} ions (0.605Å) [186]. Moreover, we see a change of slope for $x \geq 0.15$, where the variation has slowed down and this can be explained by considering the mixed valency of Fe ions and the evolution of cubic phase. Guo *et al*. [186] reported the presence of Fe ions in the mixed valence state of Fe^{3+} and Fe^{4+} from the X-ray photoelectron spectroscopy (XPS) study of Fe doped BTO whose structure is similar to that of PTO. Such mixed valent Fe ions are expected to be present in Fe substituted PTO. As the ionic radius of Fe^{4+} ions (0.585 Å) in octahedral co-ordination is less than that of Ti^{4+} (0.605 Å), some of the substituted Fe elements in Fe^{4+} state is expected to counter the increase in lattice parameter arising out of Fe^{3+} substitution at Ti^{4+} site. For $x \leq 0.15$, the substituted Fe ions are predominantly in Fe^{3+} state and hence a considerable increase in a values are observed. Further increase in Fe concentration beyond x = 0.15 is expected to increase the concentration of Fe^{4+} ions, but not dominating over the concentrations of Fe^{3+} ions and as a result the variation of lattice parameters with x is slowed down.

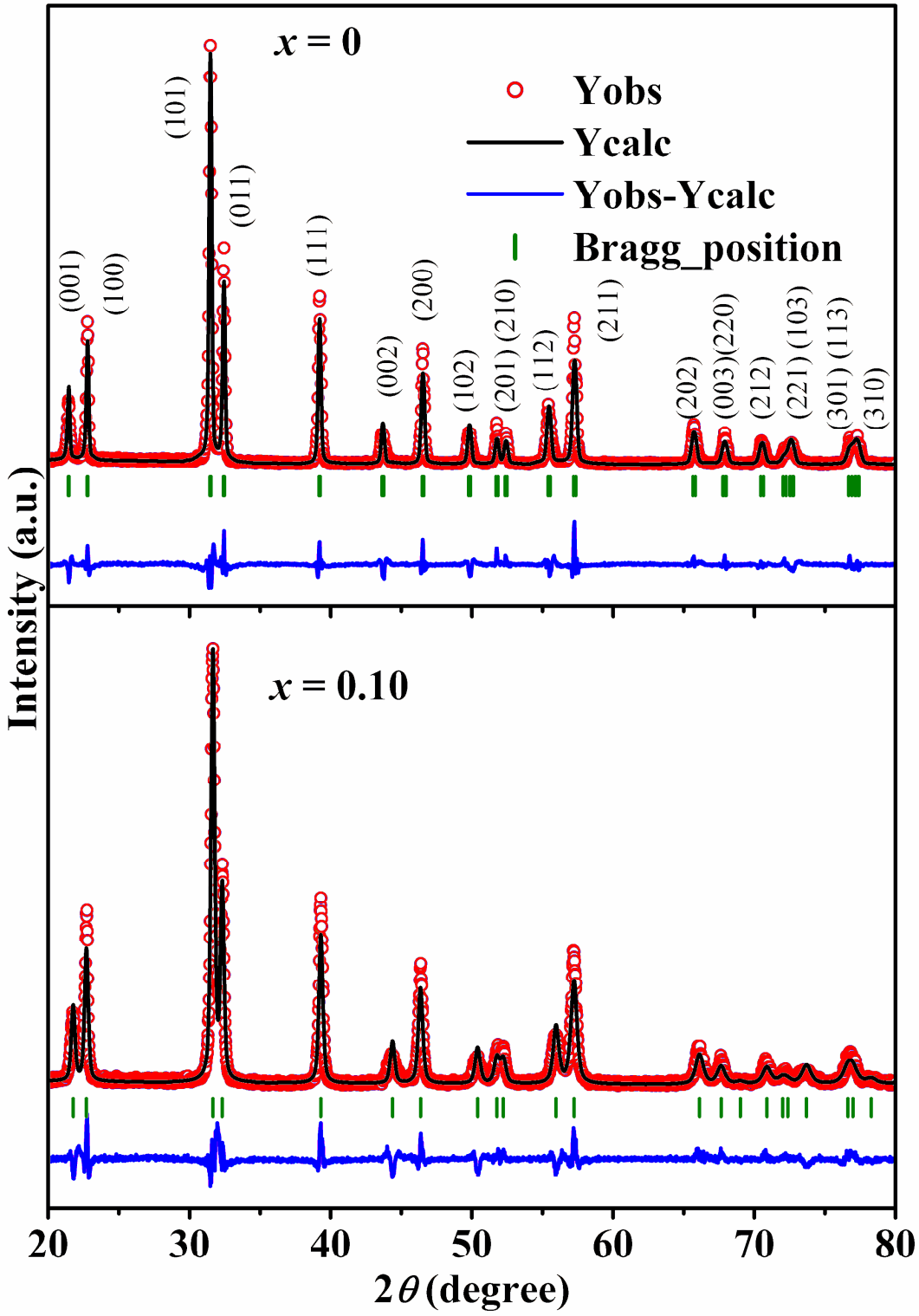

Figure 5.3 XRD patterns along with Rietveld refinements for $PbTi_{1-x}Fe_xO_3$ samples with $x = 0$ and 0.10.

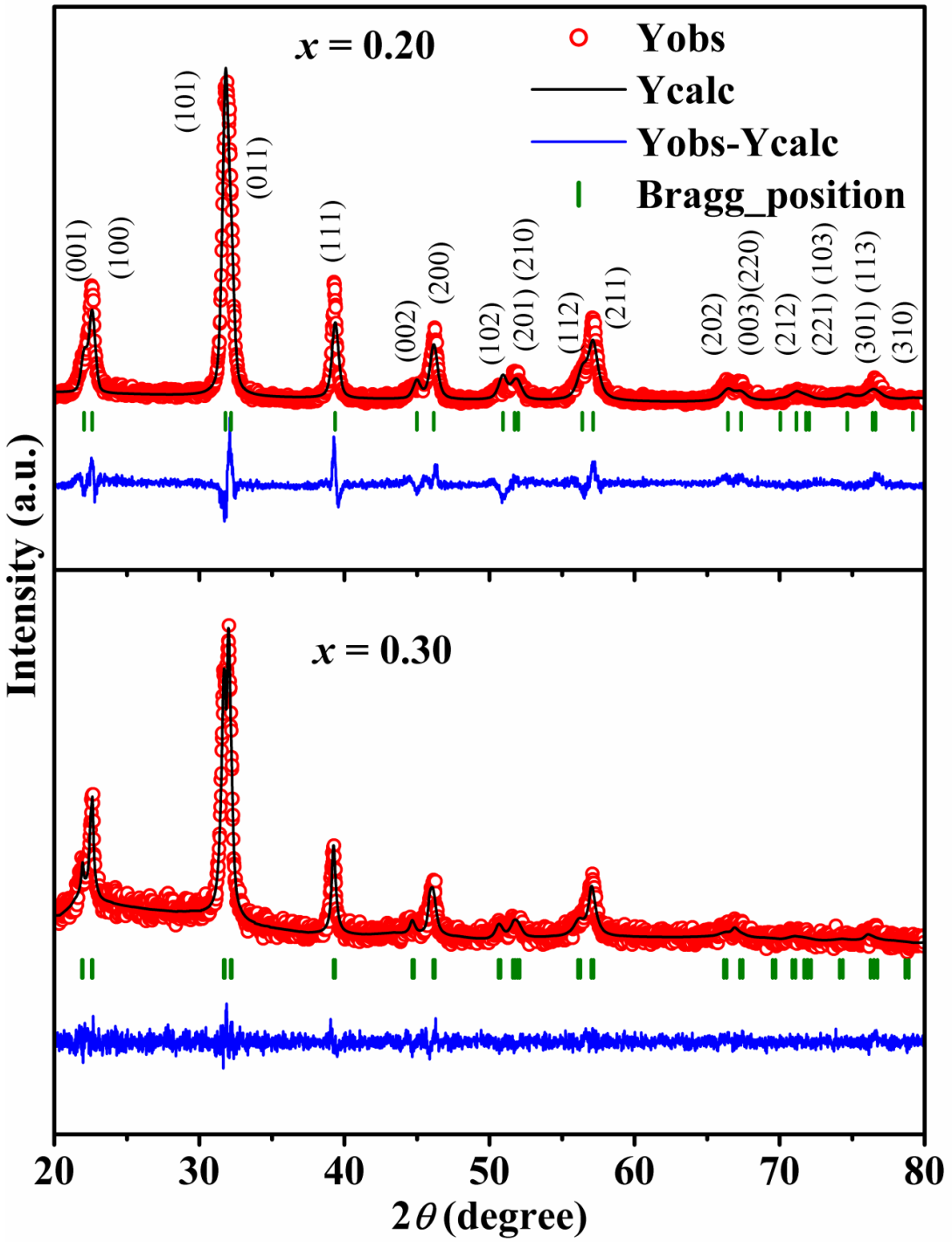

Figure 5.4 XRD patterns along with Rietveld refinements for $PbTi_{1-x}Fe_xO_3$ samples with x = 0.20 and 0.30.

Table 5.1 Parameters obtained from the Rietveld refinement of XRD patterns of $PbTi_{1-x}Fe_xO_3$ (x = 0 – 0.3) samples. R_f, R_{Bragg}, R_P and χ^2 are the reliability factors (* SG: Space group).

	Samples (x)						
Parameters	0	0.05	0.10	0.15	0.20	0.25	0.30
SG*	*P4mm*	*P4mm*	*P4mm*	*P4mm*	*P4mm*	*P4mm*	*P4mm*
$a = b$ (Å)	3.9046	3.9137	3.9251	3.9302	3.9297	3.9337	3.9391
c (Å)	4.1442	4.0791	4.0369	4.0346	4.0264	4.0202	4.0402
V (Å^3)	63.18	62.48	62.19	62.32	62.17	62.20	62.68
R_f (%)	1.68	3.33	3.67	3.85	4.32	3.35	3.08
R_{Bragg}(%)	3.21	4.51	4.99	3.84	3.96	3.17	3.04
R_P (%)	9.78	9.8	8.6	8.8	9.8	9.1	9.6
χ^2	6.33	5.2	4.42	6.3	5.7	4.5	4.00

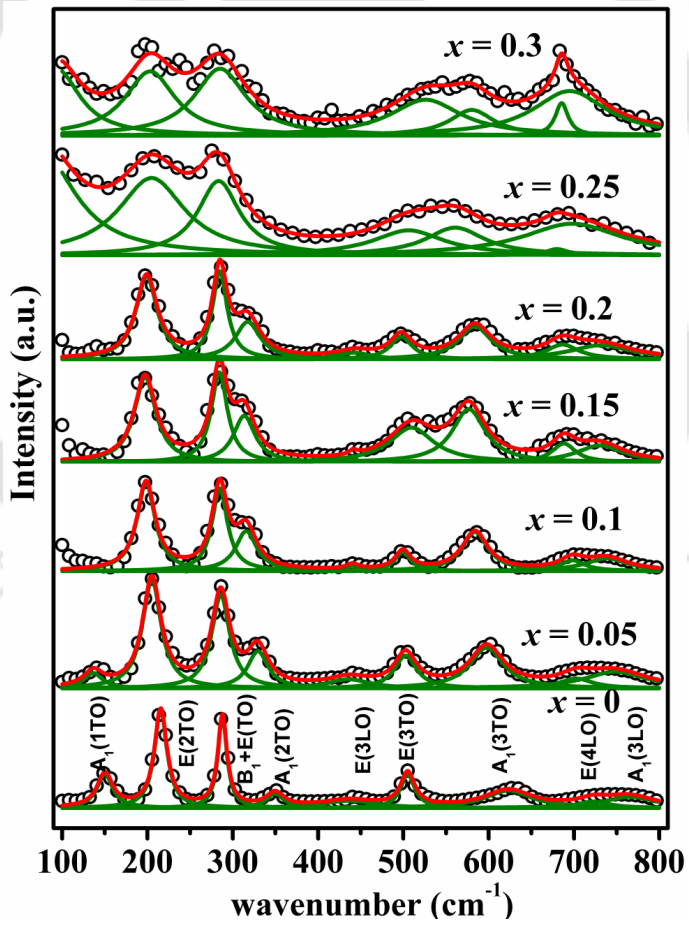

Figure 5.5 Raman scattering spectra recorded at room temperature, together with their fitted spectra (red line) and the decomposed active modes (olive green line) for $PbTi_{1-x}Fe_xO_3$ (x = 0 – 0.3) samples.

The room temperature Raman spectra of $PbTi_{1-x}Fe_xO_3$ (x = 0 – 0.3) compounds are presented in Fig. 5.5, along with the fitted spectra. Fourteen Raman active modes have been reported for PTO [187] and here we have observed nine modes in the wave number range of 100-800 cm^{-1}. The presence of E (2TO), B_1+E, E (3TO), A_1 (3TO), E (4LO) and A_1 (3LO) modes indicates the dominance of tetragonal phase in all samples and is consistent with Rietveld analysis of XRD patterns. The A_1 modes consist of the displacements of Ti ions along the c axis relative to O ions and Pb ions while E modes correspond to the displacement of Ti ions along a or b axis and the B_1 modes represent the displacement of O ions along the c axis [188].

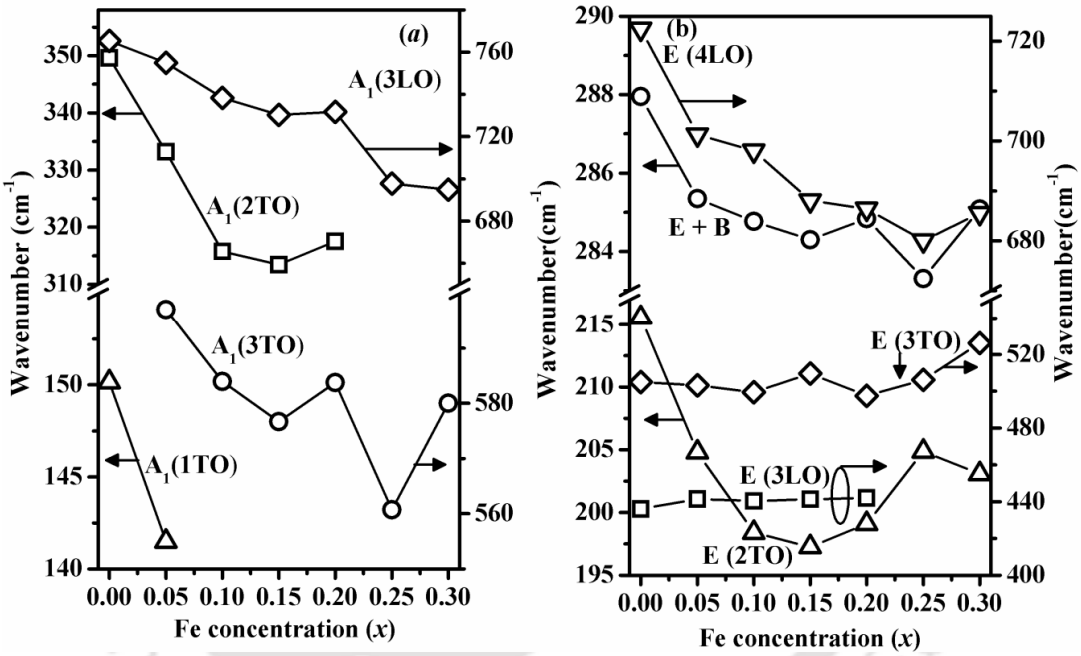

Figure 5.6 Variations of peak position of (*a*) A_1 Raman modes (*b*) E Raman modes of $PbTi_{1-x}Fe_xO_3$ (x = 0 – 0.3) samples with Fe concentration.

The variation of Raman peak position as a function of Fe concentration as shown in Fig. 5.6 (*a*) demonstrates that A_1 modes are red-shifted with increase in Fe concentration. It is attributed to the decrease in lattice parameter c which has a strong effect on the vibration of Ti ions along c-axis. The red shift in A_1 modes is similar to that observed in system undergoing structural transition from tetragonal to cubic phase with change in temperature [188] and justifies the gradual evolution of cubic phase due to Fe doping. Similar to A_1 modes, E (4LO) and E + B modes are also red shifted due to Fe doping (Fig. 5.6 (*b*)). On the contrary, E (2TO) mode is found to be first red-shifted for x

≤ 0.1, after that it shifts towards the higher wave number on further increase in Fe concentration as shown in Fig. 5.6 (*b*). The *E* (2TO) and A_1 (2TO) modes for $x \geq 0.15$ moves towards each other. Similar change in *E* (3TO) and A_1 (3TO) modes are observed. It is shown in Fig. 5.7 in terms of the decrease in $|k_{A1(2TO)} - k_{E(2TO)}|$ (= Δ (2TO)) and $|k_{A1(3TO)} - k_{E(3TO)}|$ (= Δ (3TO)) with Fe concentration, where $k_{A1(2TO)}$, $k_{E(2TO)}$, $k_{A1(3TO)}$ and $k_{E(3TO)}$ represent the wave numbers corresponding to the Raman modes denoted by their subscripts. Such behavior of *E* (TO) and A_1 (TO) modes reveal the lattice transformation from tetragonal to cubic phase [188]. However, *E* (TO) and A_1 (TO) Raman modes are still away from each other, which indicates that the complete structural phase transformation is not yet achieved.

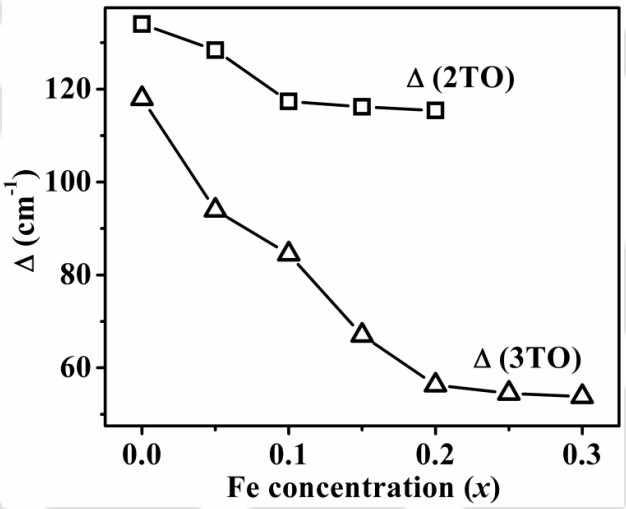

Figure 5.7 Variation of difference (Δ) in A_1 (2TO) and *E* (2TO) modes, and A_1 (3TO) and *E* (3TO) modes with Fe concentration.

The surface morphologies of the samples are studied by recording the FE-SEM micrographs at room temperatures. Typical FE-SEM images for $x = 0$, 0.10, 0.20 and 0.30 samples of $PbTi_{1-x}Fe_xO_3$ along with the EDS spectra for $x = 0$ and 0.2 samples are shown in Fig. 5.8. Well defined grains having irregular shapes are observed for $x = 0$ sample. The average size of the grains for $x = 0$ sample is estimated to be 480 nm. For Fe doped samples, the grains seem to grow abnormally and possess no specific shape. It is observed that tiny grains having a few nm of dimensions agglomerate locally to form extended regions in the doped samples. Such agglomeration increases the porosity of the samples. The EDS spectra of $x = 0$ and 0.2 samples are shown in Fig. 5.8 (*e*) and (*f*) respectively. Their cationic ratio Pb: Ti: Fe values are found to be 1.08: 0.98: 0 and 1.01: 0.81: 0.19 for

x = 0 and 0.2 samples respectively and they are comparable to the nominal starting compositions.

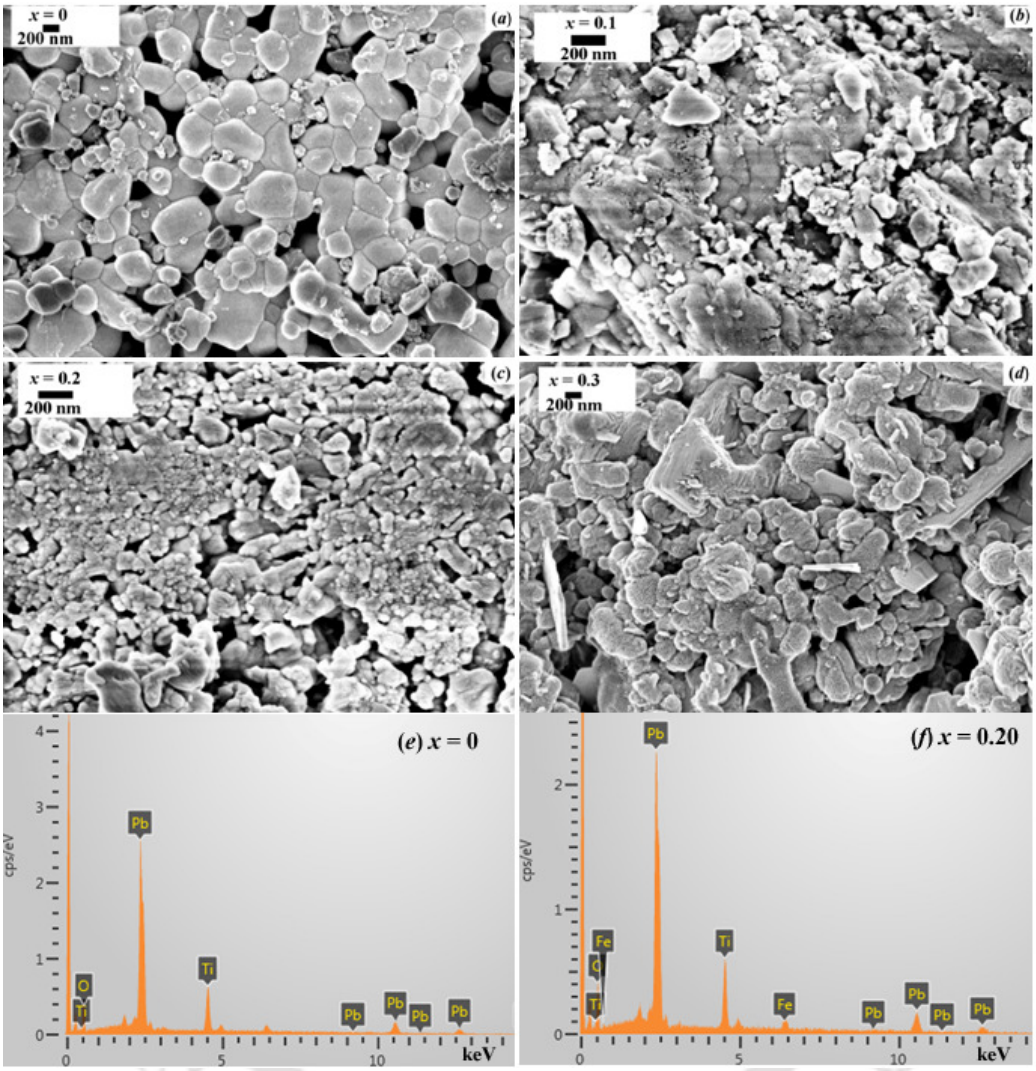

Figure 5.8 FE-SEM images for x = 0, 0.1, 0.2 and 0.3 samples of $PbTi_{1-x}Fe_xO_3$ along with the EDS spectra for (*e*) x = 0 and (*f*) x = 0.2 samples.

5.3 Complex Impedance and Electric Modulus

Fig. 5.9 shows the frequency variation of Z' of $PbTi_{1-x}Fe_xO_3$ samples with x = 0.25 and 0.3 at different temperatures. The overall value of Z' at a particular temperature decreases with the increase in frequency with the formation of plateau. The impedance response of a sample arises due to motion of charge carriers at the intragrain, intergrain regions and material-electrode interface. There are various ways of charge carrier movement such as long-range/short-range displacement, dipole reorientation and via the

formation of space charges *etc.*, and they govern the frequency dependence of Z'. The appearance of plateau-like regions in Z' spectra followed by its sharp fall with increase in frequency reveal the relaxation process in the samples. The Z' value for a particular composition decreases with increase in temperature in the range 373 K – 553 K, which suggests that the material possesses the negative temperature coefficient of resistance (NTCR). On the other hand, it is observed from the insets of Fig. 5.9 (*a*) and (*b*) that the Z' values of $x = 0.25$ and 0.3 samples follow an opposite trend and increases with increase in temperature for temperature $T < 373$ K. The increase in the value of Z' with increase in temperature reveals the positive temperature coefficient of resistance of the sample $x = 0.25$ and 0.3. The effect of increasing Fe concentration is observed in terms of the decrease in the value of Z'.

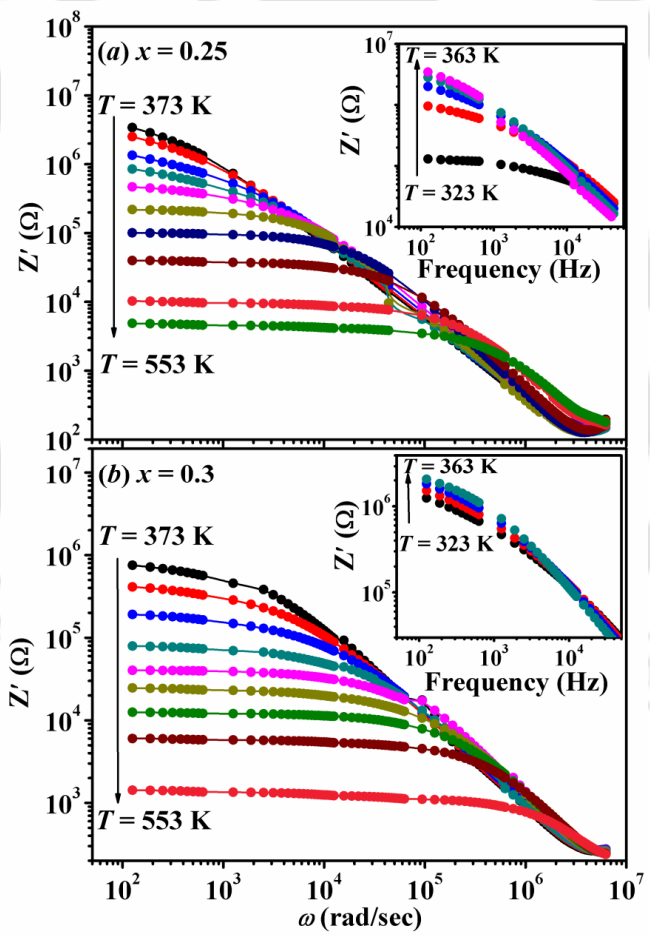

Figure 5.9 Frequency variation of Z' of $PbTi_{1-x}Fe_xO_3$samples with (*a*) $x = 0.25$ and (*b*) $x = 0.3$ in the temperature range 373 K – 553 K. Insets of (*a*) and (*b*) show the frequency variation of Z' of corresponding samples in the range 323 K – 363 K.

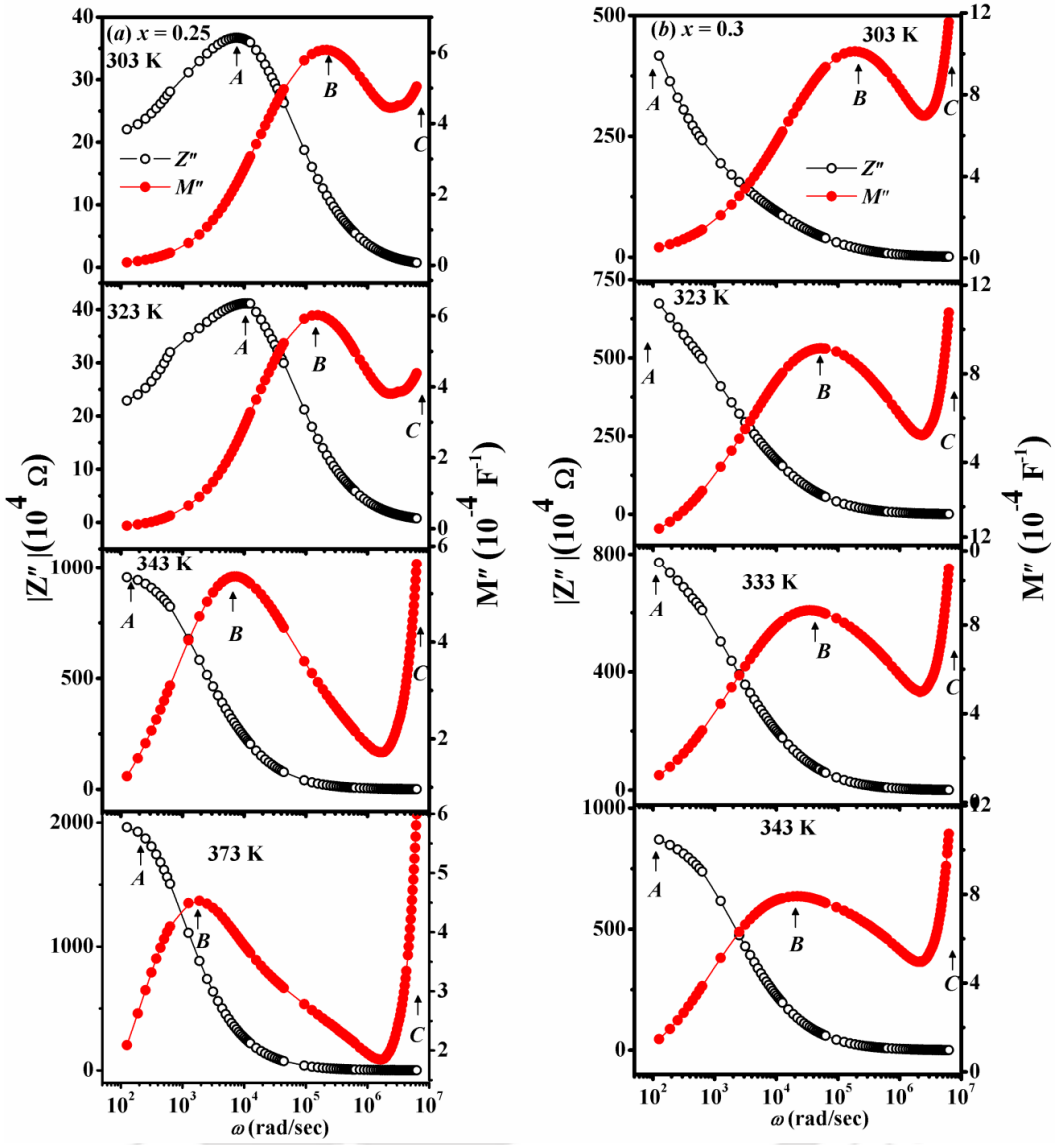

Figure 5.10 Frequency variations of Z'' and M'' for (*a*) x = 0.25 and (*b*) x = 0.3 samples of $PbTi_{1-x}Fe_xO_3$.

In order to further elucidate the PTCR behavior, we have plotted the Z'' and M'' as a function of ω for x = 0.25 and 0.3 samples in Fig. 5.10 at different temperatures. The Z'' spectra show a single relaxation peak (*A*) throughout the temperature range, while M'' plots show a relaxation peak (*B*) along with a high frequency incline. The Z'', M'' relaxation peaks and the high frequency inclination in M'' confirm that at least three electroactive regions contribute to relaxation. The approximate value of resistance (*R*) and capacitance (*C*) of such electroactive regions can be scaled from the maximum value of M'' and Z'' using the relations: $Z''_{max} = R/2$, $M''_{max} = \varepsilon_0/2C$ and ωRC = 1, where ε_0 is the

permittivity of free space and ω is peak frequency. The capacitance value, so obtained, identifies the Z'' peak to be due to grain boundaries, while the M'' peak is attributed to surface layers on individual grains. The capacitance value corresponding to the high frequency inclination could not be calculated as the peak maximum is out of the measured frequency range and is attributed to the grains. The most interesting feature observed in Fig. 5.10 is the shift of Z'', M'' peaks towards lower frequency with increase in temperature. Such shift of Z'', M'' peaks towards lower frequency for x = 0.25 was observed upto T = 373 K, while similar shift for x = 0.3 was observed upto T = 353 K. This downward shift of Z'', M'' peaks towards the lower frequency values is unusual as the relaxation dynamics in general is a thermally activated process and follows the Arrhenius type of temperature dependence. Such unusual shift in Z'' and M'' peaks along with the observed increase in Z' value (see insets of Fig. 5.9) with increase in temperature in the range 300 K – 373 K is the signature of positive temperature coefficient of resistance (PTCR). The downward shift of Z'' and M'' peaks is similar to that observed in many ceramic samples showing PTCR effect [189, 190]. Beyond T = 373 K for x = 0.25, Z' value decreases and the Z'' and M'' peaks shift towards higher frequencies with increase in temperature which is the characteristics feature of negative temperature coefficient of resistance (NTCR) of sample. The NTCR region for x = 0.30 starts from T = 353 K.

The variations of Z'' and M'' as a function of frequency at different temperatures in the NTCR region are shown in Fig. 5.11 for x = 0.25 and 0.3 samples. The Z'' and M'' peaks in both PTCR and NTCR regions are broad and not symmetric in the frequency axis. It signifies the magnitude of the slopes of Z'' and M'' variations above and below the peak frequency is not equal which reveals that the underlying relaxation process is not Debye type. For an ideal Debye relaxation, the values of slopes above and below the peak frequency must be same and the Z'' curves must be symmetric in frequency domain about the peak frequency. Such asymmetry in the Z'' and M'' in time domain can be parameterized by the Kohlrausch-Williams-Watts (KWW) decay function Φ (t) [191]:

$$\phi(t) = e^{-\left(\frac{t}{\tau}\right)^{\beta}}, \qquad 0 < \beta \leq 1 \tag{5.1}$$

The frequency domain representation of KWW function in terms of dielectric susceptibility function χ'' (M'', Z'', ε'') can be written as [36]:

$$\chi''(\omega) = \frac{\chi''_{max}(\omega)}{\frac{(1-|n-m|)}{n+m}\left(m\left(\frac{\omega}{\omega_{max}}\right)^{-n} + n\left(\frac{\omega}{\omega_{max}}\right)^{m}\right) + |n-m|} \quad (5.2)$$

where χ''_{max} is peak maximum of imaginary part (χ'') of complex susceptibility and ω_{max} is the corresponding peak frequency. The parameters n and m are the stretching parameters ($0 < n \leq 1$, $0 < m \leq 1$) at low and high frequency regions respectively *i.e.*, below and above the peak frequency.

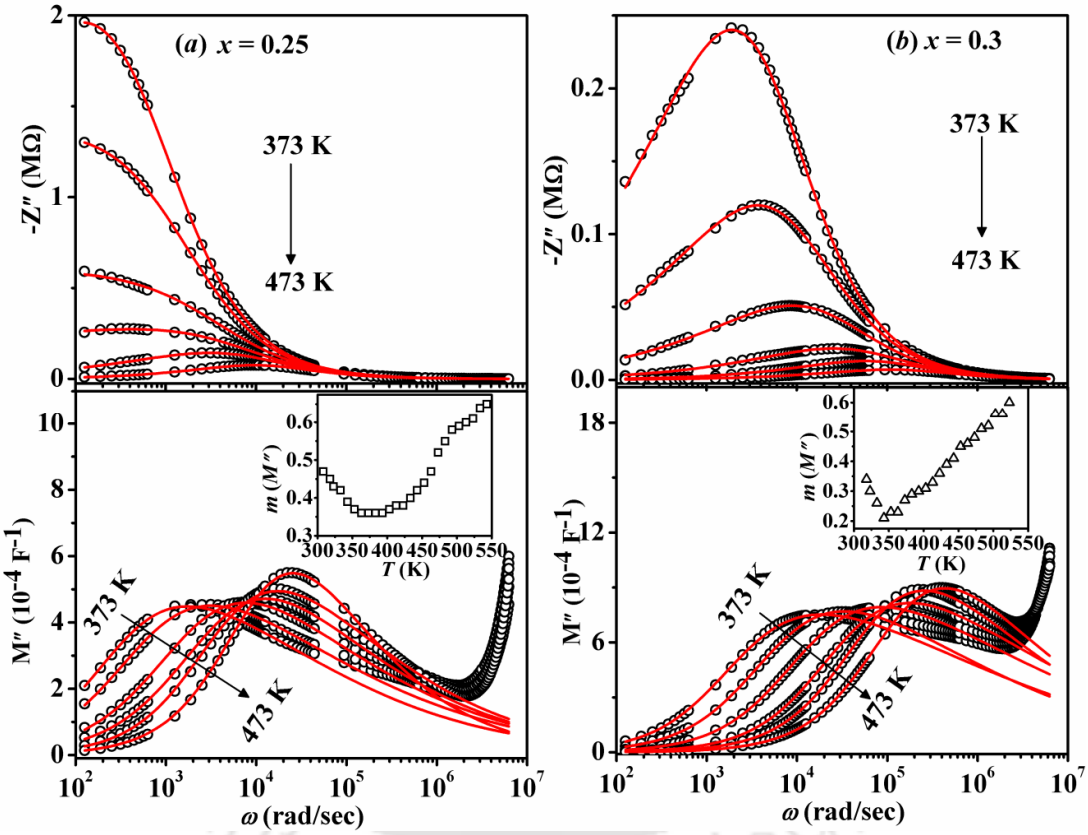

Figure 5.11 Frequency variations of Z'' and M'' of $PbTi_{1-x}Fe_xO_3$ samples with (*a*) $x = 0.25$ and (*b*) $x = 0.30$ at different temperatures. The solid lines are the fitted data to eq. (5.2). Insets show the variations of m (M'') with temperatures.

The experimental Z'' and M'' data are fitted to Bergman equation (eq. 5.2) and the fitted data are shown as solid lines in Fig. 5.11. The fitted data closely follow the experimental data. The parameters n obtained from the fit of M'' data *i.e.*, n (M'') are in the range 0.48 – 1 and 0.53 – 1 for $x = 0.25$ and 0.30 respectively and they increase with increase in temperature. Interestingly, a significant difference in the temperature

dependence of the parameters m (M'') is observed as shown in the insets of Fig. 5.11 (*a*) and (*b*) for x = 0.25 and 0.3 samples respectively, which present distinct variations in the PTCR and NTCR region. In the PTCR region of x = 0.25 sample, *i.e.*, in the temperature range 308 K – 363 K, the value of $m(M'')$ decreases from 0.47 to 0.36. As the temperature is raised further, its value increases in the NTCR region with increase in temperature and are found to be in the range of 0.37 – 0.64. Similarly, $m(M'')$ of x = 0.3 sample decreases from 0.34 to 0.21 in its PTCR region, and increases from 0.23 to 0.60 in the NTCR regions.

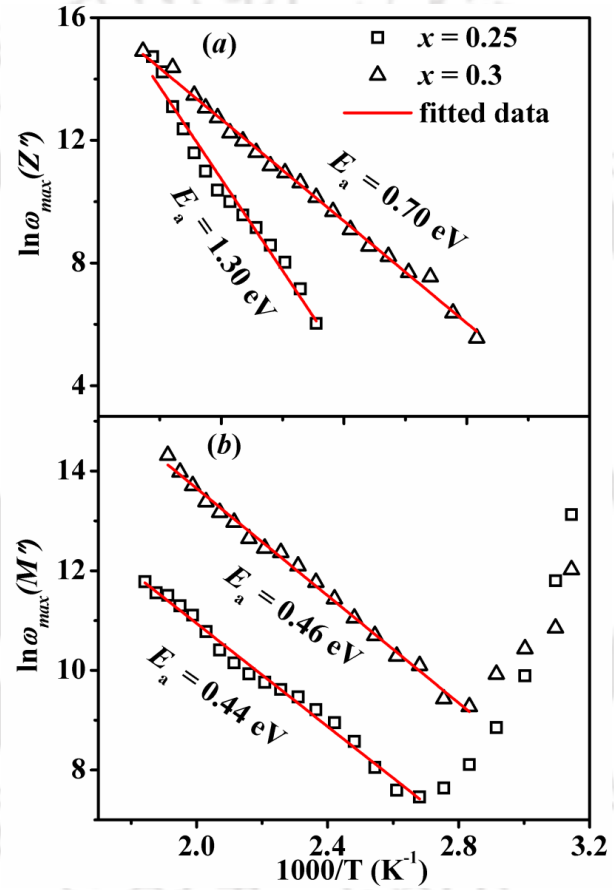

Figure 5.12 Arrhenius plots of (*a*) $\omega_{max}(Z'')$ and (*b*) $\omega_{max}(M'')$ of $PbTi_{1-x}Fe_xO_3$ samples with x = 0.25 and 0.3. The fitted data to eq. (5.3) are shown in solid lines.

The peak frequency in the NTCR region follows the Arrhenius law:

$$\omega_{max} = \omega_0 \exp\left(-E_a / k_B T\right) \tag{5.3}$$

where E_a is the activation energy required for relaxation and ω_0 are the pre-exponential factors. Fig. 5.12 shows $\ln(\omega_{max})$ of $x = 0.25$ and 0.3 plotted against 1000/T corresponding to ω_{max} of Z'' and M'' peaks. The fitted data in terms of Arrhenius law are shown as solid lines. The estimated E_a values corresponding to Z'' peaks are found to be 1.3 eV and 0.7 eV respectively. The estimated E_a values corresponding to M'' peaks for $x = 0.25$ and 0.30 samples are found to be 0.44 and 0.43 eV respectively.

5.3.1 Nyquist Plots

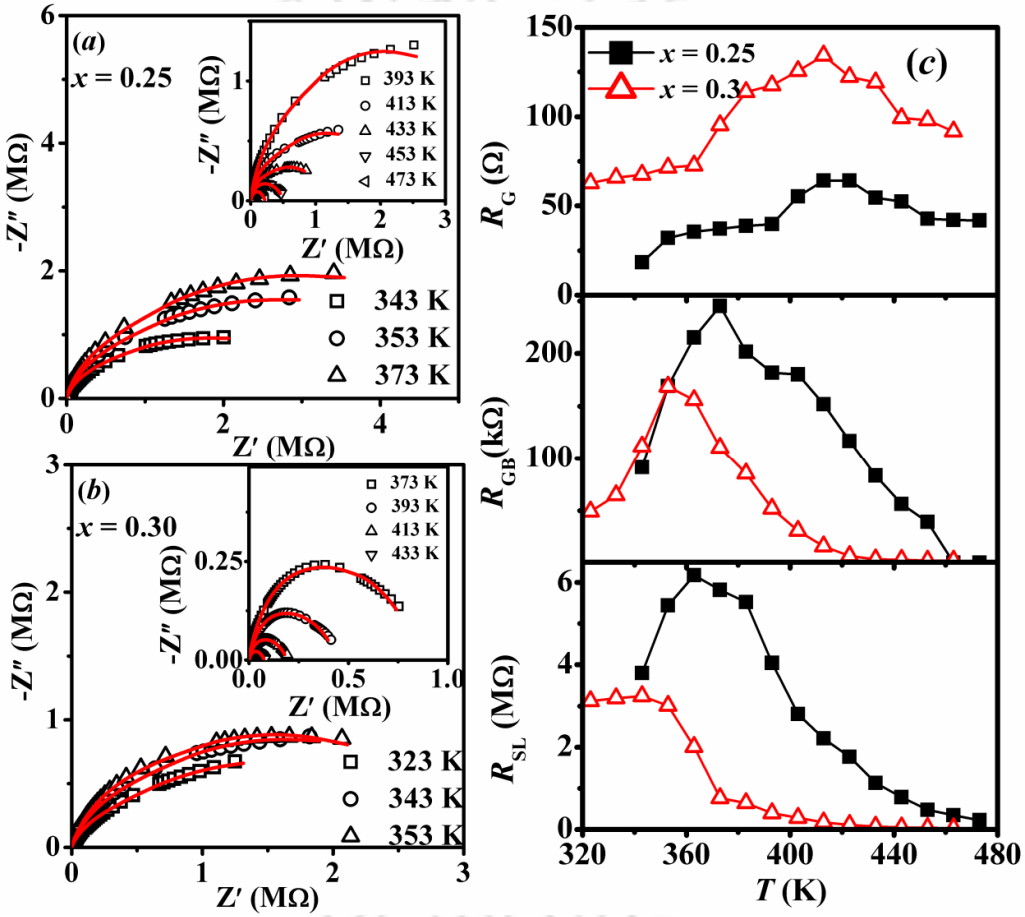

Figure 5.13 Nyquist plots for $PbTi_{1-x}Fe_xO_3$ with (*a*) $x = 0.25$ and (*b*) $x = 0.3$ at different temperatures. Variation of (*c*) grains resistance R_G, (*d*) grain boundaries resistance R_{GB} and (*e*) surface layer resistance R_{SL}. The solid lines in (*a*) and (*b*) are the simulated data obtained from using the equivalent circuit shown in Fig. 5.14.

Typical complex impedance Z^* plane (Nyquist) plots for PTFO with $x = 0.25$ and 0.3 samples are shown in Fig. 5.13 (*a*) and (*b*). These plots bear the characteristics of asymmetric, depressed semicircular arcs signifying the non-Debye like relaxation

behavior. The sizes of the semicircles are found to increase with increase in temperature in the temperature range 300 – 373 K. Such increase in the size of the semicircles reveals the increase in resistance. Hence the samples exhibit PTCR effect in the range 300 – 373 K. Beyond T = 373 K, the size of the semicircles start decreasing with increase in temperature signifying the NTCR effect.

The Nyquist plots were further analyzed by modeling it to a possible equivalent electrical circuit. As the combined Z'' and M'' spectroscopic plots reveal that there are atleast three electroactive regions present in the samples, the impedance data were modeled to an equivalent circuit comprising of resistances (R_G, R_{SL}, R_{GB}), capacitances (C_{SL}, C_{GB}) and constant phase elements (CPE, denoted by Q) with their combination as shown in Fig. 5.14 [31]. Here, R_G, R_{SL} and R_{GB} represent the resistance of grains, surface layers and grain boundaries respectively, while C_{GB} and C_{SL} represent the capacitance of grain boundaries and surface layers respectively. The temperature dependence of different parameters obtained from the modeling of Nyquist plots are presented in Fig. 5.13. It is observed that R_{GB} and R_{SL} of x = 0.25 and 0.30 increase with increase in temperature upto T = 373 K and 353K respectively. From the observed temperature variation of R_{SL} and R_{GB}, it is clear that it is the surface layers and the grain boundaries that enlarge the size of Nyquist plots with rise in temperature upto T ~ 373 K and significantly contributes towards the PTCR effect. Beyond T = 373 K, both R_{GB} and R_{SL} show the NTCR behavior. It is very interesting to observe a PTCR behavior for grains resistance too as can be seen from Fig. 5.13, which persists upto a temperature range higher than that observed for R_{GB} and R_{SL}. The resistivity of grains is attributed to the scattering of electrons by the domain walls, while the movement of domain walls is responsible for H_C. The anomalous increase of H_C with increase in temperature as discussed in section 5.6 may lead to the observed increase in R_G with increase in temperature and may signify a possible coupling between magnetic and electric order.

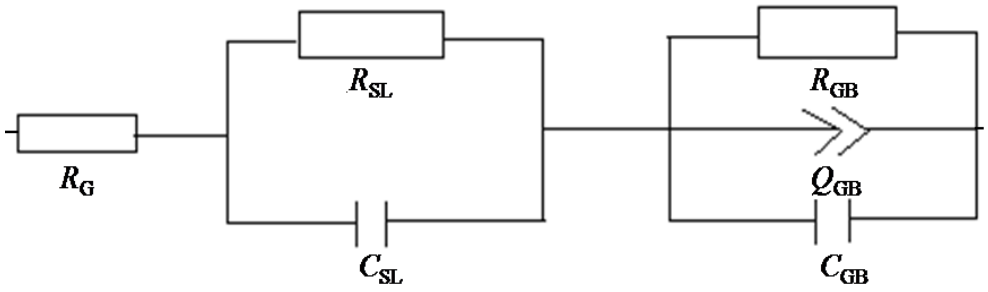

Figure 5.14 Equivalent electrical circuit.

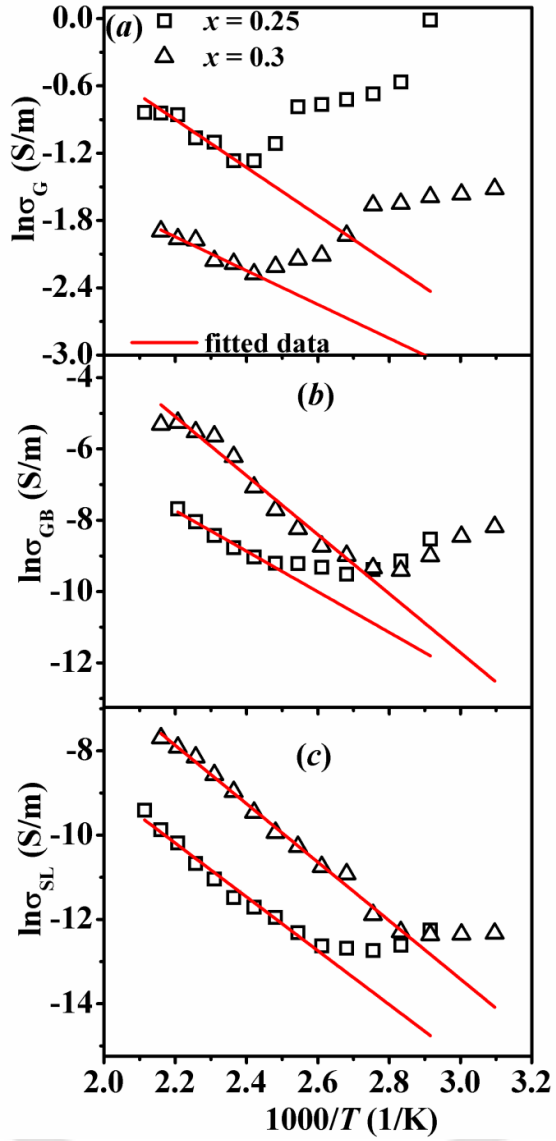

Figure 5.15 Arrhenius plots for σ_G, σ_{GB} and σ_{SL} for x = 0.25 and 0.3 samples of $PbTi_{1-x}Fe_xO_3$. The solid lines are the fitted data to eq. (5.4).

The dc conductivity σ_G, σ_{GB} and σ_{SL} of x = 0.25 and 0.30 samples corresponding to R_G, R_{GB} and R_{SL} respectively were estimated using the relations $\sigma = t/AR$ where t and A are respectively the thickness and area of the samples. The conduction activation energy are estimated using the Arrhenius law [111]:

$$\sigma = \sigma_0 \exp\left(-E_C / k_B T\right) \tag{5.4}$$

where σ_0 is the pre-exponential factor, E_C is the activation energy for conduction, k_B is Boltzmann constant and T is the temperature. Fig. 5.15 shows the plots of $\ln\sigma_G$, $\ln\sigma_{GB}$ and $\ln\sigma_{SL}$ vs. $1000/T$ for $x = 0.25$ and 0.30 samples. The E_C values are estimated by carrying out the linear fitting of $\ln\sigma_G$ and $\ln\sigma_{GB}$ vs. $1000/T$ plots. The values of E_C estimated from dc conductivity corresponding to grains are 0.18 and 0.13 eV for $x = 0.25$ and 0.30 samples respectively. Similarly, the E_C values corresponding to grain boundaries are 0.50 and 0.71 eV, while that for surface layer is found to be 0.55 and 0.59 eV.

5.4 Complex Dielectric Permittivity

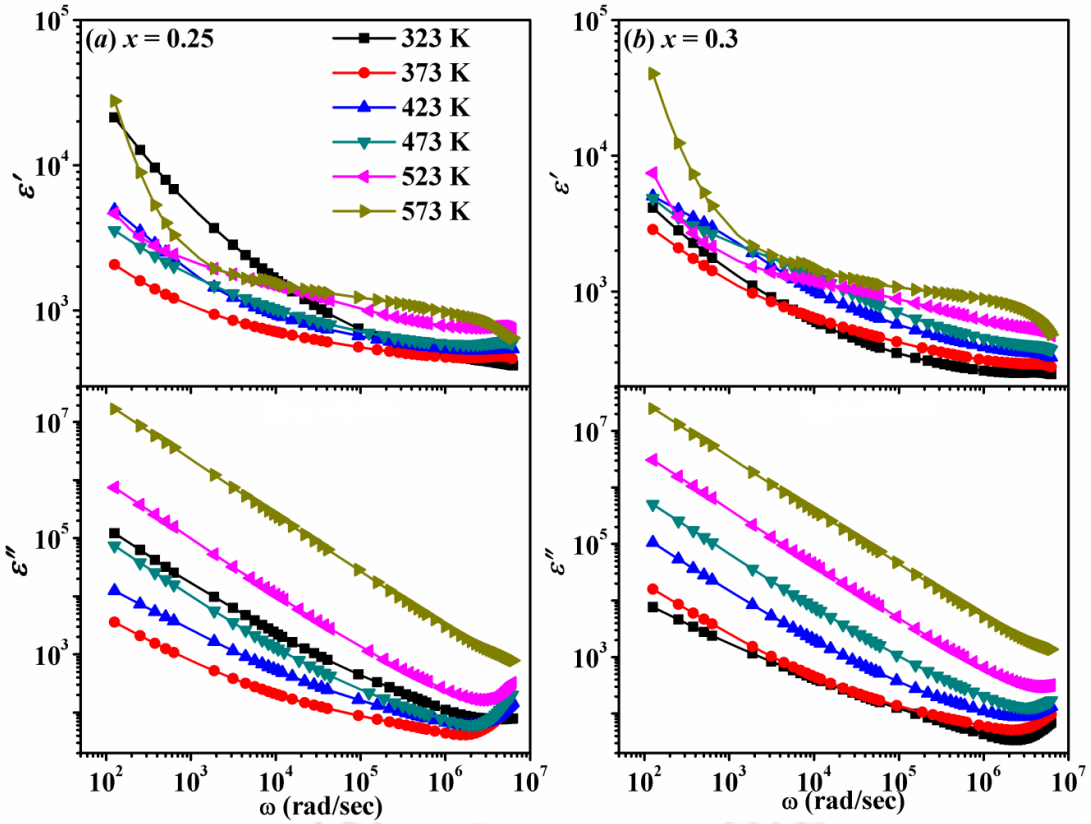

Figure 5.16 Frequency dispersion of ε' and ε'' for (*a*) $x = 0.25$ and (*b*) $x = 0.30$ samples of $PbTi_{1-x}Fe_xO_3$ at different temperatures.

The frequency dispersion of ε' and ε'' of $x = 0.25$ and 0.30 samples of $PbTi_{1-x}Fe_xO_3$ at different temperatures are shown in Fig. 5.16. At all temperature ε' decreases with increase in frequency. The decreasing trend is significant especially at low frequency region, representing Maxwell-Wagner type relaxation arising from the grain-grain boundaries heterogeneity. The slope of ε'' versus ω plots in log-log scale in the lower

frequency region is nearly equal to -1, which suggests the effect of hopping conductivity leading to typical power-law frequency dependences of the dielectric response.

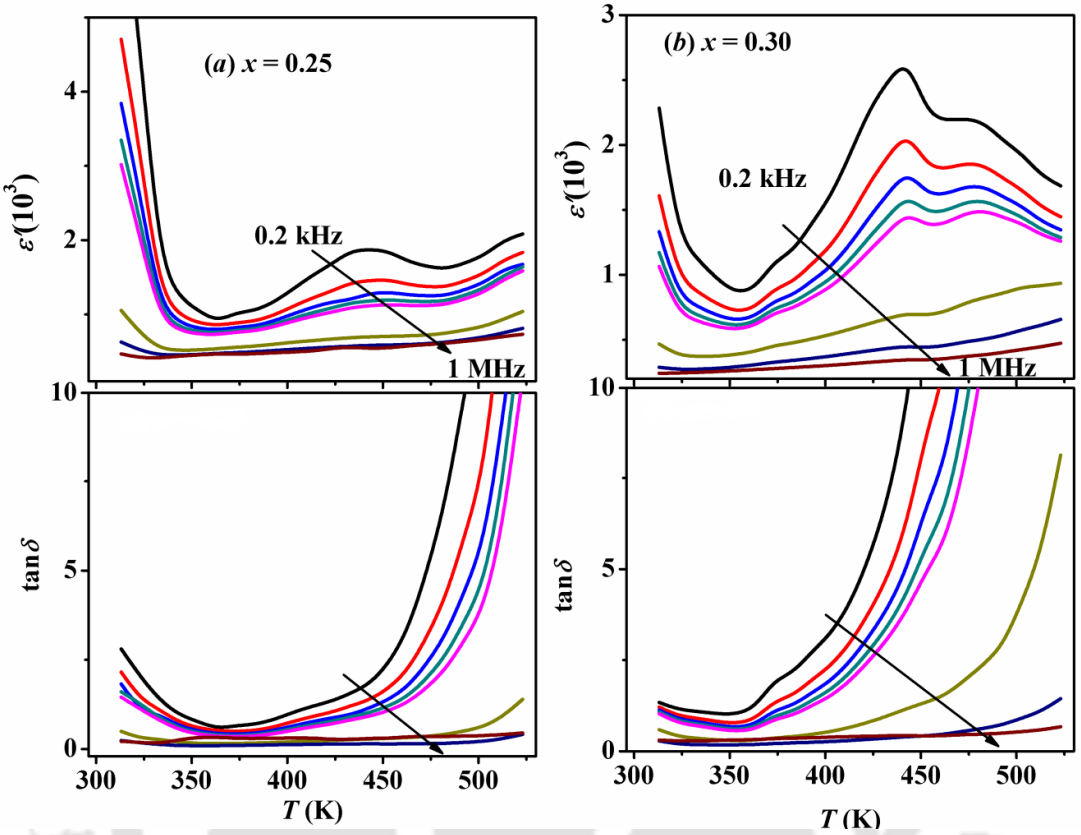

Figure 5.17 ε' – T and tanδ – T curves for (a) x = 0.25 and (b) x = 0.30 samples of $PbTi_{1-x}Fe_xO_3$ measured at different frequencies. The arrow head shows the increase of measuring frequency.

The temperature dependences of ε' and loss tangent (tanδ = $\varepsilon''/\varepsilon'$) of x = 0.25 and 0.30 samples measured in the frequency range of 0.2 kHz – 1MHz are shown in Fig. 5.17. It can be seen that both ε' and tanδ decrease with increase in temperatures below T ~ 360 K. The decrease of ε' and tanδ for T < 360 K depicts the structural transitions in the compounds. It is well known that $PbTiO_3$ undergoes structural transition from tetragonal to cubic phase at 763 K, which is also a ferroelectric-to-paraelectric transition. The ferroelectric transition temperature is reported to decrease with doping at A- and B-sites of the compound. It is observed in many ferroelectric compounds that both ε' and tanδ in the paraelectric state decrease with increase in temperature. It is possible that the increase in Fe doping concentration upto x = 0.25 and 0.30 shift the ferroelectric transition down the room temperature and they undergo ferroelectric-to-paraelectric transition around the

room temperature. Therefore, ε' and tanδ values decrease with increase in temperature for $T < 360$ K. For temperature $T > 360$ K, ε' and tanδ increases with increase in temperature. The dielectric constant exhibits anomalies at high temperature, while tanδ increases exponentially, which is attributed to the thermal activation of hopping conduction, leading to increase in the loss of the samples. The anomalies in ε' is known as diffuse dielectric anomalies commonly observed in perovskite ferroelectrics due to the dipolar effects of oxygen vacancies and the conduction electrons created from the ionization of oxygen vacancies.

5.5 AC Conductivity

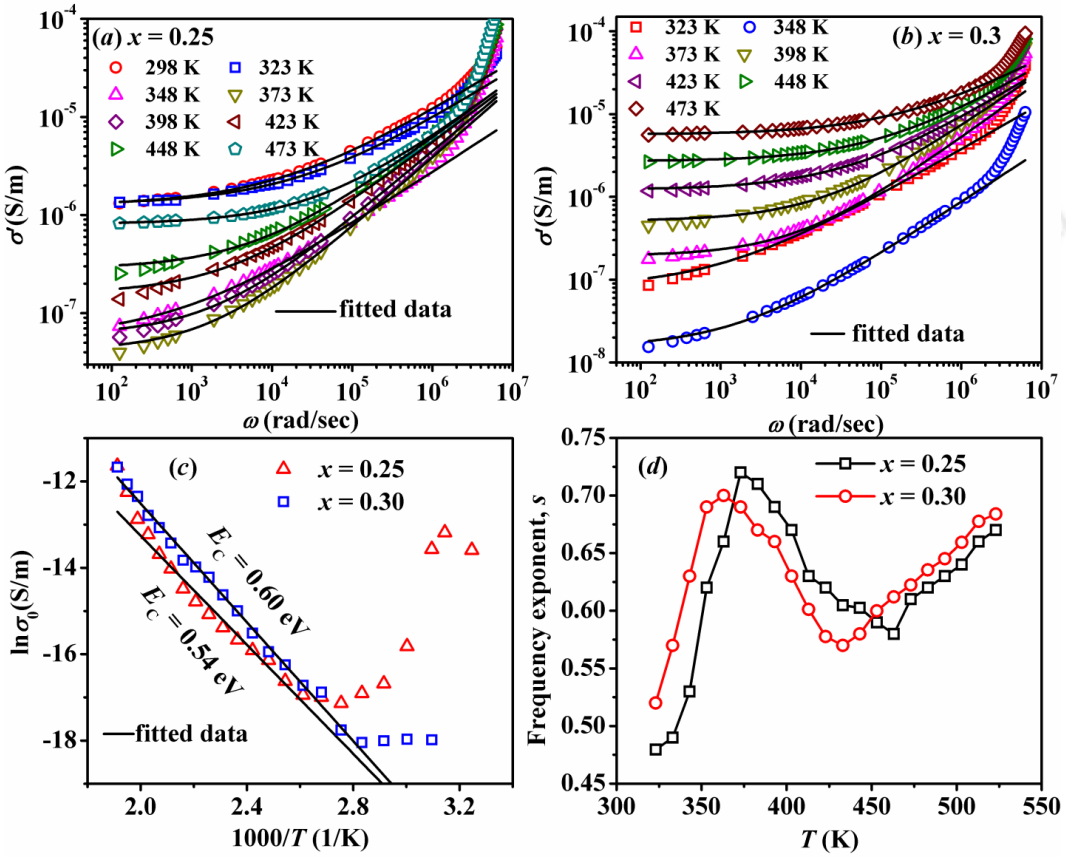

Figure 5.18 Frequency dispersion of conductivity (σ') at several temperatures for (*a*) x = 0.25 and (*b*) x = 0.3 samples of $PbTi_{1-x}Fe_xO_3$. (*c*) Arrhenius plots for dc conductivity, $\sigma(0)$ and (*d*) Temperature variations of frequency exponent (s).

The real part (σ') of ac conductivity (σ^*) is calculated using the relation [114]:

$$\sigma'(\omega) = \omega\varepsilon_0\varepsilon'' \tag{5.5}$$

where ω is angular frequency and ε_0 is the permittivity of vacuum. The frequency variations of σ' of x = 0.25 and 0.30 samples of $PbTi_{1-x}Fe_xO_3$ are shown in Fig. 5.18. As can be seen from the Fig. 5.18, the conductivity plot at a particular temperature is characterized by the appearance of a frequency independent plateau region (dc conductivity) at lower frequency and a frequency dispersive region at higher frequency. The frequency independent plateau at low frequency is attributed to long range translational motion of charge carriers. The dispersion of conductivity at higher frequency region can be explained in terms of Funke's jump relaxation model (JRM) [120]. Such a frequency dispersion of σ' can be described in terms of Jonscher Power Law (JPL) [37]:

$$\sigma'(\omega) = \sigma(0) + A\omega^s \tag{5.6}$$

where $\sigma'(\omega)$ is the real part of conductivity, $\sigma(0)$ is the frequency independent (dc) conductivity. The term $A\omega^s$ represents the frequency dispersion and characterizes all dispersion phenomena. The pre-exponential factor A and the frequency exponent s depend on temperature and the materials' intrinsic properties. The parameter s signifies the degree of interaction of mobile charges with the lattice around them and its temperature dependence can reveal the underlying conduction mechanism. Moreover, the value of s defines if the motion of the charge carriers is either translational or localized. If the value of $s < 1$, the motion is translational, and if the value of $s > 1$, the motion is localized. The conductivity spectra of x = 0.25 and 0.30 samples are fitted to Jonscher power law, as shown in Fig. 5.18 (*a*) and (*b*) respectively, where the fitted data are shown in solid lines. The fitted data closely follow the experimental data. It is observed from Fig. 5.18 (*a*) that the value of $\sigma'(\omega)$ of x = 0.25 sample decreases with increase in temperature upto 373K and beyond that it increases. Similar temperature variations of $\sigma'(\omega)$ is observed for x = 0.3 samples. In order to further elucidate the temperature dependence of $\sigma'(\omega)$, we have estimated the $\sigma(0)$ and the frequency exponent (s) from the fitting of conductivity spectra of x = 0.25 and 0.3 samples to Jonscher power law. The variation of $\sigma(0)$ with temperatures is shown in Fig. 5.18 (*c*) in the form of $\ln\sigma(0)$ versus 1000/T plots. It is clear from the figure that $\sigma(0)$ of the samples first decreases with increase in temperature upto a certain temperature and beyond that it increases. The decrease of $\sigma(0)$ for $T < 373$ K suggests the PTCR behavior of the samples. The variations of $\sigma(0)$ in the temperature range $T > 373$ K can be fitted to Arrhenius law (eq. 5.4). The fitted data to Arrhenius law are shown as solid lines in Fig. 5.18 (*c*). From the fitting of $\sigma(0)$ data to Arrhenius law,

the activation energies for conduction (E_C) are estimated, which are found to be 0.54 and 0.60 eV respectively for x = 0.25 and 0.3 samples. These values are comparable to that obtained from the dc conductivity corresponding to grain boundaries and surface layer as discussed in section 5.3.1.

In order to understand the underlying conduction mechanism, the frequency exponents (s) obtained from the Jonscher power law fit of ac conductivity are plotted in Fig. 5.18 (*d*) for x = 0.25 and 0.3 samples of $PbTi_{1-x}Fe_xO_3$. It is well known that if s shows an increasing trend as a function of temperature then the conduction mechanism is attributed to the small polaron tunneling (SPT) [125, 126]. In contrast, if s decreases with increase in temperature and reaching a minimum followed by increase in its value at higher temperature can be attributed to the overlapping large polaron tunneling model (OLPT) [127]. The temperature independence of s corresponds to quantum mechanical tunneling (QMT) of conduction mechanism [127]. On the otherhand, a continuous decreasing value of s with temperature corresponds to correlated barrier hopping (CBH) phenomenon [127]. In the present case, it is observed that s first increases with increase in temperature for T < 375 K and T < 365 K for x = 0.25 and 0.30 samples respectively and beyond these temperatures, the values of s decrease with increase in temperature, attain a minimum followed by further increase in its value at higher temperature. Such variation of s in present case suggests that the conduction mechanism is temperature dependent. The continuous increase in s value with increase in temperature for x = 0.25 and 0.30 samples indicates SPT as the conduction mechanism for these samples for T < 375 K and 365 K respectively. On the otherhand, a decrease of s to a minimum value followed by its continuous increase with further rise in temperature for T > 375 K and 365 K respectively for x = 0.25 and 0.30 samples confirm the OLPT as the underlying conduction mechanism in this range of temperature. This suggests that the conduction mechanism is temperature dependent and it indicates a transition of conduction mechanism from SPT to OLPT. Interestingly, we observed PTCR behavior for x = 0.25 and 0.3 samples in the temperature region below 375 and 365 K respectively and at higher temperature NTCR behavior is observed. Therefore, the conduction mechanism in the PTCR and NTCR regions are SPT and OLPT respectively.

It is well known that oxygen vacancies form in perovskites during the process of sintering due to the escape of oxygen from the lattice. Conduction electrons are created from the ionizations of oxygen vacancies as:

$$V_O \leftrightarrow V_O' + e^- \tag{5.7}$$

$$V_O' \leftrightarrow V_O'' + e^- \tag{5.8}$$

where V_O, V_O' and V_O'' represent the neutral, singly and doubly ionized oxygen vacancies respectively. The oxygen vacancies lead to the shallow level electrons. These electrons are easily thermally activated to become conducting electrons. The present analysis gives the value of activation energy estimated from ω_{max} (Z'') and ω_{max} (M'') data in the range 0.7 – 1.3 eV and 0.44 – 0.46 eV respectively. On the other hand, the analysis of dc conductivity and ac conductivity gives the activation energies in the range 0.50 – 0.70 eV and 0.54 – 0.60 eV respectively. It has been reported that oxygen vacancies exist in the singly ionized state with activation energy values in the range 0.3 – 0.4 eV, while they can exist in doubly ionized state with activation energy in the range 0.6 – 1.2 eV. Hence, it is clear that the relaxation and conduction process is due to singly and doubly ionized oxygen vacancies.

5.6 Magnetic Properties

Figure 5.19 shows the $M - H$ loops of $PbTi_{1-x}Fe_xO_3$ (x = 0 – 0.3) samples recorded at room temperature. The negative slopes of $M - H$ loops of x = 0 and 0.05 samples reveal their diamagnetic nature. The diamagnetic nature in $PbTiO_3$ is attributed to Ti^{4+} ions having no d-electrons. For x = 0.05 sample, the slope of the $M - H$ loop is lesser than that of x = 0 sample which indicates the incorporation of paramagnetic moments (Fe ions) in the diamagnetic matrix of $PbTiO_3$. With further increase in Fe concentration, *i.e.*, for x = 0.1 – 0.2 samples, the magnetization values increase linearly with increase in magnetic field depicting the typical paramagnetic behavior. Further increase in Fe concentration to x = 0.25 and 0.3 leads to a non-linear behavior of magnetization curves comparable to that of typical ferromagnetic materials but without any magnetic saturation. A considerable linearity is observed at higher field.

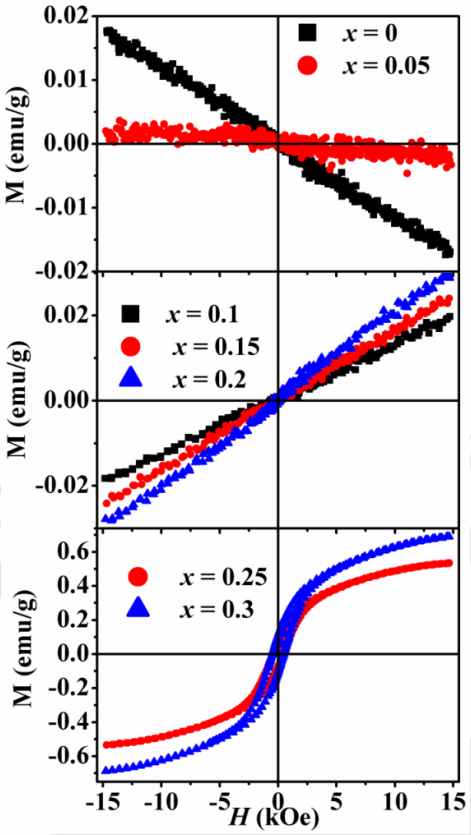

Figure 5.19 M – H loops of $PbTi_{1-x}Fe_xO_3$ (x = 0 – 0.3) samples recorded at room temperature.

The temperature variation of magnetization (M – T) for x = 0.05 – 0.3 samples are shown in Fig. 5.20 (*a*) and (*b*) measured in the warming mode under an applied field of 100 Oe. It reveals the paramagnetic behavior of x = 0.05 – 0.2 samples down to 25 K. On the other hand, the sharp rise in magnetization of x = 0.25 and 0.3 samples for $T \leq 650$ K as shown in Fig. 5.20 (*b*) highlights the typical ferromagnetic like transition but its magnitude is found to be quite small compared to conventional ferromagnet. The transition temperature (T_C) determined from the peaks of dM/dT vs. T plots is found to be 650 K for x = 0.25, which slightly increases to 660 K for x = 0.3 sample. The susceptibility data (χ) in the paramagnetic region for all samples were fitted to Curie-Weiss law: $\chi = C/(T - \theta_C)$, where C is Curie constant and θ_C is Curie-Weiss temperature. The experimental susceptibility data for x = 0.05 – 0.3 along with their corresponding fitted data to Curie-Weiss law in the paramagnetic region are presented in Fig. 5.20 (*c*) and (*d*).

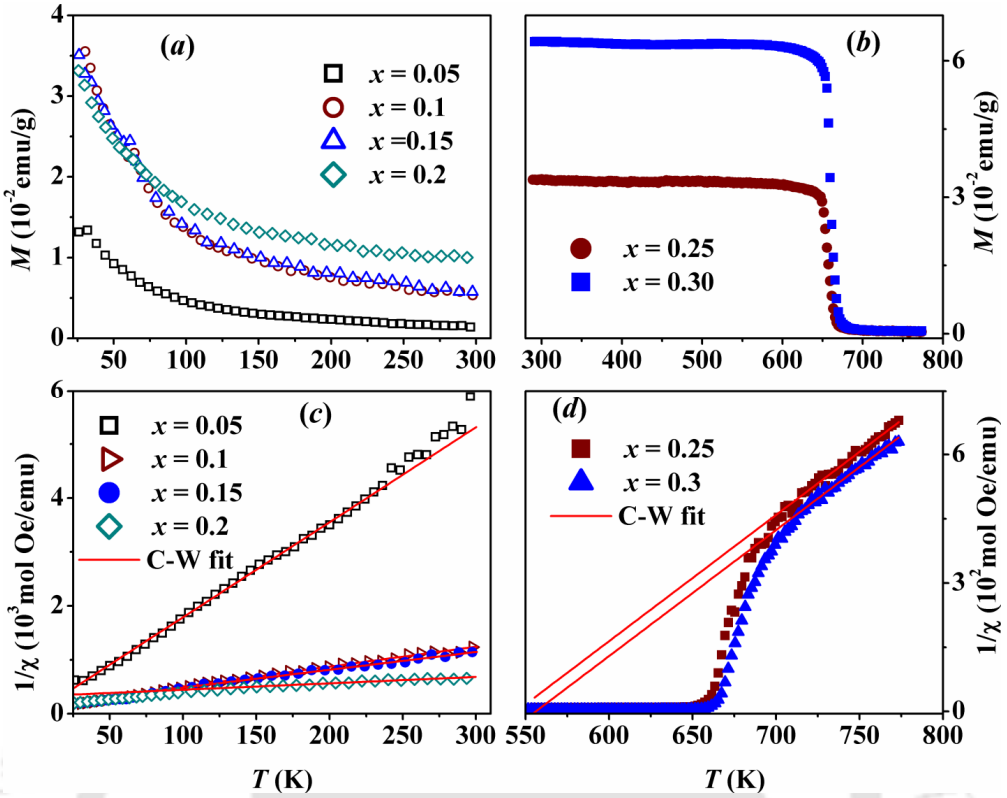

Figure 5.20 (*a* & *b*) $M - T$ and (*c* & *d*) $1/\chi - T$ plots of $PbTi_{1-x}Fe_xO_3$ samples for $x = 0.05 - 0.3$. The solid lines represent the fitted data using Curie-Weiss law.

From the fitted Curie constant values, we have calculated the effective magnetic moment (μ_{eff}) by using the relation $\mu_{eff} = \sqrt{3k_B C/xN_A}$ where k_B is the Boltzmann constant, N_A is the Avogadro's number and x represents the concentration of magnetic ions. The estimated values of Curie temperature are found to be –1.5 K, – 20.0 K, – 46.0 K, – 50.0 K, 540.0 K and 550.0 K for $x = 0.05$, 0.10, 0.15, 0.25 and 0.3 respectively. The positive value of Curie temperature for $x \geq 0.25$ samples reveals ferromagnetic (FM) interaction among the magnetic ions. The experimental value of μ_{eff} for $x = 0.25$ and 0.3 samples are found to be 1.10 μ_B/Fe ion and 1.0 μ_B/Fe ion respectively and they are smaller than the expected theoretical μ_{eff} value of 1.73μ_B/ion for Fe^{3+} ions in the low spin state. This can be attributed to the presence of considerable Fe ions in Fe^{4+} state. On the other hand, the experimental μ_{eff} values for $x = 0.1 - 0.2$ samples are found to be in the range 0.16 – 0.46 μ_B/Fe ion and they are far below the theoretical μ_{eff} values of Fe^{3+} ions. This discrepancy can be attributed to the engagement of some of Fe ions in the formation of magnetically dilute $(Fe'_{Ti} - V_O^{\cdot\cdot})^{\cdot}$ defect dipoles rather than behaving completely as a paramagnetic entity. The formation of such defect dipoles could be identified from the

room temperature EPR spectra of these samples as depicted in Fig. 5.21. The EPR spectra of x = 0.0 – 0.2 samples are dominated by two resonances: a relatively sharp resonance at H_r ~ 1000 – 1100 Oe and a broad resonance at H_r ~ 3100 Oe – 3190 Oe. The broad resonance with the value of g = 2.2 for x = 0 sample is accounted for Pb^{3+} ions [192]. The resonance line further broadens with increase in Fe concentration due to the appearance of another resonance line related to Fe^{3+} ions. The low field EPR resonance line with the g-factor value 6.7 – 7.4 for x = 0 – 0.2 samples suggests the formation of $(Fe'_{Ti} - V_O^{\cdot\cdot})^{\cdot}$ defect dipoles due to the large tetragonal crystal field produced by oxygen vacancy [193-195] and it reveals that some of Fe ions are taking part in the formation of defect dipoles. Further increase in Fe concentration beyond x = 0.20, the local crystal field changes to cubic symmetry and it prohibits the formation of such dipoles. The Fe^{3+} ions are no longer associated to oxygen vacancies through defect dipoles and take part in the long range FM interaction.

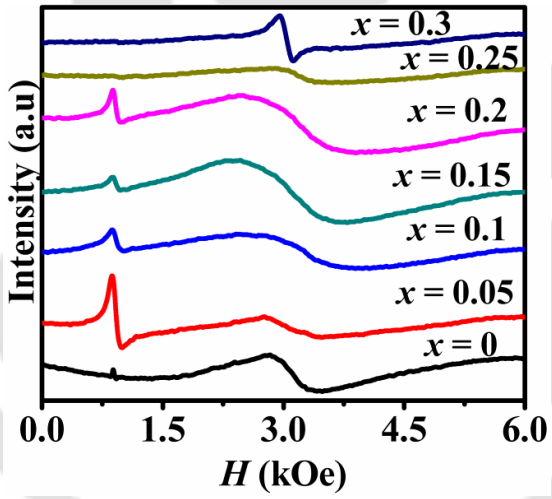

Figure 5.21 EPR spectra of $PbTi_{1-x}Fe_xO_3$ samples (x = 0 – 0.3) recorded at room temperature.

There are several mechanisms to explain the magnetic ordering in transition metal (TM) ions doped non-magnetic perovskites, such as Ruderman-Kittel-Kasuya-Yosida (RKKY) interaction [91], bound magnetic polaron, *F*-center exchange mechanism [85], double exchange interaction [186] *etc*. Ren *et al.* [85] explained the FM ordering in Fe doped PTO nanocrystals on the basis of *F*-center exchange mechanism through Fe^{3+}–V_O^{2-}–Fe^{3+}. They observed deterioration of magnetization with increase in Fe concentration due to growing Fe^{3+} – O – Fe^{3+} networks which facilitate the antiferromagnetism through superexchange interaction. The estimated value of M_S (~ 0.8 emu/g) at room temperature

in our samples is much larger than that reported by Ren *et al*. [85] who explained the magnetism in the framework of *F*-center exchange mechanism. Moreover, the formation of magnetic impurities such as AFM γ-Fe_2O_3 (T_N = 900 K), ferrimagnetic Fe_3O_4 (T_C = 850 K) [91] and AFM $PbFe_{12}O_{19}$ (T_N = 725 K) [196] can be ruled out as the obtained T_C value is quite small compared to these impurities. Interestingly, we have observed a positive Curie temperature (θ_C) for PTFO which suggests the ferromagnetic ordering in the samples. The observed magnetic ordering could be due to the double exchange interaction in Fe^{3+} –O^{2-} –Fe^{4+} networks similar to that observed for Fe doped $BaTiO_3$ samples [186].

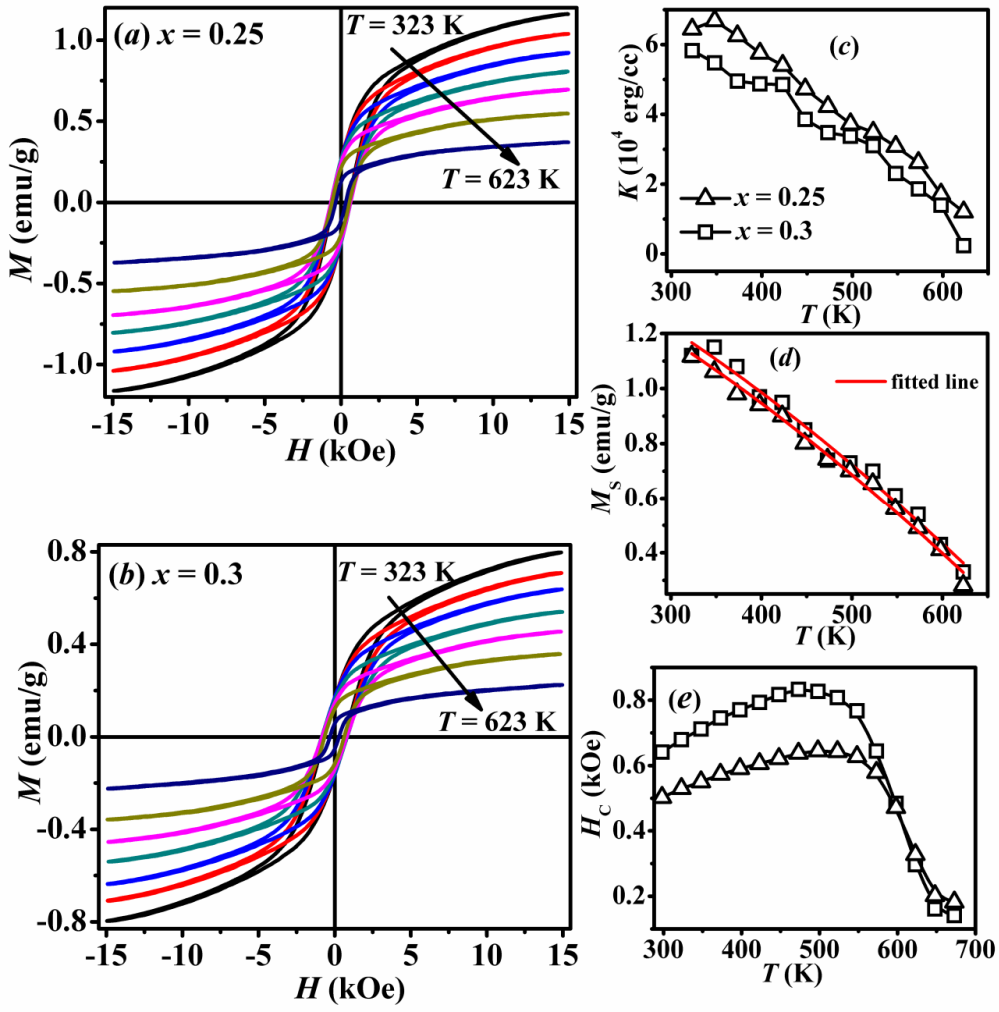

Figure 5.22 *M* – *H* loops for $PbTi_{1-x}Fe_xO_3$ samples with (*a*) x = 0.25 and (*b*) x = 0.3 at several temperatures. Temperature variations of (*c*) effective anisotropy constant *K*, (*d*) saturation magnetization M_S and (*e*) coercivity H_C. The solid lines in (*d*) represent the fit to Bloch equation.

Figure 5.22 (*a*) and (*b*) show the isothermal $M - H$ loops for x = 0.25 and 0.3 samples recorded in the temperature range of 300 – 700 K. The well-observed opening of $M - H$ loops and its linear increase at higher applied magnetic field is the signature of weak ferromagnetism. The $M - H$ loops are analyzed employing the law of approach to saturation (LAS) [22, 197]:

$$M(H) = M_S\left(1 - b/H^2\right) + \kappa H \tag{5.9}$$

where M_S represents the saturation magnetization, κ is the forced magnetization, and b is a constant related to the crystal anisotropy [22]. The effective anisotropy constant (K) for a polycrystalline sample can be estimated from b employing the relation $b = 4K^2/15M_S^2$ for a tetragonal symmetry [198]. The magnetization data in the high field regime (> 10 kOe) were fitted to eq. (5.9) and the estimated K and M_S values are presented as a function of temperature in Fig. 5.22 (*c*) and (*d*). Both K and M_S values decrease with increase in temperature. The temperature variations of M_S are fitted to Bloch's equation: $M_S(T) = M_S(0)(1 - BT^{3/2})$ where $M_S(0)$ is the saturation magnetization at T = 0 K and B is the Bloch's constant. The fitted data are shown as solid lines in Fig. 5.22 (*d*) for x = 0.25 and 0.3 samples. The $T^{3/2}$ type temperature dependence of M_S suggests the spin wave excitation in the temperature range 300 – 800 K. From the fitting, the estimated values of $M_S(0)$ for x = 0.25 and 0.3 are found to be 1.64 emu/g and 1.60 emu/g respectively. The B values are found to be 5.0×10^{-5} $K^{-3/2}$and 5.1×10^{-5} $K^{-3/2}$ for x = 0.25 and 0.3 respectively. The estimated values of B are larger than that observed for simple metals such as α-Fe (~ 0.34×10^{-5} $K^{-3/2}$) which could be probably due to the combined effect of exchange interaction and DM interaction. Similar values of B are reported for $NiFe_2O_4$, $YFeO_3$ [131]. The coercive field H_C is estimated using the relation $H_C = |H_{C1} - H_{C2}|/2$ where H_{C1} and H_{C2} are the magnetic field corresponding to M = 0 for the ascending and descending branches of $M - H$ loop and their temperature variation are presented in Fig. 5.22 (*e*). Surprisingly, the H_C value is found to increase with increase in temperature upto 500 K and for further increase in temperature it falls quite sharply. Since H_C is proportional to K/M_S [199], the decreasing trend of H_C with increase in temperature is expected as both K and M_S values decrease with increase in temperature. The unusual behavior of H_C in the temperature range T = 300 to 500 K for x = 0.25 and 0.3 samples can be attributed to magneto-electric coupling [181, 200, 201]. Such anomalous behavior of H_C with temperature is reported for many magneto-electric compounds such as

ceramics of $BiFeO_3$–$PbTiO_3$ [200], solid solution of $BiFeO_3$ – $BaTiO_3$ [201] and Gd and Ti co-doped $BiFeO_3$ ceramics [181], etc.

5.7 Conclusion

Polycrystalline samples of $PbTi_{1-x}Fe_xO_3$ (x = 0 – 0.3) were prepared by solid state reaction method and they are found to be crystallized in tetragonal unit cell with *P4mm* space group. Substitution of Fe into Ti site leads to the expansion of *ab* plane and the contraction of the *c* axis such that the tetragonality (*c*/*a*) decreases. The overall lattice parameter variation is explained in terms of substitution of Ti ions predominantly by Fe^{3+} ions. The samples with x = 0.25 and 0.3 exhibit ferromagnetic behavior and are explained in terms of double exchange interaction in Fe^{3+} – O^{2-} – Fe^{4+} networks. An unusual increase in H_C value with increase in temperature upto T = 500 K is observed for x = 0.25 and 0.3 samples, and it is attributed to the magneto-electric coupling. We have explored interesting positive temperature co-efficient of resistance for x = 0.25 and 0.3 samples. As per the analysis of Nyquist plots in terms of fitting to electric equivalent circuit, three electroactive regions *viz.* grains, grain boundaries and surface layer are responsible for the PTCR behavior. The analysis of impedance and modulus spectra in terms of Bergman's general expression shows the considerable interaction among charge carriers in the PTCR region.

Chapter 6

Fe doped $BaTiO_3$ series

$BaTiO_3$ (BTO) is one of the interesting ferroelectric materials having ferroelectric transition ($T_{C\text{-}FE}$) above room temperature (410K) [186]. It has tetragonal structure at room temperature, but upon transition element doping it transforms into hexagonal [202, 203]. Such structural transition influences the magnetic and ferroelectric properties. The ferroelectric compounds like BTO do not exhibit any ferromagnetic (FM) behavior due to the lack of partially filled *d*-orbital in Ti^{4+} ions and they are found to be mostly in diamagnetic. However, the first-principle calculations suggest that Ti and O vacancy can induce FM in BTO [204]. FM in Cr, Mn and Fe doped $BaTiO_3$was predicted by Nakayama and Katayama-Yoshida [90]. Xu *et al.* [91] have predicted the co-existence of ferroelectricity and FM in Fe doped $BaTiO_3$. Apostolova *et al.* [205] predicted the multiferroic properties in both Mn and Fe doped $BaTiO_3$ samples and they have also shown that magnetization and FM T_C values increase with increase in Fe concentration, while the electric polarization decreases. Ray *et al*. [92] have reported the room temperature FM in 5 at. % and 7 at. % Fe doped $BaTiO_3$ single crystals. Room temperature FM in polycrystalline samples of Fe doped BTO has been reported by Lin *et al.* [206] and Guo *et al.* [186] but the saturation magnetization (M_s) as a function of Fe concentration does not follow a consistent behavior.

6.1 Sample Preparation and Characterization

Polycrystalline samples of $BaTi_{1-x}Fe_xO_3$ (x = 0 – 0.30) were prepared by solid state reaction method. Stoichiometric ratios of $BaCO_3$, TiO_2 and Fe_2O_3 of purity better than 99 %were weighed and mixed under acetone medium using an agate mortar and pestle. The mixture is presintered at 1173 K for 12h. The presintered powders were pressed into

cylindrical pellets of approximately 12 mm diameter and 2 mm of thickness at a pressure of 2.94×10^8 N/m^2 by using a hydraulic press. The final sintering in pellet form was carried out at 1473 K for 36 h. X-ray diffraction (XRD) patterns were recorded using Rigaku make TTRAX III high power X-ray diffractometer by employing Cu-K_α (λ = 1.54056 Å) radiation. Raman spectra at room temperature were obtained by using micro-Raman spectrometer (LabRam HR800, Jobin Yvon) in the wave number range of 150 to 1000 cm^{-1} with an excitation wavelength of 514 nm. The microstructure of the samples was studied by recording FE-SEM images by using HITACHI make field effect scanning electron microscope (model: S-480) equipped with EDS facility. Magnetization as a function of temperature in the range 25 K – 1073 K and hysteresis loops were measured by using Lakeshore make vibrating sample magnetometer (VSM, Model 7410). Dielectric constant and loss tangent as a function of temperature in the range of 300 K – 500 K under an ac voltage of 1.0 V_{rms} with frequency 10 kHz was measured using an LCR meter (Wayne Kerr, model 1J43100). For the electrical characterizations, electrodes were fabricated by painting silver pastes on both sides of the sample of typical thickness 1 to 1.5 mm. These samples were fired at 423 K in air for 2 h and furnace cooled to room temperature before carrying out the electrical measurements. The ferroelectric hysteresis loops (P – E loops) at room temperature were measured using a P – E loop tester (Radiant Technologies Inc., PPM20310-792).

6.2 Structural Properties

The XRD patterns of all samples of $BaTi_{1-x}Fe_xO_3$ are shown in Fig. 6.1 and they are found to be free from any impurity phase. The XRD peaks corresponding to x = 0 sample can be indexed to tetragonal unit cell having *P4mm* space group. Interestingly, the gradual increase in Fe concentration brings in some new peaks in the XRD pattern of x = 0.1, for instance the encircled peak shown in Fig. 6.2 and it could not be indexed to tetragonal unit cell in *P4mm* space group. The intensity of these additional peaks increases for further increase in Fe concentration such that the XRD patterns for $x \geq 0.10$ could not be indexed to *P4mm* space group alone, signifying a structural transition.

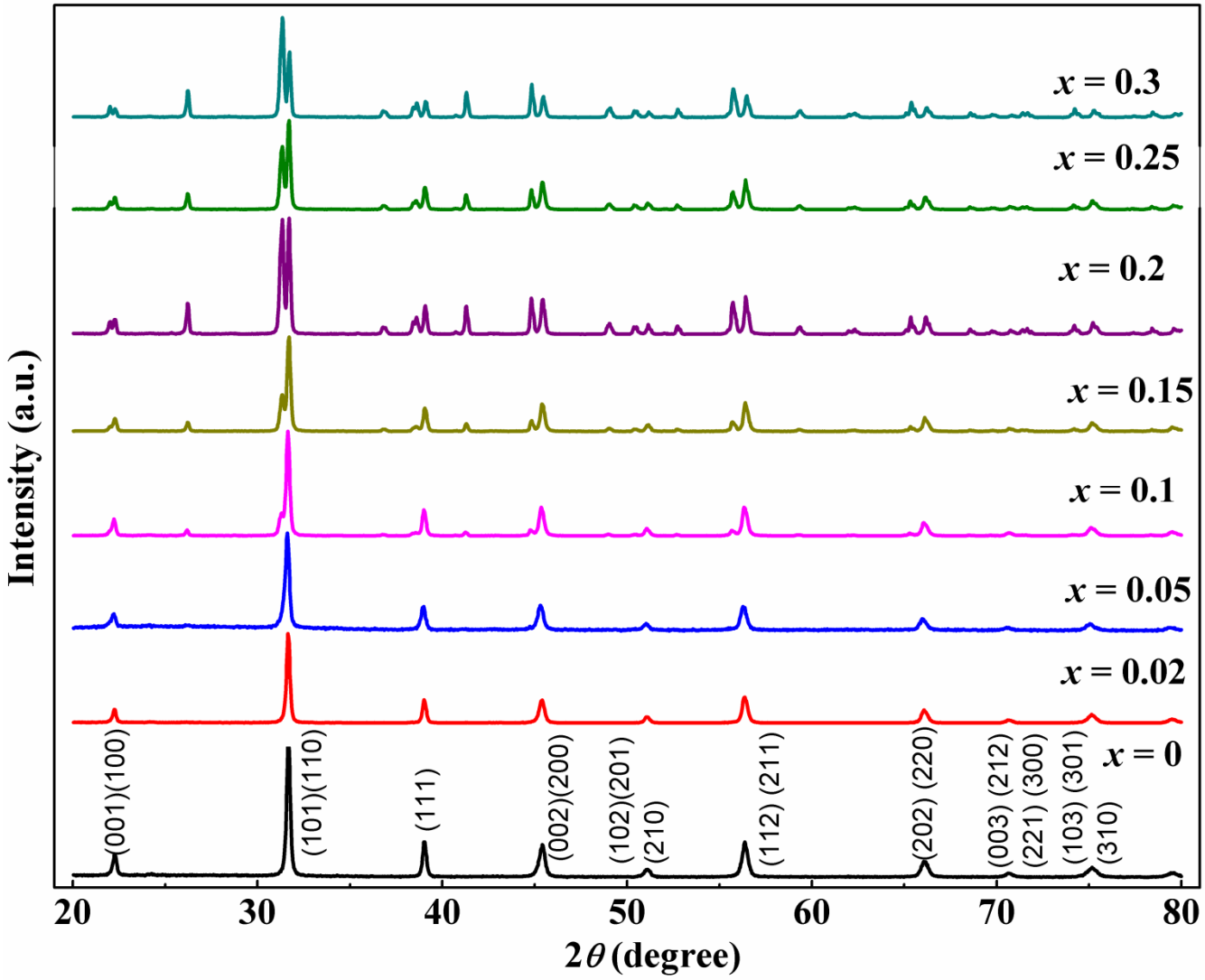

Figure 6.1 XRD patterns of $BaTi_{1-x}Fe_xO_3$ (x = 0 – 0.30) samples.

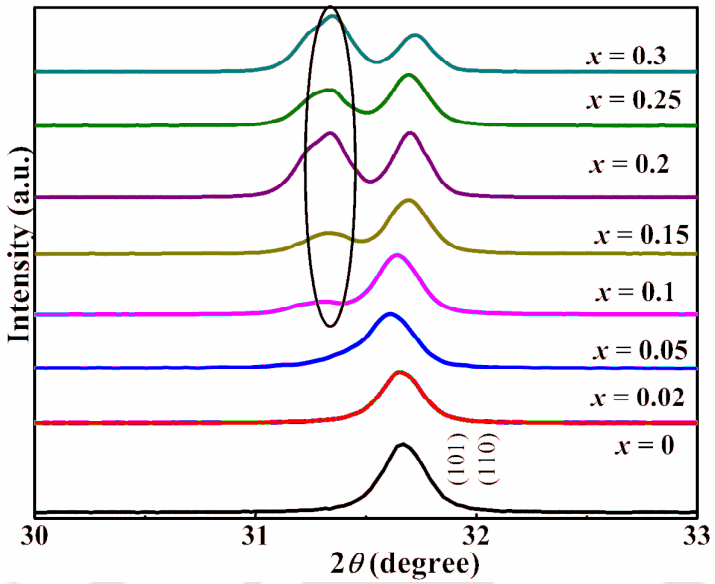

Figure 6.2 Expanded view of XRD patterns of $BaTi_{1-x}Fe_xO_3$ (x = 0 – 0.3) samples in the 2θ range of 30 – 33°.

The main reflections in XRD peaks of x = 0, 0.02 and 0.05 could be Rietveld refined using tetragonal unit cell with *P4mm* space group. On the other hand, we carried out a double phase refinement for $x \geq 0.1$, where best refinement was obtained by considering the mixture of tetragonal (*P4mm*) and hexagonal ($P6_3/mmc$) phases. Typical Rietveld refinement of XRD patterns of $BaTi_{1-x}Fe_xO_3$ samples are shown in Figs. 6.3 and 6.4 for x = 0, 0.10, 0.20 and 0.30. The weight fractions of individual phases are determined by using the relation [95] :

$$Wp = S_p\left(ZMV\right)_p \Big/ \sum_{i=1}^{n} S_i\left(ZMV\right)_i \qquad (6.1)$$

where W_p is the weight fraction of a phase p in a mixture of n phases. S, Z, M and V are respectively the scale factor, the number of formula units per cell, molecular mass of the phase and the unit cell volume (in $Å^3$) [95]. The weight percentage of each phase was obtained by multiplying Wp by 100. The various structural parameters obtained from the Rietveld refinement of XRD patterns of $BaTi_{1-x}Fe_xO_3$ samples are tabulated in Table. 6.1.

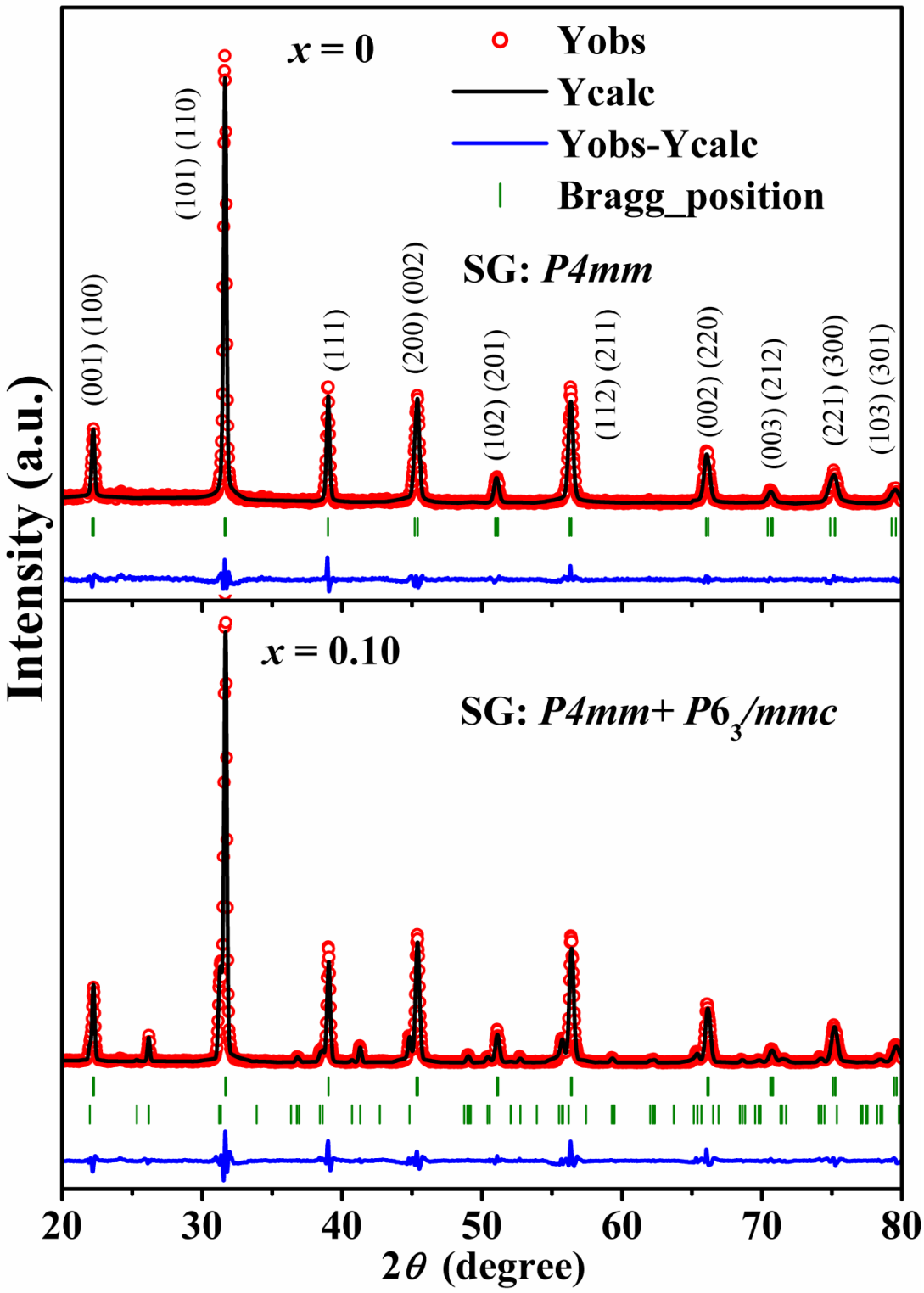

Figure 6.3 XRD patterns along with Rietveld refinement of $BaTi_{1-x}Fe_xO_3$ samples with x = 0 and 0.10.

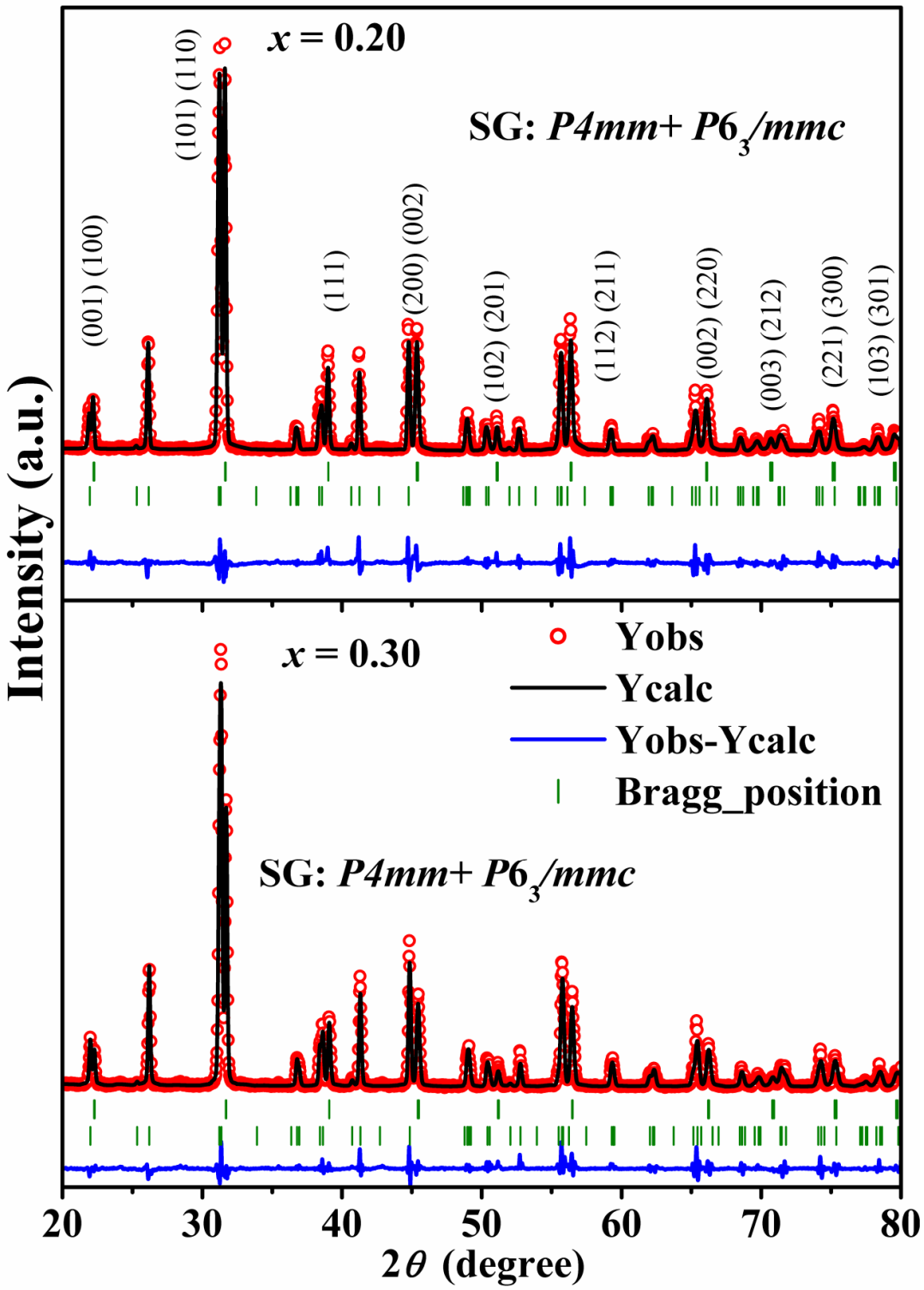

Figure 6.4 XRD patterns along with Rietveld refinement of $BaTi_{1-x}Fe_xO_3$ samples with x = 0.20 and 0.30.

Table 6.1 Structural parameters obtained from the Rietveld refinement of XRD patterns of $BaTi_{1-x}Fe_xO_3$ samples (x = 0 – 0.3). (SG = Space group).

SG	Parameters	Samples(x)							
		0	0.02	0.05	0.1	0.15	0.2	0.25	0.3
P4mm	$a = b$ (Å)	3.9903	3.9901	3.9900	3.9894	3.9885	3.9851	3.9845	3.9833
	c (Å)	4.0081	4.0042	4.0006	3.999	3.9982	3.9941	3.9920	3.9898
	V (Å^3)	63.82	63.75	63.69	63.65	63.56	63.43	63.38	63.30
	R_f (%)	1.67	2.01	6.29	2.52	1.32	1.99	3.13	3.50
	R_{Bragg}(%)	2.93	3.04	9.78	4.48	1.75	3.21	5.18	4.11
	Wt.%	100	100	100	77	71	52	51	35
P6$_3$/mmc	$a = b$ (Å)	--	--	--	5.703	5.705	5.702	5.704	5.700
	c (Å)	--	--	--	14.047	14.050	14.046	14.044	14.046
	V (Å^3)	--	--	--	395.76	396.05	395.59	395.76	395.33
	R_f (%)	--	---	--	5.10	6.08	3.57	5.66	5.88
	R_{Bragg}(%)	--	--	--	4.53	5.47	4.22	5.25	6.47
	Wt.%	--	--	--	23	29	48	49	65
	R_P (%)	8.73	9.54	8.42	9.10	8.19	10.2	10.0	8.75
	χ^2	2.85	2.91	2.53	5.84	4.66	6.32	6.16	5.38

It is observed that lattice parameters a and c corresponding to tetragonal cell decrease with increase in Fe concentration. Similar trend is observed for the unit cell volume. On the other hand, no systematic variation in the lattice parameters of hexagonal phase is observed. Substitution of Ti^{4+} ions (r_i = 0.605 Å) in $BaTiO_3$ by Fe^{3+} ion (r_i = 0.645 Å) is expected to expand the unit cell volume of $BaTiO_3$, and such unit cell volume expansion due to ionic size mismatch is reported in literatures. So, in addition to the substitution of Ti^{4+} ions by Fe^{3+} ions, there is a possibility of considerable concentration of Fe^{4+} ions at Ti^{4+} site and this gives rise to decrease in lattice constant values with increase in Fe concentration.

In order to further probe the doping induced structural change, we have recorded Raman spectra of $BaTi_{1-x}Fe_xO_3$ samples at room temperature as shown in Fig. 6.5. Four prominent Raman peaks at 261, 303, 516 and 720 cm^{-1} are observed for x = 0, which is in agreement with that reported in literature [207-210]. These peaks are ascribed to the A1

(TO), E (TO+LO) / B1, A1 (TO) / E (TO) and A1 (LO) + E (LO) modes respectively, which are the characteristic modes of tetragonal structure with *P4mm* space group [207, 211]. The Raman peak at 303 cm^{-1} signifies the non-centrosymmetric displacement of Ti atom from TiO_6 octahedra, suggesting the intrinsic structural distortion in tetragonal $BaTiO_3$ [212]. Thus, the Raman scattering experiment further confirms the formation of tetragonal phase in $x = 0$ sample. As the Fe concentration is increased, the Raman peaks corresponding to tetragonal phase are found to diminish and another prominent peak at 640 cm^{-1} for $x \geq 0.1$ is observed, as shown within the encircled region of Fig. 6.5. The peak at 640 cm^{-1} corresponds to the A_{1g} mode of hexagonal $BaTiO_3$ [207] and it further confirms the structural transition from tetragonal to hexagonal structure due to Fe doping.

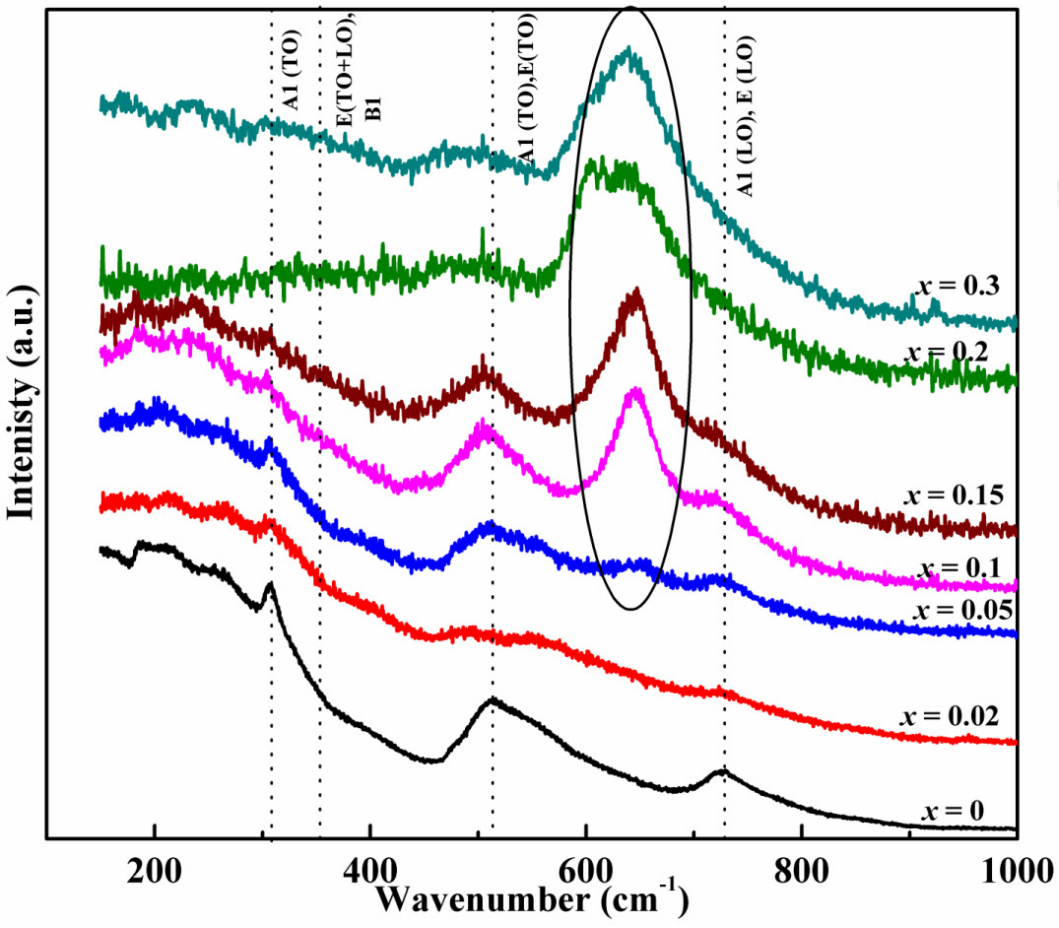

Figure 6.5 Raman spectra of $BaTi_{1-x}Fe_xO_3$ (x = 0 – 0.3) samples recorded at room temperature.

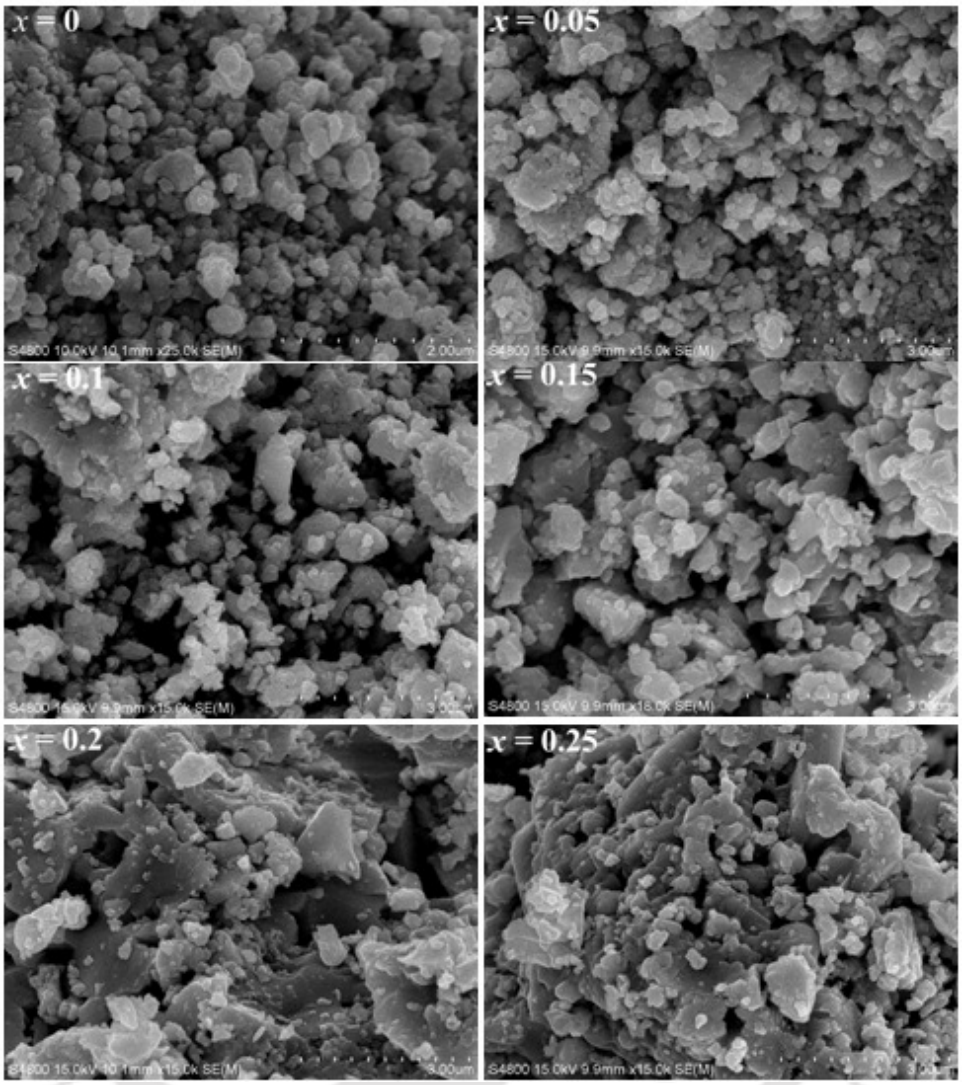

Figure 6.6 FE-SEM images of $BaTi_{1-x}Fe_xO_3$ samples with x = 0, 0.05, 0.10, 0.15, 0.20 and 0.25.

The surface morphology of the samples is studied by recording the FE-SEM micrographs. Typical FE-SEM micrographs of $BaTi_{1-x}Fe_xO_3$ with = 0, 0.05, 0.1, 0.15, 0.2 and 0.25 are shown in Fig. 6.6. Grains with wide size distribution are observed for $x \leq$ 0.1. In fact, the observed large grains are the agglomeration of smaller particles. The agglomeration of smaller particles is reduced for $x \geq 0.1$. Typical EDS spectra of $BaTi_{1-x}Fe_xO_3$ samples for x = 0, 0.10, 0.20 and 0.25 are shown in Fig. 6.7. The values of cationic ratio Ba: Ti: Fe estimated from the EDS analysis are given in Table 6.2 and they are found to be comparable to their nominal starting compositions.

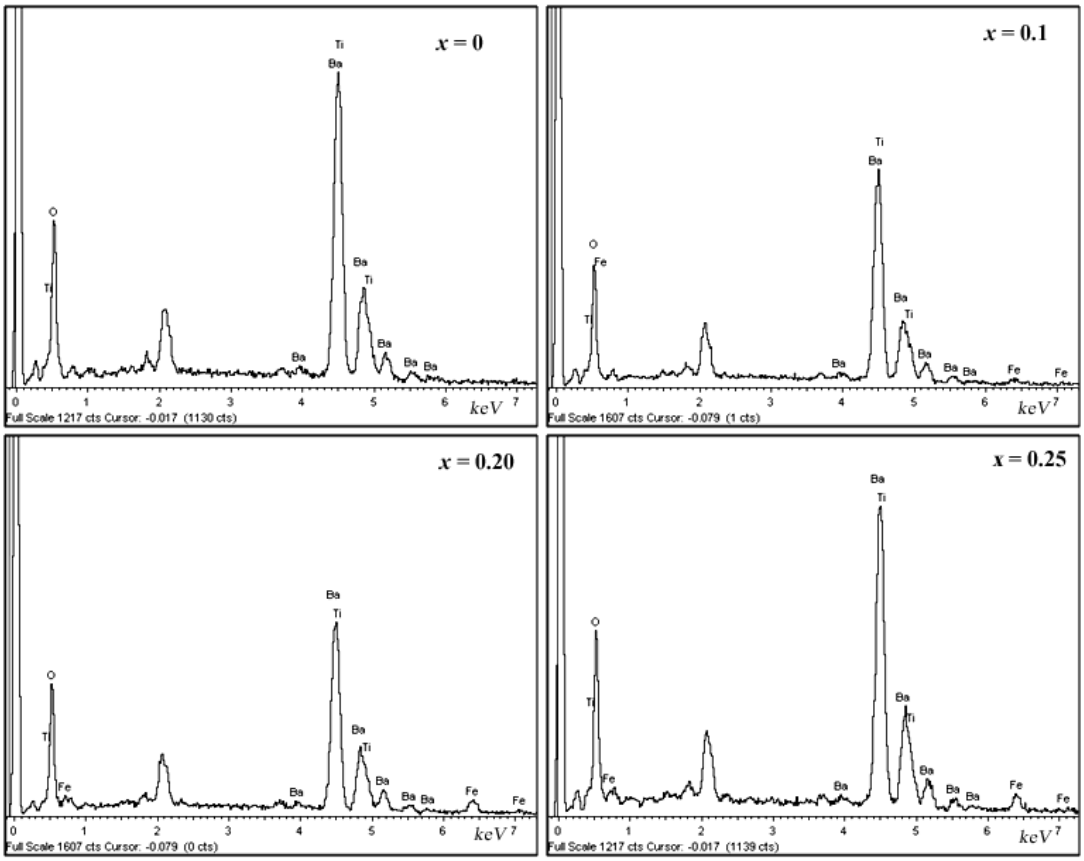

Figure 6.7 EDS spectra of $BaTi_{1-x}Fe_xO_3$ samples with x = 0, 0.10, 0.20 and 0.25.

Table 6.2 Cationic ratio estimated from the EDS spectra of $BaTi_{1-x}Fe_xO_3$ (x = 0 – 0.25) samples.

Samples	Cationic Ratio		
	Ba	Ti	Fe
$BaTiO_3$	1.02	0.972	-
$BaTi_{0.98}Fe_{0.02}O_3$	0.99	0.982	0.018
$BaTi_{0.95}Fe_{0.05}O_3$	1.01	0.954	0.045
$BaTi_{0.9}Fe_{0.1}O_3$	0.98	0.930	0.070
$BaTi_{0.85}Fe_{0.15}O_3$	1.01	0.863	0.137
$BaTi_{0.8}Fe_{0.2}O_3$	1.02	0.815	0.215
$BaTi_{0.75}Fe_{0.25}O_3$	1.02	0.775	0.225

6.3 Dielectric Properties

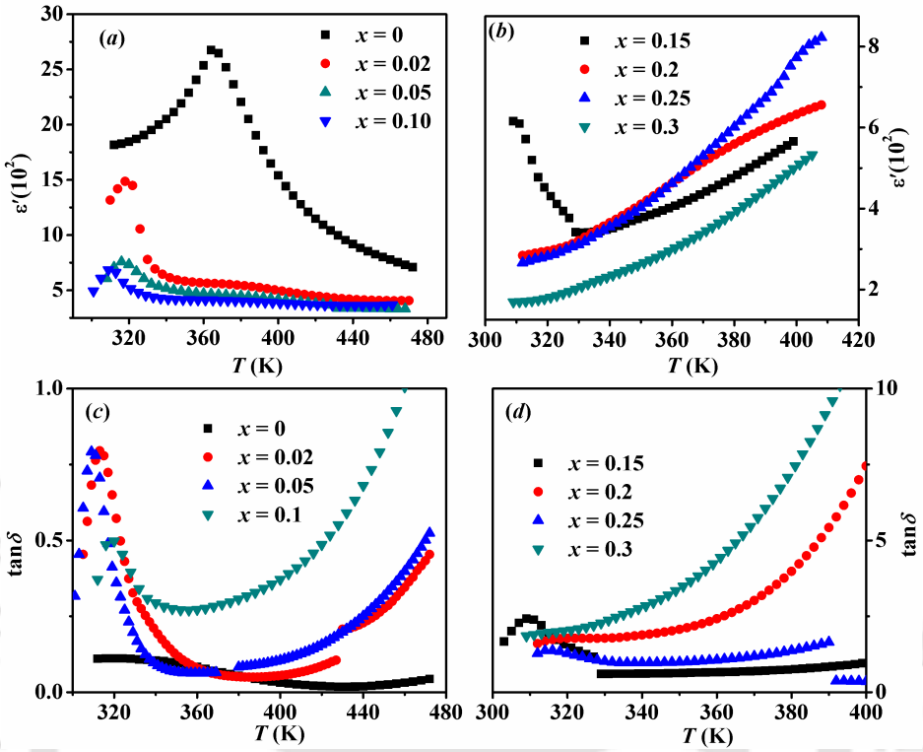

Figure 6.8 Temperature dependence of ε' and tanδ of $BaTi_{1-x}Fe_xO_3$ (x = 0 – 0.3) samples measured at frequency 10 kHz.

The dielectric properties are studied by measuring the temperature dependent dielectric constant (ε') and tanδ at 10 kHz frequency as shown in Fig. 6.8. The parent compound BTO exhibits a clear ferroelectric transition, at $T_{C\text{-}FE}$ = 365 K with a maximum value of dielectric constant, ε_m' = 2683, which is comparable to literatures [213, 214]. Fe substitution induces drastic decrease in the dielectric properties which can be seen in terms of decrease in the value ε_m' and the disappearance of $T_{C\text{-}FE}$. For instance, Fe substitution by 2 at%., reduces the value of ε_m' by 50 % *i.e.,* to 1509 and shift the $T_{C\text{-}FE}$ towards the lower temperature *i.e.*, down to 320 K. A continuous decrease of ε' and $T_{C\text{-}FE}$ values are induced by the substitution of Fe for Ti. The ferroelectricity in BTO is caused by the off-centering of Ti ions from the centre of oxygen octahedra. The Ti ions form strong covalent bond with the surrounding oxygen ions though its empty *d*-orbitals. The substitution of Fe for Ti destabilizes such covalent bonding, thus reduces the polarization which can be seen in terms of decrease in the value of ε' of the samples with increase in Fe concentration. Moreover, the evolution of centrosymmetric hexagonal phase is also

detrimental towards the ferroelectricity. The value of ε_m', $T_{C\text{-}FE}$ of $BaTi_{1-x}Fe_xO_3$ samples are listed in the Table 6.3.

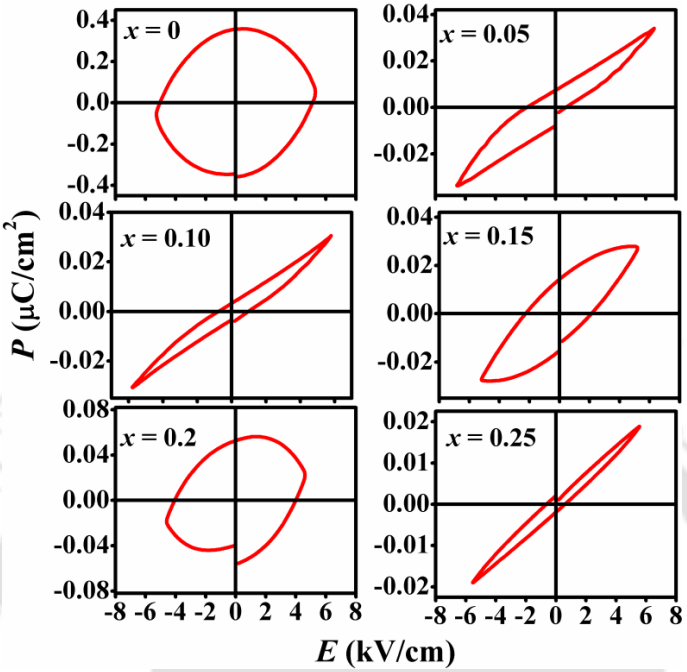

Figure 6.9 *P* – *E* loops of $BaTi_{1-x}Fe_xO_3$ samples with x = 0, 0.05, 0.10, 0.15, 0.20, and 0.25.

In conjunction to weakening of ferroelectric order observed from the temperature dependent dielectric properties, we have further studied the ferroelectric properties of the samples by recording their *P* – *E* loops at room temperature as shown in Fig. 6.9. At the first sight of the loops, the distorted loops mimic the lower density of the samples. The remnant polarization (P_r) of x = 0 sample is 0.35 μC/cm^2 and is comparable to the value reported by some authors for $BaTiO_3$ [215, 216]. The values of P_r are found to decrease for increasing x upto x = 0.1, after that it increases slightly for x = 0.15 and 0.2, and finally decreases with further increase in x values. However, the P_r value decreases with increase in Fe concentration as compared to x = 0, which is understood in terms of breaking of Ti – O covalent bonds which are responsible for ferroelectric off-center and due to the evolution of non-ferroelectric hexagonal phase with increase in Fe concentration. The slight increase in the value of P_r for x = 0.15 and 0.2 is attributed to the microscopic strain in the samples due to the co-existence of tetragonal and hexagonal phase. The P_r values of $BaTi_{1-x}Fe_xO_3$ samples are listed in the Table 6.3.

Table 6.3 ε_m', $T_{C\text{-}FE}$ and P_r of $BaTi_{1-x}Fe_xO_3$ (x = 0 – 0.3) samples.

Samples	ε'_m	$T_{C\text{-}FE}$ (K)	P_r (μC/cm^2)
0	2863	364	0.35
0.02	1486	318	0.10
0.05	756	316	0.007
0.1	685	309	0.004
0.15	-	-	0.01
0.2	-	-	0.05
0.25	-	-	0.002
0.3	-	-	0.002

6.4 Magnetic Properties

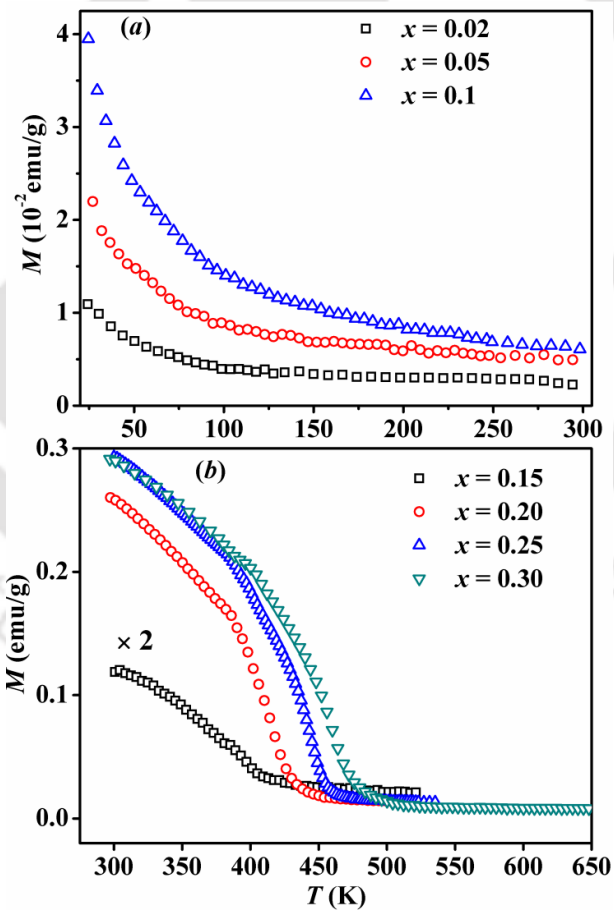

Figure 6.10 M – T plots of $BaTi_{1-x}Fe_xO_3$ (x = 0.02 – 0.3) samples measured under an applied field H = 1 kOe. For clarity the magnetization of x = 0.15 sample is multiplied by a factor two.

The magnetizations plots of $BaTi_{1-x}Fe_xO_3$ (x = 0.02 – 0.3) samples as a function of temperature under ZFC condition for the applied field of H = 1 kOe are shown in Fig. 6.10. The magnetization plots of x = 0.02 to 0.10 samples exhibit typical paramagnetic behavior with increase in magnetization with decrease in temperature without undergoing any magnetic transition. On the other hand, x = 0.15 – 0.30 samples show clear ferromagnetic transition as shown in Fig. 6.10 (*b*). The transition temperatures (T_C) determined from the peaks of dM/dT vs. T plots are found to be 397 K, 420 K, 445 K and 464 K for x = 0.15, 0.20, 0.25 and 0.30 samples respectively. The observed value of T_C is comparable to that reported for $BaTi_{0.95}Fe_{0.05}O_3$ single crystal [91] and polycrystalline samples of $Ba(Ti,Fe)O_3$ [186].

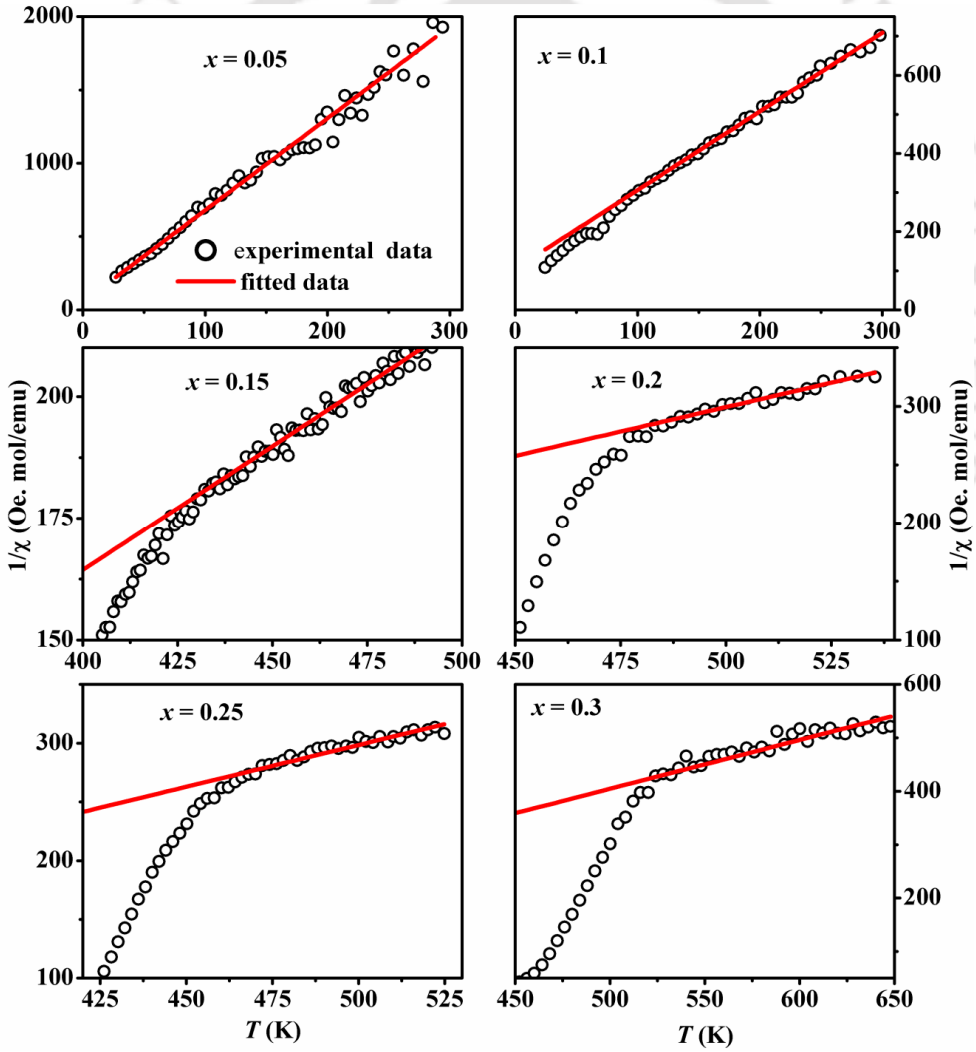

Figure 6.11 Inverse magnetic susceptibility data of x = 0.05 – 0.3 samples of $BaTi_{1-x}Fe_xO_3$ along with the fitted data (solid lines) to Curie-Weiss law.

The susceptibility data (χ) of x = 0.02 – 0.3 samples in the paramagnetic region were analyzed by fitting them to Curie-Weiss law: $\chi = C/(T-\theta_C)$, where C is Curie constant and θ_C is Curie temperature. The inverse susceptibility data of x = 0.05 – 0.3 samples along with the Curie-Weiss law fittings are shown in Fig. 6.11, where the solid lines represent the fitted data. From the values of C obtained from the above fit, the experimental effective magnetic moment (μ_{eff}) values were determined by using the relation $\mu_{eff} = \sqrt{3k_B C/xN_A}$ where k_B is the Boltzmann constant, N_A is the Avogadro's number and x represents the concentration of substituted Fe ions. The estimated values of μ_{eff} and θ_C are given in Table 6.4. The μ_{eff} values are found to be in the range 4.97 – 6.30 μ_B/Fe ion, which are mostly comparable to that of theoretical μ_{eff} values of Fe^{3+} ions having high spin configuration (S = 5/2, μ_{eff}^{th} = 5.92 μ_B/Fe). However, for samples having low Fe concentration *i.e.*, for x = 0.02 and x = 0.05, the experimental values are found to be smaller than that of theoretical values. This could be mostly due to some of the doped Fe ions oxidizing to higher valence state or a small deviation in the actual Fe concentration entering into lattice. The θ_C values for x = 0.02 – 0.10 samples are found to be negative and it indicates the presence of antiferromagnetic interaction. The θ_C values become positive for $x \geq 0.15$, which support the presence of ferromagnetic ordering

Table 6.4 Parameters obtained from the Curie-Weiss law fit of $BaTi_{1-x}Fe_xO_3$ (x = 0 – 0.3) samples.

Parameters	Samples (x)						
	0.02	0.05	0.10	0.15	0.2	0.25	0.3
T_C (K)	-	-	-	397	420	445	464
θ_C (K)	-3	-8.46	-50.0	34.7	109	81.3	86.1
μ_{eff} (exp) (μ_B/Fe)	5.06	5.06	6.32	5.20	5.88	6.31	5.40

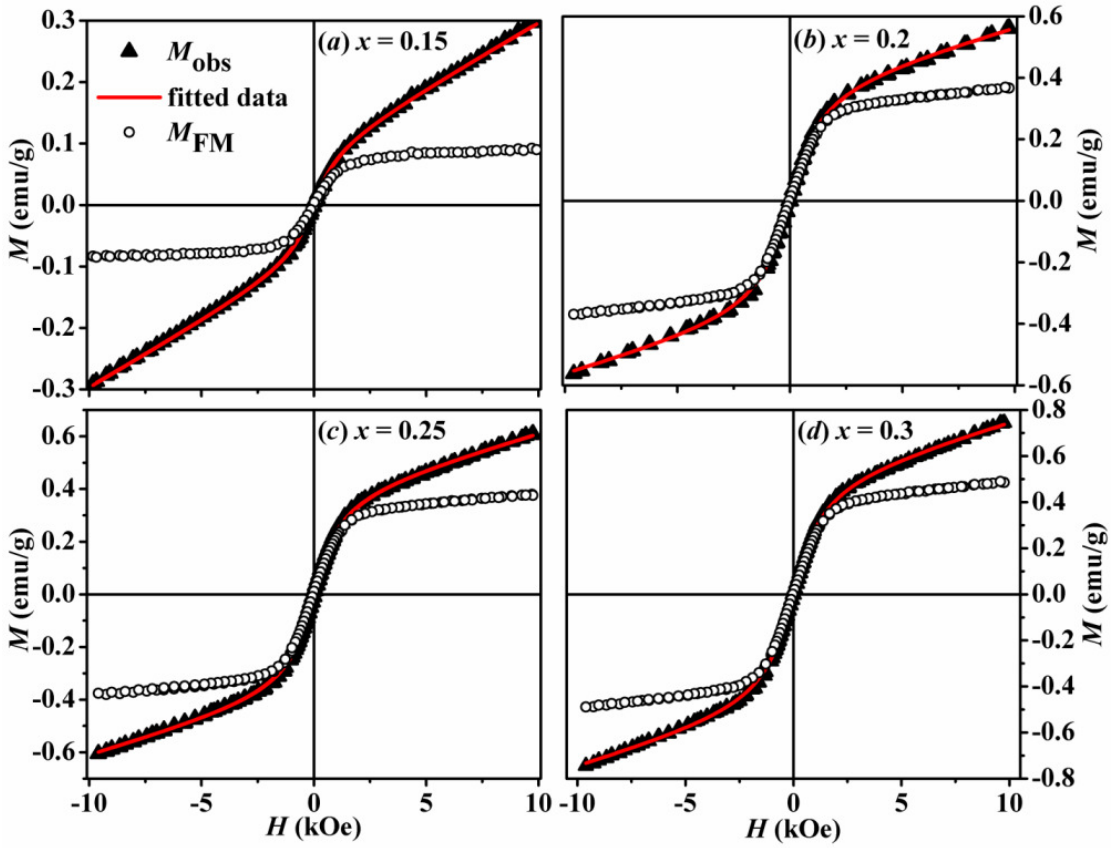

Figure 6.12 Experimental $M - H$ loops measured at T = 50 K (solid triangle) for x = 0.15 – 0.30 samples of $BaTi_{1-x}Fe_xO_3$. The solid lines are the fitted data to eq. (6.2). The FM components are shown separately as open circles.

In order to further investigate the magnetic properties, we have recorded $M - H$ loops for x = 0.15 – 0.3 samples at several temperatures in the range 50 K – 300 K. $M - H$ loops of x = 0.15 – 0.30 samples recorded at 50 K are shown in Fig. 6.12 and they show typical FM behavior with considerable value of remnant magnetization and coercivity along with a linear behavior at higher fields. Such linear increase in magnetization at higher applied field signifies the presence of PM/AFM matrix in the samples. Similar behavior was observed for x = 0.25 and 0.30 samples also. In order to estimate the ferromagnetic components from the measured $M - H$ loops, they were analyzed in terms of following equation [217]:

$$M(H) = \left[2\frac{M_S}{\pi} \tan^{-1}\left\{ \left(\frac{H \pm H_c}{H_c} \right) \tan\left(\frac{\pi M_r}{2M_S} \right) \right\} \right] + \chi H \qquad (6.2)$$

Here, the first term within the bracket is the ferromagnetic contribution with saturation magnetization (M_S), remnant magnetization (M_r) and the coercive field (H_C). The second term is to account for the linear PM/AFM contributions with susceptibility χ. The fitted data are shown as solid line in Fig. 6.12. Similar fitting was carried out for $M - H$ loops measured in the temperature range 50 K – 300 K for x = 0.15 – 0.3 samples. The estimated values of M_S and H_C from the above fit as a function of temperature are shown in Fig. 6.13 and they are found to decrease with increase in temperature due to increase in thermal energy.

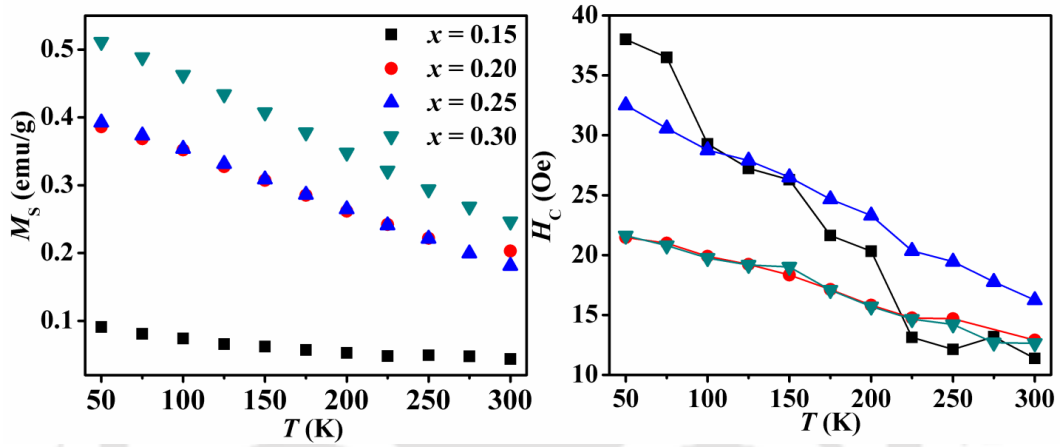

Figure 6.13 Temperature variations of M_S and H_C for x = 0.15, 0.20, 0.25 and 0.30 samples of $BaTi_{1-x}Fe_xO_3$.

The origin of FM in TM doped BTO is a subject of debate. Several mechanisms including double exchange, superexchange, RKKY interaction, cation ordering, and lattice strain have been reported to explain the FM in TM ions doped $BaTiO_3$ [91, 186, 206, 218, 219]. Guo *et al.* [186] reported FM in Fe doped $BaTiO_3$, where they found linear increase in the value of M_S and T_C with increase in Fe concentration. They found *M*s values in the range 1.72 – 22 emu/g and Curie temperatures in the range 770K – 800 K, which are higher than that we obtained in the present investigation. Such large M_S value and high ferromagnetic T_C are expected for the strong ferromagnetic interaction arising from the double exchange interaction in $Fe^{3+} - O_2^{2-} - Fe^{4+}$ networks. Considering the small value of M_S and comparatively low T_C, double exchange interaction is unlikely to play a role in the present series of samples. The RKKY interaction induced FM was reported for tetragonal $BaTi_{0.95}Fe_{0.05}O_{3-\delta}$ [91] and is based on free electrons that mediate the exchange interaction among the isolated magnetic ions. However, the resistance value

in the present series of samples is found to be in the order of MΩ, which certainly rules out the presence of adequate free electrons to mediate such interaction. However, as explained in section 6.2, the samples with x = 0.15 – 0.30 are in biphasic structure containing tetragonal and hexagonal phases such that hexagonal phase dominates in the samples having higher Fe concentration. Therefore, it is imperative to consider the crystallographic positions of substituted Fe ions to explain the possible mechanism behind the magnetic properties in these samples. In the hexagonal $BaTiO_3$, Ti atoms occupy two crystallographic positions such as face-sharing octahedra (Ti1) and corner sharing octahedra (Ti2) [91, 220]. The Fe ions at Ti2 site interact ferromagnetically with other Fe ions in Ti2 site. On the other hand the interaction among Fe ions in Ti1 and Ti2 sites or within Ti1 sites is reported to be antiferromagnetic in nature [91, 206]. Considering such intra-site and inter-site interactions among the Fe ions, Lin *et al.* [206] reported decrease in M_s values with increase in Fe concentration. This observation is in contradiction to our results where we have observed increase in M_S values with increase in Fe concentration and rules out such interaction for the observed FM. Valant *et al.* [218] reported FM in Fe doped hexagonal $BaTiO_3$, synthesized at 1500 °C, in terms of continuous order-disorder transition of Fe ions between the two Ti^{4+} crystallographic sites. The sintering temperature was found to be critical for such ordering and for the FM ordering. No cation ordering, and hence FM was observed for the sample sintered below 1500 °C [218]. Since the sintering temperature for the present series of samples is far below 1500 °C, such cation ordering induced FM is not expected in our sample. On the other hand, Zorko *et al.* [219] argued the presence of pseudocubic local regions in hexagonal $Ba(Ti, Fe)O_3$ that produces strain and hence FM at the interface of two regions. On increasing Fe concentration, the strain was found to reduce due to the destabilization of pseudocubic regions by Fe substitution and hence it results in decreased magnetization [219]. Similar strain-induced FM can not be accounted for the present series of samples as we observe increase in magnetization with increase in Fe concentration. As discussed earlier, we observed positive value of θ_C which confirms the ferromagnetic interaction among the Fe ions in the compounds. Guo *et al.* [186] reported a large M_S value of the order of 6 emu/g for x = 0.25 sample of $BaTi_{1-x}Fe_xO_3$ where it was attributed to the double exchange interaction in the $Fe^{3+} - O_2^{2-} - Fe^{4+}$ networks. However, the observed value of M_S in the present series of samples is quite small; moreover the measured resistance is quite high. Hence double exchange interaction is not expected to play a role. The

observed small value of M_S hints that the FM interaction in the present series of samples could be due to the similar exchange interaction as observed in diluted magnetic semiconductors [221]. Fe substitution in Ti ions creates oxygen vacancies, which act as an electron trap center. The trapped electron occupies an orbit that overlaps with the *d*-shells of neighboring TM ions and constitutes a ferromagnetic bubble, which is known as Bound Magnetic Polaron (BMP) [222, 223]. In such case, the measured initial $M - H$ curves can be analyzed by fitting to the following equation [221]:

$$M = M_0 L(x) + \chi_m H \tag{6.3}$$

The first term in eq. (6.3) is the ferromagnetic contribution from BMPs and the second term is due to PM/AFM matrix. Here, $M_0 = Nm_s$ where N is the number of BMPs involved and m_s is the actual spontaneous moment per BMP. $L(x) = \coth x - 1/x$ is the Langevin function with $x = m_{eff}H/k_BT$, where m_{eff} is effective spontaneous moment per BMP and χ_m is susceptibility of the matrix. The initial $M - H$ curves for $x = 0.15 - 0.30$ could be fitted to eq. (6.3) and such fittings in $T = 50$ K to 300 K are shown in Fig. 6.14. It is seen that the experimental data are well fitted to the BMP model. The estimated values of M_0, m_{eff} and χ_m at $T = 50$ K and 300 K are given in Table 6.5. For a given doping concentration, the M_0 values are found to decrease with increase in temperature and this could be understood in terms of reduction in FM interaction among the BMPs due to increased thermal energy. However, m_{eff} follows a temperature dependence that is contradictory to M_0. Such temperature variation of m_{eff} could be related to the increase in the size of BMPs with increase in temperature [221]. In the present series of samples, the parameter M_0/m_{eff} is found to vary with temperature, signifying that one can not assume $m_{eff} = m_s$. In view of this restriction, we could not estimate N, the number density of BMPs. The average radius of BMP is found to be comparable to the unit cell volume of hexagonal phase of the corresponding compound similar to many oxide-based diluted magnetic semiconductors [221, 224]. It signifies that the BMPs are exclusively formed and accommodated easily within the hexagonal phase. The formation of BMPs within the hexagonal phase is favorable because of the high concentration of oxygen vacancies and it signifies the importance of hexagonal phase in introducing FM. However, one can not rule out the possibility of FM clusters in the AFM/PM matrix, since such scenario is also expected to follow an expression similar to that of eq. (6.3) [225]. However, such isolated FM clusters are expected to behave like superparamagnetic particles below certain blocking

temperature, and such blocking temperature is not noticed from the present magnetization measurements.

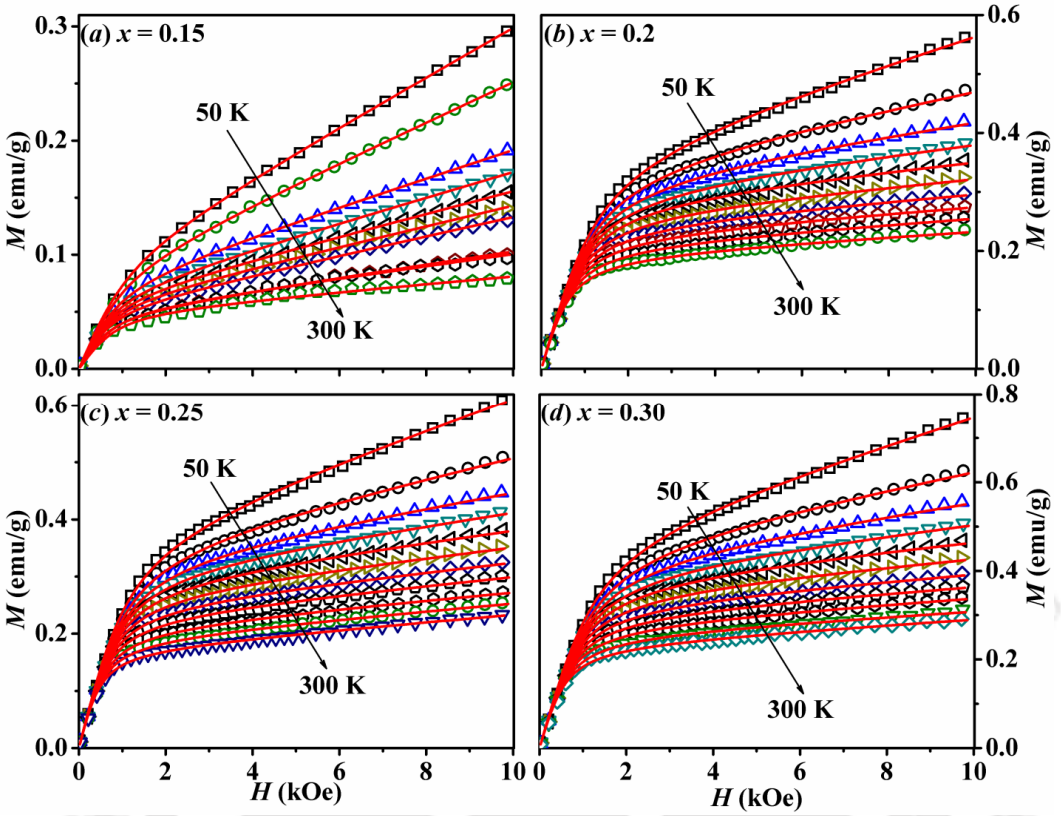

Figure 6.14 Initial magnetization curves (open symbols) for $BaTi_{1-x}Fe_xO_3$ with x = 0.15 – 0.3 along with the fitted data to Bound Magnetic Polaron model (eq. 6.3) at T = 50 K and 300 K.

Table 6.5 Parameters obtained from BMP model fit at T = 50 K and 300 K.

	M_0 (emu/g)		m_{eff} (10^{-17} emu)		χ_m (10^{-6}cgs unit)		BMP radius(Å)		Hexagonal cell volume (Å^3)
x	50 K	300K	50K	300K	50K	300K	50K	300K	
0.15	0.09	0.05	1.51	10.90	0.21	3.24	200	470	396.05
0.20	0.36	0.14	1.36	15.50	0.22	4.32	114	313	395.59
0.25	0.36	0.17	1.54	20.57	0.26	6.33	107	311	395.76
0.30	0.47	0.24	1.36	17.01	0.30	6.07	104	310	395.33

6.7 Conclusion

The structural and magnetic properties of Fe doped $BaTiO_3$ samples prepared by solid state reaction method have been investigated. Fe substitution induces a gradual transition of crystal structure from tetragonal to hexagonal unit cell. The samples with x = 0.15 – 0.3 exhibit the room temperature ferromagnetism with their T_C in the range of 397 K to 464 K. The observed FM is explained in terms of formation of bound magnetic polaron exclusively at the hexagonal phase. Although Fe substitution induces room temperature ferromagnetism in $BaTiO_3$, such substitution is detrimental towards the ferroelectric properties of the samples. The Fe substitution leads to the disappearance of ferroelectricity, which can be understood in terms of the evolution of non-ferroelectric hexagonal phase and the reduction in the Ti – O covalent bonds.

Chapter 7

Conclusion

The summary of results obtained from the structural, dielectric and magnetic studies carried out in Mn doped-$YFeO_3$, Sm doepd-$BiFeO_3$, Fe doped-$PbTiO_3$ and Fe doped-$BaTiO_3$ samples are presented in this chapter.

$YFe_{1-x}Mn_xO_3$ (x = 0 – 0.3) samples were prepared by solid state reaction method and they are found to be in single phase form. The XRD patterns were Rietveld refined using *Pnma* space group *i.e.*, with orthorhombic crystal structure. Substitution of Mn in Fe site leads to the expansion of unit cell along *a*-axis as well as the contraction of *bc*-plane. It is explained in terms of the ionic size mismatch between Mn^{3+} and Fe^{3+} ions and the Jahn-Teller distortion associated with the Mn^{3+} ions. The microstructural studies based on FE-SEM images reveal well defined grains with their size in the range 1 – 2 μm.

The frequency spectra of Z'' of $YFe_{1-x}Mn_xO_3$ (x = 0 – 0.3) samples exhibit two relaxation peaks corresponding to the grains and grain boundaries. The asymmetric and broad relaxation peaks suggest their departure from the ideal Debye behavior. Similar asymmetric and broad peaks corresponding to grains are observed in the frequency spectra of M'' of $YFe_{1-x}Mn_xO_3$ (x = 0 – 0.3) samples. The peaks are found to shift towards the higher frequency with increase in temperature revealing a thermally active relaxation process. The activation energy associated with the relaxation dynamics suggests that ionized oxygen vacancies play a major role in the relaxation process. The activation energy values corresponding to grains mostly decrease from 1.5 eV for x = 0 to 0.2 eV for x = 0.3 sample. Similarly, the activation energy values corresponding to grain boundaries

decrease from 1.8 eV for $x = 0$ to 0.4 eV for $x = 0.3$ sample. Substitution of Mn in $YFeO_3$ is expected to increase the concentration of oxygen vacancy and their cluster. Such cluster of oxygen vacancies makes the relaxation process easier and reduces the activation energy of relaxation. The Nyquist plots of the samples exhibit two depressed semicircles such that their center lie below the Z' axis. These plots are successfully modeled to an equivalent circuit consisting of two parallel circuits corresponding to grains and grain boundaries connected in series. The circuit for grains consists of parallel combination of a resistor and capacitance, while the circuit corresponding to grain boundaries consists of parallel combination of a resistor and a constant phase element (CPE). The values of resistance of grains and grain boundaries decrease with increase in temperature and is attributed to the increase in oxygen vacancies. The conductivity activation energy corresponding to grains is found to decrease from 1.62 eV for $x = 0$ to 0.41 eV for $x = 0.3$ sample. Similarly, the conductivity activation energy corresponding to grain boundaries is found to decrease from 1.92 eV for $x = 0$ to 0.45 eV for $x = 0.2$ sample. The increase in dc conductivity related to oxygen vacancies gives rise to universal dielectric response. The similarity in the values of activation energy for relaxation and conduction suggests that the same species are responsible for relaxation and conduction process. Analysis of frequency dispersions of ac conductivity of the samples shows that the conductivity of $x = 0$ to 0.25 samples is controlled by the overlapping large polaron tunneling (OLPT) model and for $x = 0.3$ sample both small polaron tunneling (SPT) and OLPT are found to play a role. The frequency dispersions of ε' and ε'' are studied in terms of Cole-Cole equation and by considering the contribution of electrical conductivity to the dielectric response. The temperature variations of ε' and $\tan\delta$ of $x = 0 - 0.1$ samples show distinct anomalies in the vicinity of their magnetic transition and it is explained in terms of the fluctuations of polar order. The value of ε' and $\tan\delta$ measured at a particular frequency and temperature increases with increase in Mn concentration.

The parent compound $YFeO_3$ exhibits antiferromagnetic transition with Néel temperature (T_N) ~ 646 K. Substitution of Mn^{3+} for Fe^{3+} ions weakens the superexchange interaction and hence decrease the T_N to 428 K for $x = 0.3$ sample. The magnetic susceptibility data in the paramagnetic region were analyzed in terms of Curie-Weiss law and it confirms the antiferromagnetic ordering. In addition, the Mn substitution strongly influences the spin reorientation transition *i.e.*, from Γ_4 ($A_xF_yG_z$) to Γ_1 ($G_xC_yA_z$) spin configuration. The spin reorientation transition temperature is found to increase from 81

K for x = 0.1 to 295 K for x = 0.3 sample. It is explained in terms of significant magnetic anisotropy introduced by the substituted Mn^{3+} ions. These samples exhibit interesting exchange bias behavior above room temperature. The maximum value of exchange bias field was found to be 1.2 kOe around 413 K. The observed exchange bias is explained in terms of anisotropic exchange interaction across the interface of two magnetic phases having dominant collinear antiferromagnetism with Γ_1 configuration and a weak ferromagnetism in Γ_4 configuration.

$Bi_{1-x}Sm_xFeO_3$ (x = 0 – 0.3) samples were prepared by the sol-gel method. The samples with $x \geq 0.1$ are found to be free from the commonly observed secondary phases of Bi_2O_3-Fe_2O_3 systems. The XRD patterns of x = 0 – 0.1 were Rietveld refined to rhombohedral crystal structure with *R3c* space group. The increase in Sm concentration induces structural transition from *R3c* phase to *Pnma* phase. The structural transition is further confirmed from the Raman spectra of the samples. The lattice constant values of the samples corresponding to rhombohedral phase are found to decrease with increase in Sm concentration and it is explained in terms of the smaller ionic radius of Sm^{3+} ion substituting Bi^{3+} ion. The Sm substitution is found to reduce the average grain size, *i.e.*, from 1.2 μm for x = 0 to 0.6 μm for x = 0.3 sample.

The Nyquist plots of these samples were modeled to an equivalent circuit consisting of two parallel circuits corresponding to grains and grain boundaries connected in series combination. The individual circuit for grains and grain boundaries consists of parallel combination of a resistor, capacitor and a CPE. The temperature variations of ε' and tanδ reveal that the Polomska transition shifts towards the lower temperature with increase in Sm concentration. The Polomska transition becomes more prominent for the samples having smaller grain size and large surface-to-volume ratio and it indicates that Polomska transition is associated to the surface of the samples. The frequency dispersions of ε'' exhibit at least two relaxation peaks corresponding to grains and grain boundaries. The peaks are asymmetric in nature and they shift towards the higher frequency region with increase in temperature. The frequency variations of ε' and ε'' were studied in terms of Havriliak-Negami (HN) equation as well as considering the contribution of electrical conductivity to the dielectric response. The relaxation times obey the Arrhenius law of temperature dependence. The activation energy (E_a) values corresponding to grains are found to be in the range of 0.30 – 0.45 eV and it highlights the electron hopping between Fe^{3+} and Fe^{2+} ions in the grains. On the other hand, the activation energy corresponding to

grain boundaries are found to be in the range 0.68 – 0.80 eV, which is close to the relaxation energy for the short range movement of singly ionized oxygen vacancies. The frequency dispersion of ac conductivity data were studied in terms of Jonscher Power law (JPL) with the frequency exponent (s) in the range 0 to 2. The temperature variations of s of the samples signify that both SPT and OLPT are the main conduction mechanism in these samples.

Temperature variations of magnetization ($M - T$) under zero field-cooled (ZFC) and field-cooled (FC) conditions show that these plots bifurcate from each other. The bifurcation of ZFC and FC curves along with considerable increase in magnetization below 100 K clearly indicates the weak ferromagnetic nature of the samples. A non-zero value of remnant magnetization M_r (~ 0.004 emu/g) and coercive field H_C (~150 Oe) for $x = 0$ was observed. The smaller but non-zero value of M_r and H_C for $x = 0$ is resulted from the ferromagnetic interaction among a small concentration of Fe ions which are in its mixed valence state. Ferromagnetic like behavior with a clear opening in $M - H$ loop was observed for samples with $x \geq 0.15$ along with a linear increase in magnetization at higher applied fields. The linear increase at higher field reveals the dominance of the strong antiferromagnetic interaction even for the higher doped samples. We have also observed the presence of exchange bias like behavior for $x = 0.15$ and 0.2 samples with the maximum exchange bias field of 1.36 kOe for $x = 0.15$ sample at 150 K. The anisotropic exchange interaction at the interface of collinear antiferromagnetic domains of *Pnma* phase and the weak ferromagnetic domains of ferroelectric *R3c* phase contributes towards the observed exchange bias like behavior. The disappearance of exchange bias in $x = 0.25$ and 0.3 samples is attributed to their monophasic nature of structure.

$PbTi_{1-x}Fe_xO_3$ ($x = 0 - 0.3$) samples were prepared by the solid state reaction route and they are found to be in single phase. The XRD patterns were Rietveld refined by choosing *P4mm* space group in the tetragonal structure. Lattice constant a increases with increase in Fe concentration, while c is found to decrease. The overall variation of lattice parameters and tetragonality with x is discussed in terms of substitution of Fe as Fe^{3+} and Fe^{4+} in the sites of Ti ions. Raman spectroscopic studies reveal the tendency towards gradual structural transition from tetragonal to cubic phase as the Fe concentration is increased.

Combined Z'' and M'' spectra suggest the presence of three electroactive regions and they are identified as grains, grain boundaries and surface layers based on their capacitance value. Interestingly, the Z'' and M'' peaks for $x = 0.25$ and 0.3 are found to shift towards lower frequency with increase in temperature upto $T = 373$ K and $T = 353$ K respectively. It depicts the positive temperature coefficient of resistance (PTCR) for $x = 0.25$ and 0.3. Beyond the above characteristic temperatures (373 K, 353 K) the resistance values of these samples decrease with increase in temperature. The Nyquist plots were analyzed in terms of modeling to an electrical equivalent circuit considering the contribution from the entire electroactive regions. It is found that the resistance of grain boundaries and surface layers exhibits the PTCR behavior below 373 K for $x = 0.25$ and 353 K for $x = 0.3$ sample, while the resistance of grains of both samples exhibits PTCR behavior upto 420 K. The PTCR behavior for surface layer resistance and grain boundaries resistance is explained in terms of Heywang-Jonker model. The M'' and Z'' data were further analyzed in terms of Bergman four-parameter formulae for generalized susceptibility. The activation energy values for relaxation obtained from the fitting of peak frequency to Arrhenius law are found to be 1.3 eV and 0.7 eV for grain boundaries of $x = 0.25$ and 0.30 samples and these values corresponding to surface layers are found to be 0.44 eV and 0.43 eV respectively. The values of relaxation energy suggest that the ionized oxygen vacancy acts as dipole in tuning the observed dielectric relaxation. The underlying conduction mechanism is found to be small polaron tunneling and overlapping large polaron tunneling models as per the analysis of ac conductivity data. The conduction activation energy values are found to be 0.6 eV and 0.54 eV for $x = 0.25$ and 0.3 samples respectively.

Fe substitution gradually induces ferromagnetic like behavior in $PbTiO_3$. Diamagnetic behavior is observed for $x = 0.0$ and 0.05, while the samples with Fe concentration in the range $0.1 \leq x \leq 0.2$ show paramagnetic behavior down to 25 K. The samples with $x = 0.25$ and 0.30 show ferromagnetic behavior at room temperature with transition temperature (T_C) values 650 K and 660 K respectively. Magnetic susceptibility data fitted to Curie-Weiss law suggest ferromagnetic ordering for $x = 0.25$ and 0.3 samples. The double exchange interaction in $Fe^{3+} - O^{2-} - Fe^{4+}$ networks accounts for the observed ferromagnetism. The isothermal $M - H$ loops across T_C were analyzed in terms of law of approach to saturation. The temperature dependence of saturation magnetization follows the Bloch's equation signifying the spin wave excitation in the measured

temperature range. The effective magnetocrystalline anisotropy constant value is found to decrease with increase in temperature. The coercive field is found to increase with increase in temperature upto around 550 K and beyond that it decreases. The anomalous increase in coercivity is discussed in the framework of coupling between magnetic and the electric order.

$BaTi_{1-x}Fe_xO_3$ (x = 0 – 0.3) samples were prepared by solid state reaction method and they are found to be in single phase form. Analysis of XRD patterns and Raman spectra of the samples confirm structural transition from tetragonal phase to hexagonal phase due to Fe substitution. Room temperature ferromagnetism is observed for x = 0.15 – 0.30 samples. The ferromagnetic (FM) transition temperature (T_C) increases from 397 K for x = 0.15 to 464 K for x = 0.3 sample. The FM is explained in terms of Bound Magnetic Polaron (BMP) model. The BMPs are found to form within the hexagonal phase of the samples because of higher oxygen vacancy concentrations in this phase. The temperature variation of dielectric constant reveals the decrease in ferroelectric transition temperatures with increase in Fe concentration.

Future Scope of Studies

The following are the future scopes of studies in this area:

- Measurement of electric polarization as a function of temperature across the Néel temperature of $YFe_{1-x}Mn_xO_3$ samples and it may lead the study of magnetism induced ferroelectricity in the systems.
- It will be very interesting to investigate for ferrolectricity across the spin re-orientation transition of $YFe_{1-x}Mn_xO_3$ compounds especially for x = 0.25 and 0.3 samples.
- Extend the study of exchange bias of $YFe_{1-x}Mn_xO_3$ series using higher magnetic field (~ 9 T).
- Preparation of thin films of $YFe_{1-x}Mn_xO_3$ samples to explore the exchange bias.
- $Bi_{1-x}Sm_xFeO_3$ samples with x = 0.15 and 0.2 samples may be taken up for the further systematic study of exchange bias using higher magnetic field. These two samples can be taken up for the study of exchange bias in thin film forms.

- The substitution of other rare-earth element in the Bi site of $BiFeO_3$ would give further information on magnetic and dielectric properties.
- It is useful to study the magnetoelectric/magnetodielectric properties to explore the multiferroicity in these samples.
- Substitution of other transition elements at the Ti site of $PbTiO_3$ and $BaTiO_3$ series is expected to lead to better magneto-electric materials.

References

[1] O. Muller, R. Roy, The Major Ternary Structural Families, Springer-Verlag, New York (1974.).

[2] A.S. Bhalla, R. Guo, R. Roy, Mat. Res. Innovat., **4** (2000) 3.

[3] M.A. Peña, J.L.G. Fierro, Chem. Rev., **101** (2001) 1981.

[4] H. Liu, X. Yang, Ferroelectrics, **507** (2017) 69.

[5] M. Johnsson, P. Lemmens, Handbook of Magnetism and Advanced Magnetic Materials, in, John Wiley & Sons, Ltd, 2007.

[6] V.M. Goldschmidt, Geochemistry, Oxford University Press, London, (1958).

[7] H. Schmid, Ferroelectrics, **162** (1994) 317.

[8] D. Khomskii, Physics, **2** (2009) 20.

[9] N.A. Spaldin, S.-W. Cheong, R. Ramesh, Phys. Today, **63** (2010) 38.

[10] S. Blundell, Magnetism in Condensed Matter, Oxford University Press Neywork, (2001).

[11] N.A. Spaldin, Magnetic Materials: Fundamentals and Applications, Cambridge University Press, Second edition, (2011).

[12] H. Kramer, Physica, **1** (1934) 182.

[13] J.B. Goodenough, Phys. Rev. B, **100** (1955) 564.

[14] M.A. Ruderman, C. Kittel, Phys. Rev., **96** (1954) 99.

[15] T. Kasuya, Prog. Theor. Phys., **16** (1956) 58.

[16] K. Yoshida, Phys. Rev., **106** (1957) 893.

[17] C. Zener, Phys. Rev., **81** (1951) 440.

[18] C. Zener, Phys. Rev., **82** (1951) 403.

[19] P.W. Anderson, H. Hasegawa, Phys. Rev., **100** (1955) 675.

[20] I. Dzyaloshinskii, J. Phys. Chem. Solids, **4** (1958) 241.

[21] T. Moriya, Phys. Rev., **120** (1960) 91.

[22] B.D. Cullity, C.D. Graham, Introduction to Magnetic Materials, John Wiley & Sons, 2nd edition (2009).

[23] J. Nogués, I.K. Schuller, J. Magn. Magn. Mater., **192** (1999) 203.

[24] W.H. Meiklejohn, C.P. Bean, Phys. Rev., **102** (1956) 1413.

[25] J. Nogués, J. Sort, V. Langlais, V. Skumryev, S. Suriñach, J.S. Muñoz, M.D. Baró, Phys. Rep, **422** (2005) 65.

[26] E. Barsoukov, J.R. Macdonald, Impedance Spectroscopy Theory, Experiment, and Applications, Willey-Interscience (Second edition), (2005).

[27] S. Havriliak, S. Negami, Polymer, **8** (1967) 161.

[28] A. Boersma, J. van Turnhout, M. Wübbenhorst, Macromolecules, **31** (1998) 7453.

[29] N.G. McCrum, B.E. Read, G. Williams, Anelastic and Dielectric Effects in Polymeric Solids, Wiley, New York, (1967).

[30] H. Wagner, R. Richert, Polymer, **38** (1997) 5801.

[31] D.K. Pradhan, R.N.P. Choudhary, C. Rinaldi, R.S. Katiyar, J. Appl. Phys., **106** (2009) 024102.

[32] P.B. Macedo, C.T. Moynihan, R. Boese, Phys. Chem. Glasses, **13** (1972) 171.

[33] C.T. Moynihan, L.P. Boesch, N.L. Laberge, Phys. Chem. Glasses, **14** (1973) 122.

[34] R. Kohlrausch, Progg. Ann. Phys., **91** (1854) 179.

[35] G. Williams, D.C. Watts, Trans. Faraday Soc., **66** (1970) 80.

[36] R. Bergman, J. Appl. Phys., **88** (2000) 1356.

[37] A.K. Jonscher, Nature, **267** (1977) 673.

[38] S. Geller, E.A. Wood, Acta Cryst., **9** (1956) 563.

[39] S. Geller, J. Chem. Phys., **24** (1956) 1236.

[40] R.L. White, J. Appl. Phys., **40** (1969) 1061.

[41] P. Mandal, A. Sundaresan, C.N.R. Rao, A. Iyo, P.M. Shirage, Y. Tanaka, C. Simon, V. Pralong, O.I. Lebedev, V. Caignaert, B. Raveau, Physical Review B, **82** (2010) 100416.

[42] G.W. Durbin, C.E. Johnson, M.F. Thomas, J. Phys. C: Solid State Phys, **8** (1975) 3051.

[43] I.S. Jacobs, H.F. Burne, L.M. Levinson, J. Appl. Phys., **42** (1971) 1631.

[44] H. Lütgemeier, H.G. Bohn, M. Brajczewska, J. Magn. Magn. Mater., **21** (1980) 289.

[45] Y. Ma, X.M. Chen, Y.Q. Lin, J. Appl. Phys., **103** (2008) 124111.

[46] Y. Ma, Y.J. Wu, Y.Q. Lin, X.M. Chen, J. Mater Sci: Mater Electron, **21** (2010) 838.

[47] J.-H. Lee, Y.K. Jeong, J.H. Park, M.-A. Oak, H.M. Jang, J.Y. Son, J.F. Scott, Phys. Rev. Lett., **107** (2011) 117201.

[48] M. Shang, C. Zhang, T. Zhang, L. Yuan, L. Ge, H. Yuan, S. Feng, Appl. Phys. Lett., **102** (2013) 062903.

[49] D. Sando, A. Barthélémy, M. Bibes, J. Phys.: Condens. Matter, **26** (2014) 473201.

[50] C. Michel, J.-M. Moreau, G.D. Achenbach, R. Gerson, W.J. James, Solid State Commun., **7** (1969) 701.

[51] J.M. Moreau, C. Michel, R. Gerson, W.J. James, J. Phys. Chem. Solids, **32** (1971) 1315.

[52] A.J. Jacobson, B.E.F. Fender, J. Phys. C: Solid State Phys, **8** (1975) 844.

[53] F. Kubel, H. Schmid, Acta Cryst., **B46** (1990) 698.

[54] G.A. Smolenskiĭ, I.E. Chupis, Sov. Phys. Usp., **25** (1982) 475.

[55] D. Lebeugle, D. Colson, A. Forget, M. Viret, P. Bonville, J.F. Marucco, S. Fusil, Phys. Rev. B, **76** (2007) 024116.

[56] J.D. Bucci, B.K. Robertson, W.J. James, J. Appl. Cryst., **5** (1972) 187.

[57] A. Palewicz, R. Przenioslo, I. Sosnowska, A.W. Hewat, Acta Cryst., **B63** (2007) 537.

[58] I. Sosnowska, T.P. Neumaier, E. Steichele, J. Phys. C: Solid State Phys, **15** (1982) 4835.

[59] D. Lebeugle, D. Colson, A. Forget, M. Viret, Appl. Phys. Lett., **91** (2007) 022907.

[60] A. Kumar, N.M. Murari, R.S. Katiyar, Appl. Phys. Lett., **92** (2008) 152907.

[61] S.A.T. Redfern, W. Can, J.W. Hong, G. Catalan, J.F. Scott, J. Phys.: Condens. Matter, **20** (2008) 452205.

[62] M. Polomska, W. Kaczmarek, Z. Pająk, Phys. Status Solidi B, **23** (1974) 567.

[63] G. Catalan, J.F. Scott, Adv. Mater., **21** (2009) 2463.

[64] S. Hunpratub, P. Thongbai, T. Yamwong, R. Yimnirun, S. Maensiri, Appl. Phys. Lett., **94** (2009) 062904.

[65] Q. Ke, X. Lou, Y. Wang, J. Wang, Phys. Rev. B, **82** (2010) 024102.

[66] J. Wu, J. Wang, J. Am. Ceram. Soc., **93** (2010) 2795.

[67] A.M. Kadomtseva, A.K. Zvezdin, Y.F. Popov, A.P. Pyatakov, G.P. Vorob'ev, JETP Lett., **79** (2004) 571.

[68] C. Ederer, N.A. Spaldin, Phys. Rev. B, **71** (2005) 060401.

[69] B. Ruette, S. Zvyagin, A.P. Pyatakov, A. Bush, J.F. Li, V.I. Belotelov, A.K. Zvezdin, D. Viehland, Phys. Rev. B, **69** (2004) 064114.

[70] S.-T. Zhang, Y. Zhang, M.-H. Lu, C.-L. Du, Y.-F. Chen, Z.-G. Liu, Y.-Y. Zhu, N.-B. Ming, X.Q. Pan, Appl. Phys. Lett., **88** (2006) 162901.

[71] G.L. Yuan, S.W. Or, J.M. Liu, Z.G. Liu, Appl. Phys. Lett., **89** (2006) 052905.

[72] G.L. Yuan, S.W. Or, J. Appl. Phys., **100** (2006) 024109.

[73] V.R. Palkar, D.C. Kundaliya, S.K. Malik, S. Bhattacharya, Phys. Rev. B, **69** (2004) 212102.

[74] D.H. Wang, W.C. Goh, M. Ning, C.K. Ong, Appl. Phys. Lett., **88** (2006) 212907.

[75] J.S. Kim, C.I. Cheon, Y.N. Choi, P.W. Jang, J. Appl. Phys., **93** (2003) 9263.

[76] J.S. Kim, C.I. Cheon, C.H. Lee, P.W. Jang, J. Appl. Phys., **96** (2004) 468.

[77] V.A. Khomchenko, D.A. Kiselev, J.M. Vieira, L. Jian, A.L. Kholkin, A.M.L. Lopes, Y.G. Pogorelov, J.P. Araujo, M. Maglione, J. Appl. Phys., **103** (2008) 024105.

[78] S.-T. Zhang, L.-H. Pang, Y. Zhang, M.-H. Lu, Y.-F. Chen, J. Appl. Phys., **100** (2006) 114108.

[79] V.A. Khomchenko, D.A. Kiselev, I.K. Bdikin, V.V. Shvartsman, P. Borisov, W. Kleemann, J.M. Vieira, A.L. Kholkin, Appl. Phys. Lett., **93** (2008) 262905.

[80] G. Shirane, R. Pepinsky, B.C. Frazer, Acta Cryst., **9** (1956) 131.

[81] H. Meštrić, R.A. Eichel, T. Kloss, K.P. Dinse, S. Laubach, S. Laubach, P.C. Schmidt, K.A. Schönau, M. Knapp, H. Ehrenberg, Phys. Rev. B, **71** (2005) 134109.

[82] R.J. Nelmes, W.F. Kuhs, Solid State Commun., **54** (1985) 721.

[83] V.G. Bhide, K.G. Deshmukh, M.S. Hegde, Physica, **28** (1962) 871.

[84] Z. Zhang, J. Hu, Z. Xu, H. Qin, L. Sun, F. Gao, Y. Zhang, M. Jiang, Solid State Sciences, **13** (2011) 1391.

[85] Z. Ren, G. Xu, X. Wei, Y. Liu, X. Hou, P. Du, W. Weng, G. Shen, G. Han, Appl. Phys. Lett., **91** (2007) 063106.

[86] V.R. Palkar, S.K. Malik, Solid State Commun., **134** (2005) 783.

[87] K.C. Verma, R.K. Kotnala, N.S. Negi, Appl. Phys. Lett., **92** (2008) 152902.

[88] W. Heywang, K. Lubitz, W. Wersing, Pezoelectricity: Evolution and Future of Technology, Springer (2008).

[89] G.H. Kwei, A.C. Lawson, S.J.L. Billinge, S.W. Cheong, J. Phys. Chem., **97** (1993) 2368.

[90] H. Nakayama, Y.H. Katayama, Jpn. J. Appl. Phys., **40** (2001) L1355.

[91] B. Xu, K.B. Yin, J. Lin, Y.D. Xia, X.G. Wan, J. Yin, X.J. Bai, J. Du, Z.G. Liu, Phys. Rev. B, **79** (2009) 134109.

[92] S. Ray, P. Mahadevan, S. Mandal, S.R. Krishnakumar, C.S. Kuroda, T. Sasaki, T. Taniyama, M. Itoh, Phys. Rev. B, **77** (2008) 104416.

[93] A. Rajamani, G.F. Dionne, D. Bono, C.A. Ross, J. Appl. Phys., **98** (2005) 063907.

[94] M. Attfield, P. Barnes, J.K. Cockcroft, H. Driessen, http://img.chem.ucl.ac.uk/.

[95] R.A. Young, The Rietveld Method, Oxford University Press, New York (1996).

[96] https://autodo.info/pages/s/scanning-electron-microscope-diagram/.

[97] S. Foner, Rev. Sci. Instr., **30** (1959) 548.

[98] F.E. Mabbs, D. Collison, Electron Paramagnetic Resonance of d Transition Metal Compounds, Elsevier Science Publishers B.V., Amsterdam, (1992).

[99] M. Eibschütz, S. Shtrikman, D. Treves, Phys. Rev., **156** (1967) 562.

[100] D. Treves, Phys. Rev., **125** (1962) 1843.

[101] J.A. de Jong, I. Razdolski, A.M. Kalashnikova, R.V. Pisarev, A.M. Balbashov, A. Kirilyuk, T. Rasing, A.V. Kimel, Phys. Rev. Lett., **108** (2012) 157601.

[102] S. Cao, H. Zhao, B. Kang, J. Zhang, W. Ren, Sci. Rep., **4** (2014) 5960.

[103] J. Scola, Y. Dumont, N. Keller, M. Vallée, J.G. Caputo, I. Sheikin, P. Lejay, A. Pautrat, Phys. Rev. B, **84** (2011) 104429.

[104] P. Mandal, C.R. Serrao, E. Suard, V. Caignaert, B. Raveau, A. Sundaresan, C.N.R. Rao, J. Solid State Chem., **197** (2013) 408.

[105] S. Geller, E.A. Wood, Acta Crystallogr., **9** (1956) 563.

[106] S. Acharya, J. Mondal, S. Ghosh, S.K. Roy, P.K. Chakrabarti, Mater. Lett., **64** (2010) 415.

[107] J. Rodríguez-Carvajal, Phys. B: Condens. Matter, **192** (1993) 55.

[108] Y. Sundarayya, P. Mandal, A. Sundaresan, C.N.R. Rao, J. Phys.: Condense. Matter, **23** (2011) 436001.

[109] Y. Nagata, S. Yashiro, T. Mitsuhashi, A. Koriyama, Y. Kawashima, H. Samata, J. Magn. Magn. Mater., **237** (2001) 250.

[110] Y.J. Wong, J. Hassan, M. Hashim, J. Alloy. Compd., **571** (2013) 138.

[111] S.A. Arrhenius, Z. Phys. Chem., **4** (1889) 96.

[112] A. Srivastava, A. Garg, F.D. Morrison, J. Appl. Phys., **105** (2009) 054103.

[113] Y. Qin, X. Qiang Liu, X. Ming Chen, J. Appl. Phys., **113** (2013) 044113.

[114] S. Kumari, N. Ortega, A. Kumar, S.P. Pavunny, J.W. Hubbard, C. Rinaldi, G. Srinivasan, J.F. Scott, R.S. Katiyar, J. Appl. Phys., **117** (2015) 114102.

[115] B. Ghosh, D. Bhattacharya, A.K. Raychaudhuri, S. Arumugam, J. Appl. Phys., **105** (2009) 123914.

[116] D. Rajasree, S. Tanushree, K. Mandal, J. Phys. D.: Appl. Phys., **45** (2012) 455002.

[117] M. Sánchez-Andújar, S. Yáñez-Vilar, J. Mira, N. Biskup, J. Rivas, S. Castro-García, M.A. Señarís-Rodríguez, J. Appl. Phys., **109** (2011) 054106.

[118] R. Thomas, V.K. Varadan, S. Komarneni, D.C. Dube, J. Appl. Phys., **90** (2001) 1480.

[119] A.S. Nowick, A.V. Vaysleyb, I. Kuskovsky, Phys. Rev. B, **58** (1998) 8398.

[120] K. Funke, Prog. Solid State Chem., **22** (1993) 111.

[121] S. Khadhraoui, A. Triki, S. Hcini, S. Zemni, M. Oumezzine, J. Magn. Magn. Mater., **371** (2014) 69.

[122] S. Mahajan, D. Haridas, S.T. Ali, N.R. Munirathnam, K. Sreenivas, O.P. Thakur, C. Prakash, Phys. B: Condense Matt., **451** (2014) 114.

[123] S. Ke, H. Huang, S. Yu, L. Zhou, J. Appl. Phys., **107** (2010) 084112.

[124] S.R. Elliott, Solid State Ion, **70–71, Part 1** (1994) 27.

[125] S.A. Howard, J.K. Yau, H.U. Anderson, J. Appl. Phys., **65** (1989) 1492.

[126] U. Balachandran, N.G. Eror, Commun. Am. Ceram. Soc. C, **64** (1981) 75.

[127] S.R. Elliot, Adv. Phys., **36** (1987) 135.

[128] K.A. Krezhov, P.S. Jajdzhiev, A.M. Kadomtseva, I.B. Krinettskii, M.M. Lukina, J. Phys. C: Solid State Phys., **15** (1982) 6437.

[129] L.T. Tsymbal, Y.B. Bazaliy, V.N. Derkachenko, V.I. Kamenev, G.N. Kakazei, F.J. Palomares, P.E. Wigen, J. Appl. Phys., **101** (2007) 123919.

[130] E. Lima Jr, T.B. Martins, H.R. Rechenberg, G.F. Goya, C. Cavelius, R. Rapalaviciute, S. Hao, S. Mathur, J. Magn. Magn. Mater., **320** (2008) 622.

[131] S. Mathur, M. Veith, R. Rapalaviciute, H. Shen, G.F. Goya, W.L. Martins Filho, T.S. Berquo, Chem. Mater., **16** (2004) 1906.

[132] A. Hossein, S. Hadi, K. Parviz, P. Asok, A. Mehmet, Z. Khalil, J. Phys. D: Appl. Phys., **43** (2010) 245002.

[133] K. Mukhopadhyay, A.S. Mahapatra, P.K. Chakrabarti, J. Magn. Magn. Mater., **329** (2013) 133.

[134] A. Jaiswal, R. Das, S. Adyanthaya, P. Poddar, J. Phys.Chem. C, **115** (2011) 2954.

[135] J. Barman, T. Bora, S. Ravi, J. Magn. Magn. Mater., **385** (2015) 93.

[136] Y. Sun, J.-Z. Cong, Y.-S. Chai, L.-Q. Yan, Y.-L. Zhao, S.-G. Wang, W. Ning, Y.-H. Zhang, Appl. Phys. Lett., **102** (2013) 172406.

[137] Y. Sundarayya, P. Mandal, A. Sundaresan, C.N.R. Rao, J Phys. Condense. Matter, **23** (2011) 436001.

[138] D. Deng, J. Zheng, D. Yu, B. Wang, D. Sun, M. Avdeev, Z. Feng, C. Jing, B. Lu, W. Ren, S. Cao, J. Zhang, Appl. Phys. Lett., **107** (2015) 102404.

[139] P. Ravindran, R. Vidya, A. Kjekshus, H. Fjellvåg, O. Eriksson, Phys. Rev. B, **74** (2006) 224412.

[140] J.B. Neaton, C. Ederer, U.V. Waghmare, N.A. Spaldin, K.M. Rabe, Phys. Rev. B, **71** (2005) 014113.

[141] W. Eerenstein, N.D. Mathur, J.F. Scott, Nature, **442** (2006) 759.

[142] A.K. Pradhan, K. Zhang, D. Hunter, J.B. Dadson, G.B. Loiutts, P. Bhattacharya, R. Katiyar, J. Zhang, D.J. Sellmyer, U.N. Roy, Y. Cui, A. Burger, J. Appl. Phys., **97** (2005) 093903.

[143] S.T. Zhang, M.H. Lu, D. Wu, Y.F. Chen, N.B. Ming, Appl. Phys. Lett., **87** (2005) 262907.

[144] T. Durga Rao, R. Ranjith, S. Asthana, J. Appl. Phys., **115** (2014) 124110.

[145] P. Suresh, S. Srinath, J. Appl. Phys., **113** (2013) 17D290.

[146] P. Suresh, P.D. Babu, S. Srinath, J. Appl. Phys., **115** (2014) 17D905.

[147] V.A. Khomchenko, D.V. Karpinsky, A.L. Kholkin, N.A. Sobolev, G.N. Kakazei, J.P. Araujo, I.O. Troyanchuk, B.F.O. Costa, J.A. Paixao, J. Appl. Phys., **108** (2010) 074109.

[148] V.A. Khomchenko, J.A. Paixão, V.V. Shvartsman, P. Borisov, W. Kleemann, D.V. Karpinsky, A.L. Kholkin, Scr. Mater., **62** (2010) 238.

[149] K.S. Nalwa, A. Garg, J. Appl. Phys., **103** (2008) 044101.

[150] P. Sharma, S. Satapathy, D. Varshney, P.K. Gupta, Mat. Chem. Phys., **162** (2015) 469.

[151] Q. Li, S. Bao, Y. Liu, Y. Li, Y. Jing, J. Li, J. Alloy. Compd., **682** (2016) 672.

[152] S.R. Das, R.N.P. Choudhary, P. Bhattacharya, R.S. Katiyar, P. Dutta, A. Manivannan, M.S. Seehra, J. Appl. Phys., **101** (2007) 4104.

[153] D. Kothari, V. Raghavendra Reddy, V.G. Sathe, A. Gupta, A. Banerjee, A.M. Awasthi, J. Magn. Magn. Mater., **320** (2008) 548.

[154] H. Fukumura, H. Harima, K. Kisoda, M. Tamada, Y. Noguchi, M. Miyayama, J. Magn. Magn. Mater., **310** (2007) e367.

[155] S. Chaturvedi, P. Shyam, A. Apte, J. Kumar, A. Bhattacharyya, A.M. Awasthi, S. Kulkarni, Phys. Rev. B, **93** (2016) 174117.

[156] H. Dai, Z. Chen, T. Li, Y. Li, J. Rare Earths, **30** (2012) 1123.

[157] S. Pattanayak, R.N.P. Choudhary, P.R. Das, Electron. Mater. Lett., **10** (2014) 165.

[158] P.-L. Chen, I.W. Chen, J. Am. Ceram. Soc., **79** (1996) 1793.

[159] R.K. Mishra, K.P. Dillip, R.N.P. Choudhary, A. Banerjee, J. Phys.: Condens. Matter, **20** (2008) 045218.

[160] C.-F. Chung, J.-P. Lin, J.-M. Wu, Appl. Phys. Lett., **88** (2006) 242909.

[161] S. Hemant, K.L. Yadav, J. Phys.: Condens. Matter, **23** (2011) 385901.

[162] P.C. Sati, M. Arora, S. Chauhan, S. Chhoker, M. Kumar, J. Appl. Phys., **112** (2012) 094102.

[163] P. Tirupathi, A. Chandra, J. Alloy. Compd., **564** (2013) 151.

[164] X. Martí, P. Ferrer, J. Herrero-Albillos, J. Narvaez, V. Holy, N. Barrett, M. Alexe, G. Catalan, Phys. Rev. Lett., **106** (2011) 236101.

[165] R. Jarrier, X. Marti, J. Herrero-Albillos, P. Ferrer, R. Haumont, P. Gemeiner, G. Geneste, P. Berthet, T. Schülli, P. Cevc, R. Blinc, S.S. Wong, T.-J. Park, M. Alexe, M.A. Carpenter, J.F. Scott, G. Catalan, B. Dkhil, Phys. Rev. B, **85** (2012) 184104.

[166] A. Kumar, J.F. Scott, R.S. Katiyar, Phys. Rev. B, **85** (2012) 224410.

[167] T. Prasit, T. Suwat, Y. Teerapon, M. Santi, J. Phys.: Condens. Matter, **20** (2008) 395227.

[168] C. Ang, Z. Yu, J. Appl. Phys., **91** (2002) 1487.

[169] N. Ikeda, H. Ohsumi, K. Ohwada, K. Ishii, T. Inami, K. Kakurai, Y. Murakami, K. Yoshii, S. Mori, Y. Horibe, H. Kito, Nature, **436** (2005) 1136.

[170] S.F. Shao, J.L. Zhang, P. Zheng, W.L. Zhong, C.L. Wang, J. Appl. Phys., **99** (2006) 084106.

[171] A.R. Makhdoom, M.J. Akhtar, R.T.A. Khan, M.A. Rafiq, M.M. Hasan, F. Sher, A.N. Fitch, Mater. Chem. Phys., **143** (2013) 256.

[172] A.N. Papathanassiou, I. Sakellis, J. Grammatikakis, Appl. Phys. Lett., **91** (2007) 122911.

[173] D.P. Singh, K. Shahi, K.K. Kar, Solid State Ion, **287** (2016) 89.

[174] C. Cramer, S. Brunklaus, E. Ratai, Y. Gao, Phys. Rev. Lett., **91** (2003) 266601.

[175] R.H. Chen, R.J. Wang, T.M. Chen, C.S. Shern, J Phys. Chem. C, **61** (2000) 519.

[176] R.H. Chen, R.Y. Chang, S.C. Shern, J Phys. Chem. C, **63** (2002) 2069.

[177] H.M. El-Mallah, N.A. Hegab, J. Mater Science, **42** (2006) 332.

[178] N. Ortega, A. Kumar, P. Bhattacharya, S.B. Majumder, R.S. Katiyar, Phys. Rev. B, **77** (2008) 014111.

[179] Z.M. Tian, S.L. Yuan, X.L. Wang, X.F. Zheng, S.Y. Yin, C.H. Wang, L. Liu, J. Appl. Phys., **106** (2009) 103912.

[180] T. Maity, S. Goswami, D. Bhattacharya, S. Roy, Phys. Rev. Lett., **110** (2013) 107201.

[181] A. B, K. Kensaku, K. Kunihiro, K. Shigeru, K. Hiroaki, H. Fumihiko, B. Areef, M.A. Jalil, M.A. Basith, J. Phys. D.: Appl. Phys., **49** (2016) 265003.

[182] L.W. Martin, S.P. Crane, Y.H. Chu, M.B. Holcomb, M. Gajek, M. Huijben, C.H. Yang, N. Balke, R. Ramesh, J. Phys.: Condens. Matter, **20** (2008) 434220.

[183] T. Shimada, Y. Uratani, T. Kitamura, Appl. Phys. Lett., **100** (2012) 162901.

[184] N.A. Hill, J. Phys. Chem. B, **104** (2000) 6694.

[185] G. Catalan, Appl. Phys. Lett., **88** (2006) 102902.

[186] Z. Guo, L. Yang, H. Qiu, X. Zhan, J. Yin, L. Cao, Mod. Phys. Lett. B, **26** (2012) 1250056.

[187] G. Burns, B.A. Scott, Phys. Rev. B, **7** (1973) 3088.

[188] J.D. Freire, R.S. Katiyar, Phys. Rev. B, **37** (1988) 2074.

[189] P.-H. Xiang, H. Takeda, T. Shiosaki, J. Appl. Phys., **103** (2008) 064102.

[190] D.C. Sinclair, A.R. West, J. Appl. Phys., **66** (1989) 3850.

[191] A. Molak, M. Paluch, S. Pawlus, J. Klimontko, Z. Ujma, I. Gruszka, J. Phys. D.: Appl. Phys., **38** (2005) 1450.

[192] H. Meštrić, R.-A. Eichel, K.-P. Dinse, A. Ozarowski, J.v. Tol, L.C. Brunel, J. Appl. Phys., **96** (2004) 7440.

[193] E. Erdem, R.a. Eichel, H. Kungl, M.J. Hoffmann, A. Ozarowski, J.V. Tol, L.C. Brunel, IEEE Trans. Ultrason. Ferroelectr. Freq. Control, **55** (2008) 1061.

[194] P. Jakes, E. Erdem, R.-A. Eichel, L. Jin, D. Damjanovic, Appl. Phys. Lett., **98** (2011) 072907.

[195] H.-J. Kleebe, S. Lauterbach, L. Silvestroni, H. Kungl, M.J. Hoffmann, E. Erdem, R.-A. Eichel, Appl. Phys. Lett., **94** (2009) 142901.

[196] G.-L. Tan, W. Li, J. Am. Ceram. Soc., **98** (2015) 1812.

[197] J.F. Herbst, F.E. Pinkerton, Phys. Rev. B, **57** (1998) 10733.

[198] S.V. Andreev, M.I. Bartashevich, V.I. Pushkarsky, V.N. Maltsev, L.A. Pamyatnykh, E.N. Tarasov, N.V. Kudrevatykh, T. Goto, J. Alloy. Compd., **260** (1997) 196.

[199] M. Gich, A. Roig, C. Frontera, E. Molins, J. Sort, M. Popovici, G. Chouteau, D. Martín y Marero, J. Nogués, J. Appl. Phys., **98** (2005) 044307.

[200] N. Wang, J. Cheng, A. Pyatakov, A.K. Zvezdin, J.F. Li, L.E. Cross, D. Viehland, Phys. Rev. B, **72** (2005) 104434.

[201] T.-J. Park, G.C. Papaefthymiou, A.J. Viescas, Y. Lee, H. Zhou, S.S. Wong, Phys. Rev. B, **82** (2010) 024431.

[202] N.V. Dang, T.D. Thanh, L.V. Hong, V.D. Lam, T.-L. Phan, J. Appl. Phys., **110** (2011) 043914.

[203] Ha M. Nguyen, N.V. Dang, P.-Y. Chuang, T.D. Thanh, C.-W. Hu, T.-Y. Chen, V.D. Lam, C.-H. Lee, L.V. Hong, Appl. Phys. Lett. , **99** (2011) 202501.

[204] Q.-L. Fang, J.-M. Zhang, K.-W. Xu, Phys. B: Condense Matt., **424** (2013) 79.

[205] I.N. Apostolova, A.T. Apostolov, S.G. Bahoosh, J.M. Wesselinowa, J. Appl. Phys., **113** (2013) 203904.

[206] F. Lin, D. Jiang, X. Ma, W. Shi, J. Magn. Magn. Mater., **320** (2008) 691.

[207] N.G. Eror, T.M. Loehr, B.C. Cornilsen, Ferroelectrics, **28** (1980) 321.

[208] G.-h. Margarita, C. Geneviève, B. Damien, G.-m. Antonieta, C.-r. Felipe, M. Rachid, Nano-Micro Lett., **5** (2013) 57.

[209] W.-S. Cho, E. Hamada, K. Takayanagi, J. Appl. Phys., **81** (1997) 3000.

[210] U.D. Venkateswaran, V.M. Naik, R. Naik, Phys. Rev. B, **58** (1998) 14256.

[211] N.V. Dang, T.-L. Phan, T.D. Thanh, V.D. Lam, L.V. Hong, J. Appl. Phys., **111** (2012) 113913.

[212] F.A. Rabuffetti, R.L. Brutchey, J. Am. Chem. Soc., **134** (2012) 9475.

[213] P.K. Dutta, J.R. Gregg, Chem. Mater., **4** (1992) 843.

[214] S. Rajan, P.M.M. Gazzali, G. Chandrasekaran, J. Alloy. Compd., **656** (2016) 98.

[215] D. Ginting, S.C. Yu, T.L. Phan, N.V. Dang, T.D. Thanh, V.D. Lam, J. Kor. Phys. Soc., **62** (2013) 2128.

[216] P.P. Khirade, S.D. Birajdar, A.V. Raut, K.M. Jadhav, Ceram. Int., **42** (2016) 12441.

[217] M.B. Stearns, Y. Cheng, J. Appl. Phys., **75** (1994) 6894.

[218] M. Valant, I. Arčon, I. Mikulska, D. Lisjak, Chem. Mater., **25** (2013) 3544.

[219] A. Zorko, M. Pregelj, M. Gomilšek, Z. Jagličić, D. Pajić, M. Telling, I. Arčon, I. Mikulska, M. Valant, Sci. Rep., **5** (2015) 7703.

[220] S. Chikada, K. Hirose, T. Yamamoto, Jpn. J. Appl. Phys., **49** (2010) 091502.

[221] S. Mohanty, S. Ravi, Solid State Commun., **150** (2010) 739.

[222] T. Dietl, J. Spałek, Phys. Rev. Lett., **48** (1982) 355.

[223] A.C. Durst, R.N. Bhatt, P.A. Wolff, Phys. Rev. B, **65** (2002) 235205.

[224] G.H. McCabe, T. Fries, M.T. Liu, Y. Shapira, L.R. Ram-Mohan, R. Kershaw, A. Wold, C. Fau, M. Averous, E.J. McNiff, Phys. Rev. B, **56** (1997) 6673.

[225] M. Tadica, M. Panjanb, V. Damnjanovic, I. Milosevic, Appl. Surf. Sci., **320** (2014) 183.

Paper Published in National/International Journals

1. Ferromagnetism and Ferroelectricity in Fe doped $BaTiO_3$.
   Bipul Deka, S. Ravi, A. Perumal and D. Pamu
   *Physica B: Condensed Matter, **448** (2014) 204-206*

2. Study of exchange bias in Mn doped $YFeO_3$ compounds.
   Bipul Deka, S. Ravi and A. Perumal
   *Journal of Superconductivity and Novel Magnetism, **29** (2016) 2165-2170*

3. Effect of Mn doping on magnetic and dielectric properties of $YFeO_3$.
   Bipul Deka, S. Ravi, A. Perumal and D. Pamu
   *Ceramics International, **43** (2017) 1323-1334*

4. Study of Impedance Spectroscopy and Electric Modulus of $PbTi_{1-x}Fe_xO_3$ (x = 0.0 – 0.3) Compounds.
   Bipul Deka, S. Ravi
   *Journal of Alloys and Compounds **720** (2017) 589-598*

5. Evolution of structural transition, grain growth inhibition and collinear antiferromagnetism in $(Bi_{1-x}Sm_x)FeO_3$ (x = 0 to 0.3) and their effects on dielectric and magnetic properties.
   Bipul Deka, S. Ravi and D. Pamu
   *Ceramics International **43** (2017) 16580*

6. Ferromagnetism in Fe doped $BaTiO_3$ ceramics
   Bipul Deka, S. Ravi
   Journal of Superconductivity and Novel Magnetism, doi:10.1007/s10948-017-4321-0

Publications From Other Related Works

1. Impedance spectroscopy and ac conductivity mechanism in Sm doped Yttrium Iron Garnet
   Aakansha, **Bipul Deka**, S. Ravi and D. Pamu
   *Ceramics International **43** (2017) 10468-10477*

2. Magnetic and dielectric properties of $Y_{3-x}Sm_xFe_5O_{12}$ (x = 0.0 to 3.0)
   Aakansha, **Bipul Deka**, S. Ravi
   Journal of Superconductivity and Novel Magnetism doi: 10.1007/s10948-017-4436-3

Papers Presented in Conferences/Seminars

1. Positive temperature coefficient of coercivity and resistivity in Fe doped $PbTiO_3$ ceramics
Oral Presentation
Bipul Deka, S. Ravi and D. Pamu
National Seminar on Advances in Materials Science
Gauhati University during 24-25th March 2017

2. High temperature weak ferromagnetism in Fe doped $PbTiO_3$
Oral Presentation
Bipul Deka, S. Ravi and A. Perumal
International conference TECHNOVA 2016
Gauhati University, 22–23 November 2016

3. Study of electric modulus and scaling behavior in $YFeO_3$
Oral Presentation
Bipul Deka, S. Ravi and D. Pamu
International conference TECHNOVA 2016
Gauhati University, 22–23 November 2016

4. Spin Re-orientation in Mn doped $YFeO_3$
Poster presentation
Bipul Deka, S. Ravi and A. Perumal
International Conference on Magnetic Materials and Applications
VIT University during 2 – 4 December 2015

5. Effect of Sm doping on the structural, magnetic and dielectric properties of $BiFeO_3$
Poster presentation
Bipul Deka, S. Ravi, A. Perumal and D. Pamu
International Conference on Magnetic Materials and Applications
Pondicherry University, 15 – 17 September 2014

6. Ferromagnetism and ferrolectricity in Fe doped $BaTiO_3$
Poster presentation
Bipul Deka, S. Ravi, A. Perumal and D. Pamu
International Conference on Magnetic Materials and Applications
IIT Guwahati during 5 – 7 December 2013

Workshops Attended

1. National Workshop on Advanced Probing Techniques in TEM
   Jointly organized by Electron Microscopic Society of India and Department of Physics, Indian Institute of Technology Guwahati, Guwahati at IIT Guwahati, India during 15-16 February 21, 2016.

2. IUCr workshop on X-ray diffraction system and related applications
   Organized by PANalytical held at IIT Guwahati during 11-12 September 2014

3. QIP AICTE sponsored short term course on "Computational Techniques in Physics" IIT Guwahati during 1st – 6th August 2011.

----------×----------